

Microfluidics for
Molecular Measurements
and Quantitative
Distributable Diagnostics

Thesis by
David Anthony Selck

In Partial Fulfillment of the Requirements for
the degree of
Doctor of Philosophy

The logo for the California Institute of Technology (Caltech), featuring the word "Caltech" in a bold, orange, sans-serif font.

CALIFORNIA INSTITUTE OF TECHNOLOGY
Pasadena, California

2017
(Defended July 8, 2016)

© 2016

David Anthony Selck
ORCID: 0000-0002-0591-4165

ACKNOWLEDGEMENTS

There are countless people who both could and should be acknowledged in the completion of this phase of my life. Chief among them, however, is my wife Maxanne. She has provided unparalleled support throughout my time here at Caltech. She has sacrificed greatly, and provided encouragement, a positive attitude, and a cheery disposition at every corner. I thank also my parents for instilling in me the desire, determination, and drive to achieve difficult things and pursue whatever path I deemed most interesting. I thank also my children Gilbert and Susan for always greeting me with a smile and a laugh. Whether it be excitement after coming home from a long day of work, or a kiss and a smile to wake me up they have provided more joy and happiness than a parent could ask for.

Also to my advisor Rustem Ismagilov. He has been a great support, mentor, and advisor throughout my five years at Caltech. He has taught me how to think critically, tackle difficult problems, and do effective research. He has also provided me with countless opportunities to stretch, grow, and learn through a wide variety of experiences, opportunities, and interactions. I will ever be indebted to him for the many lessons learned.

I would also like to thank the members of the Ismagilov lab. While I have learned from all members of the lab, those to whom I owe the greatest thanks are those with whom I have collaborated. Those people are Bing Sun, Mikhail Karymov, Jesus Rodriguez-Manzano, Eugenia Khorosheva, Stefano, Begolo, Dmitriy Zhukov, Liang Li, and Erik Jue. Not only did I find the science that was done in the lab stimulating and fulfilling, but the discussions that I was able to have with all of the members outside of the realm of science broadened my perspective and helped me greater understand the world around me.

It would also be a great oversight if I did not acknowledge the members of the Guttman lab for their contributions during the course of my degree. Mitch Guttman as a member of my thesis committee and collaborator has been instrumental in broadening my perspective into thinking about single cells and how and why to study them. I would also specifically like to thank both Sofia Quinodoz for all of the time and energy that she has spent helping on our collaborative work as well as Ward Walkup for invaluable insight and experience.

I would also like to thank the ARCS Foundation for their fellowship support while working on my PhD. Their generous support allowed me to be able to support my family while working toward my degree without fear about when the next paycheck would arrive.

I am also grateful to Professors Long Cai and Bil Clemons for serving alongside Mitch Guttman and Rustem Ismagilov on my thesis committee and providing insightful comments and help in achieving this degree.

ABSTRACT

A major challenge in global health care is a lack of portable and affordable quantitative diagnostic devices. This is because classic quantification of biomolecules is typically performed using kinetic assays that require strict control only found in controlled laboratory environments. By using the power of microfluidics, quantitative assays can be performed robustly in a “digital” format that is decoupled from precise kinetics through highly parallelized qualitative reactions. The benefits of performing quantitative assays in a digital format extend beyond just assay robustness to reduction of instrumental complexity, increase in quantitative precision, and an increase in the amount of information that can be gained from a single experiment. These microfluidic architectures, however, are not limited to usage in scenarios of quantification of biomolecules. These architectures can also potentially be extended to answering complex biological questions in single cells, such as determining the 3-dimensional organization of nuclear DNA and RNA.

PUBLISHED CONTENT AND CONTRIBUTIONS

Chapter 2: Selck, D. A., Karymov, M. A., Sun, B., & Ismagilov, R. F. (2013). Increased robustness of single-molecule counting with microfluidics, digital isothermal amplification, and a mobile phone versus real-time kinetic measurements. *Analytical chemistry*, 85(22), 11129-11136. DOI: 10.1021/ac4030413

This article was co-first authored by Selck, Karymov, and Sun. The paper describes a method of quantifying HIV viral load using isothermal chemistry, microfluidics, and a cell-phone fluorescence based quantification method. The roles that I held in the project were principle writer of the paper, software and algorithm development, and device design. Responsibilities that I shared were experimental design and analysis.

Chapter 3: Rodriguez-Manzano, J., Karymov, M. A., Begolo, S., Selck, D. A., Zhukov, D. V., Jue, E., & Ismagilov, R. F. (2016). Reading Out Single-Molecule Digital RNA and DNA Isothermal Amplification in Nanoliter Volumes with Unmodified Camera Phones. *ACS nano*, 10(3), 3102-3113. DOI: 10.1021/acsnano.5b07338

This article describes a method of using isothermal chemistry, microfluidics, and an unmodified cell-phone to quantify HCV viral load. The role that I held in the project was algorithm development, software design, contributions to assay design, and theoretical predictions of cell-phone ratiometric values.

Chapter 4: Begolo, S., Zhukov, D. V., Selck, D. A., Li, L., & Ismagilov, R. F. (2014). The pumping lid: investigating multi-material 3D printing for equipment-free, programmable

generation of positive and negative pressures for microfluidic applications. *Lab on a Chip*, 14(24), 4616-4628. DOI: 10.1039/C4LC00910J

This article describes a method of using rapid prototyping to develop methodologies to pump liquids into microfluidic devices precisely and controllably. The role that I held in the project was designing, writing the software for, and validating the pressure measurement system, as well as designing, manufacturing, and validating the vacuum loaded microfluidic device.

Chapter 5: Selck, D.A., Ismagilov, R.F. (2016). Instrument for Real-Time Digital Nucleic Acid Amplification on Custom Microfluidic Devices. *PLOS One*, in submission

This article describes an instrument that can be used for digital real-time analyses. The role that I held in the project was leading the design, construction, and validation, including all aspects from hardware to software other than the optical designs which were provided by David Tracy.

Chapter 6: Sun, B., Rodriguez-Manzano, J., Selck, D. A., Khorosheva, E., Karymov, M. A., & Ismagilov, R. F. (2014). Measuring Fate and Rate of Single-Molecule Competition of Amplification and Restriction Digestion, and Its Use for Rapid Genotyping Tested with Hepatitis C Viral RNA. *Angewandte Chemie International Edition*, 53(31), 8088-8092. DOI: 10.1002/anie.201403035

This article describes a method of using a competition reaction between amplification and degradation of genotype specific strands of the HCV virus to perform both genotyping and quantification. The role that I held in the project was in instrumentation and analysis.

Specifically, I designed and built the large-format real-time digital PCR instrument used to collect information on reaction kinetics on microfluidic devices.

Chapter 7: Khorosheva, E. M., Karymov, M. A., Selck, D. A., & Ismagilov, R. F. (2015).

Lack of correlation between reaction speed and analytical sensitivity in isothermal amplification reveals the value of digital methods for optimization: validation using digital real-time RT-LAMP. *Nucleic Acids Research*, 44(2), e10. DOI: 10.1093/nar/gkv877

This article describes a method of using kinetic information from nanoliter scale reactions on microfluidic devices to design better overall quantitative assays. The roles that I held in the project were in instrumentation, analysis, and compilation. Specifically, I designed and built the large-format real-time digital PCR instrument used to collect information on reaction kinetics on microfluidic devices, as well as analyze and compile into figures the data presented in the paper.

TABLE OF CONTENTS

Acknowledgements	iii
Abstract	v
Published Content and Contributions.....	vi
Table of Contents.....	ix
List of Illustrations and Tables	xiii
Chapter 1: Summary Introduction and Theme of the Thesis.....	1
Chapter 2: Single-Molecule Counting with Microfluidics, Digital Isothermal Amplification, and Mobile Phone Is Robust, Unlike Real-Time Kinetics	5
Abstract	5
Introduction.....	6
Experimental.....	11
Results and Discussion	14
Conclusions.....	25
References.....	27
Chapter 3: Reading out Single-Molecule Digital RNA and DNA Isothermal Amplification in Nanoliter Volumes with Unmodified Camera Phones	34
Abstract	34

Introduction.....	35
Results and Discussion	38
Conclusions.....	54
Methods	56
References.....	64
Chapter 4: The Pumping Lid: Investigation Multi-Material 3D Printing for Equipment-Free, Programmable Generation of Positive and Negative Pressures for Microfluidic Applications.....	74
Abstract	74
Introduction.....	75
Results and Discussion	78
Conclusions.....	103
References.....	106
Chapter 5: Instrument for Real-Time Digital Nucleic Acid Amplification on Custom Microfluidic Devices	112
Abstract	112
Introduction.....	113
Results and Discussion	116

Materials and Methods	133
Conclusions.....	132
References.....	141
Chapter 6: Measuring the Fate and Rate of Single-Molecule Competition of Amplification and Restriction Digestion, and Its Use for Rapid Genotyping Tested with Hepatitis C Viral RNA	145
Abstract.....	145
Results Discussion and Conclusions.....	145
References.....	158
Chapter 7: Lack of Correlation between Reaction Speed and Analytical Sensitivity in Isothermal Amplification Reveals the Value of Digital Methods for Optimization: Validation Using Digital Real-Time RT-LAMP.....	162
Abstract.....	162
Introduction.....	163
Materials and Methods	168
Results.....	174
Discussion.....	187
References.....	192

Chapter 8: Progress toward 3-Dimensional Mapping of Nuclear	
Compartments in Single-Cells Using a Novel Sequencing Based Method ...	202
Introduction.....	202
Split-and-Pool Barcoding	204
Microfluidic Method for Single-Cell Mapping	206
Simplified Single-Cell Preparation Technique.....	211
Conclusions.....	219
References.....	221
Chapter 8-Supplement: Intra-Chromosomal Interaction Matrices	229

LIST OF ILLUSTRATIONS AND TABLES

<i>Number</i>	<i>Page</i>
Figure 2-1.....	10
Figure 2-2.....	16
Figure 2-3.....	20
Figure 2-4.....	21
Figure 2-5.....	23
Figure 3-1.....	39
Figure 3-2.....	45
Figure 3-3.....	47
Figure 3-4.....	50
Figure 3-5.....	51
Figure 3-6.....	53
Figure 4-1.....	79
Figure 4-2.....	86
Figure 4-3.....	89
Figure 4-4.....	92

Figure 4-5.....	93
Figure 4-6.....	96
Figure 4-7.....	98
Figure 5-1.....	118
Figure 5-2.....	120
Figure 5-3.....	122
Figure 5-4.....	126
Figure 5-5.....	127
Figure 5-6.....	131
Figure 6-1.....	147
Figure 6-2.....	149
Figure 6-3.....	151
Figure 6-4.....	154
Figure 6-5.....	155
Figure 7-1.....	164
Figure 7-2.....	176
Table 7-1	177
Figure 7-3.....	179

Figure 7-4.....	181
Figure 7-5.....	183
Figure 7-6.....	186
Figure 8-1.....	206
Figure 8-2.....	207
Figure 8-3.....	211
Figure 8-4.....	213
Figure 8-5.....	215
Figure 8-6.....	216
Figure 8-7.....	217
Figure 8-8.....	218
Figure 8-9.....	219
Figure 8S-1	230
Figure 8S-2	231
Figure 8S-3	232
Figure 8S-4	233
Figure 8S-5	234

Chapter 1:

Summary Introduction and Theme of the Thesis

Microfluidics as a tool have been used in a variety of different scenarios to investigate a wide multitude of problems. Two widely explored areas of microfluidics that will be discussed in this thesis are those of quantitative nucleic acid amplification tests (NAATs), and single cell studies. Microfluidics are uniquely suited to these two areas as both can be performed well through a process of compartmentalization whereby a solution is distributed evenly among thousands of smaller volumes typically in the picoliter to nanoliter range.

Classically, NAATs have been performed by amplifying a specific sequence of a nucleic acid strand and monitoring its amplification rate as compared to a standard. While performing NAATs in this manner is highly effective, it is only suitable for first world scenarios where a tightly controlled environment and access to advanced instrumentation can be guaranteed. These conditions are required because different environmental factors can alter the kinetics of the amplification reaction which impedes the ability to perform direct and accurate quantitative tests. There are a variety of different situations in which these conditions cannot be guaranteed, such as diagnostic viral load testing outside of centralized laboratories. Therefore, a better alternative would be a NAAT which does not require any advanced instrumentation and is more robust to a wide variation in environmental conditions.

In chapter 2 of this thesis, previously published work on which I am co-first author is presented to directly address these issues by showing that a microfluidics-based digital

NAAT is able to be more robust to changes in environmental conditions through utilizing a process of limiting dilution wherein not all of the reactions get amplifiable nucleic acids. In this manner, only the proportion of total positive reactions and reaction volume is required to determine initial concentration as opposed to the rate at which those reactions proceeded. We also showed that the outcome of these reactions can be visualized and automatically interpreted using a modified smart phone based fluorescent reader. This dramatically reduces the assay requirements, and shows how quantitative NAATs could be transferred from the laboratory to the field.

In chapter 3 of this thesis, previously published work on which I am a contributing author is presented which extends the work outlined in chapter 2. The work is extended by the development of a ratiometric color based readout which does not require any modifications to the cell phone being used. This was accomplished by adjusting the chemistry of the amplification reaction such that a distinct color change occurs if there was amplifiable DNA in the reaction well. The ratiometric nature of the readout is critical to the robustness of the assay as the color change is not dramatic, and as such depending on light levels and color during imaging different biases could be introduced in the analysis. We showed that using this type of readout method is potentially robust enough that it can be successfully applied to any phone or other imaging device as long as the quality of the images produced is sufficient.

Chapter 4 of this thesis contains a previously published article on which I am a contributing author that details the usage of 3d printed attachments for microfluidic devices for reliable and equipment free fluid pumping. Typical microfluidic devices rely on complex equipment to introduce the fluids onto the device. This would inhibit their

usability in remote applications as access to that equipment and even electricity may be impeded. The 3d printed attachments outlined in the article can be rapidly manufactured with a tailored flow profile that matches what is required for a particular microfluidic device including positive and negative pressures. It is also shown in the article that the pumping lids are sufficiently fault tolerant and easy to use that loading of a microfluidic SlipChip device was demonstrated by a 6-year old untrained user.

While performing NAATs in a digital format as described in chapter 2 and 3 provides for a robust and reliable method of quantification, optimization of the required assays can be difficult without the type of kinetic information that is provided in a traditional assay. Commercial instrumentation exists for monitoring the kinetics of NAATs on digital devices, however, the types of microfluidic devices which can be run are limited to those produced by the manufacturer. Therefore, if one wants to study unsupported chemistries or use custom microfluidic devices then settling for end-point readouts has usually been required. Chapter 5 details unpublished work of designing, constructing, and validating an instrument which is able to obtain kinetic traces of reactions on custom microfluidic devices with a multi-channel fluorescent readout and tight temperature control. This instrument also is supported by a full software suite which simplifies the collection and analysis of software through an easy to use application.

Chapter 6 contains a previously published article on which I am a contributing author that uses the instrumentation outlined in chapter 5 to optimize a digital loop-mediated amplification (LAMP) assay of hepatitis C virus (HCV) RNA. We were able to show that optimization of this assay for the digital format greatly benefits from the individual reactions' kinetic traces as the reaction rate is not tightly coupled with the reaction

efficiency. The reaction rate and overall reaction efficiency in LAMP can be decoupled due to a complex arrestable initiation step followed by a rapid and ungated amplification step. Optimization of these reactions for a digital format with information about both kinetics and statistics decouples these two problems as arrested one is able to observe the individual amplification profiles from hundreds to thousands of individual molecules.

Chapter 7 contains a previously published article which used the technology detailed in chapter 5 to obtain detailed information about a method whereby quantification and genotyping of the HCV virus were performed at the same time. Both sets of information are important in treating HCV infections as both potentially impact drug choice. Certain genotypes of HCV respond differently to treatments, and higher concentrations of the virus may warrant a more aggressive course of medicine. Kinetic information was critical in truly understanding how these reactions performed in a digital format, as the genotyping reactions occurred via a competition reaction between universal amplification of HCV and targeted degradation of specific genotypes of HCV.

Chapter 8 of this thesis contains unpublished progress towards using microfluidics to obtain information about chromatin conformation in single cells. Understanding the chromosomal structure of cells, and what part RNAs play in that structure is key in continuing to gain insights into cellular function. Currently there are methods whereby DNA-DNA contacts can be elucidated in single cells; however, they have a somewhat limited efficiency, and cannot provide information about DNA-RNA contacts. Through a collaboration with the Mitchell Guttman group at the California Institute of Technology we have made progress towards applying a high-efficiency method of globally mapping high order interactions between DNA and RNA from single cells using microfluidics.

Chapter 2:

Single-Molecule Counting with Microfluidics, Digital Isothermal Amplification, and Mobile Phone Is Robust, Unlike Real-Time Kinetics*

Abstract

Quantitative bioanalytical measurements are commonly performed in a kinetic format, and are known to not be robust to perturbation that affects the kinetics itself, or the measurement of kinetics. We hypothesized that the same measurements performed in a “digital” (single-molecule) format would show increased robustness to such perturbations. Here, we investigated the robustness of an amplification reaction (reverse-transcription loop-mediated amplification, RT-LAMP) in the context of fluctuations in temperature and time when this reaction is used for quantitative measurements of HIV-1 RNA molecules under limited-resource settings (LRS). The digital format that counts molecules using dRT-LAMP chemistry detected a two-fold change in concentration of HIV-1 RNA despite a 6 °C temperature variation (p-value = 6.7×10^{-7}), whereas the traditional kinetic (real-time) format did not (p-value = 0.25). Digital analysis was also robust to a 20-minute change in reaction time, to poor imaging conditions obtained with a consumer cell-phone camera, and to automated cloud-based processing of these images ($R^2 = 0.9997$ vs. true counts over a 100-fold dynamic range). Fluorescent output of multiplexed PCR amplification could also be imaged with the cell phone camera using flash as the excitation source. Many nonlinear amplification schemes based on organic, inorganic, and biochemical reactions have been developed but their robustness is not well

* This chapter was first published in *Analytical Chemistry* with authorship belonging to David A. Selck, Mikhail A. Karymov, Bing Sun, and Rustem F. Ismagilov. The original manuscript can be found at: <http://dx.doi.org/10.1021/ac4030413>

understood. This work implies that these chemistries may be significantly more robust in the digital, rather than kinetic, format. It also calls for theoretical studies to predict robustness of these chemistries, and more generally to design robust reaction architectures. The SlipChip that we used here and other digital microfluidic technologies already exist to enable testing of these predictions. Such work may lead to identification or creation of robust amplification chemistries that enable rapid and precise quantitative molecular measurements under LRS. Furthermore, it may provide more general principles describing robustness of chemical and biological networks in digital formats.

Introduction

A wide range of nonlinear and especially autocatalytic chemical amplification schemes are being developed and studied using organic, inorganic, and biochemical reactions.¹⁻¹² These studies are motivated both by understanding of signal transduction in natural systems, and by opportunities for rapid, ultrasensitive detection and quantification of analyte molecules. In natural systems, networks of biochemical reactions crucial for the function of living organisms are robust to intrinsic and extrinsic fluctuations, to environmental changes, and even to some perturbations not likely to be previously encountered by the organism.¹³⁻¹⁶ However, robustness of synthetic nonlinear chemical amplification schemes is not yet fully understood: despite tremendous progress in experimental and theoretical studies of nonlinear chemical dynamics,¹¹ it is not clear which specific reactions or general reaction architectures are robust to which perturbations. Robustness becomes an especially relevant property of a nonlinear chemical amplification scheme when the amplification is used for quantitative analytical measurements. Quantitative measurements of biomolecules are essential for addressing a

range of societal problems in human health, food and water safety,^{17,18} environmental monitoring,¹⁹ and biosecurity.²⁰

Typically, kinetic assays are used for quantitative measurements.²¹ These assays are performed through monitoring the progress of a reaction at a single time point in an end-point measurement, or at multiple time points in a real-time measurement. Because both extent of reaction (e.g., a concentration measured by an optical imaging method) and time must be measured in kinetic assays, one would expect the results of such assays to be sensitive to changes in reaction conditions and to fluctuations in the performance of the readout instrument. For a linear amplification scheme in a kinetic format, a temperature change leading to a 50% change in the rate constant would lead to a 50% error in quantification. One would expect an autocatalytic amplification scheme to be especially sensitive to these fluctuations because small kinetic perturbations would become exponentially compounded: a 50% change in the rate constant could lead to over a 400,000% error in quantification (see Supplementary Information online). This problem is avoided in real-time polymerase chain reactions (qPCR) because temperature cycling “gates” the amplification process: to a first approximation, as long as amplification kinetics remain fast enough to complete one doubling of the nucleic acid target within one PCR cycle, changes in the rate of this amplification should not affect the result.^{22,23} The majority of biological and chemical amplification strategies are isothermal and therefore cannot take advantage of this “gating.”

Any study of robustness must be defined within a particular context that sets the type and magnitude of perturbations that might affect the system being studied. We chose the context of quantitative measurements performed under limited-resource settings (LRS).

These settings lack sophisticated equipment and expertise²⁴ and span both the developing and the developed world (e.g., at-home or field testing). Under these settings, one may expect variation of temperature of several degrees Celsius, imaging performed with non-quantitative consumer electronic devices such as cell phones, and variations in assay time due to operator error. While a number of robust qualitative tests, such as home pregnancy tests, are already compatible with LRS, suitable quantitative assays are needed. For instance, a high-quality, inexpensive, rapid HIV-1 viral load assay for LRS would enable infant diagnosis and monitoring of the emergence of drug resistance during therapy.²⁵ While clinically used HIV-1 viral load assays measure HIV-1 RNA with relatively high precision (< 30% CV),²⁶ at least 3-fold change in viral load is considered to be clinically significant.²⁷ Autocatalytic amplification schemes¹⁻¹² are attractive for these settings; in principle they could convert the presence of a few molecules to a large signal observed and quantified by eye or an inexpensive optical setup. In practice, among other factors, their use under LRS is hampered by the lack of robustness to experimental perturbations.

We hypothesized that autocatalytic, exponential amplification would be more robust to variations in temperature, time, and imaging quality in a “digital” format rather than a kinetic, real-time format (Figure 2-1). In a typical digital analysis,²⁸⁻³¹ a sample is separated into discrete volumes such that not all volumes contain a molecule of interest (Figure 2-1a). After amplification, only those volumes that contained one or more molecules of interest produce a fluorescent signal. This information can be used to calculate the concentration of the target molecule using Poisson statistics. We hypothesized that, since for quantification, these “digital” methods require simply

counting “positive” and “negative” reaction wells—and thus do not require knowledge of time, reaction kinetics, or precise measurement of reaction progress—the results obtained by digital methods would not be affected strongly by temperature fluctuations (Figure 2-1b) or reaction time (Figure 2-1c) and should not require precise imaging instruments or very sophisticated analysis algorithms (Figure 2-1d). Therefore, we also hypothesized that as long as the amplification chemistry produces a specific and sufficiently bright optical signal, semi-quantitative imaging devices such as cell phone cameras³²⁻³⁴ should be able to detect positive signals and differentiate them from negative signals, thereby providing quantitative information. This hypothesis relies on a significant assumption: it can become true only if initiation of amplification reactions from single molecules is robust to these perturbations. Digital PCR is now commercially available and is used for a number of research applications. The limits of its robustness remain to be investigated; it is not obvious that it would be robust because results of digital PCR are known to be affected by experimental conditions.³⁵ Such work is outside the scope of the present paper, as we are focusing on the more general question of robustness of isothermal amplification strategies, which also has not been investigated in this context.

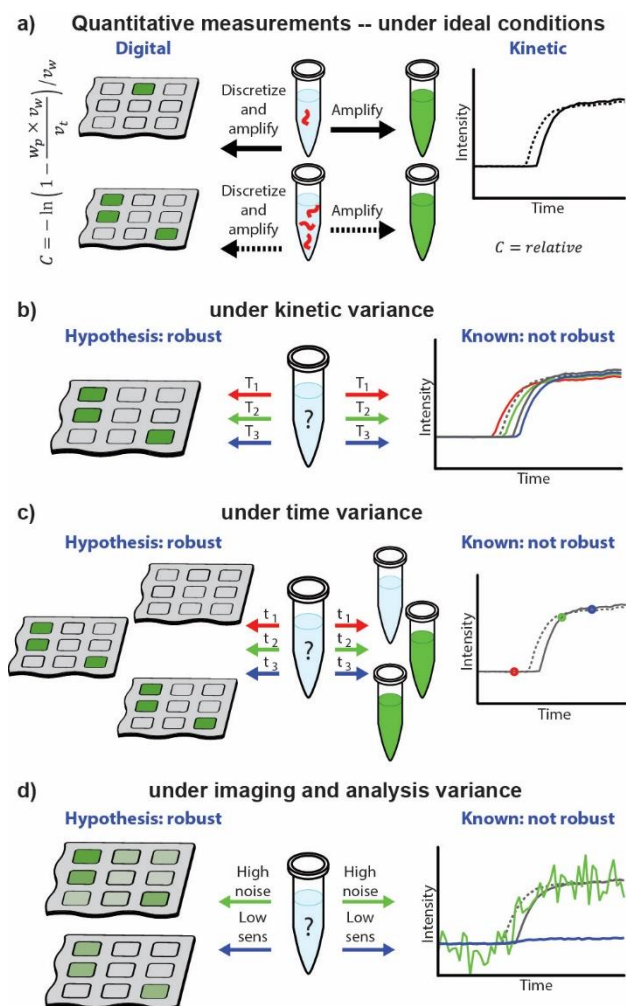


Figure 2-1. Robustness of quantification in digital vs. kinetic formats. Cartoons for the curves in the kinetic format are drawn to resemble a specific case of real-time nucleic acid amplification. (a) An illustration comparing digital and kinetic formats under ideal conditions. In a digital format, individual molecules are separated into compartments and amplified, requiring only an end-point readout. The original concentration (C) of the analyte can be calculated by the equation on the left (where w_p = the number of positive wells, v_t = the total device volume, and v_w = the volume of each well). In a kinetic format, the analyte is amplified in a bulk culture and the progress of amplification, measured as intensity, is monitored as a function of time. The original concentration is determined by comparing the reaction trace to standard curves from solutions of known concentration. (b) An illustration of the effects of kinetic variation (shown as differences in amplification temperature) in digital and real-time formats. In a digital format, we hypothesized that variance in the kinetic rate of amplification would not affect the end-point readout. In a real-time format, the kinetic rate determines the reaction curve and thus the relative concentration; therefore, it is known to be not robust. (c) An illustration of the effects of time variance (shown as readout time) in digital and real-time formats. Since digital requires only end-point readout, we hypothesized that exact knowledge of

time would not be required and the output should be robust to variation in reaction time beyond the optimal reaction time. In a real-time format, precise knowledge of time and sufficient time points are required in order to accurately quantify concentration; therefore, it is known to be not robust to variation in reaction time. (d) An illustration of the effects of imaging in digital and real-time formats. In a digital format, one only needs to be able to distinguish a positive from a negative signal, and therefore we hypothesized that imaging conditions with either increased noise or decreased sensitivity would not affect the measurement or data analysis. In a real-time format, imaging conditions with increased noise or decreased sensitivity can affect quantitative ability by producing reaction traces that cannot be compared to standards; therefore, it is known to be not robust to variation in imaging conditions.

Experimental

Real-time RT-LAMP amplification of HIV-1 RNA

For two-step RT-LAMP amplification, a first solution (20 μ L) containing 10 μ L RM, 1 μ L BSA, 0.5 μ L EXPRESS SYBR® GreenER™ RT module, 0.5 μ L BIP primer (10 μ M), various amounts of template, and nuclease-free water, was first incubated at 50 °C for 10 min and then mixed with a second solution (20 μ L), containing 10 μ L RM, 1 μ L BSA, 2 μ L EM, 1 μ L or 2 μ L FD, 2 μ L other primer mixture, 1 μ L Hybridase™ Thermostable RNase H, and nuclease-free water. The 40 μ L mixture was split into 4 aliquots and loaded onto an Eco real-time PCR machine. For one-step RT-LAMP amplification, a 40 μ L RT-LAMP mix contained the following: 20 μ L RM, 2 μ L BSA (20 mg/mL), 2 μ L EM, 2 μ L FD, 2 μ L of primer mixture, various amount of template solution, and nuclease-free water. The mixture was split into 4 aliquots and loaded onto the Eco real-time PCR machine. Data analysis was performed using Eco software (See details in Supplementary Information online).

Two-step dRT-LAMP amplification of HIV-1 RNA on SlipChip

The procedures used to perform two-step dRT-LAMP amplification on SlipChip were described in a previous publication.³⁶ A first solution (equivalent to the one described above) was loaded onto a SlipChip device and incubated at 50 °C for 10 min, and then a second solution (equivalent to the one described above) was loaded onto the same device and mixed with the first solution. The entire filled device was incubated at various temperatures (57 °C, 60 °C, or 63 °C) for 60 min.

Multiplexed PCR amplification on SlipChip

The PCR mixture used for amplification of *Staphylococcus aureus* genomic DNA on a multiplexed SlipChip contained the following: 10 µL 2X SsoFast Evagreen SuperMix (BioRad, CA), 1 µL BSA (20 mg/mL), 1 µL of 1 ng/µL gDNA, 0.5 µL SYBR Green (10x) and 7.5 µL nuclease-free water. Primers were pre-loaded onto the chip using a previously described technique (See details in Supplementary Information online). The PCR amplification was performed with an initial 95 °C step for 5 min, and then followed by 40 cycles of (i) 1 min at 95 °C, (ii) 30 sec at 55 °C, and (iii) 45 sec at 72 °C. An additional 5 min at 72 °C was performed to allow thorough dsDNA extension.

Cell phone camera setup and settings

A Nokia 808 Pureview cell phone was used to image and count microwells containing the amplification product. The Nokia 808 features 41-megapixel sensor with a pixel size of 1.4 µm. The camera uses pixel oversampling technology, which combines multiple pixels to increase the sensitivity of each individual pixel in the final image. Using a commercially available 0.67 x objective, we were able to obtain images at a distance of 6.5 cm, thus further improving imaging sensitivity. A set of two filters was used both to

excite and detect fluorescence. Two excitation filters (FD1B) were stacked and attached in front of the camera flash. For fluorescence detection, two 5CGA-530 long-pass filters were inserted into magnetically mounted lens (See Supplementary Information online for more details).

Cell phone imaging of dRT-LAMP devices was performed with the devices tilted at ~10 degrees relative to the cell phone plane to prevent direct reflection of the flash into the lens. All images were taken using the standard cell phone camera application. The white balance was set to automatic, the ISO was set at 800, the exposure value was set at +2, the focus mode was set to “close-up,” and the resolution was adjusted to 8 MP.

Cell phone imaging of multiplexed PCR devices was performed by imaging the devices in a shoebox painted black. The white balance was set to automatic, the ISO was set at 1600, the exposure value was set at +4, the focus mode was set to “close-up,” and the resolution was adjusted to 8 MP. Images were processed using a free Fiji image processing package available on the Internet (See Supplementary Information online for details of the procedure).

Cloud-based automatic analysis

The Symbian software on which the Nokia 808 cell phone is based can access Skydrive, a cloud-based storage service. This service can automatically upload images to the cloud directly after imaging, without any user intervention. Here, we used a central computer with a custom Labview program to process all the uploaded files automatically. The process detailing the image analysis, as well as videos showing the process as seen by the user, can be found in the Supplementary Information online.

Results and Discussion

To test these hypotheses, we selected HIV-1 RNA as a target molecule and selected isothermal digital reverse transcription-loop-mediated amplification (dRT-LAMP) as the amplification chemistry. We chose LAMP amplification chemistry for three reasons: i) when performed with a qualitative readout, in at least one example it is known to tolerate a number of perturbations,³⁷ so the question of robustness with a quantitative readout is a meaningful one; ii) while it is an autocatalytic, exponential amplification chemistry, its mechanism³⁸ is sufficiently complex that it was not obvious whether its initiation phase or propagation phase, and therefore the digital or kinetic format, would be more affected by perturbations; and iii) digital LAMP has been recently demonstrated on various microfluidic platforms.^{36,39,40} We used a microfluidic SlipChip device⁴¹ because it is well-suited for simple confinement and amplification of single molecules,⁴² it is convenient for performing multi-step reactions on single molecules,^{36,43} and because it has been validated with dRT-LAMP.³⁶ We used a two-step RT-LAMP protocol because it is more efficient³⁶ than one-step RT-LAMP for the specific sequences used in this study. Also, RT-LAMP is an attractive amplification chemistry⁴⁴ for LRS because it does not require thermocycling equipment and can be run using chemical heaters that do not require electricity.^{45,46} Furthermore, it is compatible with highly fluorescent calcein-based readout chemistry.⁴⁷

First, we asked whether quantitative measurements by real-time RT-LAMP assays are robust to changes in temperature. We tested the robustness of a two-step real-time RT-LAMP assay to temperature fluctuations using a commercial instrument (Figure 2-2a).

The precision of the assay for measuring two concentrations (1×10^5 copies/mL and $2 \times$

10^5 copies/mL) of HIV-1 RNA at three temperatures over a 6-degree temperature range (57 °C, 60 °C, 63 °C) was tested by comparing the reaction time (see Supplementary Information online) for these two concentrations measured on an Eco real-time PCR machine. At each individual temperature, the real-time RT-LAMP assay could successfully distinguish between the two concentrations (at 57 °C $p = 0.007$, at 60 °C $p = 0.01$, at 63 °C $p = 0.04$, the null hypothesis being that the two concentrations were identical). Therefore, we concluded that the assay itself was performing properly. The assay, however, was not robust to temperature fluctuations: changes of 3 °C introduced a larger change in the assay readout (reaction time) than the 2-fold change in the input concentration. Therefore, when temperature is not controlled precisely, this real-time RT-LAMP assay cannot resolve a 2-fold change in concentration of the input HIV-1 RNA.

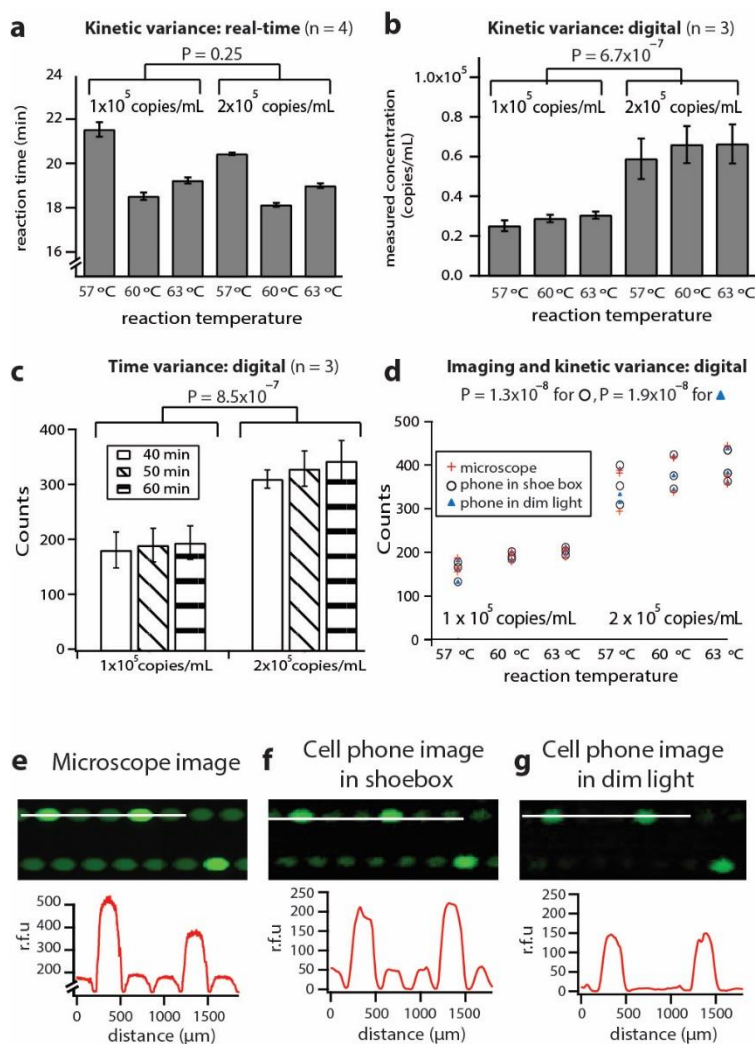


Figure 2-2. Evaluation of the robustness of real-time RT-LAMP versus digital RT-LAMP with respect to changes in temperature, time, and imaging conditions. (a-b), Graphs showing the results of (a) real-time RT-LAMP experiments and (b) digital RT-LAMP experiments for two concentrations across a 6-degree temperature range. Imaging was performed with a microscope. (c) A graph showing the number of positive counts from dRT-LAMP experiments for two concentrations at various reaction times. (d) A plot comparing the data obtained from imaging with a microscope in part (b), data obtained from imaging dRT-LAMP with a cell phone in a shoebox, and data obtained from imaging dRT-LAMP in dim lighting (~3 lux) across a 6-degree temperature range. P-values denote statistical significance of all data for each concentration at a given imaging condition, irrespective of temperature (the null hypothesis being that the two concentrations were equivalent). (e-g) Top: Cropped and enlarged images of a dRT-LAMP reaction imaged with a microscope (e), a cell phone and shoe box (f), and a cell phone in dim lighting (g). Bottom: A corresponding line scan indicates fluorescence output from the region marked in white in each image. False color has been added in (e). The number of positives in each dRT-LAMP experiment imaged with a cell phone was counted manually. Error bars represent the standard deviation of the distribution.

We then tested whether a digital format of this RT-LAMP assay performed on a chip was robust to the same changes in temperature as those tested in the real-time RT-LAMP experiments (Figure 2-2b). For the dRT-LAMP experiments, the concentrations of HIV-1 RNA were determined by counting the number of positive wells on each chip after a 60-min reaction and then using Poisson statistics (detailed in the Supplementary Information online). The dRT-LAMP assay could also distinguish between the two concentrations at each temperature (at 57 °C $p = 0.03$, at 60 °C $p = 0.02$, at 63 °C $p = 0.02$). In contrast to the real-time assay, the dRT-LAMP assay was robust to these temperature changes and resolved a 2-fold change in concentration despite these fluctuations ($p = 7 \times 10^{-7}$). In these experiments, a Leica DMI-6000 microscope equipped with a Hamamatsu ORCA R-2 cooled CCD camera was used to image the dRT-LAMP devices. This setup provides an even illumination field and, therefore, intensity of the positive well was not a function of position (see Supplementary Information online).

Next, we tested whether the dRT-LAMP assay was robust to variance in reaction time. We performed dRT-LAMP reactions with concentrations of 1×10^5 and 2×10^5 copies/mL at a reaction temperature of 63 °C and imaged the reaction every minute using a Leica MZFLIII fluorescent stereomicroscope (detailed in the Supplementary Information online). At each time point, the number of positive reactions was counted, and the results were averaged over three replicates (Figure 2-2c). For each of the two concentrations, we grouped together the raw counts at 40-, 50-, and 60 min-reaction times. Statistical analysis was used to reject the null hypothesis that these groups were the

same (p-value of 8.5×10^{-7}). Therefore, we conclude that the dRT-LAMP assay is robust to variance in reaction time, and an exact reaction time is not needed in the digital assay.

Next, we tested the robustness of the dRT-LAMP assay to poor imaging conditions using a Nokia 808 PureView cell phone with simple optical attachments (detailed in the Supplementary Information online). The flash function of the cell phone was used to excite fluorescence through an excitation filter attached to the phone, and the camera of the cell phone was used to image fluorescence through an emission filter also attached to the cell phone. The results obtained with the cell phone were compared with those obtained with a microscope (Figure 2-2d). We tested the cell phone's imaging abilities under two lighting conditions: first, the dRT-LAMP assays were photographed in a shoe box, and second, in a dimly lit room with a single fluorescent task light in a corner. The light intensity at the point where the measurements were taken in the dimly lit room was ~3 lux as measured by an AEMC Instruments Model 810 light meter.

To evaluate whether imaging with a cell phone yields robust results, we performed statistical analysis of data obtained by cell phone imaging under each of the two lighting conditions. For imaging with a shoe box, we grouped all data obtained at the first concentration (1×10^5 copies/mL) across all three temperatures into a first set, and all data obtained at the second concentration (2×10^5 copies/mL) across all three temperatures into a second set. We then calculated a p-value of 1.3×10^{-8} for the two sets (the null hypothesis being that the two concentrations were identical), which suggests that this imaging method could be used to differentiate between the two concentrations both at constant temperatures and even despite temperature changes. When we repeated this procedure for imaging in a dimly lit room, we calculated a p-value of 1.9×10^{-8} ,

indicating that the two concentrations could be distinguished with statistical significance in this scenario as well. Therefore, this dRT-LAMP assay was robust to the double perturbation of non-ideal imaging conditions and temperature fluctuations.

We then tested whether other digital assays, such as digital PCR (dPCR), were sufficiently robust to poor imaging conditions to be analyzed with a cell phone. PCR amplification monitored with an intercalating dye such as Evagreen produces only a 2- to 4-fold change in fluorescence intensity as the reaction transitions from negative to positive.⁴² In our devices the absolute intensity of fluorescence in the positive reaction in dPCR was approximately 8-15 times lower than that in dRT-LAMP monitored with the calcein dye. When we conducted a dRT-PCR experiment using the same reaction volumes as those in the dRT-LAMP assays, we could easily distinguish positive from negative counts when the chip was imaged using a microscope,³⁶ as expected.⁴² While it was also possible to image some of the dPCR chips using the cell phone, the signal was not sufficiently bright and robust for unambiguous analysis, and therefore we did not pursue this direction further in this manuscript. We also tested the cell phone's ability to image the results on a spatially multiplexed PCR chip.⁴⁸ This chip uses larger reaction volumes (78 nL as opposed to 6 nL), thus enabling more fluorescent light to be emitted and collected per well. In this chip (Figure 2-3a, b), multiple primer pairs are preloaded into one set of wells, a sample is loaded into the second set of wells, and a "slip" combines the two sets of wells, thus enabling subsequent PCR amplification. Here, we used a five-plexed assay, in which one primer set was specific to the *S. aureus* genome (Figure 2-3b, detailed in the Supplementary Information online). When *S. aureus*

genomic DNA was loaded onto the device and the PCR reaction was performed, no non-specific amplification was observed and a positive result was indicated by the appearance of the pattern on the device, as designed. This pattern, formed by PCR amplification in these larger wells, could be also visualized by the cell phone (Figure 2-3c).

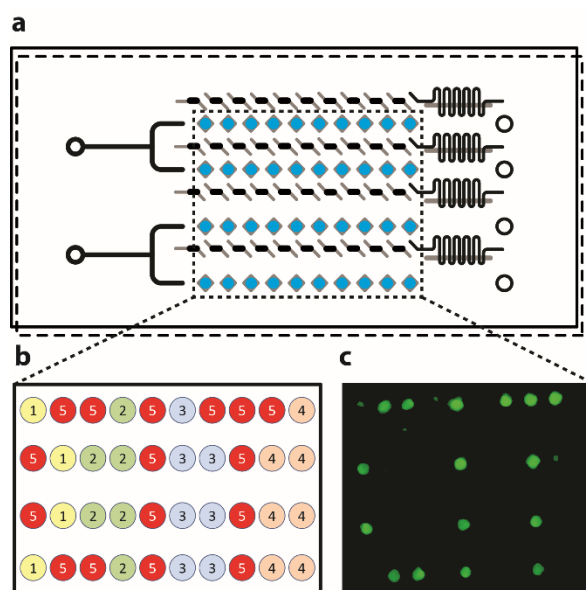


Figure 2-3. Cell phone imaging of multiplexed PCR on a SlipChip device using five different primer sets and a single template. (a) A schematic drawing of a SlipChip device that has been pre-loaded with primers. (b) A schematic drawing showing the arrangement of the five primer sets on the device: 1 = *E. coli* nlp gene, 2 = *P. aeruginosa* vic gene, 3 = *C. albicans* calb gene, 4 = *Pseudomonas* 16S, 5 = *S. aureus* nuc gene; sequences are provided in Supplementary Table S1. (c) A cell phone image of a SlipChip after loading it with *S. aureus* genomic DNA and performing PCR amplification. Wells containing the primer for *S. aureus* (green) increased in fluorescence to form the designed pattern. The intensity levels of the image have been adjusted and the image has been smoothed to enhance printed visibility (details are included in the Supplementary Information).

Finally, we tested whether this combination of dRT-LAMP amplification chemistry and cell phone imaging was robust to automated processing of images and data analysis.

When high-quality images, such as those taken with a microscope, are available, image

processing and quantification of the positive signals can be performed simply by setting an intensity threshold and then counting the number of spots on the resulting image that exceed this threshold. For example, a threshold of 190 a.u. was set for the data obtained with the microscope, and similar results were obtained by adjusting that threshold by as much as 150 units (Figure 2-4).

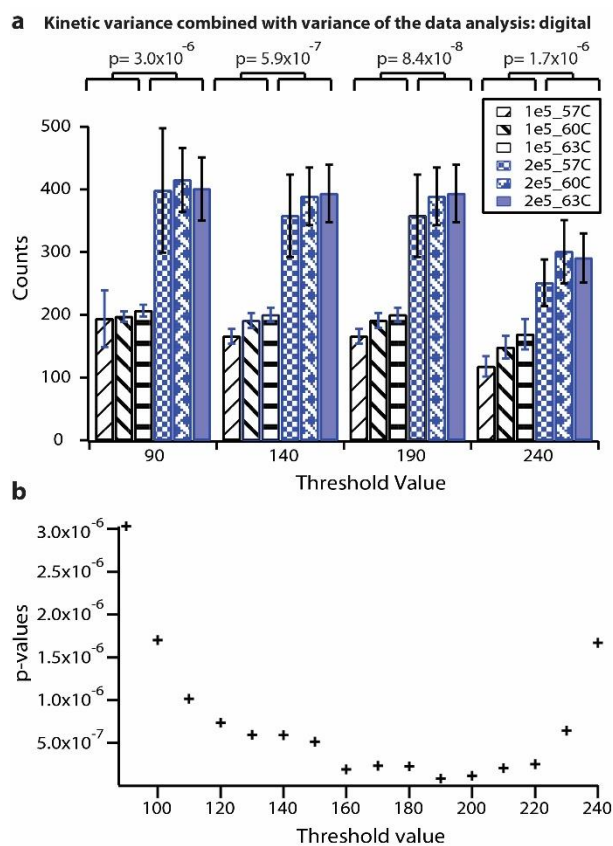


Figure 2-4. Robustness of digital dRT-LAMP amplification imaged with a microscope to thresholding used to differentiate positive and negative wells. a) A graph showing the number of positive reactions observed when imaging the dRT-LAMP reactions with a microscope as a function of the threshold value used to calculate the number of positives. Separation of the two data sets is easily observed even when changing the threshold value by 150 fluorescence units. b) A plot of the p-values generated by comparing the two concentrations at threshold values between 90 and 240. The minimum p-value is observed at a threshold of 190.

This method is not, however, suitable for images taken with a cell phone for two reasons: (i) the short focal length (6 cm) creates significant variation in the illumination intensity of the flash, and (ii) the imaging sensor has a much lower signal-to-noise ratio than those typically found in scientific instrumentation. Therefore, to test whether accurate automatic analysis of assays was possible, we wrote a custom image processing algorithm and implemented it in Labview software (detailed in the Supplementary Information online). Once an image was taken, it was automatically transferred to a remote server in “the cloud” (Figure 2-5b). The uploaded file was automatically analyzed by the server, and then the results were reported via email (Figure 2-5c). Two videos showing the process as experienced by the user are available in the Supplementary Information online (Video S1 and S2). We included error detection in the custom algorithm to ensure that the image included the device in its entirety (Figure 2-5c and Supplementary Information online). This detection algorithm looked for four red circles on the device (Figure 2-5a), and if fewer than four were found, it generated an error message (Figure 2-5c, right). We tested the robustness of this cell phone imaging procedure to automated processing by directly comparing microscope images results quantified with Metamorph to cell phone images quantified with Labview over more than a hundred-fold concentration range (Figure 2-5d). A line of best fit of the compared data was found to have a slope of 0.968 and an R^2 value of 0.9997, suggesting that this digital assay is robust to automated image processing even under poor imaging conditions, and is suitable for use over a wide dynamic range.

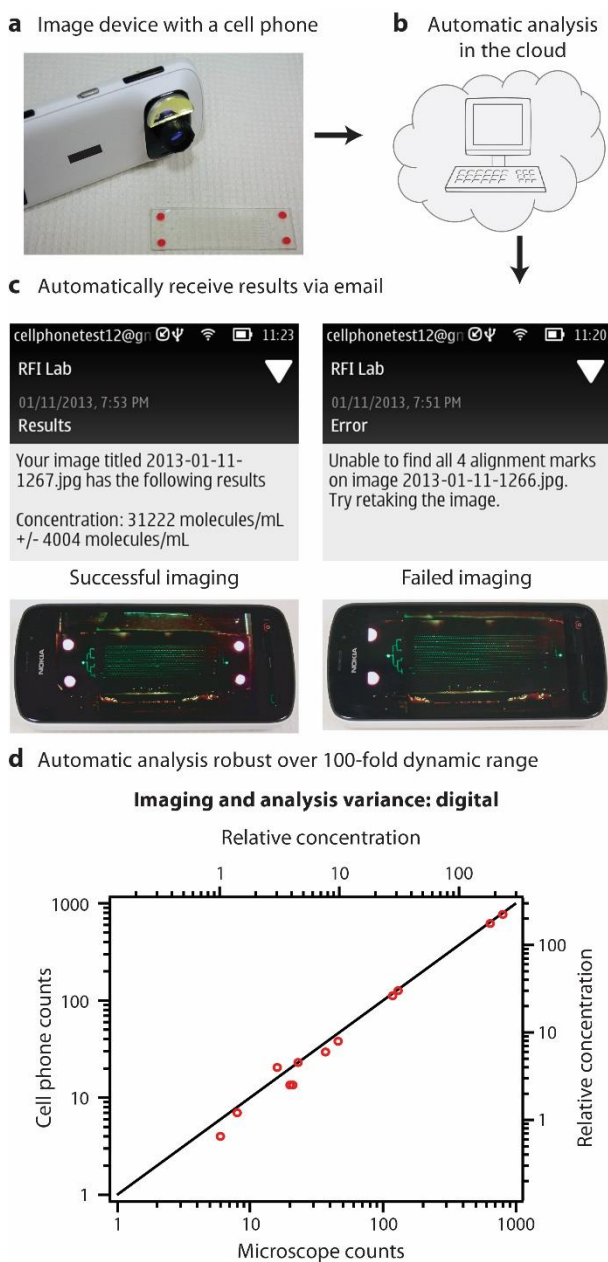


Figure 2-5. The image analysis workflow used to count molecules via digital amplification with a SlipChip and a cell phone. (a) Left: A cell phone with objective for detecting fluorescence. Nokia logo has been redacted per Journal policy. Right: A device labeled with four red circles that the imaging processing algorithm uses to confirm that the entire device has been imaged. (b) A cartoon representing a cloud-based server that analyzes photographs taken by the user, archives the raw data, and sends the results to the appropriate party. (c) Top: Screenshots of a cell phone screen showing email messages received by a pre-specified recipient after analysis of successful (left) and unsuccessful (right) imaging. Bottom: the images that were analyzed in each case. (d) A graph comparing the raw positive counts from a cell phone processed automatically by Labview

software (y-axis) to imaging and thresholding performed with an epifluorescence microscope (x-axis) using a more than 100-fold concentration change.

We emphasize that while we established robust automated counting of HIV-1 RNA molecules using digital amplification chemistry and a cell phone, this is only one part of the full diagnostic assay and several additional advances are needed for deployment under LRS. Simple chemical heaters^{45,46} that have been shown to work with RT-LAMP in qualitative assays would need to be incorporated into a digital platform. LRS-suitable techniques for sample preparation would need to be incorporated as well as standard laboratory procedures were used for these experiments. The robustness of dRT-LAMP to factors such as sequence diversity of viruses present in clinical samples, changes in activity of reagents during storage, and quality of sample preparation remains to be tested. While offloading the analysis of images to “the cloud” provides a number of benefits, including traceability and archiving of raw data, global access, and compatibility with virtually all smartphone operating systems, it requires a wireless data connection of sufficiently high bandwidth; thus, direct on-phone analysis could be preferable in some scenarios. As cell phone technology evolves at a rapid pace and smartphone operating systems converge with classic point-and-shoot cameras, advanced imaging sensors and excitations sources could offer additional opportunities for robust imaging of other amplification assays in LRS. In addition, for this study we have used lab-produced glass microfluidic chips; under LRS, mass-produced variants of this device would need to be used.

Conclusions

We have shown that HIV-1 RNA amplification using RT-LAMP assays in the traditional real-time format is, as expected, not robust to temperature fluctuations. In contrast, digital counting of HIV-1 RNA molecules using dRT-LAMP is robust not only to temperature fluctuations, but also to changes in reaction time, artifacts introduced by poor-quality cell phone imaging, and automatic analysis. Bright fluorescent output with a high ratio of positive to negative signals of the digital LAMP chemistry was necessary to observe robustness to imaging and automated analysis. Below, we point out several implications of these findings.

Given the complexity of the mechanism of the LAMP amplification reaction,³⁸ we were surprised to find it was robust, in the digital format, to changes in temperature and time. This result suggests that the probability of initiation of the amplification cascade from a single molecule does not significantly change and this initiation is not delayed with changes in temperature, despite temperature-dependent changes in the equilibria of DNA-DNA hybridization, enzyme-DNA binding, and changes in the rates of the various enzymatic steps of the reaction. We hypothesize that as long as the efficiency of the initiation step is high and is not strongly affected by the perturbation of interest, robustness to this perturbation should be a general property of digital amplification schemes. We are interested in a future direct comparison of robustness of real-time and digital recombinase polymerase amplification (RPA)⁴³ to temperature, time, and imaging perturbations. Additional experimental studies are needed to test whether other nonlinear and autocatalytic amplification systems¹⁻¹² satisfy this criterion and show robustness in the digital format to changes in temperature, time, and other experimental perturbations.

SlipChip devices are attractive for such studies because they support multi-step manipulations of single molecules^{36,43} and can be made in glass to be compatible with a wide range of chemistries. In general, such studies could be performed using any microfluidic platforms that support digital single-molecule manipulations. Theoretical studies are also needed to predict the level of robustness of specific amplification reactions, and also to predict more generally which reaction architectures are likely to be robust to which perturbations, leading to the design of new amplification chemistries. Robustness of biological systems, e.g., robustness of circadian clocks to temperature fluctuations,¹⁶ may provide an inspiration for such studies.

If these experimental and theoretical studies are successful, we may see an emergence of nonlinear amplification schemes that are especially suitable for quantitative measurements under LRS because they are ultra-rapid, specific, provide bright positive and dim negative signals, and are robust to experimental perturbations. Finally, we share the analogy that motivates our work to explore the robustness of quantitative measurements and their applicability to LRS. Many countries in the developing world recently underwent a technological revolution. Their growth had been hindered by lack of a communication infrastructure, since replicating the land-line based model of the developed world would have been impractical and prohibitively expensive. The revolution happened when these countries bypassed the land-line paradigm and leapfrogged directly to wireless technologies. An analogous technological transformation may occur for quantitative molecular measurements under LRS without the need to create the infrastructure required to carefully control and analyze kinetic assays. Instead, studies of robustness of chemical amplification and signal transduction schemes may

allow the quantitative molecular measurements and diagnostics in the developing world, the field, and the home to leapfrog directly to the more robust digital, single-molecule approaches.

References

- 1 Baker, M. S. & Phillips, S. T. A Two-Component Small Molecule System for Activity-Based Detection and Signal Amplification: Application to the Visual Detection of Threshold Levels of Pd(II). *J. Am. Chem. Soc.* **133**, 5170-5173, doi:10.1021/ja108347d (2011).
- 2 Gerdts, C. J., Sharoyan, D. E. & Ismagilov, R. F. A synthetic reaction network: chemical amplification using nonequilibrium autocatalytic reactions coupled in time. *J. Am. Chem. Soc.* **126**, 6327-6331 (2004).
- 3 Jiang, Y., Li, B., Milligan, J. N., Bhadra, S. & Ellington, A. D. Real-Time Detection of Isothermal Amplification Reactions with Thermostable Catalytic Hairpin Assembly. *J. Am. Chem. Soc.* **135**, 7430-7433, doi:10.1021/ja4023978 (2013).
- 4 Kottani, R. *et al.* Photoinduced signal amplification through controlled externally sensitized fragmentation in masked sensitizers. *J. Am. Chem. Soc.* **128**, 14794-14795 (2006).
- 5 Mohapatra, H., Schmid, K. M. & Phillips, S. T. Design of small molecule reagents that enable signal amplification via an autocatalytic, base-mediated cascade elimination reaction. *Chem. Commun.* **48**, 3018-3020 (2012).

- 6 Olea, C., Horning, D. P. & Joyce, G. F. Ligand-Dependent Exponential Amplification of a Self-Replicating l-RNA Enzyme. *J. Am. Chem. Soc.* **134**, 8050-8053, doi:10.1021/ja302197x (2012).
- 7 Taton, T. A., Mirkin, C. A. & Letsinger, R. L. Scanometric DNA array detection with nanoparticle probes. *Science* **289**, 1757-1760 (2000).
- 8 Tian, L. & Weizmann, Y. Real-Time Detection of Telomerase Activity Using the Exponential Isothermal Amplification of Telomere Repeat Assay. *J. Am. Chem. Soc.* **135**, 1661-1664, doi:10.1021/ja309198j (2012).
- 9 Zuo, X., Xia, F., Xiao, Y. & Plaxco, K. W. Sensitive and Selective Amplified Fluorescence DNA Detection Based on Exonuclease III-Aided Target Recycling. *J. Am. Chem. Soc.* **132**, 1816-1818, doi:10.1021/ja909551b (2010).
- 10 Bánsági, T., Vanag, V. K. & Epstein, I. R. Tomography of reaction-diffusion microemulsions reveals three-dimensional Turing patterns. *Science* **331**, 1309-1312 (2011).
- 11 Epstein, I. R. & Pojman, J. A. *An Introduction to Nonlinear Chemical Dynamics: Oscillations, Waves, Patterns, and Chaos*. (Oxford University Press, 1998).
- 12 Qian, L. & Winfree, E. Scaling up digital circuit computation with DNA strand displacement cascades. *Science* **332**, 1196-1201 (2011).
- 13 Alon, U., Surette, M. G., Barkai, N. & Leibler, S. Robustness in bacterial chemotaxis. *Nature* **397**, 168-171 (1999).
- 14 Kitano, H. Towards a theory of biological robustness. *Mol. Syst. Biol.* **3**, 137 (2007).

- 15 Lucchetta, E. M., Lee, J. H., Fu, L. A., Patel, N. H. & Ismagilov, R. F. Dynamics of *Drosophila* embryonic patterning network perturbed in space and time using microfluidics. *Nature* **434**, 1134-1138 (2005).
- 16 Buhr, E. D., Yoo, S.-H. & Takahashi, J. S. Temperature as a Universal Resetting Cue for Mammalian Circadian Oscillators. *Science* **330**, 379-385, doi:10.1126/science.1195262 (2010).
- 17 Girones, R. *et al.* Molecular detection of pathogens in water - The pros and cons of molecular techniques. *Water Res.* **44**, 4325-4339, doi:10.1016/j.watres.2010.06.030 (2010).
- 18 Postollec, F., Falentin, H., Pavan, S., Combrisson, J. & Sohier, D. Recent advances in quantitative PCR (qPCR) applications in food microbiology. *Food Microbiol.* **28**, 848-861, doi:10.1016/j.fm.2011.02.008 (2011).
- 19 *The FEM Microbiology Action Team. Method Validation of U.S. Environmental Protection Agency Microbiological Methods of Analysis.*
http://www.epa.gov/fem/pdfs/final_microbiology_method_guidance_110409.pdf
(accessed June 19, 2013),
<http://www.epa.gov/fem/pdfs/final_microbiology_method_guidance_110409.pdf> (2009).
- 20 West, J. S., Atkins, S. D., Emberlin, J. & Fitt, B. D. L. PCR to predict risk of airborne disease. *Trends Microbiol.* **16**, 380-387, doi:10.1016/j.tim.2008.05.004 (2008).
- 21 Heid, C. A., Stevens, J., Livak, K. J. & Williams, P. M. Real time quantitative PCR. *Genome Res.* **6**, 986-994, doi:10.1101/gr.6.10.986 (1996).

- 22 Belgrader, P. *et al.* PCR detection of bacteria in seven minutes. *Science(Washington)* **284**, 449-450 (1999).
- 23 Neuzil, P., Zhang, C., Pippert, J., Oh, S. & Zhuo, L. Ultra fast miniaturized real-time PCR: 40 cycles in less than six minutes. *Nucleic Acids Res.* **34**, e77-e77 (2006).
- 24 Yager, P. *et al.* Microfluidic diagnostic technologies for global public health. *Nature* **442**, 412-418, doi:10.1038/nature05064 (2006).
- 25 Calmy, A. *et al.* HIV viral load monitoring in resource-limited regions: Optional or necessary? *Clin. Infect. Dis.* **44**, 128-134, doi:10.1086/510073 (2007).
- 26 Roche Diagnostic Systems, Inc. *AMPLICOR HIV-1 MONITOR™ TEST Standard/UltraSensitive.*
<http://www.fda.gov/downloads/BiologicsBloodVaccines/BloodBloodProducts/ApprovedProducts/PremarketApprovalsPMAs/UCM093317.pdf> (accessed June 19, 2013),
<<http://www.fda.gov/downloads/BiologicsBloodVaccines/BloodBloodProducts/ApprovedProducts/PremarketApprovalsPMAs/UCM093317.pdf>> (
- 27 *Panel on Antiretroviral Guidelines for Adults and Adolescents. Guidelines for the use of antiretroviral agents in HIV-1-infected adults and adolescents. Department of Health and Human Services.* <http://aidsinfo.nih.gov/ContentFiles/AdultandAdolescentGL.pdf> (accessed June 19, 2013),
<<http://aidsinfo.nih.gov/contentfiles/lvguidelines/adultandadolescentgl.pdf>> (2013).

- 28 Sykes, P. *et al.* Quantitation of targets for PCR by use of limiting dilution. *BioTechniques* **13**, 444 (1992).
- 29 Ottesen, E. A., Hong, J. W., Quake, S. R. & Leadbetter, J. R. Microfluidic digital PCR enables multigene analysis of individual environmental bacteria. *Science* **314**, 1464-1467, doi:10.1126/science.1131370 (2006).
- 30 Rissin, D. M. & Walt, D. R. Digital readout of target binding with attomole detection limits via enzyme amplification in femtoliter arrays. *J. Am. Chem. Soc.* **128**, 6286-6287 (2006).
- 31 Kreutz, J. E. *et al.* Theoretical design and analysis of multivolume digital assays with wide dynamic range validated experimentally with microfluidic digital PCR. *Anal. Chem.* **83**, 8158-8168, doi:10.1021/ac201658s (2011).
- 32 Martinez, A. W. *et al.* Simple telemedicine for developing regions: Camera phones and paper-based microfluidic devices for real-time, off-site diagnosis. *Anal. Chem.* **80**, 3699-3707, doi:Doi 10.1021/Ac800112r (2008).
- 33 Breslauer, D. N., Maamari, R. N., Switz, N. A., Lam, W. A. & Fletcher, D. A. Mobile phone based clinical microscopy for global health applications. *PloS ONE* **4**, e6320, doi:10.1371/journal.pone.0006320 (2009).
- 34 Zhu, H. Y., Isikman, S. O., Mudanyali, O., Greenbaum, A. & Ozcan, A. Optical imaging techniques for point-of-care diagnostics. *Lab Chip* **13**, 51-67, doi:10.1039/c2lc40864c (2013).
- 35 Bustin, S. A. *et al.* The MIQE guidelines: minimum information for publication of quantitative real-time PCR experiments. *Clin. Chem.* **55**, 611-622 (2009).

- 36 Sun, B. *et al.* Mechanistic evaluation of the pros and cons of digital RT-LAMP for HIV-1 viral load quantification on a microfluidic device and improved efficiency via a two-step digital protocol. *Anal. Chem.* **85**, 1540-1546, doi:10.1021/ac3037206 (2013).
- 37 Francois, P. *et al.* Robustness of a loop-mediated isothermal amplification reaction for diagnostic applications. *FEMS Immunology and Medical Microbiology* **62**, 41-48, doi:10.1111/j.1574-695X.2011.00785.x (2011).
- 38 Nagamine, K., Hase, T. & Notomi, T. Accelerated reaction by loop-mediated isothermal amplification using loop primers. *Mol. Cell. Probes* **16**, 223-229 (2002).
- 39 Gansen, A., Herrick, A. M., Dimov, I. K., Lee, L. P. & Chiu, D. T. Digital LAMP in a sample self-digitization (SD) chip. *Lab Chip* **12**, 2247-2254, doi:10.1039/c2lc21247a (2012).
- 40 Zhu, Q. Y. *et al.* Self-priming compartmentalization digital LAMP for point-of-care. *Lab Chip* **12**, 4755-4763, doi:10.1039/c2lc40774d (2012).
- 41 Du, W., Li, L., Nichols, K. P. & Ismagilov, R. F. SlipChip. *Lab Chip* **9**, 2286-2292, doi:10.1039/b908978k (2009).
- 42 Shen, F., Du, W., Kreutz, J. E., Fok, A. & Ismagilov, R. F. Digital PCR on a SlipChip. *Lab Chip* **10**, 2666-2672, doi:10.1039/c004521g (2010).
- 43 Shen, F. *et al.* Digital isothermal quantification of nucleic acids via simultaneous chemical initiation of recombinase polymerase amplification reactions on SlipChip. *Anal. Chem.* **83**, 3533-3540, doi:10.1021/ac200247e (2011).

- 44 Curtis, K. A., Rudolph, D. L. & Owen, S. M. Rapid detection of HIV-1 by reverse-transcription, loop-mediated isothermal amplification (RT-LAMP). *J. Virol. Methods* **151**, 264-270, doi:<http://dx.doi.org/10.1016/j.jviromet.2008.04.011> (2008).
- 45 Liu, C. C., Mauk, M. G., Hart, R., Qiu, X. B. & Bau, H. H. A self-heating cartridge for molecular diagnostics. *Lab Chip* **11**, 2686-2692, doi:10.1039/c1lc20345b (2011).
- 46 Curtis, K. A. *et al.* Isothermal amplification using a chemical heating device for point-of-care detection of HIV-1. *PloS ONE* **7**, e31432 (2012).
- 47 Tomita, N., Mori, Y., Kanda, H. & Notomi, T. Loop-mediated isothermal amplification (LAMP) of gene sequences and simple visual detection of products. *Nature Protocols* **3**, 877-882 (2008).
- 48 Shen, F. *et al.* Nanoliter multiplex PCR arrays on a SlipChip *Anal. Chem.* **82**, 4606-4612, doi:10.1021/ac1007249 (2010).

Chapter 3:

Reading out Single-Molecule Digital RNA and DNA Isothermal Amplification in Nanoliter Volumes with Unmodified Camera Phones*

Abstract

Digital single-molecule technologies are expanding diagnostic capabilities—enabling the ultrasensitive quantification of targets, such as viral load in HIV and hepatitis C infections, by directly counting single molecules. Replacing fluorescent readout with a robust visual readout that can be captured by any unmodified cell phone camera will facilitate the global distribution of diagnostic tests, including into limited-resource settings where the need is greatest. This paper describes a methodology for developing a visual readout system for digital single-molecule amplification of RNA and DNA by (i) selecting colorimetric amplification-indicator dyes that are compatible with the spectral sensitivity of standard mobile phones, and (ii) identifying an optimal ratiometric image-process for a selected dye to achieve a readout that is robust to lighting conditions and camera hardware and provides unambiguous quantitative results—even for colorblind users. We also include an analysis of the limitations of this methodology, and provide a microfluidic approach that can be applied to expand dynamic range and improve reaction performance, allowing ultrasensitive, quantitative measurements at volumes as low as 5 nanoliters. We validate this methodology using SlipChip-based digital single-molecule isothermal amplification with lambda DNA as a model and hepatitis C viral RNA as a clinically relevant target. The innovative combination of isothermal amplification

* This chapter was originally published in *ACS Nano* with authorship belonging to Jesus Rodriguez-Manzano, Mikhail A. Karymov, Stefano Begolo, David A. Selck, Dmitriy V. Zhukov, Erik Jue, and Rustem F. Ismagilov. The original manuscript can be found at: <http://dx.doi.org/10.1021/acsnano.5b07338>

chemistry in the presence of a judiciously chosen indicator dye and ratiometric image processing with SlipChip technology allowed the sequence-specific visual readout of single nucleic acid molecules in nanoliter volumes with an unmodified cell phone camera. When paired with devices that integrate sample preparation and nucleic acid amplification, this hardware-agnostic approach will increase the affordability and the distribution of quantitative diagnostic and environmental tests.

Introduction

This paper shows that single nucleic acid molecules confined in nanoliter volumes in microfluidic devices can be detected and counted by an unmodified cell phone camera, in combination with isothermal amplification chemistry, a judiciously chosen indicator dye and ratiometric image processing. We describe a novel methodology that can be used to develop a visual readout for digital single-molecule amplification of sequence-specific RNA and DNA that can be used with any camera phone—without modifications or attachments. Single-molecule visual readout has never been achieved before. Diagnostic tests that incorporate such a visual readout will greatly expand the applicability of emerging digital single-molecule technologies, including limited resource settings (LRS). Ultrasensitive and quantitative detection of nucleic acid molecules is of particular interest for infectious disease diagnosis in LRS, such as the quantification of viral load for human immunodeficiency virus (HIV) and hepatitis C virus (HCV),¹⁻³ as many of these infections occur far from centralized laboratories where diagnostic tests are routine. Increasing diagnoses in these locations will lead to faster and more appropriate treatment and have a major impact on disease burden^{4,5} Most point of care (POC) tests are not amenable to LRS because they don't meet the World Health Organization's ASSURED

criteria of being affordable, sensitive, specific, user-friendly, rapid, robust, equipment-free, and deliverable.⁵ The tests that do meet the requirements for LRS (*e.g.* immunochromatography to detect antigens or antibodies in a dipstick or lateral-flow format, or the visualization of antigen-antibody lattice formation) have poor reported sensitivities and thus are unable to detect and quantify analytes at low concentrations.^{4,6} Nucleic acid amplification tests (NAATs), such as PCR, have the desired high sensitivity and target specificity, providing accurate quantification, but these technologies are costly, time-consuming, and require skilled technicians and laboratory settings.⁷

Of the NAATs, isothermal amplification methods (*e.g.* loop-mediated isothermal amplification, LAMP) are among the most attractive for LRS because they do not require thermocycling or capital equipment and can be run in water baths, using simple heaters or with exothermic chemical heating that does not require electricity.⁸⁻¹¹ Still, acquiring quantitative and ultrasensitive measurements outside of the lab remains challenging because the methods are not robust to variability in reaction conditions and readouts rely on precise measures of fluorescence intensity. Running isothermal amplification chemistries in a digital, single-molecule format maintains the high sensitivity and quantification capabilities typically achieved only in lab settings.¹²⁻¹⁵ In digital single-molecule isothermal amplification, single, stochastically confined DNA or RNA molecules are randomly distributed among discrete nanoliter or picoliter volumes and amplified under controlled conditions.¹⁶⁻¹⁸ This creates relatively high local concentrations of target DNA or RNA, making digital amplification more efficient and robust compared to bulk reactions with the same number of starting target molecules. Nucleic acid amplification of even a single target molecule produces a clear fluorescent

signal and the results of digital amplification can be read by a modified cell phone (*e.g.* a phone camera with an optical filter) under dim lighting.¹⁴

Microfluidic technology has been an instrumental tool in developing single nucleic acid molecule capabilities,¹⁹⁻²⁷ and the integration of sample-preparation modules into portable microfluidic devices will further enable their use by untrained users in any setting.²⁸⁻³⁰ To bring these emerging technological capabilities to LRS, however, such devices capable of ultrasensitive, quantitative measurements should provide a rapid, visual readout that can be captured easily, *e.g.* by any mobile phone without modifications or attachments. Cell phone cameras provide a convenient, nearly universal tool to pair with emerging diagnostic technologies to transform global healthcare as ~7 billion mobile cellular subscribers exist worldwide and 70% of users live in developing countries.³¹ Mobile devices are emerging as a powerful platform to create cost-effective alternatives for molecular diagnostics in LRS³²⁻⁴² and colorimetric diagnostics based on unmodified cell phones have been used before,^{38,43-46} but not in a digital format, where the short path lengths and nanoliter volumes have constrained visual-based methods. Here, we describe an approach that enables visual readout of single nucleic acid molecule amplification by (i) selecting an appropriate colorimetric indicator dye based on spectral properties that align well with the RGB sensitivities of common cell phone camera sensors and (ii) identifying the optimal ratiometric image-processing for the selected dye to achieve a readout that is robust to lighting conditions and camera hardware. Using this approach, after sequence-specific single-molecule isothermal amplification, a visual readout is captured by an unmodified camera phone and the resulting image is analyzed using a ratiometric approach, wherein the measured intensities of two of the three RGB

color channels are divided to provide a binary result (a positive or negative reaction) for each well. The automation of this ratiometric analysis provides a clear, reliable digital readout without requiring the user to differentiate color change by eye or manipulate lighting (Figure 3-1a). We further show how limitations related to reaction inhibition by the readout dye can be solved with SlipChip microfluidics technology to decouple the amplification and readout steps. We validated our visual readout method with SlipChip-based digital single-molecule isothermal amplification reactions using phage lambda DNA as a model and HCV RNA as a clinically relevant target, in reaction volumes as low as 5 nL, using a variety of common cell phones and a range of illumination conditions.

Results and Discussion

Selecting an indicator dye. To eliminate the need for a fluorescent readout in single-molecule amplification and produce a readout that can be imaged by any cell phone camera under various illumination conditions, one can use a nucleic acid amplification-indicator dye that changes color in response to amplification. A robust colorimetric readout balances two opposing requirements: the indicator dye must be sufficiently concentrated (or present in a large enough volume) to provide readable absorbance (*i.e.* smaller volumes and shorter path lengths require greater concentrations of dye for sufficient absorbance to be detected) but not so concentrated that the dye interferes with the amplification reaction. To optimize a visual readout system for single-molecule counting with an unmodified cell phone camera, we first identified the factors that contribute to hypothetical limitations of a visual readout system, including the range of reaction volumes (or path lengths) at which a particular indicator could be used to

monitor amplification and the range of indicator concentrations that would not interfere with the amplification reaction. Where these ranges overlap are the optimal volumes and dye concentrations at which a reaction is not inhibited and can provide a change in absorbance that is sufficient for readout with an unmodified camera phone (dotted green region of Figure 3-1b).

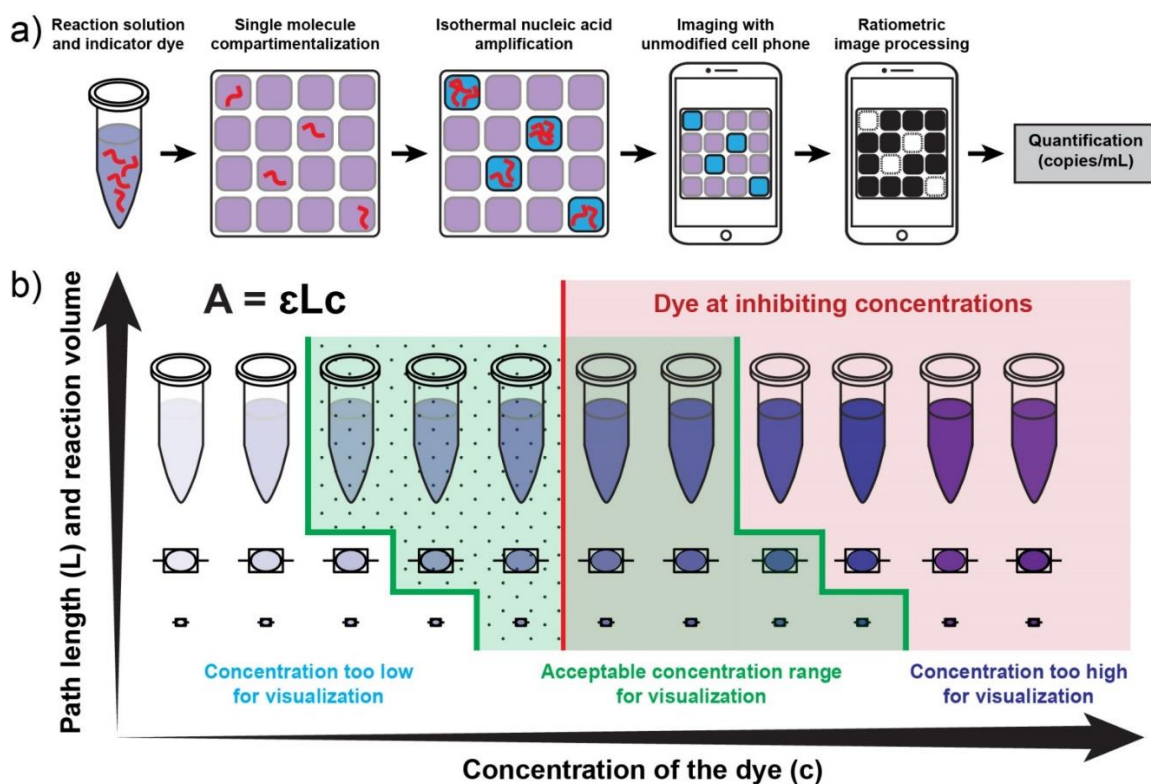


Figure 3-1. A visual readout approach for digital single-molecule isothermal amplification for use with an unmodified cell phone camera. (a) A workflow for visual readout of digital single-molecule amplification. Single nucleic acid molecules and indicator dye are compartmentalized on a microfluidic device and followed by isothermal nucleic acid amplification. Positive reaction solutions are blue; negative reactions are purple. After ratiometric image processing, positive reactions become white and negative reactions become black—an unambiguous binary result. The number of positive wells is then used to quantify the concentration of the input target. (b) A diagram for delineating the optimal range of dye concentrations as a factor of path length (reaction volume) and the threshold for reaction inhibition. The green-shaded region indicates the range of acceptable dye concentrations for visualization with an unmodified cell phone camera. Concentrations to the left of the green region are too low for visualization; concentrations to the right of the green region are too high. Within this green region, the dotted area

indicates dye concentrations that both enable readout with an unmodified cell phone camera and do not inhibit the amplification reaction. The area to the right of the red line indicates dye concentrations that interfere with amplification making accurate quantification based on real-time data challenging.

We validated this visual readout approach using loop-mediated isothermal amplification (LAMP)^{47,48} (Supporting Information Tables S1–S2) because this method has been well characterized and validated previously for single-molecule analyses.^{12,14-17,49} LAMP chemistry is based on an auto-cycling strand displacement reaction performed at a constant temperature to synthesize large amounts of amplified product; a LAMP reaction generate more than 10^9 copies of template within 1 h of incubation at 60–65 °C.⁴⁸ We used a cubic reaction volume of 8 nL ($200 \times 200 \times 200 \mu\text{m}^3$), which is in the range of volumes used in digital experiments.^{12,14,15,17,49} We assume that an appropriate indicator of an amplification reaction will have a change in absorbance that equates to a change of extinction coefficient of $\sim 25,000 \text{ L mol}^{-1} \text{ cm}^{-1}$ upon reaction (this number approaches the maximum achievable change in absorbance for small-molecule dyes). We use the Beer-Lambert law ($A = \epsilon(A)$, which describes the relevant parameters to consider for visualization, wherein A = absorbance (the percentage of light absorbed); ϵ = extinction coefficient ($\text{L mol}^{-1} \text{ cm}^{-1}$); L = length of the light's path through the solution (cm); c = concentration of absorbing species (mol/L). At a path length of 0.2 mm, an estimated ~ 2 mM concentration of the dye is required to reach a change of absorbance of 1 unit. Given these parameters, to obtain a readout that can be captured by an unmodified mobile phone, we predicted that an appropriate indicator dye would be one that responds to each nucleotide incorporation (present in mM concentrations), as opposed to responding only to the number of produced molecules (amplicons), which would not exceed primer concentration (present in the μM range).

Colorimetric approaches to visual detection of nucleic acid amplification typically measure absolute changes in color intensity,⁵⁰⁻⁵⁴ however distinguishing color change—*e.g.* purple *vs.* blue—is difficult and therefore not an appropriate way to quantify readout under variable conditions, such as in LRS. Ratiometric measurements, which take the ratio of two independent measurements under the same conditions, improve the robustness of a colorimetric approach, converting results to a yes/no binary outcome, eliminating the need for the user to differentiate colors. We hypothesized that a cell phone camera's sensor, which reads in three color channels (red, green, and blue, RGB) could provide suitable information for using a ratiometric approach to read amplification reactions at the single molecule level. The example we considered here is the back-illuminated Exmor R CMOS image sensor⁵⁵ used on popular cell phones such as the Samsung Galaxy 4, iPhone 4S, and iPhone 5, which has a sensitivity maxima of ~520 nm (green), ~459 nm (blue) and ~597 nm (red) (Figure 3-2a).

To illustrate our methodology for a hardware-agnostic visual readout with a ratiometric approach, we selected eriochrome black T (EBT), a magnesium ion indicator that meets the aforementioned dye specifications and has been used previously for visualization of LAMP products.^{56,57} During an isothermal amplification reaction, as nucleotides are incorporated, protons and bi-product pyrophosphate ions ($P_2O_7^{4-}$) are produced and these ions can strongly bind metal ions (*e.g.* Mg^{2+} ions) and form insoluble salts, decreasing the concentration of metal ions in the reaction solution. Before the amplification reaction, EBT is bound to magnesium ions and the reaction solution is purple. As a LAMP reaction proceeds in the presence of target nucleic acid, it is suggested that EBT is deprived of Mg^{2+} by newly generated pyrophosphate ions, and the reaction solution turns blue.

We hypothesized that EBT would be amenable to colorimetric analysis with a cell phone camera because, in RGB terms, in a positive LAMP reaction containing EBT dye, there is higher transmittance in the blue channel (blue LAMP reaction solution), while in a negative LAMP reaction transmittance remains high in the blue and red channels (purple LAMP reaction solution) (Figure 3-2a). These observed changes in transmittance between positive and negative reactions can be captured by the Exmor R optical sensor (Figure 3-2a), which matches well with the observed differences between positive and negative transmittance profiles of LAMP reactions containing EBT (Figure 3-2a).

Selecting the optimal ratiometric approach. We tested whether the suitability of an indicator dye can be evaluated for a ratiometric approach prior to experimental validation by predicting the RGB values read by a cell phone camera for a positive and a negative reaction. First, we took the transmittance spectra for positive and negative amplification reactions containing EBT and convoluted them with the normalized spectral responses for each of the RGB channels in an Exmor R CMOS sensor⁵⁸ providing six curves (a positive and negative for each of the three color channels). Next, we calculated the area under each curve and took its square root (to correct for the standard square-root scaling that occurs when an image data is compressed to be stored in the memory card of a cell phone), providing the predicted RGB values (Figure 3-2b) for positive (R=185, G=197 and B=209) and negative (R=219, G=190 and B=212) RT-LAMP reaction solutions in the presence of EBT at this particular concentration. These values can then be evaluated to select the optimal ratiometric approach for this particular indicator dye. In an RGB color scheme, there are three possible combinations for ratiometric analysis: G/R, B/R, or G/B. The predicted RGB values for a positive and a negative reaction are used to

calculate the ratios for each channel combination (Figure 3-2d); the ratio with the greatest difference between positive and negative outcomes (G/R in this example) is predicted to be the most robust ratiometric analysis.

Using the approach described above, we predicted the RGB ratios for a positive and negative RT-LAMP reaction in the presence of two additional indicator dyes: hydroxynaphthol blue (HNB) and calmagite. HNB is being reported increasingly in the literature for LAMP visualization^{50,59-62} and calmagite is an analogue of EBT dye with the nitro group absent (more stable version).⁶³ A side-by-side comparison showed that the greatest predicted difference between positive and negative RT-LAMP reaction, as captured by an unmodified cell phone camera, would be achieved using EBT as the indicator dye and G/R as the ratiometric combination. Based on these predicted ratios, we decided to validate our methodology using EBT as the indicator dye. We confirmed the storage stability of the EBT dye stock solution in the dried state, as this is a critical requirement for the use of a dye in real point-of-need diagnostic applications. EBT serves as our validation dye in this paper; however, our methodology is designed to be applicable to alternative dyes.

To experimentally validate this approach to predicting an optimal ratiometric combination, we performed an RT-LAMP reaction for HCV RNA containing EBT as the indicator dye and captured an image of the readout with an unmodified camera phone (iPhone 4S) (Figure 3-2c). We processed the readout image; color channels of the original image were split and all three channel ratios (G/R, B/R, G/B) were calculated to derive a ratiometric image for each ratiometric combination. These experimental ratios obtained with an unmodified cell phone camera (Figure 3-2e) matched well with the

predicted values (Figure 3-2d) for each of the three ratiometric combinations, confirming the predictive power of this approach. The G/B ratio was identified as less appropriate for distinguishing positive and negative reactions because the values for positive and negative reactions were similar; G/R and B/R ratios were identified as suitable because there was sufficient contrast between the values for positive and negative reactions. For the G/R combination, the ratio obtained after a negative reaction was 0.91 and the ratio from a positive reaction was 1.03—a difference of 0.12 (Figure 3-2e). For the B/R combination, the ratios for negative and positive reactions were 0.98 and 1.07—a difference of 0.09 (Figure 3-2e). Therefore, we selected the G/R combination for our subsequent validation experiments. Counting positives is a more intuitive approach, so the B/R ratio (where the positive ratio had the greatest difference from the background) can be a useful and attractive method. However, it is generally more desirable to select a ratio that includes the green channel because most single-chip digital image sensors used in digital cameras, including cell phones, utilize a Bayer filter mosaic pattern that is composed of 50% green, 25% red, and 25% blue pixels.⁶⁴

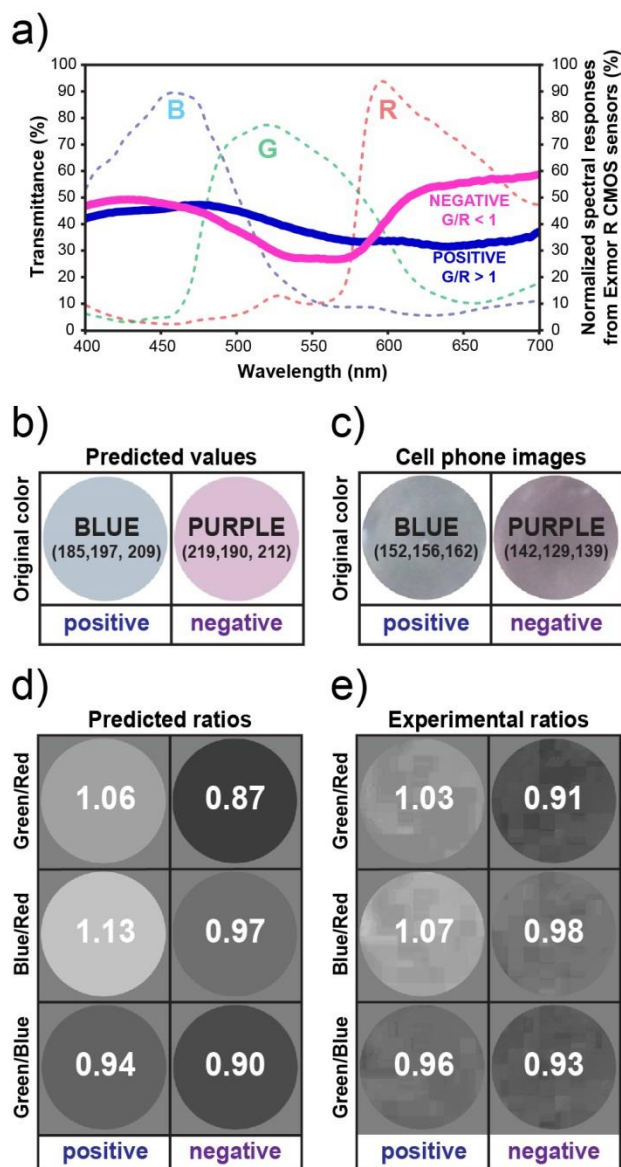


Figure 3-2. Predicted values and experimental validation of the first step of the ratiometric approach. (a) Measured spectral transmittance (%) in the range of visible light (400–700 nm) for positive (solid purple line) and negative (solid blue line) RT-LAMP reaction solutions, each containing 0.7 mM of eriochrome black T (EBT) as the amplification indicator dye. Dashed lines correspond to normalized spectral responses for red (R), green (G) and blue (B) channels of an Exmor R CMOS sensor, a common sensor in cell phone cameras. (b–e) Analysis of the three possible RGB ratiometric combinations for positive and negative RT-LAMP reaction solutions. (b) The predicted RGB values and corresponding colors for positive and negative LAMP amplification reactions obtained by convoluting the transmittance spectrum and Exmor R spectral responses described in panel (a). (c) The cropped and enlarged color images collected with an Apple iPhone 4S for positive and negative RT-LAMP reaction solutions containing 90 μM of EBT dye. (d) Predicted images and ratiometric values for positive and negative

amplification reactions processed for each ratiometric combination, G/R, B/R, and G/B. (e) Experimental images and ratiometric values for positive and negative amplification reactions for each combination: G/R, B/R, and G/B. All experiments were performed with HCV RNA as template.

To test the robustness of our approach to different hardware and illumination conditions, we used HCV RNA amplified by RT-LAMP at two-fold increasing concentrations of indicator dye ranging from 10.9 μM to 1.4 mM (for a total of eight dye concentrations). After RT-LAMP amplification, 50 μL of each reaction solution were transferred to 96-well plates (path length of ~ 1.5 mm) and the readout was imaged with cameras from four common cell phone models: Apple iPhone 4S (Figure 3-3a), HTC inspire 4G (Figure 3-3b), Motorola Moto G (Figure 3-3c), and Nokia 808 PureView (Figure 3-3d). Under fluorescent light and using the G/R ratiometric process (green channel divided by red channel followed by a threshold adjustment to generate a binarized black and white image), we determined that EBT concentrations lower than 0.175 mM provided an insufficient color change for detection with a cell phone camera (Figure 3-3, region I, white background), while concentrations of 1.4 mM inhibited the amplification reaction (Figure 3-3, region III, red background). For this particular indicator dye, the range of concentrations at which color change could be detected by an unmodified cell phone camera and no inhibition was observed at the endpoint of the reaction was identified as 0.175 mM to 0.7 mM (Figure 3-3, region II, green background). Some cell phone cameras were more sensitive (*e.g.* HTC inspire 4G was able to distinguish a positive result at EBT concentrations as low as 0.0875 mM) (Figure 3-3b), but all four cell phone models distinguished a positive reaction at concentrations between 0.175–0.7 mM (Figure 3-3, region II, green background). We then chose one cell phone with the most representative performance (Apple iPhone 4S) to test the robustness of the G/R approach

to different lighting conditions. Under all conditions tested (incandescent light (Figure 3-3e), direct sunlight (Figure 3-3f), and indirect sunlight (Figure 3-3g)), the optimal EBT concentration range that we identified under fluorescent light (0.175–0.7 mM) could be read clearly, confirming the robustness of the ratiometric approach to variations in illumination.

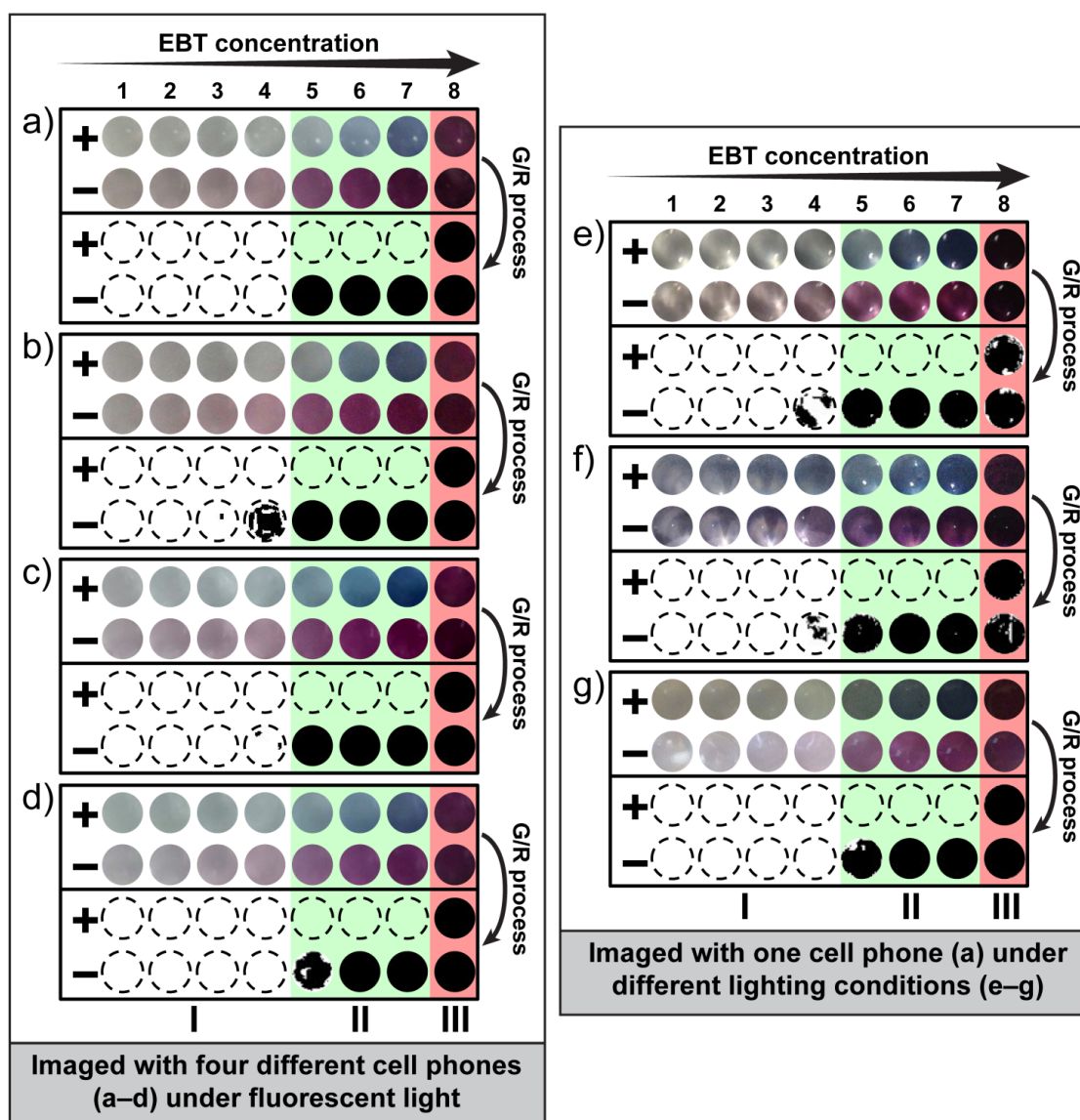


Figure 3-3. Validation of the robustness of the G/R ratiometric approach to different hardware (cell phone cameras) and lighting conditions. (a–g) Enlarged and cropped color images (top two rows of each individual panel) captured by an unmodified cell phone

camera from positive (+) and negative (-) RT-LAMP reactions at two-fold increases in EBT concentration from 10.9 μM to 1.4 mM (1 = 0.011 mM; 2 = 0.022 mM; 3 = 0.044 mM, 4 = 0.088 mM, 5 = 0.175 mM; 6 = 0.35 mM; 7 = 0.7 mM; 8 = 1.4 mM). Positive wells are blue and negative wells are purple. After G/R ratiometric processing (bottom two rows of each individual panel) negative wells are black. Regions I, II, III in each panel indicate the effect of dye concentration: (II) Acceptable concentration range for visualization (green regions); (I) Concentrations too low for visualization (white regions); and (III) Concentrations too high for visualization (red regions). (a–d) Images captured by four common cell phones under fluorescent light: (a) Apple iPhone 4S, (b) HTC inspire 4G, (c) Motorola Moto G and (d) Nokia 808 PureView. (e–g) Images captured by an Apple iPhone 4S under three additional light conditions: (e) incandescent light, (f) direct sunlight and (g) indirect sunlight. All experiments were performed with HCV RNA as a clinically relevant target. All images were acquired with unmodified cell phone cameras. Detailed information for the G/R ratiometric process and additional cell phone camera images are provided in the supporting information.

One-step method for digital visual readout. Microfluidic devices enable ultrasensitive digital quantification. Small well volumes are valuable because they enable faster reactions (because concentrations are high in single wells), minimize the effects of inhibitory materials (due to their isolation into wells) and expand the upper limit of the dynamic range (because single molecules can be confined from samples containing high template concentrations).^{18,65,66} However, as well volumes (and path lengths) decrease, color visualization becomes challenging for a mobile phone. To compensate, the concentration of the indicator dye can be increased; however, high concentrations of some dyes inhibit amplification reactions. Thus, there are inherent physical limits to a colorimetric approach. To validate that this visual readout approach could be applied to single-molecule amplification at nanoliter volumes, we used digital LAMP (dLAMP) and phage lambda DNA (λDNA) as a target. We specifically aimed to resolve three questions: (i) Can we obtain a visual readout for amplified single molecules that can be captured by an unmodified cell phone camera? (ii) Is volume a factor in achieving a digital visual readout? (iii) Does ratiometric processing work for small volumes?

To answer these questions, we designed a multivolume rotational SlipChip device containing 1,240 wells of eight volumes ranging from 15 nL to 50 nL. We loaded these devices with LAMP reaction solution containing an appropriate target concentration in the middle of the device's dynamic range, a fluorescent DNA-detecting intercalation dye (Syto 9), and EBT dye at 0.7 mM (the highest non-inhibiting concentration identified in Figure 3-3). We imaged this device with a house-built real-time fluorescence imager, with a Leica stereoscope (optimal imaging conditions) and with an Apple iPhone 4S. The number of positive counts based on fluorescence was 261, while 260 positives were counted using the indicator dye and G/R process both with the stereoscope and the cell phone (Figure 3-4). This experiment showed that the G/R method could be used in place of fluorescence readout to count amplified single molecules and that the readout capture and G/R processing performed on an unmodified cell phone matched the results obtained under optimal lighting conditions (stereoscope). Additionally, using a device containing 800 wells of 27 nL, we observed excellent correlation among positive counts obtained from the stereoscope, fluorescence imager, and cell phone camera.

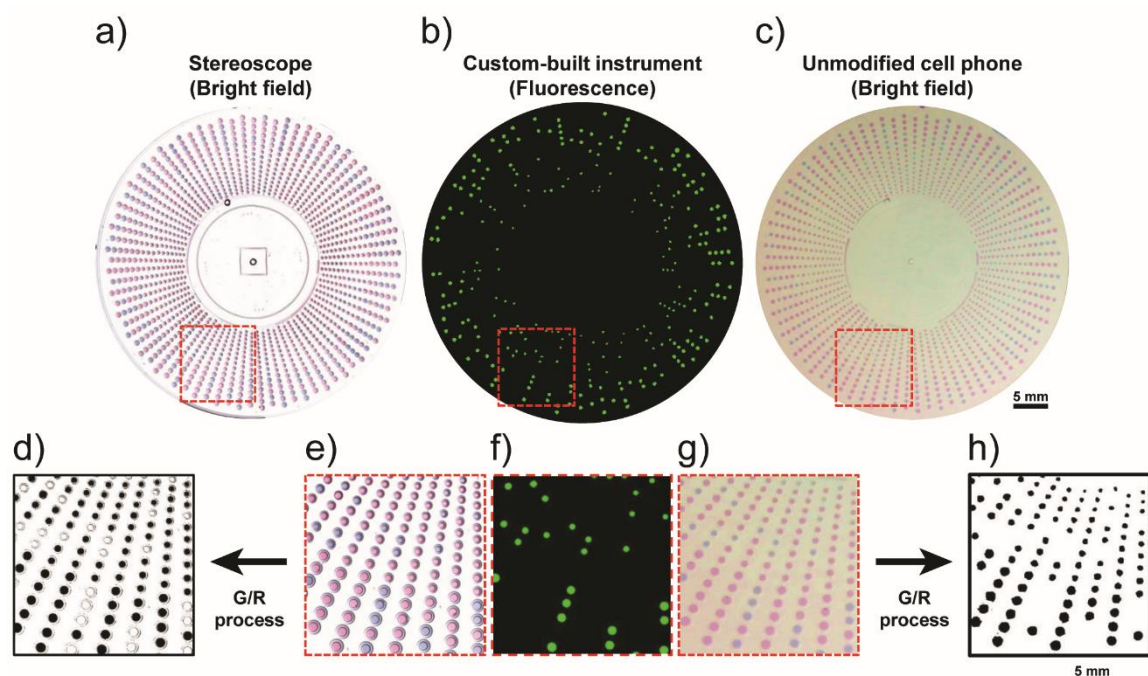


Figure 3-4. Readout from single-molecule digital LAMP reactions performed with lambda DNA on a multivolume rotational SlipChip device imaged by (a) a stereoscope, (b) a fluorescence microscope and (c) an unmodified cell phone camera. (e–g) Callouts are magnified to show visual correlation among the three imaging methods. (d) The results of the ratiometric processing for the stereoscope G/R processed image and (h) the cell phone G/R-processed image. Colors were enhanced in these figures for clarity of publication; raw images were used in all ratiometric analyses. These devices contained 1,240 wells of eight volumes ranging from 15 nL to 50 nL.

While investigating the limits that reaction volume may impose on visual readout, we observed that the estimated template concentration determined from each of the eight well volumes produced similar Most Probable Numbers (MPN) of molecules (mean $8,500 \pm 1,500$ copies/mL) (Figure 3-5a) (estimated concentration from all volumes are within 95% confidence interval at each volume). In addition, all SlipChip devices, analyzed independently, gave similar target concentrations ($8,400 \pm 500$ copies/mL) (Figure 3-5b), suggesting that the selected indicator dye did not impair quantification of single molecules in well sizes 15–50 nL and that these well volumes can be imaged reliably with either a stereoscope or an unmodified cell phone camera. However, the cell

phone camera images of well volumes of 15 nL were less clear than those obtained from the stereoscope, suggesting that volumes of ~15 nL may approach the limit of colorimetric imaging with current camera phone sensors, although as higher quality sensors are integrated into commercial cell phones, this limit would change.

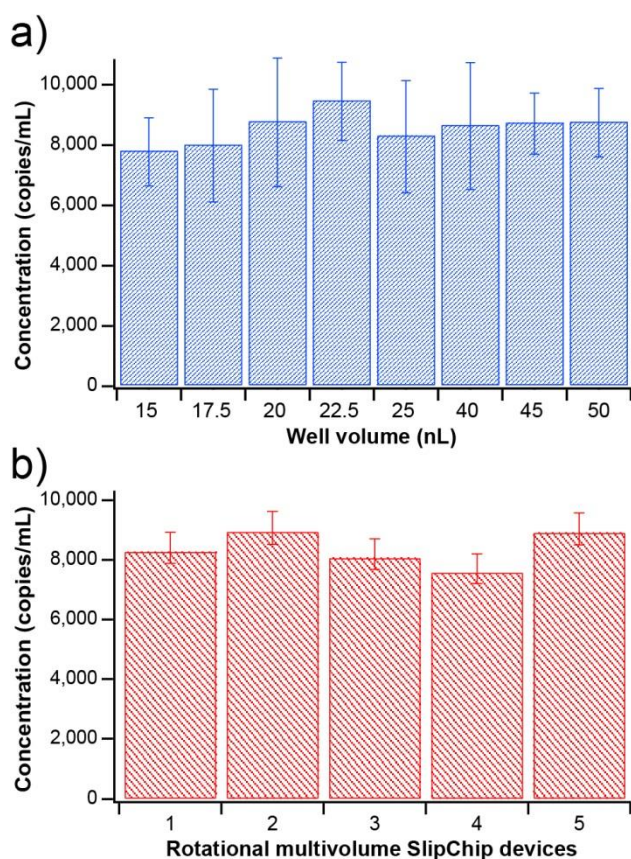


Figure 3-5. Robustness of digital visual readout at different well volumes. Concentration of lambda DNA was estimated by digital LAMP using five multivolume rotational SlipChip devices, each of which contained eight well volumes ranging from 15–50 nL. (a) Measured template concentration for each well volume averaged over five devices. (b) Mean template concentration for each of five rotational SlipChip devices. Concentrations were calculated using MPN theory⁶⁵ and error bars represent standard deviation. Images were captured by a stereoscope and processed with the ratiometric approach (G/R process).

Two-step method for digital visual readout. We next developed a method to apply the visual readout approach to digital devices that contain smaller well volumes. To be able to image at small volumes (*e.g.* 5 nL) on a microfluidic device, one must balance the

need for greater indicator color intensity for visualization with the need to keep dye concentrations below the level of inhibition (Figure 3-3 region III) for an amplification reaction. High concentrations of indicator dye can completely halt an amplification reaction, and we knew from performing real-time bulk experiments that even when reactions are positive, an indicator dye can still interfere to some extent with isothermal nucleic acid amplification—for both RNA and DNA we observed delays in the time-to-positive, and this delay increased at greater concentrations of the indicator dye, even though reactions were positive. We hypothesized that we could prevent inhibition completely by decoupling the amplification step from the readout step. To do this, we designed a two-step SlipChip device (based on previous SlipChip designs)¹³ in which the amplification solution and the detection solution are loaded into separate wells (Figure 3-6a). We validated this two-step protocol with a clinically relevant target, purified HCV RNA, using digital reverse transcription-LAMP (dRT-LAMP). First, we performed digital isothermal amplification in the set of small (5 nL) amplification wells (in the absence of the indicator dye) (Figure 3-6a (i)). After amplification, a “slip” was performed and the amplification wells came into contact with a second set of larger (9.5 nL) wells, which contained the indicator dye—for a total well volume of 14.5 nL (Figure 3-6a (ii)). After mixing, negative wells lacking target molecules stayed purple and wells containing positive reactions turned blue (Figure 3-6a (iii)). Counts obtained by a house-built real-time imaging instrument (to read fluorescence), and counts obtained by G/R processing from an image captured by an unmodified cell phone camera were significantly correlated (Pearson’s $\text{Corr} = 0.9998$; $R^2 = 0.9996$) (Figure 3-6h), showing

that this two-step SlipChip-based protocol provides a suitable visual readout for digital single-molecule amplification for devices containing wells of small volumes.

Devices shown in this manuscript were not designed to achieve clinically relevant concentrations in the lower detection limit of quantification (LDL) because larger well volumes do not represent a challenge when imaging with a mobile phone. Instead, we studied the performance of our approach with wells of small volumes to ensure that this method meets the ULQ required for clinical relevance. The upper limit of quantification (ULQ) is determined by the total number of wells with the smallest volume. As an example, for SlipChip devices with 800 wells of 5 nL the ULQ is 1,162,413 copies/mL, while a SlipChip device with 10,000 wells of 5 nL the ULQ is 1,622,660 (calculations performed according to Krutz, *et al.* 2011).⁶⁵

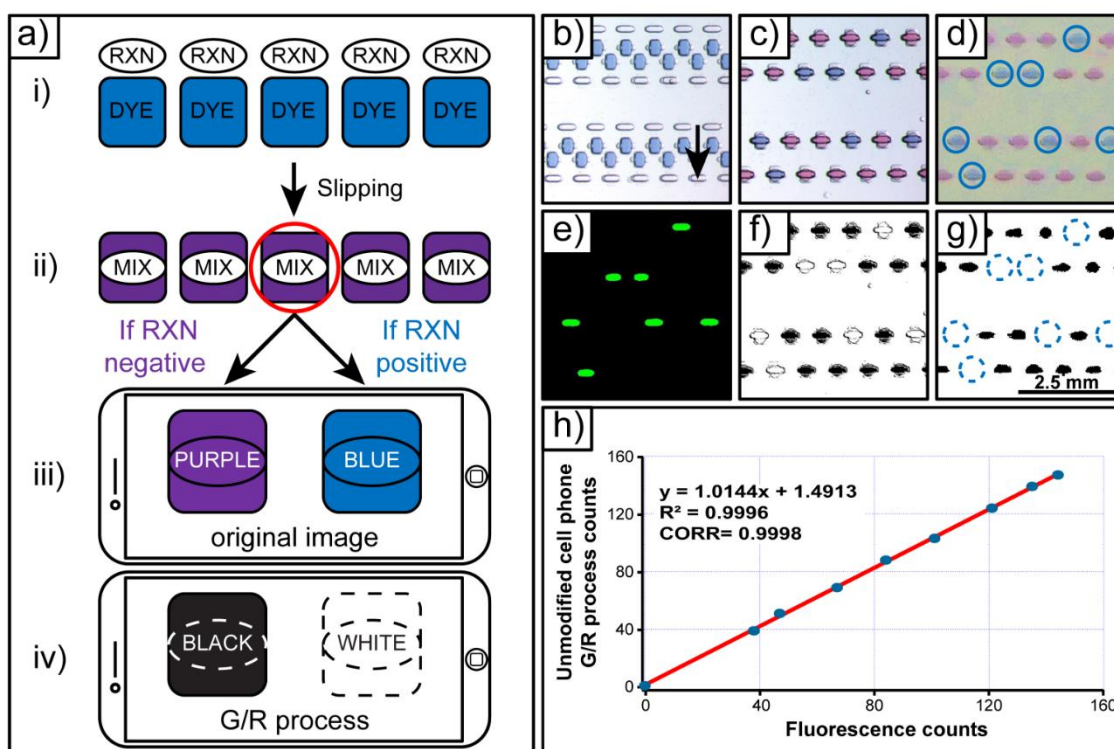


Figure 3-6. Experimental validation of two-step SlipChip devices for single molecule counting with an unmodified cell phone camera. (a) A flow-chart of detection of single molecules in two-step SlipChip: (i) 5 nL amplification wells are loaded with amplification reaction solution (RXN) and 9.5 nL detection wells are loaded with indicator dye (DYE). (ii) After amplification, a slip is performed and the RXN and DYE wells are combined. (iii) Immediately after mixing, positive reaction solutions become blue, while negative reactions remain purple. The readout is imaged by an unmodified cell phone camera. (iv) Ratiometric image processing (G/R process) provides a single binary result (positive or negative). (b) Stereoscope and (c) fluorescence images of the device before the amplification and readout wells are merged (arrow designates direction of slip). (d) Stereoscope and (f) cell phone camera images after the device is slipped and the wells are merged. (e) Stereoscope and (g) cell phone camera images after G/R image processing. (h) Correlation between fluorescence counts and cell phone (G/R processed) counts. Colors were enhanced in figure panels (b, c, d, and f) for clarity of publication; raw images were used in all ratiometric analyses. In these experiments HCV RNA was amplified by dRT-LAMP.

Conclusions

Here we show that single nucleic acid molecules can be detected and counted with an unmodified cell phone camera by employing microfluidic technology, sequence-specific isothermal amplification, and a judiciously chosen amplification-indicator dye. We further show that ratiometric processing of the cell phone image enables robust quantification without the need for a user to differentiate colors. The general methodology we developed can be used as a guideline to enable others to develop their own cell phone based single-molecule counting approach. The methodology includes the following steps: first, an appropriate amplification indicator should be selected. Indicators should respond optically to each nucleotide incorporation event (as opposed to responding to number of produced molecules), resulting in a change in the transmittance profile in the wavelength range of visible light (400–700 nm). The indicator dye should have a change in absorbance matched to the spectral sensitivity of the image sensor in an unmodified cell phone; for ratiometric processing, the solution should have a large relative change in transmittance in color channels for which the camera's image sensor is

most sensitive. Second, the color ratio used in the ratiometric approach is chosen based on the spectral sensitivity of the image sensor in an unmodified cell phone. This step can be done *in silico* to identify the dye with the ratio that provides an unambiguous binary readout of positive and negative reactions that is robust to illumination and hardware conditions. We hope others will use this algorithm to identify even better dyes that will move this field forward. Third, the selected dye and ratiometric approach should be validated using the desired amplification chemistry. Experiments should be performed to establish the range of dye concentrations and well volumes at which an amplification reaction is not inhibited and at which imaging can be done with an unmodified cell phone. For some indicator dyes, the range of suitable well volumes and concentrations will be too narrow. In such situations, an alternative approach is to use a two-step device that separates the amplification and readout steps. Processing can be done directly on a cell phone or uploaded wirelessly to a cloud server to swiftly communicate results, as we have shown previously.¹⁴ We anticipate that the capabilities of visual readout for counting single molecules will extend further as cell phone camera technology advances, as additional indicators are available (*e.g.* metal ions, pH indicators) and as additional types of amplification reactions are developed. Devices that integrate sample preparation, nucleic acid amplification and a visual digital readout that can be captured easily will be a critical breakthrough toward bringing quantitative, ultrasensitive measurements outside of central laboratories—a key step for *in vitro* diagnostics, pandemic surveillance, and environmental monitoring. We hope this work will stimulate regulatory agencies such as the FDA to consider the use of cell phones as valuable diagnostic components.

Methods

Chemicals and materials. All chemicals were purchased from commercial sources. The LoopAmp® RNA amplification kit (Eiken Chemical Co., Ltd., Japan) was purchased from SA Scientific (San Antonio, TX, USA). The LoopAmp® RNA amplification kit contains 2X Reaction Mix (RM) (40 mM Tris-HCl pH 8.8, 20 mM KCl, 16 mM MgSO₄, 20 mM (NH₄)₂SO₄, 0.2% Tween20, 1.6 M Betaine and dNTPs 2.8 mM each), Enzyme Mix (EM) (mixture of Bst DNA polymerase and AMV reverse transcriptase), and distilled water (DW). Bovine serum albumin (BSA) was purchased from Roche Diagnostics (Indianapolis, IN, USA). Phage lambda DNA (500 µg), SUPERase In RNase Inhibitor (20 U/µL), Eriochrome Black T (EBT) dye, mineral oil (DNase, RNase, and Protease free), tetradecane, Costar™ Clear Polystyrene 96-Well Plates, Corning® Universal Optical Microplate Sealing Tape, and DEPC-treated nuclease-free water were purchased from Thermo Fisher Scientific (Hanover Park, IL, USA). Chelex® 100 resin was purchased from Bio-Rad (Hercules, CA, USA). Trehalose Solution (1 M) was purchased from Amersham Life Science (Cleveland, Ohio, USA). Tris-HCl buffer stock solution (1 M, pH 8.0) was purchased from Affymetrix (Santa Clara, CA, USA). All primers were produced by Integrated DNA Technologies (Coralville, IA, USA). Dichlorodimethylsilane was purchased from Sigma-Aldrich (St. Louis, MO, USA). SYTO® 9 Stain and AcroMetrix® HCV High Control were purchased from Life Technologies (Grand Island, NY, USA). Nucleic acid extraction kit QIAamp Viral RNA Mini kit was purchased from QIAGEN Inc. (Valencia, CA, USA). Eppendorf Mastercycler Gradient PCR Thermal Cycler was purchased from Eppendorf (Hamburg, Germany). POLARstar Omega microplate reader was purchased from BMG Labtech

(Durham, NC, USA). Leica MZ Fl III stereoscope with PLAN 0.5x lens was purchased from Leica Microsystems (Bannockburn, IL, USA). Photomasks were designed in AutoCAD 2013 and ordered from CAD/Art Services, Inc. (Bandon, OR, USA). Soda-lime glass plates coated with layers of chromium and photoresist were ordered from the Telic Company (Valencia, CA, USA).

SlipChip device design. The multivolume rotational SlipChip device design was used to demonstrate the one-step method for digital visual readout; this device was composed of 1,240 microfluidic wells, with the following volumes: 160 wells x 15 nL, 160 x 17.5 nL, 160 x 20 nL, 160 x 22.5 nL, 160 x 25 nL, 160 x 40 nL, 160 x 45 nL, 120 x 50. The total combined volume of all wells was 35.6 μ L. For loading, one inlet hole (in the middle ring structure) and four oil escape holes (in the outer ring structure) were drilled in the top plate. The two-step SlipChip device was used to demonstrate a two-step method for digital visual readout; this device was based on previously published SlipChip designs.¹³ For the two-step SlipChip design used in this study, the device was modified in the following ways: (i) the number of each type of well was reduced to 800; (ii) space was added between the arrays to allow for the incubation conformation; (iii) the sequence of well loading was reversed (the smaller 5 nL wells are loaded before the larger 9.5 nL wells). SlipChip multivolume designs for HCV and HIV viral load quantification at clinically relevant dynamic ranges⁶⁷⁻⁶⁹ are provided in the SI (Table S3).

SlipChip device fabrication. The procedure for fabricating the multivolume rotational SlipChip and two-step SlipChip devices was based on previous work.⁷⁰ The device features were etched to a depth of \sim 100 μ m for the multivolume rotational SlipChip devices and \sim 67 μ m for the two-step SlipChip devices. After etching and drilling access

holes, both devices were subjected to the same glass silanization process, previously described,⁶⁶ where the glass plates were first thoroughly cleaned with piranha mix and dried sequentially with 200 proof ethanol and nitrogen gas, and then oxidized in a plasma cleaner for 2 min and immediately transferred into a vacuum desiccator for 1.5 h for silanization with dimethyldichlorosilane. After silanization, the devices were rinsed thoroughly with chloroform, acetone, and ethanol, and dried with nitrogen gas before use. When a glass SlipChip device needed to be reused, it was first cleaned with acid Piranha Solution and then subjected to the same silanization and rinsing procedure described above.

Assembling and loading SlipChips. The SlipChips used for both the dLAMP and the dRT-LAMP reactions were assembled under degassed oil (mineral oil: tetradecane 1:4 v/v). Both top and bottom plates were immersed in the oil phase and placed face to face. The two plates were aligned under a stereoscope (Leica, Germany) and stabilized using binder clips. Through-holes were drilled into the top plate to serve as fluid inlets and oil outlets in dead-end filling. The reagent solutions were loaded through the inlets by pipetting.

HCV viral RNA purification from AcroMetrix® HCV High Control. 200 μ L plasma containing HCV RNA (viral load estimate provided by the company: 1.1 IU/mL – 3.5 IU/mL) was extracted using the QIAamp Viral RNA Mini Kit (QIAGEN Inc, Valencia, CA, USA) according to the manufacturer's instructions. The elution volume was 60 μ L. The purified HCV viral RNA was analyzed immediately or stored at -80 °C until further analysis.

Preparation of EBT solution. The EBT stock solutions were prepared by dissolving EBT dye in deionized water. The aqueous solution was sonicated for 10–20 min and the free volume was filled with argon gas and mixed on a rotator at 65 °C for 1 h. To remove any potential impurities from the EBT dye, Chelex® 100 ion exchange resin was added to the resulting solution (5% w/v) and placed on rotator for 1 h. Resin was centrifuged at 3,000 rpm for 5 min and the top fraction was collected in a Falcon tube, flushed with argon, and stored at room temperature for no more than 2 days.

Storage stability of amplification indicator dyes by drying in the presence of

stabilizer trehalose. EBT, HNB, and calmagite stock solutions at 0.7 mM were prepared by dissolving the dyes in 20 mM Tris-HCl buffer (pH 8.8) and adding 30 mM of trehalose. The solutions were sonicated for 10 min and mixed on a rotator at room temperature for 1 h. Chelex® 100 ion exchange resin was added (5% w/v) and placed on rotator for 1 h. Resin was centrifuged at 3,000 rpm for 5 min and the top fraction was collected in a Falcon tube. The resulting stock solutions were transferred to a Costar™ Clear Polystyrene 96-Well Plate (40 µL per well) and sealed with Corning® Universal Optical Microplate Sealing Tape before spectrophotometric analysis (time 0 h).

Immediately after analysis, the sealing cover was removed and the plate was placed in a desiccator under vacuum overnight until the dye stock solutions were completely dry. Then, at 24-hour time points over the next 120 h (for a total of 5 time points), three wells of each dried amplification indicator solution were resuspended with 40 µL of deionized water and spectrophotometric analyses were performed. After each measurement, the plate was sealed again (to prevent hydration of the dried solutions in the other wells) and kept in the dark at room temperature. The absorption spectra analyses were performed by

using the POLARstar Omega microplate reader with Omega Data analysis software. Absorbance in the range of 400–700 nm was recorded at 2-nm intervals. Blank solutions (20 mM Tris-HCl buffer with 30 mM Trehalose) were also loaded at time 0 h, desiccated after the first measurement, and treated as the rest of the solutions. The measured spectral absorbance from these control solutions was subtracted at each time point from the plotted data.

RT-LAMP amplification of HCV RNA in-tube. The purified HCV RNA described above was used for in-tube RT-LAMP amplification. The RT-LAMP mix contained the following: 20 μ L of RM, 2 μ L of EM, 2 μ L of SYTO® 9 Stain from a 40 μ M stock, 4 μ L of LAMP primer mixture (20 μ M BIP/FIP, 10 μ M LB/LF, and 2.5 μ M B3/F3), 1 μ L of SUPERase In RNase Inhibitor (20 U/L), EBT solutions of various concentrations and with various amounts of RNA template solution, and enough nuclease-free water to bring the volume to 40 μ L. The solution was loaded into 0.2 mL PCR tubes and heated at 63 °C for 50 min and 85 °C for 5 min (heat inactivation) on an Eppendorf Mastercycler Gradient PCR Thermal Cycler.

Spectrophotometric analysis for positive and negative RT-LAMP reactions. Fifty- μ L of positive and negative RT-LAMP reaction solutions containing 0.7 mM of EBT, HNB and calmagite dyes were transferred to a Costar™ Clear Polystyrene 96-Well Plates, the plate was sealed with a Corning® Universal Optical Microplate Sealing Tape and then used for spectrophotometric analysis. An absorption spectra analysis was performed by using the POLARstar Omega microplate reader with Omega Data analysis software. The instrument was first set to zero at 700 nm for distilled water, and absorbance in the range

of 400 nm to 700 nm was recorded at 2-nm intervals. Transmittance was calculated from absorbance values using the following equation: $T = 10^{(2-A)}$.

Prediction of RGB values. Predicted RGB values for a positive and negative LAMP amplification reaction containing EBT were calculated as follows: (i) the spectral response curves for a Exmor R CMOS image sensor were available only in a graphical format, so data was extracted using Plot Digitizer (ver. 2.6.6) and new plots were generated. (ii) The area under the curve for each of the three color channel spectra was normalized (selecting 1,000 arbitrary values under each curve). Uniform white-balanced light source was assumed. (iii) Convolution of the spectral transmittance spectral profiles of the indicator dye for a positive and a negative LAMP reaction solution (experimentally obtained) with the normalized spectral responses from the Exmor R CMOS image sensor was performed. We ignored the light scattering caused by pyrophosphate release during the amplification reaction. As a result, six curves were generated (a positive and negative for each of the three color channels). (iv) The area under each curve was calculated and its square root taken, providing the predicted RGB values for positive and negative RT-LAMP reaction solutions in the presence of EBT at this particular concentration.

dLAMP amplification of phage lambda DNA on multivolume rotational SlipChip devices. To amplify lambda phage DNA using dLAMP method, the LAMP mix contained the following: 20 μ L of RM, 2 μ L of EM, 2 μ L of SYTO® 9 Stain from 40 μ M stock, 4 μ L of primer mixture (20 μ M BIP/FIP, 10 μ M LB/LF, and 2.5 μ M B3/F3), 2 μ L of BSA (20 mg/mL), various amounts of DNA template solution, 4.7 μ L of 6 mM EBT dye (0.7 mM final concentration) and enough nuclease-free water to bring the volume to 40 μ L. The solution was loaded onto a multivolume rotational SlipChip device and

heated at 63 °C for 50 min on flat block PCR machine (Eppendorf Mastercycler). Five minutes of heating at 85 °C was used to stop the reaction.

Real-time dRT-LAMP of HCV RNA on two-step SlipChip devices. To amplify HCV viral RNA using dRT-LAMP method on house-built real-time instrument, the RT-LAMP mix contained the following: 20 µL of RM, 2 µL of EM, 2 µL of SYTO® 9 Stain from 40 µM stock, 4 µL of primer mixture (20 µM BIP/FIP, 10 µM LB/LF, and 2.5 µM B3/F3), 2 µL of BSA (20 mg/mL), 1 µL of SUPERase In RNAase inhibitor, various amounts of RNA template solution, and enough nuclease-free water to bring the volume to 40 µL. The solution was loaded into the 5 nL wells of two-step SlipChip devices. The other set of wells (9.5 nL) were loaded with 2.4 mM solution of EBT solution (1.57 mM final concentration). SlipChips were heated at 63 °C for 50 min on a house-built real-time instrument; reactions were stopped by heating to 85°C for 5 min.

House-built real-time instrument imaging. Experiments were performed on a Bio-Rad PTC-200 thermocycler with a custom machined block. The block contains a flat 3” x 3” portion onto which the devices are placed ensuring optimal thermal contact. The excitation light source used was a Philips Luxeon S (LXS8-PW30) 1315 lumen LED module with a Semrock filter (FF02-475). Image acquisition was performed with a VX-29MG camera and a Zeiss Macro Planar T F2-100mm lens. A Semrock filter (FF01-540) was used as an emission filter. Images acquired were analyzed using LabVIEW software.

House-built real-time instrument data analysis. Fluorescent images were analyzed using self-developed Labview software. The data were analyzed by first creating a binary mask that defined the location of each reaction volume within the image. The masked spots were then overlaid on the stack of images collected over the course of the

experiment and the average intensity of each individual masked spot was tracked over the course of the stack. Background subtraction of the real-time trace was performed by creating a least mean square fit of each individual trace. Threshold was then manually set at the half height of the averaged maximum intensity, and the time-to-positive of each reaction was then determined as the point at which the real-time curve crossed the defined threshold.

Bright-field image acquisition. A mobile phone was used to capture the readout under standard fluorescent light, using the camera's default autofocus and autoexposure settings. Photographs of the 96-well plate were also taken using alternate commercial cell phones and under different lighting conditions (Figure 3-3). Stereoscope imaging was done using Leica MZ Fl III stereoscope with a PLAN 0.5x lens. The stereoscope was equipped with a Diagnostic Instruments color mosaic model 11.2 megapixel camera and images were acquired using Spot imaging software. An automatic white-balance adjustment was done for each image using Spot software. Multiple images were acquired to capture all wells in the device, and assembled to form a complete image of the device to compare with the image acquired from the cell phone camera by using the freeware Image Composite Editor (ver. 2.0).

Bright field image processing and data analysis. Images acquired with cell phone and stereoscope were processed using open source Image J software (ver.1.49) according to the standard procedure. Briefly: (i) white balance was corrected as needed, (ii) color channels of the original image were split and (iii) one channel was divided by a second channel (*e.g.*, green channel divided by the red channel in the G/R approach) to derive a ratiometric image; and (iv) automatic thresholding was applied to make a binary (black

and white) image. Semi-automatic counting on the two-step Slipchip images was accomplished using a freeware Fiji image processing. Acquired bright field images for the multivolume rotational SlipChips were counted manually.

References

- 1 Calmy, A. *et al.* HIV viral load monitoring in resource-limited regions: Optional or necessary? *Clinical Infectious Diseases* **44**, 128-134, doi:10.1086/510073 (2007).
- 2 Johannessen, A. Where we are with point-of-care testing. *Journal of Viral Hepatitis* **22**, 362-365, doi:10.1111/jvh.12385 (2015).
- 3 Wang, S., Xu, F. & Demirci, U. Advances in developing HIV-1 viral load assays for resource-limited settings. *Biotechnol. Adv.* **28**, 770-781, doi:10.1016/j.biotechadv.2010.06.004 (2010).
- 4 Yager, P. *et al.* Microfluidic diagnostic technologies for global public health. *Nature* **442**, 412-418, doi:10.1038/nature05064 (2006).
- 5 Peeling, R. W., Holmes, K. K., Mabey, D. & Ronald, A. Rapid tests for sexually transmitted infections (STIs): the way forward. *Sex Transm Infect* **82 Suppl 5**, 1-6, doi:10.1136/sti.2006.024265 (2006).
- 6 Yager, P., Domingo, G. J. & Gerdes, J. Point-of-care diagnostics for global health. *Annu Rev Biomed Eng* **10**, 107-144, doi:10.1146/annurev.bioeng.10.061807.160524 (2008).
- 7 Niemz, A., Ferguson, T. M. & Boyle, D. S. Point-of-care nucleic acid testing for infectious diseases. *Trends Biotechnol.* **29**, 240-250, doi:10.1016/j.tibtech.2011.01.007 (2011).

- 8 Thom, N. K., Yeung, K., Pillion, M. B. & Phillips, S. T. "Fluidic batteries" as low-cost sources of power in paper-based microfluidic devices. *Lab Chip* **12**, 1768-1770, doi:10.1039/c2lc40126f (2012).
- 9 Labarre, P. *et al.* in *Conf Proc IEEE Eng Med Biol Soc.*2010/11/26 edn 1097-1099.
- 10 Curtis, K. A. *et al.* Isothermal amplification using a chemical heating device for point-of-care detection of HIV-1. *PloS one* **7**, e31432, doi:10.1371/journal.pone.0031432 (2012).
- 11 Liu, C., Mauk, M. G., Hart, R., Qiu, X. & Bau, H. H. A self-heating cartridge for molecular diagnostics. *Lab on a Chip* **11**, 2686-2692, doi:10.1039/c1lc20345b (2011).
- 12 Sun, B. *et al.* Mechanistic evaluation of the pros and cons of digital RT-LAMP for HIV-1 viral load quantification on a microfluidic device and improved efficiency *via* a two-step digital protocol. *Analytical Chemistry* **85**, 1540-1546, doi:10.1021/ac3037206 (2013).
- 13 Shen, F. *et al.* Digital isothermal quantification of nucleic acids *via* simultaneous chemical initiation of recombinase polymerase amplification reactions on SlipChip. *Analytical Chemistry* **83**, 3533-3540, doi:10.1021/ac200247e (2011).
- 14 Selck, D. A., Karymov, M. A., Sun, B. & Ismagilov, R. F. Increased robustness of single-molecule counting with microfluidics, digital isothermal amplification, and a mobile phone *versus* real-time kinetic measurements. *Analytical Chemistry* **85**, 11129-11136, doi:10.1021/ac4030413 (2013).

- 15 Sun, B. *et al.* Measuring fate and rate of single-molecule competition of amplification and restriction digestion, and its use for rapid genotyping tested with hepatitis C viral RNA. *Angew. Chem. Int. Edit.* **53**, 8088-8092, doi:10.1002/anie.201403035 (2014).
- 16 Zhu, Q. Y. *et al.* Self-priming compartmentalization digital LAMP for point-of-care. *Lab on a Chip* **12**, 4755-4763, doi:10.1039/c2lc40774d (2012).
- 17 Gansen, A., Herrick, A. M., Dimov, I. K., Lee, L. P. & Chiu, D. T. Digital LAMP in a sample self-digitization (SD) chip. *Lab on a Chip* **12**, 2247-2254, doi:10.1039/c2lc21247a (2012).
- 18 Witters, D. *et al.* Digital biology and chemistry. *Lab on a Chip* **14**, 3225-3232, doi:10.1039/c4lc00248b (2014).
- 19 Sidorova, J. M., Li, N., Schwartz, D. C., Folch, A. & Monnat, R. J., Jr. Microfluidic-assisted analysis of replicating DNA molecules. *Nat. Protoc.* **4**, 849-861, doi:10.1038/nprot.2009.54 (2009).
- 20 Chou, H. P., Spence, C., Scherer, A. & Quake, S. A microfabricated device for sizing and sorting DNA molecules. *Proc Natl Acad Sci U S A* **96**, 11-13 (1999).
- 21 Marcus, J. S., Anderson, W. F. & Quake, S. R. Microfluidic single-cell mRNA isolation and analysis. *Analytical Chemistry* **78**, 3084-3089, doi:10.1021/ac0519460 (2006).
- 22 Ottesen, E. A., Hong, J. W., Quake, S. R. & Leadbetter, J. R. Microfluidic digital PCR enables multigene analysis of individual environmental bacteria. *Science* **314**, 1464-1467, doi:10.1126/science.1131370 (2006).

- 23 Beer, N. R. *et al.* On-chip, real-time, single-copy polymerase chain reaction in picoliter droplets. *Analytical Chemistry* **79**, 8471-8475, doi:10.1021/ac701809w (2007).
- 24 Kiss, M. M. *et al.* High-Throughput Quantitative Polymerase Chain Reaction in Picoliter Droplets. *Analytical Chemistry* **80**, 8975-8981, doi:10.1021/ac801276c (2008).
- 25 Sundberg, S. O., Wittwer, C. T., Gao, C. & Gale, B. K. Spinning Disk Platform for Microfluidic Digital Polymerase Chain Reaction. *Analytical Chemistry* **82**, 1546-1550, doi:10.1021/ac902398c (2010).
- 26 Lagally, E. T., Medintz, I. & Mathies, R. A. Single-molecule DNA amplification and analysis in an integrated microfluidic device. *Anal. Chem.* **73**, 565-570 (2001).
- 27 Shen, F., Du, W., Kreutz, J. E., Fok, A. & Ismagilov, R. F. Digital PCR on a SlipChip. *Lab Chip* **10**, 2666-2672, doi:10.1039/c004521g (2010).
- 28 Chin, C. D., Linder, V. & Sia, S. K. Lab-on-a-chip devices for global health: past studies and future opportunities. *Lab Chip* **7**, 41-57, doi:10.1039/b611455e (2007).
- 29 Chin, C. D. *et al.* Microfluidics-based diagnostics of infectious diseases in the developing world. *Nat. Med.* **17**, 1015-1019, doi:10.1038/nm.2408 (2011).
- 30 Chin, C. D., Linder, V. & Sia, S. K. Commercialization of microfluidic point-of-care diagnostic devices. *Lab Chip* **12**, 2118-2134, doi:10.1039/c2lc21204h (2012).

- 31 International Telecommunication Union. ICT Facts and Figures--The World in 2015. (2015). <<http://www.itu.int/en/ITU-D/Statistics/Pages/facts/default.aspx>>.
- 32 Whitesides, G. M. A glimpse into the future of diagnostics. *Clin Chem* **59**, 589-591, doi:10.1373/clinchem.2013.204347 (2013).
- 33 Berg, B. *et al.* Cellphone-Based Hand-Held Microplate Reader for Point-of-Care Testing of Enzyme-Linked Immunosorbent Assays. *Acs Nano* **9**, 7857-7866, doi:10.1021/acsnano.5b03203 (2015).
- 34 Wei, Q. *et al.* Imaging and sizing of single DNA molecules on a mobile phone. *ACS Nano* **8**, 12725-12733, doi:10.1021/nm505821y (2014).
- 35 Laksanasopin, T. *et al.* A smartphone dongle for diagnosis of infectious diseases at the point of care. *Sci. Transl. Med.* **7**, 273re271, doi:10.1126/scitranslmed.aaa0056 (2015).
- 36 Yetisen, A. K., Akram, M. S. & Lowe, C. R. Paper-based microfluidic point-of-care diagnostic devices. *Lab on a Chip* **13**, 2210-2251, doi:10.1039/c3lc50169h (2013).
- 37 Besant, J. D. *et al.* Ultrasensitive visual read-out of nucleic acids using electrocatalytic fluid displacement. *Nat. Commun.* **6**, 6978, doi:10.1038/ncomms7978 (2015).
- 38 Martinez, A. W. *et al.* Simple telemedicine for developing regions: Camera phones and paper-based microfluidic devices for real-time, off-site diagnosis. *Analytical Chemistry* **80**, 3699-3707, doi:10.1021/ac800112r (2008).

- 39 Martinez, A. W., Phillips, S. T., Whitesides, G. M. & Carrilho, E. Diagnostics for the developing world: microfluidic paper-based analytical devices. *Anal. Chem.* **82**, 3-10, doi:10.1021/ac9013989 (2010).
- 40 Park, T. S., Li, W. Y., McCracken, K. E. & Yoon, J. Y. Smartphone quantifies Salmonella from paper microfluidics. *Lab on a Chip* **13**, 4832-4840, doi:10.1039/c3lc50976a (2013).
- 41 Vashist, S. K., Mudanyali, O., Schneider, E. M., Zengerle, R. & Ozcan, A. Cellphone-based devices for bioanalytical sciences. *Analytical and Bioanalytical Chemistry* **406**, 3263-3277, doi:10.1007/s00216-013-7473-1 (2014).
- 42 You, D. J., Park, T. S. & Yoon, J. Y. Cell-phone-based measurement of TSH using Mie scatter optimized lateral flow assays. *Biosensors & bioelectronics* **40**, 180-185, doi:10.1016/j.bios.2012.07.014 (2013).
- 43 Shen, L., Hagen, J. A. & Papautsky, I. Point-of-care colorimetric detection with a smartphone. *Lab on a Chip* **12**, 4240-4243, doi:10.1039/c2lc40741h (2012).
- 44 Tyburski, E. A. *et al.* Disposable platform provides visual and color-based point-of-care anemia self-testing. *J Clin Invest* **124**, 4387-4394, doi:10.1172/jci76666 (2014).
- 45 Garcia, A. *et al.* Mobile phone platform as portable chemical analyzer. *Sensors and Actuators B-Chemical* **156**, 350-359, doi:10.1016/j.snb.2011.04.045 (2011).
- 46 Wang, S. Q. *et al.* Integration of cell phone imaging with microchip ELISA to detect ovarian cancer HE4 biomarker in urine at the point-of-care. *Lab on a Chip* **11**, 3411-3418, doi:10.1039/c1lc20479c (2011).

- 47 Nagamine, K., Hase, T. & Notomi, T. Accelerated reaction by loop-mediated isothermal amplification using loop primers. *Molecular and Cellular Probes* **16**, 223-229, doi:10.1006/mcpr.2002.0415 (2002).
- 48 Notomi, T. *et al.* Loop-mediated isothermal amplification of DNA. *Nucleic Acids Research* **28**, doi:10.1093/nar/28.12.e63 (2000).
- 49 Nixon, G. *et al.* Comparative Study of Sensitivity, Linearity, and Resistance to Inhibition of Digital and Nondigital Polymerase Chain Reaction and Loop Mediated Isothermal Amplification Assays for Quantification of Human Cytomegalovirus. *Analytical Chemistry* **86**, 4387-4394, doi:10.1021/ac500208w (2014).
- 50 Goto, M., Honda, E., Ogura, A., Nomoto, A. & Hanaki, K. I. Colorimetric detection of loop-mediated isothermal amplification reaction by using hydroxy naphthol blue. *Biotechniques* **46**, 167-+, doi:10.2144/000113072 (2009).
- 51 Tanner, N. A., Zhang, Y. & Evans, T. C., Jr. Visual detection of isothermal nucleic acid amplification using pH-sensitive dyes. *Biotechniques* **58**, 59-68, doi:10.2144/000114253 (2015).
- 52 Wang, D. G. in *Materials, Machines and Development of Technologies for Industrial Production*. 264-267.
- 53 Yetisen, A. K., Martinez-Hurtado, J. L., Garcia-Melendrez, A., Vasconcellos, F. D. & Lowe, C. R. A smartphone algorithm with inter-phone repeatability for the analysis of colorimetric tests. *Sensors and Actuators B-Chemical* **196**, 156-160, doi:10.1016/j.snb.2014.01.077 (2014).

- 54 Safavieh, M. *et al.* A simple cassette as point-of-care diagnostic device for naked-eye colorimetric bacteria detection. *The Analyst* **139**, 482-487, doi:10.1039/c3an01859h (2014).
- 55 Sony Corp. Sony “Exmor R” CMOS Image Sensors Achieve a Dramatic Increase in Performance. *CX-News Archives, Vol. 59* (2010).
<http://www.sony.net/Products/SC-HP/cx_news_archives/img/pdf/vol_59/featuring_Exmorr.pdf>.
- 56 Oh, S. J. *et al.* Centrifugal loop-mediated isothermal amplification microdevice for rapid, multiplex and colorimetric foodborne pathogen detection. *Biosensors & bioelectronics* **75**, 293-300, doi:10.1016/j.bios.2015.08.052 (2016).
- 57 Wang, D. G. Visual Detection of *Mycobacterium tuberculosis* Complex with Loop-Mediated Isothermal Amplification and Eriochrome Black T. *Applied Mechanics and Materials* **618**, 264-267 (2014).
- 58 Sony Corp. High Picture Quality Cellular Phone CMOS Image Sensors Feature Full HD Video. *CX-News Archives, Vol. 65* (2011).
<http://www.sony.net/Products/SC-HP/cx_news_archives/img/pdf/vol_65/imx081_091_111pq.pdf>.
- 59 Ma, X. J. *et al.* Visual detection of pandemic influenza A H1N1 Virus 2009 by reverse-transcription loop-mediated isothermal amplification with hydroxynaphthol blue dye. *Journal of virological methods* **167**, 214-217, doi:10.1016/j.jviromet.2010.03.027 (2010).
- 60 Nie, K. *et al.* Visual detection of human infection with influenza A (H7N9) virus by subtype-specific reverse transcription loop-mediated isothermal amplification

- with hydroxynaphthol blue dye. *Clin. Microbiol. Infect.* **19**, E372-375, doi:10.1111/1469-0691.12263 (2013).
- 61 Duan, Y. B., Ge, C. Y., Zhang, X. K., Wang, J. X. & Zhou, M. G. Development and evaluation of a novel and rapid detection assay for *Botrytis cinerea* based on loop-mediated isothermal amplification. *PloS one* **9**, e111094, doi:10.1371/journal.pone.0111094 (2014).
- 62 Yang, B. Y. *et al.* Rapid and sensitive detection of human astrovirus in water samples by loop-mediated isothermal amplification with hydroxynaphthol blue dye. *BMC microbiology* **14**, 38, doi:10.1186/1471-2180-14-38 (2014).
- 63 Lindstrom, F. & Diehl, H. Indicator for the Titration of Calcium Plus Magnesium with (Ethylenedinitrilo)tetraacetate. *Analytical Chemistry* **32**, 1123-1127, doi:10.1021/ac60165a022 (1960).
- 64 Bayer, B. E. Color imaging array. US 05/555,477 (1976).
- 65 Kreutz, J. E. *et al.* Theoretical design and analysis of multivolume digital assays with wide dynamic range validated experimentally with microfluidic digital PCR. *Analytical Chemistry* **83**, 8158-8168, doi:10.1021/ac201658s (2011).
- 66 Shen, F. *et al.* Multiplexed quantification of nucleic acids with large dynamic range using multivolume digital RT-PCR on a rotational SlipChip tested with HIV and hepatitis C viral load. *Journal of the American Chemical Society* **133**, 17705-17712, doi:10.1021/ja2060116 (2011).
- 67 Arnedo, M. *et al.* Monitoring HIV viral load in resource limited settings: still a matter of debate? *PloS one* **7**, e47391, doi:10.1371/journal.pone.0047391 (2012).

- 68 Feeney, E. R. & Chung, R. T. Antiviral treatment of hepatitis C. *BMJ (Clinical research ed.)* **348**, g3308, doi:10.1136/bmj.g3308 (2014).
- 69 Cobb, B., Pockros, P. J., Vilchez, R. A. & Vierling, J. M. HCV RNA viral load assessments in the era of direct-acting antivirals. *The American journal of gastroenterology* **108**, 471-475, doi:10.1038/ajg.2012.248 (2013).
- 70 Du, W. B., Li, L., Nichols, K. P. & Ismagilov, R. F. SlipChip. *Lab on a Chip* **9**, 2286-2292, doi:10.1039/b908978k (2009).

Chapter 4:

The Pumping Lid: Investigating Multi-Material 3D Printing for Equipment-Free, Programmable Generation of Positive and Negative Pressures for Microfluidic Applications*

Abstract

Equipment-free pumping is a challenging problem and an active area of research in microfluidics, with applications for both laboratory and limited-resource settings. This paper describes the pumping lid method, a strategy to achieve equipment-free pumping by controlled generation of pressure. Pressure was generated using portable, lightweight, and disposable parts that can be integrated with existing microfluidic devices to simplify workflow and eliminate the need for pumping equipment. The development of this method was enabled by multi-material 3D printing, which allows fast prototyping, including composite parts that combine materials with different mechanical properties (*e.g.* both rigid and elastic materials in the same part). The first type of pumping lids we describe was used to produce predictable positive or negative pressures via controlled compression or expansion of gases. A model was developed to describe the pressures and flow rates generated with this approach and it was validated experimentally. Pressures were pre-programmed by the geometry of the parts and could be tuned further even while the experiment was in progress. Using multiple lids or a composite lid with different inlets enabled several solutions to be pumped independently in a single device. The second type of pumping lids, which relied on vapor-liquid equilibrium to generate

* This chapter was first published in *Lab on a Chip* with authorship belonging to Stefano Begolo, Dmitriy V. Zhukov, David A. Selck, Liang Li, and Rustem F. Ismagilov. The original manuscript can be found at: <http://dx.doi.org/10.1039/c4lc00910j>

pressure, was designed, modeled, and experimentally characterized. The pumping lid method was validated by controlling flow in different types of microfluidic applications, including the production of droplets, control of laminar flow profiles, and loading of SlipChip devices. We believe that applying the pumping lid methodology to existing microfluidic devices will enhance their use as portable diagnostic tools in limited resource settings as well as accelerate adoption of microfluidics in laboratories.

Introduction

This paper describes an equipment-free method for generating positive and negative pressures in a microfluidic device using a pumping lid. Most of the microfluidic devices developed in the past two decades rely on external equipment for operation, including the use of pumps, gas cylinders, or other external controllers,¹⁻⁵ for precise pumping and loading. Achieving the same degree of flow control without expensive or bulky equipment is necessary for making microfluidic devices more accessible. Currently, equipment-free pumping is both a challenging problem and an active area of research, with several proposed approaches.⁶⁻¹⁵ For applications in which the total sample volume is less than the internal volume of the device, the sample's surface energy is known and stable flow rate isn't required, capillary-based pumping (wicking) can be used.⁶⁻¹⁰ This has been done by flowing samples through microchannels^{9,10} or using fibrous materials, such as paper.⁶⁻⁸ For cases when the device can be pre-loaded with a solution, and the solution's surface energy is known, the flow of the solution can be driven by the difference in capillary pressure between droplets of different sizes of this solution placed at the inlet and outlet of the device. For this method the pressure difference can be restored constantly by the addition of solution to the smaller droplet.^{11,12} When only small

sample volumes are used (a few microliters or less) and the application does not require flow rates greater than a few nanoliters per second, pre-degassed microfluidic devices can be used to generate flow.^{13,14} Finally, when the density and volume of the sample are known, and the device can be stabilized in a precisely horizontal position, gravity can generate predictable pressure drops and drive the flow in a microfluidic device. In this approach, the difference in height of fluid in separate reservoirs generates the desired pressure drop.¹⁵ These methods have a wide variety of applications, and some of them showed precision in the order of 10-20% of the measured values,^{10,14} and one demonstrated 10% accuracy.¹² However, none of these methods can provide precise and predictable control of pumping while exhibiting all of the following features: absence of external equipment, capability of achieving a wide range of flow rates and achieving predictable flow rates that are independent of the sample's volume, surface energy, and density.

Here we describe the theory, characterize the method, and validate the design of a range of equipment-free pumping lids for controlled-pressure generation in microfluidic applications. This pressure generation approach is based on controlled gas expansion or compression, so it does not depend on the nature of the liquid being pumped, the geometry of the channels, or the device's orientation. It can also be coupled with evaporation of a volatile liquid to generate pressure. Development and characterization of this method was enabled by multi-material 3D printing, which allows fast prototyping of composite parts that have sections with different mechanical properties. In addition, the pumping lid approach has the following beneficial features that have not been combined previously in a single method:

- a) The same setup can pump liquids of different density and/or surface energy with no difference in the resulting flow rate.
- b) The pressure source is integrated with the device, so the method does not require the use of external connectors or tubing.
- c) A simple model can be used to predict the pressure/flow rate generated by a specific lid/cup combination, matching or improving the precision and accuracy demonstrated for other methods.
- d) Pumping lids are interchangeable, so the same microfluidic device can be used with different lids to generate different flow rates. Pressures can be tuned by choosing the pumping lid with the appropriate dimensions and/or by modifying the lid's geometry.
- e) The user can alter the pressure by simply changing the position of the pumping lid, without interrupting the experiment.
- f) Flow rates can be tuned precisely, with values ranging from a few nanoliters to more than a microliter per second, and remain consistent for long periods (hours in some cases).
- g) The sample volume pumped can be larger than the internal volume of the device, making the method appropriate for handling samples that range from a few microliters to milliliters.
- h) Both positive and negative pressures can be produced in a predictable way and used to generate and control flow.

- i) While pumping is in progress, the lid keeps the sample isolated from the external environment, preventing contamination and evaporation.
- j) The combined weight of all parts is less than 50 g, making it portable.
- k) The device can be made of low-cost, disposable/recyclable polymeric materials, making it adaptable to resource-limited settings.

Results and discussion

Principle of pumping lid operation

The pumping lid method described in this paper is based on controlled compression or expansion of gas (Figure 4-1). To generate positive pressure, the user places the sample at the device inlet and then places the pumping lid on the cup integrated into the microfluidic device (Figure 4-1A). When the user pushes the lid down to its final position, the air in the lid's cavity is isolated and compressed, creating positive-gauge pressure. The lid's position is held by friction, but to increase robustness, guiding and locking structures can be integrated into the design (Figure 4-1A-1B). Conversely, to create negative pressure, a pumping lid is pre-placed on the cup (Figure 4-1B) and the user pulls up on the pumping lid, expanding the air in the cavity. The degree of expansion is controlled by guiding structures.

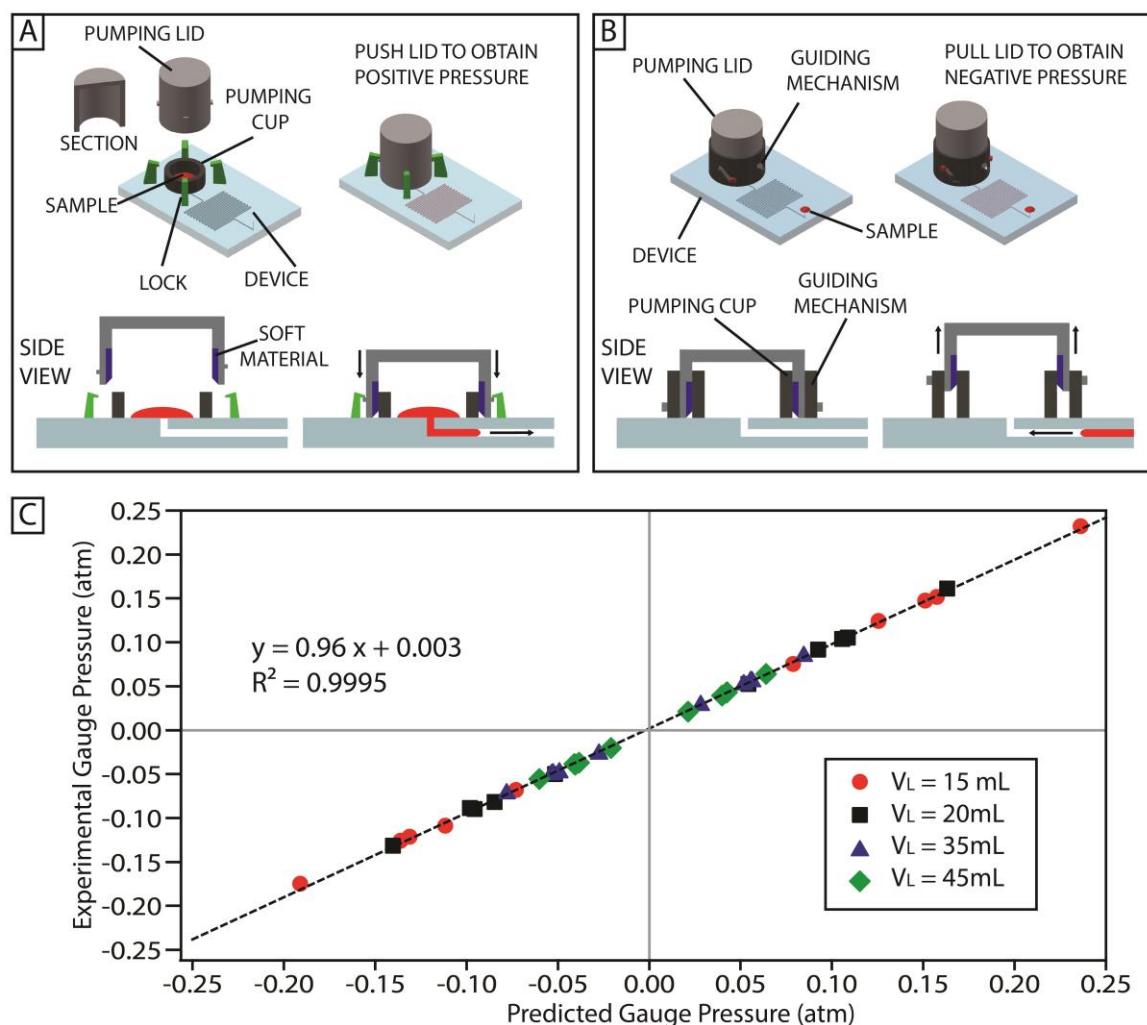


Figure 4-1. Principle of pumping lid operation. (A) Schematic of the method to generate positive pressure. A device is equipped with a cup (black) and locks (green). A sample (red) is placed in the cup before pumping. The pumping lid (grey) contains a cavity as shown in the side view. Part of the pumping lid is composed of a soft, deformable material (blue). Placing the lid on the cup compresses the air in the cavity and generates the pressure used to pump the sample in the device. The locks hold the lid in place to maintain the pressure over time. (B) Schematic of the method to generate negative pressure. The pumping lid (grey) is placed on the inner cup (black, visible only in the side view) before the experiment, and is equipped with guiding pins (red). These pins slide on a guiding structure (black) to guide the movement of the lid. When the user pulls the lid, the air in the cavity expands, creating a negative gauge pressure that pumps the sample into the device. (C) Pressures obtained from 40 experimental cup-lid combinations ($N=3$) plotted against the pressure values obtained from the model (Eq. 2 and Eq. 6). The colors denote lids of different cavity volumes. The dashed black line indicates the linear fit of

the data and its parameters are reported in the graph. Standard deviations for all of these experiments were below 5% of the measured value.

Theoretical model for prediction of the pressure generated with the pumping lid

First, we analyze the initial pressure generated by the pumping lid and cup, prior to pumping. We use the Boyle law for isothermal gas compression: $P_0V_0 = P_1V_1$; assumptions of ideal gas behavior are appropriate in this case because the pressures are low (~ 1 atm) and the temperatures are sufficiently high (~ 300 K).

Positive pressures

The positive pumping pressure depends on four main parameters: the volume of the cavity in the pumping lid (V_L), the volume of the cup walls (V_W), the volume of the empty space inside the cup (V_C) and the volume of sample loaded in the cup (V_S). When the lid is placed on the cup and first creates the seal, the volume of air enclosed is defined as $V_0 = V_L + V_C - V_S$, and the initial pressure is $P_0 \sim 1$ atm. After the user pushes down the lid, the air is compressed and the final volume is given by $V_1 = V_L - V_W - V_S$. Applying Boyle's law, the pressure at this point is calculated as follows:

$$P_1 = \frac{P_0 (V_L + V_C - V_S)}{(V_L - V_S - V_W)} = P_0 + \frac{P_0 (V_W + V_C)}{(V_L - V_S - V_W)} \quad (\text{Eq. 1})$$

A more generalized formula can be used for the case when the lid is already pre-placed on the cup, at a distance d from the final position. The pressure is generated when the user pushes the lid to the final position. In this case, the pressure depends on the four volumes described above (V_L, V_C and V_S, V_W) and on the ratio x , between d and the total height of the cup (h), defined as $x = d/h$. The initial volume in this case is given by $V_0 = V_L - (1 - x) V_W + x V_C - V_S$ and the initial pressure is again the atmospheric

pressure, $P_0 \sim 1$ atm. After the lid has been pushed down by a distance d , the final volume is given by $V_1 = V_L - V_W - V_S$. The pressure at this point is calculated by using the same relation, $P_0 V_0 = P_1 V_1$, and is defined as:

$$P_1 = \frac{P_0 [V_L + x V_C - (1-x)V_W - V_S^0]}{V_L - V_W - V_S^0} = P_0 + \frac{P_0 x(V_W + V_C)}{V_L - V_W - V_S^0} \quad (\text{Eq. 2})$$

V_S^0 defines the initial sample volume.

Second, we analyzed changes in pressure due to pumping. The pressure as a function of time is expressed as:

$$P_1(t) = \frac{P_0 [V_L + x V_C - (1-x)V_W - V_S(t)]}{V_L - V_W - V_S(t)} \quad (\text{Eq. 3})$$

$V_S(t)$ defines the volume of sample present in the cup at time t . When the sample volume is substantially smaller than the difference between the cavity and pumping cup volumes, $V_L - V_W$, the change in the only time-dependent term, $V_S(t)$, becomes negligible and the pressure can be considered constant, and Eq. 3 becomes identical to Eq. 2. This assumption was verified in all the experiments described in this paper, unless otherwise stated. Eq. 3 can be used to guide the design of pumping lids and cups, in order to predict the variation in pressure due to pumping and tune it if needed. Pumping lids and cups designed to produce gauge pressures up to 1.5 atm were successfully used to flush samples out of microfluidic devices. No problems were observed when these pressures were applied to the devices.

When the sample volume is large enough to affect the pressure, the following set of equations can be used to describe the change in pressure. Given the hydraulic resistance

(R_H) of the device, the time-resolved drop in positive pressure can be calculated as the sample is pumped out of the cup:

$$P_1(t) = \frac{P_0(V_L - (1-x)V_W + xV_C - V_S^0)}{\sqrt{(V_L - V_W)^2 + 2\left(\frac{P_0 t}{R_H}(V_L - (1-x)V_W + xV_C - V_S^0) - V_S^0\left(V_L - V_W - \frac{V_S^0}{2}\right)\right)}} \quad (\text{Eq. 4})$$

Eq. 4 is only valid for $P_1 \geq P_0$ and while pumping is in progress. We assumed that the values of R_H remained constant in our experiments, because we pre-filled the channels with the solution being pumped. If the channel is not pre-filled, the initial variation of R_H during filling would need to be accounted for. To calculate the time required to pump the whole sample volume, the following equation is used:

$$t^* = \frac{\left(V_L - V_W - \frac{V_S^0}{2}\right)V_S^0}{\frac{P_0}{R_H}(V_L - (1-x)V_W + xV_C - V_S^0)} \quad (\text{Eq. 5})$$

Eq. 5 relies on the same assumptions as Eq. 4.

Negative pressures

For generation of negative gauge pressures, the pumping lid is pre-placed onto the cup, and the user pulls it by a distance d . Assuming the cup is empty prior to pumping, the initial volume is given by $V_0 = V_L - V_W$. The initial pressure is the atmospheric pressure, $P_0 \sim 1$ atm. If the channel is not pre-filled with solution prior to pumping, the channel volume needs to be accounted for in V_0 . After the lid has been pulled by a length d , the final volume of air is given by $V_1 = V_L + xV_C - (1-x)V_W$. Using previously defined parameters and the relation $P_0V_0 = P_1V_1$, the pressure at this point is defined as:

$$P_1 = \frac{P_0(V_L - V_W)}{V_L + xV_C - (1-x)V_W} = P_0 - \frac{P_0 x(V_W + V_C)}{V_L + xV_C - (1-x)V_W} \quad (\text{Eq. 6})$$

Similarly to the case of the positive pressure, once pumping commences, the time dependence of P_1 is given by the expression:

$$P_1(t) = \frac{P_0 (V_L - V_W)}{V_L + x V_C - (1-x)V_W - V_S(t)} \quad (\text{Eq. 7})$$

$V_S(t)$ represents the volume of sample pumped into the cup at a given time t . When the sample volume is much smaller than $V_L + x V_C - (1-x)V_W$, the only time dependent term in Eq. 7, $V_S(t)$, becomes negligible and the pressure can be considered constant.

Whenever this assumption cannot be made, one can calculate the time-resolved drop in pressure as the sample is pumped into the cup, given the hydraulic resistance (R_H) of the device:

$$P_1(t) = \frac{P_0(V_L - V_W)}{\sqrt{(V_L - (1-x)V_W + xV_C)^2 - 2\frac{P_0 t}{R_H}(V_L - V_W)}} \quad (\text{Eq. 8})$$

Eq. 8 is only valid for $P_1 \leq P_0$ and while pumping is in progress. To calculate the time required to pump a given sample volume one should use the following equation:

$$t^* = \frac{\left(V_L + xV_C - (1-x)V_W - \frac{V_S^f}{2} \right) V_S^f}{(V_L - V_W)} \cdot \frac{R_H}{P_0} \quad (\text{Eq. 9})$$

V_S^f represents the total sample volume to be pumped into the cup.

Generation of predictable positive and negative pressures

We experimentally tested (Figure 4-1C) predictions of the model for generating both positive (Figure 4-1A) and negative (Figure 4-1B) gauge pressures. We report (Figure 4-1C) the pressures obtained from 40 combinations of cups and pumping lids, plotted against the pressure value predicted by Eq. 2 and Eq. 6. Cups were 3D-printed directly on

a rigid support and not connected to a device. We used a 5 psi differential pressure sensor (PXCPC-005DV, Omega Engineering), which was connected to a power supply (Portrans FS-02512-1M, 12V, 2.1 Amp power supply, Jameco Electronics) and to a data acquisition board (OMB-DAQ-2408, Omega Engineering). A custom program was written in LabVIEW (National Instruments) to convert the signal collected by the sensor to gauge pressure. The sampling frequency was 2 Hz. Each condition varied in at least one model parameter (V_L : 14.7 mL – 44.8 mL; V_C : 0 – 2.7 mL; V_W : 0.8 μ L – 3.6 μ L; x : 0.25 – 0.75). The pumping lids used for these experiments included a nozzle that could be connected to the positive side of the pressure sensor using a short piece of Tygon tubing (1 cm long). Lid volumes were calculated using CAD software, accounting for the extra volume introduced by the nozzle, tubing, and the sensor. The other side of the sensor was exposed to the external environment, so all data collected were in terms of gauge pressure. The results were a close match to the predicted outcome, with an R^2 value of 0.9995 and a slope of 0.96. The pressures produced in this experiment spanned more than an order of magnitude (Table S1). Furthermore, the model predicts that even higher pressure could be obtained by decreasing the volume of the empty parts (V_L , V_C) and/or by increasing the other volumes (V_W and V_S).

Design guidelines for the pumping lid and cup

We found three guidelines to be helpful in designing pumping lids and cups: (1) the model can be used to either predict the pressure generated by a particular lid/cup combination, or to determine the lid and cup dimensions needed to achieve a particular pressure. All parameters can be tuned and the resulting pressure for each combination can be predicted using the equations described in the previous section. (2) To ensure effective

sealing between the pumping lid and the cup, at least one of the two parts (lid or cup) should contain a deformable (soft) portion. The design requires a small overlap between the parts, so the soft portion is forced to deform when the lid is placed on the cup, thus creating a hermetic seal. Typical overlaps were in the order of 100 μm to 200 μm , which corresponds to $\sim 1\text{-}2\%$ of the cup diameter. We used multi-material 3D printing provided by Objet 260 system (Stratasys, Eden Prairie, MN, USA), which can produce parts composed of two different materials, and mixtures of these two materials. (3)

Compression deforms the soft portion of the lid, and the material tends to be squeezed laterally. We observed that if this deformed material goes between the pumping lid and the base of the cup, the lid cannot be pushed to its final position and the obtained pressure will be lower than the one predicted by the model. This effect can be minimized by ensuring that the thickness of the soft layer is significantly larger than the overlap between the lid and cup, typically in the order of 1-1.5 mm. Another solution is to use soft layers with a tapered profile (Figure 4-1A).

Controlled pressure variation during an experiment

Next, we wished to test whether it would be possible to switch the pressure applied by the pumping lid without interrupting the flow or exposing the sample to the environment (to minimize contamination or evaporation). This capability is desired when several flow rates need to be tested in one continuous experiment. Pressure is changed by compressing or expanding air in the cavity. Therefore, here we investigated whether the level of compression or expansion, and therefore the pressure, can be controlled precisely by using the guiding structures (Figure 4-2). For example, for both positive- and negative-gauge pressures, we designed lids that can be placed in three positions, labeled (i), (ii),

and (iii). Each position provides a defined, specific pressure, and the user can switch between the positions by rotating the lid on its axis (Figures 4-2D, 4-2H). The lids for these experiments were 3D-printed with a nozzle for the pressure sensor and pressure data was collected with the same setup as described in previous sections. For both positive- and negative-pressure devices, the starting position, (i), corresponds to zero gauge pressure (Figure 4-2). This adjustable design thus enables customized, “pre-programmed” pressure control during an experiment (e.g. to initiate or stop flow, and to change the flow rate) and allows the fully assembled device to be stored without applying pressure before use. While the devices demonstrated here are able to produce three specific pressures, more lid positions can be designed to enable finer tuning.

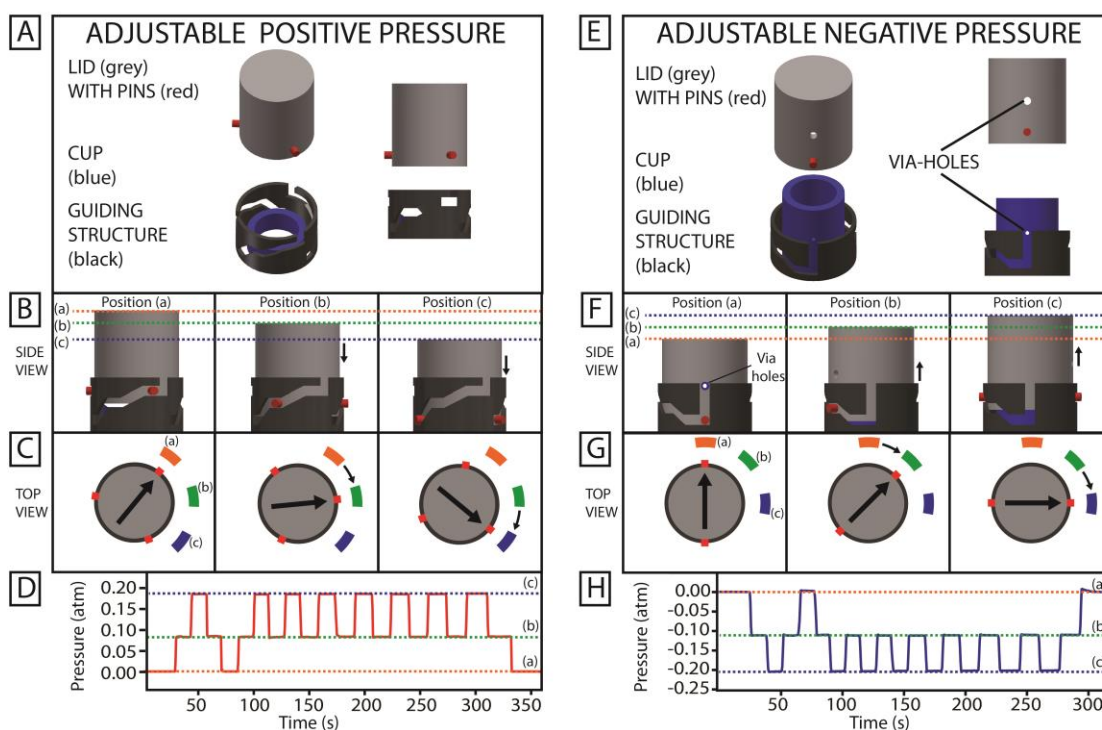


Figure 4-2. Strategies for producing multiple pressure values in a single device using a cup and pumping lid. (A-D) Positive pressures produced by turning a pumping lid (grey) using a cup (blue) fit with a guiding structure (black) (A). Turning the lid within the guiding structure yields three potential lid positions, which are shown in side (B) and top

(C) views, each of which produces a different pressure. In Position (i) the lid is not in contact with the cup, so no pressure is produced. In Position (ii) the lid is lowered and positive pressure is produced. In Position (iii) the lid is lowered further, and the pressure increases. The horizontal dashed lines show the level of the lid in the three positions. Panel D shows an experimental pressure profile obtained by turning the lid between the three positions. (E-H) Negative pressures produced by turning a pumping lid (grey), using a cup (blue) fit with a guiding structure (black) (E). Turning the guiding structure yields three potential lid positions, which are shown in side (F) and top (G) views, each of which produce a different pressure. The pumping lid and the cup have via-holes that align only in Position (i), so there is no gauge pressure in this configuration. In Position (ii) the lid is raised and negative pressure is produced. In Position (iii) the lid is raised further, and the pressure decreases. The horizontal dashed lines show the level of the lid in the three positions. Panel H shows an experimental pressure profile obtained by turning the lid between the three positions.

Generation of flow using the pumping lid approach

Next, we tested the prediction that for a given channel geometry, the pumping lid method would provide consistent flow rate that depends on viscosity, but not on surface energy or density of the fluid being pumped. We used Eq. 1 to predict the pressure applied by the pumping lid, and Eq. 10 to predict hydraulic resistance R_H that depends on the viscosity and the dimensions of the channel¹⁶.

$$R_H = \frac{12\mu L}{h^3 w \left(1 - 0.63 \left(\frac{h}{w}\right)\right)} \quad (\text{Eq. 10})$$

L defines the channel length, h the channel height, and w the width of the channel. The volumetric flow rate can thus be predicted with Eq. 11:

$$Q = \frac{P}{R_H} = \frac{Ph^3 w \left(1 - 0.63 \left(\frac{h}{w}\right)\right)}{12\mu L} \quad (\text{Eq. 11})$$

To test these predictions, we first characterized pumping of water through a microfluidic device using seven pumping lids, each providing a different pressure (Figure 4-3A). The

device consisted of glass-bonded PDMS layer¹⁷, pumping cup, PTFE tubing, and the pumping lid. A 30.8 cm long, 58 μm high, 110 μm wide serpentine was molded into the PDMS layer, and was pre-filled with each solution prior to pumping experiment, as described in SI. The slope of the fitting curve is the inverse of the hydraulic resistance (R_H) for the experimental setup, as suggested by Eq. 11.

The experimental value for R_H obtained from the fit is $2.59 \times 10^{14} \text{ Pa s / m}^3$, which matched the theoretical value calculated for the microfluidic channel geometry: $2.58 \times 10^{14} \text{ Pa s / m}^3$ ¹⁶. Thus, it was possible to predict the flow rate for a given pumping lid used with a given microfluidic device, and the design was robust enough to give reproducible results. The flow rates in this experiment were 1 – 5 $\mu\text{L/min}$, and this range was chosen to minimize the experimental errors when measuring flowing time. Higher flow rates could be produced by increasing the pressure generated by the pumping lid (as described in the previous sections), or by using a device with lower hydraulic resistance. For example, a device with a channel 150 μm tall x 150 μm wide x 20 mm long will have a hydraulic resistance almost 200 times less than the devices used for these experiments, so the flow rate generated with the same pumping lids would approach 1 mL/min.

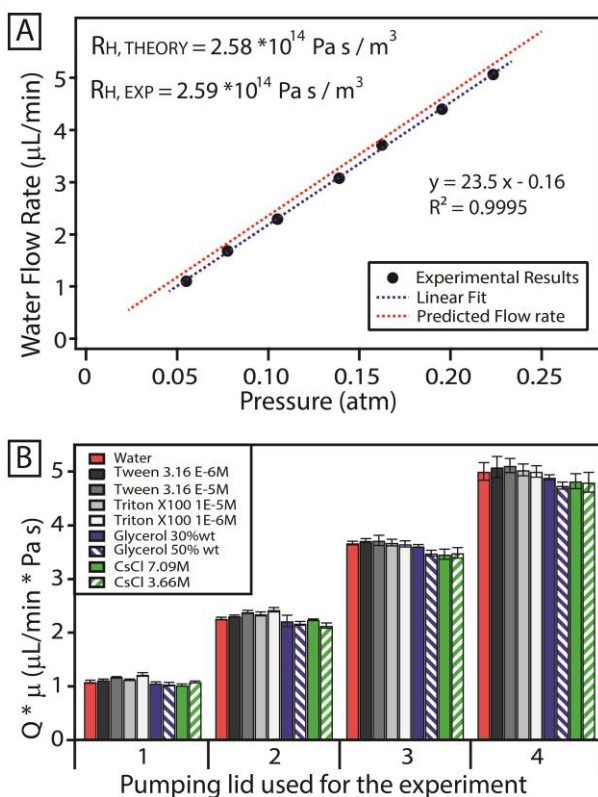


Figure 4-3. Experimentally and quantitatively testing the model describing pumping with a pumping lid as a function of hydraulic resistance of the channel and properties of the fluid. (A) Flow rate of water in a microfluidic device using different pumping lids to generate different pressures. The dotted red line indicates the predicted flow rate based on the device geometry, while the dotted blue line shows the linear fit of the data and its parameters are reported on the graph ($N=3$; error bars smaller than the size of the marker). Standard deviations for all of these experiments were below 5% of the measured value. (B) A plot of experimental flow rates, multiplied by the viscosity, for different aqueous solutions. Flow rates were inversely proportional to viscosity and independent of the surface energy or density of the solutions. Schematics of the setup used for these experiments are provided in the supplementary material.

Generation of flow rate independent of density and surface energy

To verify that the flow rate in the pumping lid method is independent of solution density and surface energy, we pumped nine aqueous solutions of different properties using seven different lids to measure the flow rate at different inlet pressures. Solutions of viscosity similar to water, but with different surface energies (30 – 72 mN/m) and

different densities (1 – 1.9 g/mL), had flow rates comparable to those obtained for water. We experimentally measured viscosities of all nine solutions to confirm this result. Note that the viscosity-adjusted flow rate values ($Q \cdot \mu$) were similar for all liquids (Figure 4-3B), which is explained in the next section.

Generation of flow for solutions of different viscosities

We then tested whether the pumping lid is appropriate to produce flow in solutions with viscosities higher than that of water. In our experiments, solutions had viscosities between 1 mPa*s and 4 mPa*s (Figure 4-3B). The flow rates for high viscosity solutions were lower than those obtained for pure water, because the value of the hydraulic resistance R_H described above is directly proportional to the viscosity of the liquid pumped (Eq. 10)¹⁶. Eq. 11 can be re-written as:

$$Q \cdot \mu = \frac{Ph^3w\left(1-0.63\left(\frac{h}{w}\right)\right)}{12L} \quad (\text{Eq. 12})$$

Eq. 12 predicts that if the same lid-cup combination is used on the same device, the product of the flow rate and the viscosity of the solution will be constant¹⁶. Our experimental results (Figure 4-3B) corroborated this prediction, since the $\mu \cdot Q$ values for all the solutions analyzed were comparable to those obtained for water (Figure 4-3B). This means that the pressure generated by a pumping lid depended solely on the lid-cup dimensions, and not on the nature of the solution to be pumped.

Use of multiple lids on the same device to achieve complex flow control over long timescales

Next, we tested the idea that using separate cups and lids at different inlets makes it possible to simultaneously pump more than one solution and to independently control the pressure imposed at each inlet (Figure 4-4A). First, we used multiple lids to produce nanoliter droplets (Figure 4-4B)¹⁸⁻²⁰. Immiscible fluids can be difficult to handle under pressure-driven flow because the applied pressure should be higher than capillary pressure but not so high to generate an excessive capillary number that would cause droplet deformation²¹. Also, when multiple inlets are controlled with different pressures, liquid could potentially flow from one cup to another. To avoid this, we designed devices with geometries that included a serpentine channel between the inlets and the junction used to produce the droplets. This serpentine channel had a fluidic resistance higher than that of the outlet channel, and ensured that liquids were not transferred from one cup to the other during experiments. This approach was used to generate nanoliter droplets (plugs) of water in fluorinated oil, using flow focusing and T-junction geometries (Figure 4-4B), with volumes that ranged from 0.5 to 2.5 nL.

Parallel laminar flow profiles can also be produced (Figure 4-4C). We achieved stable flow patterns for more than 2.5 h, with a total pumped amount of 0.9 mL. The predicted decrease of flow rate in this system over a 2.5 h period was 45% of the original value (Eq. 4), which was consistent with our experimental observations (Figure 4-4C).

Increased diffusion between the dyes was observed, due to the longer residence time in the channel. Because we used lids of the same size and loaded samples of the same volume and viscosity, over time we observed a decrease in the absolute value of the flow rates, but not a decrease in their ratios. We emphasize that if the volumes of the lids,

cups, sample volumes and/or viscosities are different, the flow rates will drop at different rates (Eq. 4).

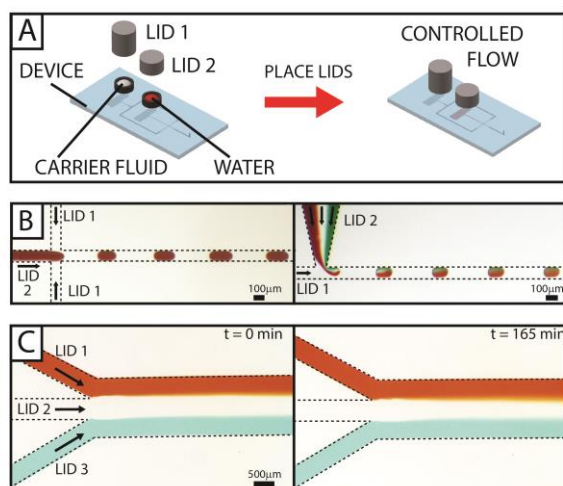


Figure 4-4. Use of the pumping lid approach to control pumping of each of several fluids with different properties in a microfluidic device. (A) Schematic of the pumping approach using multiple solutions in the same device. Each sample was pumped in the device with a different pumping lid, each lid producing a different pressure. (B) Left: Experimental photographs illustrating production of nanoliter plugs (red) in fluorinated oil (transparent), using a microfluidic device with flow focusing geometry. Right: Production of multicomponent aqueous droplets in fluorinated oil using a T-junction. The solutions (red, transparent and green) were pumped independently and used to produce nanoliter plugs. (C) Experimental photographs illustrating that the parallel laminar flow profile of three separate streams of aqueous solution (red, transparent and light blue) was stable even after 165 min (2.75 h). A total volume of 0.9 mL (300 μ L of each solution) was pumped in this experiment.

Use of composite lids to produce different flow patterns in the same device

A “composite lid,” a pumping lid with multiple cavities, was designed to simultaneously seal multiple cups (Figure 4-5). The cavities in the composite lid can be isolated or connected to one another. For example, if inlets require identical pressures, their corresponding cavities can be linked (Figure 4-5C).

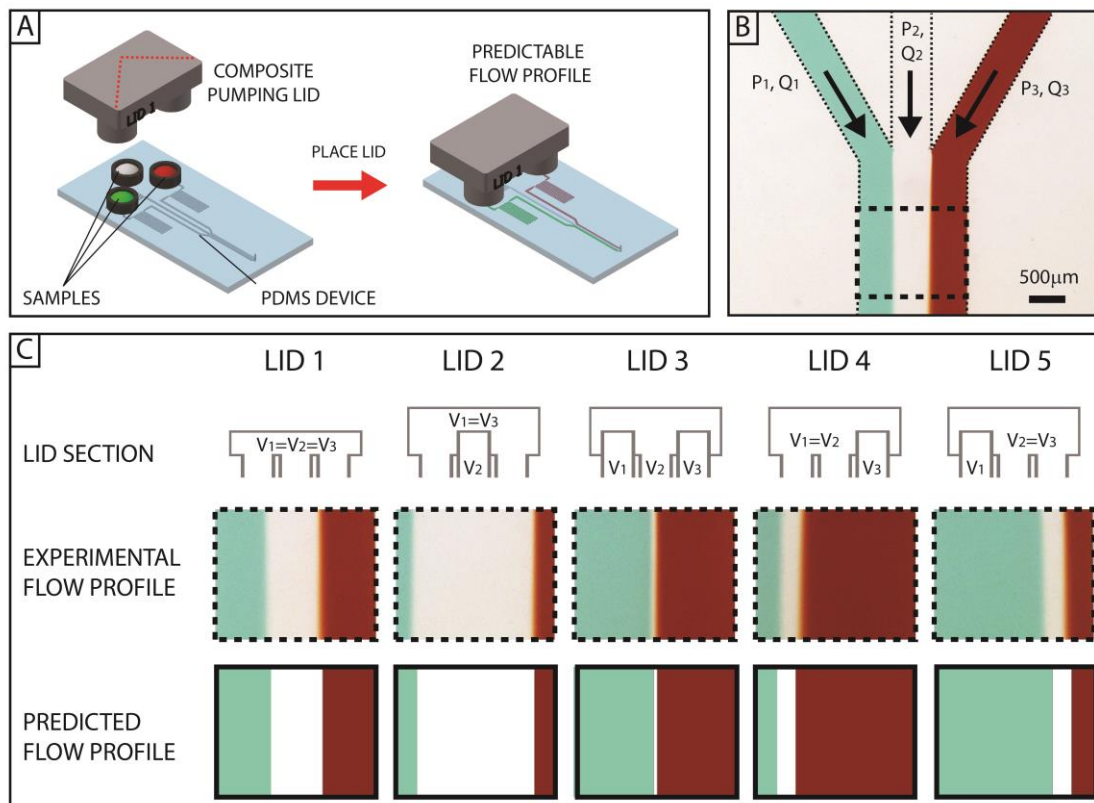


Figure 4-5. Production of different flow profiles in the same device using composite pumping lids. (A) Schematics of the setup used for the experiments. The microfluidic device has three cups, each dedicated to a different aqueous solution (from left to right: green, transparent, and red). A composite lid controls the pressure at each of the three inlets, thus controlling the flow rate of each solution. (B) Micrograph of the junction at which the three inlet branches combine into a single channel and the streams from the three inlets produce parallel laminar flow. (C) Different composite lids can be used to produce different flow profiles. The top row shows the cross-section of five different lids, cut along the red dashed line in panel A. The middle row shows the experimental flow profiles obtained with these five lids in the same microfluidic device. The sketches (bottom row) show the expected flow profiles based on the pressures produced by the lids and the device geometry. For the channel used in these experiments the width (1.5 mm) was more than 35 times bigger than the channel height (40 μm), so the effect of parabolic flow near the lateral walls was negligible¹⁶

To test these devices quantitatively, we measured the width of each solution stream in the three-stream aqueous laminar flow, (the Reynolds number was always less than 1 in our experiments). The gauge pressures at the three inlets are defined as P_1 , P_2 , and P_3 , while

the pressure at the device outlet is zero. Fluidic resistances for the three inlet branches (before the junction) are defined as R , while the resistance of the main channel (formed by the junction of the three inlet branches) is defined as r . In the experiments described in this paper, the fluidic resistance R of the inlet branches was intentionally set larger than the outlet resistance r , to increase the range of pressures that could be applied to the three inlets without generating back-flow in the branch with the lowest pressure. Under these conditions, theory predicts that Q_i is proportional to P_i and can be approximated by Eq. 11. Ignoring the effects of three-dimensional diffusion^{22,23} and ignoring the effect of the parabolic flow profile for these wide channels, we predicted the flow profiles as described in the supplementary material, and found them to be in good agreement with experiments.

These lids were used to produce parallel laminar flow profiles in a microfluidic device (Figure 4-5B). Each composite lid had a different geometry (Figure 4-5C) and generated a different set of pressures at the three device inlets. These pressures were used to predict the flow profile in the microfluidic device, as described in the supplementary material, and experimental results matched the flow profiles predicted by the flow rate model (Figure 4-5C). Based on the geometries of the device and the composite pumping lid, flow profiles can be controlled and predicted.

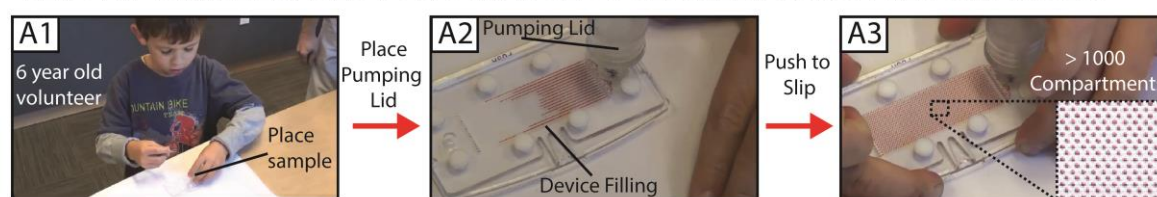
Use of pumping lids to load SlipChip devices by positive and negative pressures

Next, we showed that the pumping lid could be used to reliably and easily load SlipChip devices²⁴ using either positive or negative pressures. This is a good test because loading SlipChip devices requires control of the inlet pressure within a defined range,²⁵ and SlipChips are intended to be used in limited resource settings (LRS) by untrained users.²⁶⁻

²⁹ First, we tested the pumping lid on a SlipChip designed for a digital nucleic acid detection assay²⁶ (Figure 4-6A), pumping a total of 5 μL of solution with 0.03 atm pressure (Eq. 1). We asked a 6-year-old volunteer to use the pumping lid to operate the device. We found that pumping proceeded to completion despite the variation of pressure applied to the pumping lid by the volunteer.^{30,31} We expect the simplicity of the pumping lid to be valuable in both LRS and laboratory settings, e.g. for digital single-molecule measurements.³¹

In another experiment, we tested loading of a different SlipChip device by negative pressure. To further illustrate the applicability of the pumping lid method to complex tests, we used a SlipChip designed for multivolume digital nucleic acid amplification,^{32,33} which presents challenges in filling due to variation of capillary pressure among wells of different sizes. Previously this type of device was filled by positive pressure and dead end filling.²⁵ We modified the device for negative-pressure filling by adding a sealing ring filled with high-vacuum grease (sealing structure) around the active area containing the amplification wells (Figure 4-6B). We also added an outlet for oil to the device, over which the negative-pressure pumping lid was placed. The device was assembled such that the lubricating oil (5 cSt silicone oil) was filling the wells. For loading, sample (50 μL of 0.5 M FeSCN aqueous solution) was placed onto the inlet, and the pumping lid was pulled up to create negative pressure of 0.1 atm, remove excess oil and draw the sample into all of the wells of the device (Figure 4-6B). This experiment demonstrated that bubble-free filling can be accomplished using the pumping lid, and that complex devices (a combination of immiscible fluids and wells with different capillary pressures) can be handled.

SLIPCHIP DEVICE LOADED BY A 6 YEAR OLD VOLUNTEER USING THE PUMPING LID



SLIPCHIP DEVICE LOADED BY VACUUM USING A PUMPING LID

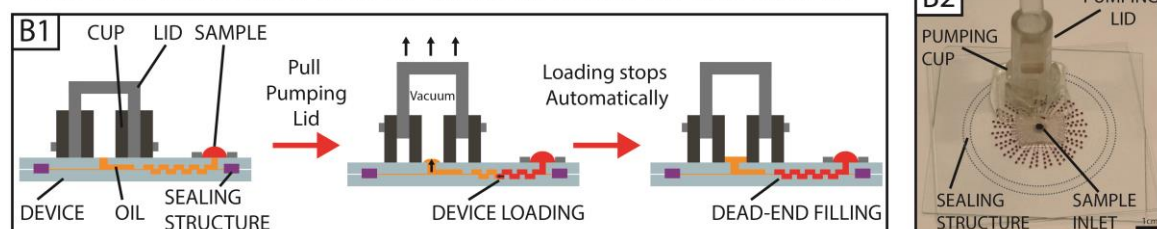


Figure 4-6 Use of the pumping lid for loading of SlipChip devices. (A) Photographs of a 6-year-old volunteer with minimal training using the pumping lid to load a SlipChip device. The sample is placed in the cup at the device inlet (A1), the pumping lid is placed on the cup, and when the lid is pushed, positive pressure is generated and sample pumping starts (A2). Once the sample loading is complete, slipping two plates generates discrete compartments (A3). A video of this experiment is provided.³⁰ (B) SlipChip sample loading by negative pressure. (B1) Schematic outline of the steps. The lid is pre-placed on the cup, and the sample is placed at a separate inlet in the device. Pulling the lid creates negative gauge pressure and initiates loading. Dead-end filling ensures that the loading stops once the device is completely filled. (B2) Photograph of a multivolume SlipChip device for digital nucleic acid quantification loaded with negative pressure pumping lid method.

Vapor-liquid equilibrium (VLE) method for pressure generation

We then explored how vapor pressure of a volatile liquid can aid the pumping process by isolating its effect from compression, and investigated the potential to harness the vapor pressure for pumping a non-volatile sample. Our hypotheses were that (i) by taking advantage of vapor-liquid equilibrium (VLE), one would be able to pump large volumes of liquid over extended periods of time at a relatively constant pressure, without the need to compress a large volume of a gas inside the device; (ii) a single lid design could be

used to generate different pressures by using liquids of different vapor pressure; (iii) a single combination of a lid design and a volatile liquid could be used to generate different pressures by tuning the temperature. In this approach, a volatile liquid is stored in a sealed compartment inside a pre-assembled vapor pressure pump, comprised of a lid and cup (Figure 4-7A). The design of this lid and cup differ from those described previously, as turning this lid connects or disconnects the compartments in the cup, rather than compressing or expanding the gas enclosed in the cavity, as in a SlipChip device²⁴. In addition, the cup is divided to contain the volatile liquid and one or more separate sample compartments. When the user turns the lid, the volatile liquid evaporates into the cavity (Figure 4-7B). The cavity in the pumping lid is isolated from the atmosphere, so evaporation of the volatile liquid increases the pressure in the cavity. Once the volatile liquid reaches equilibrium with its vapor, the pressure will be higher than the atmospheric pressure, and its value can be calculated using the thermodynamic VLE model. The user can initiate pumping by opening a valve or removing a plug. During pumping, evaporation of additional liquid provides additional pressure, although there is a drop in pressure, since the volume previously occupied by sample is now available to the gas phase, effectively causing expansion. Similarly to the pressure change observed in the pumping lid method, this pressure drop can often be neglected, if the sample volume being pumped is much smaller than the pump gas compartment volume. Once the entire sample has been pumped through the device, the vapor in the lid connects to the atmosphere and the gauge pressure drops to zero. This method of vapor pressure pumping can be used independently or in conjunction with compression.

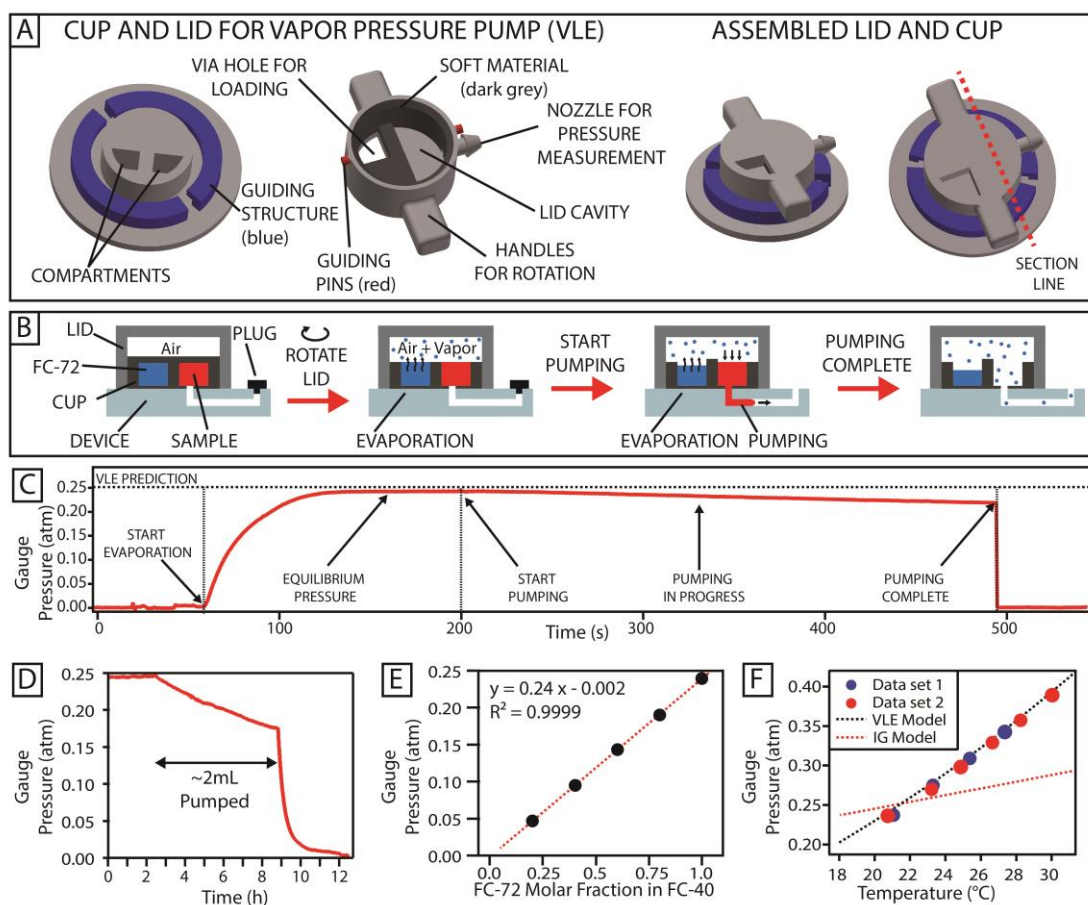


Figure 4-7 Generation of pressure using vapor liquid equilibrium (VLE). (A) Schematics of the parts used for VLE pressure generation. (B) Schematics of the method used to generate pressure. The figures show the cross section of the lid and cup assembly along the red line shown in panel A. Prior to the experiment, a volatile liquid (FC-72, blue) and the sample (red) are placed in isolated compartments of the cup. At this stage, the pressure in the lid cavity is equilibrated with the atmosphere. When the lid is rotated, the volatile liquid is exposed to the air in the cavity and starts to evaporate to reach its equilibrium pressure. When the plug is removed from the device outlet, the sample starts flowing. After the entire sample has been pumped, the cavity is in contact with the external atmosphere and the pressure returns to zero. (C) An experimental pressure profile obtained by performing the steps described in panel B, for pumping 20 μ L of water. (D) Pressure profile obtained when pumping a 2 mL sample volume through a microfluidic device. (E) Equilibrium pressures obtained by using mixtures of liquids (FC-72 and FC-40) at different molar fractions ($N=3$; error bars smaller than the size of the marker). The dashed line indicates the linear fit of the data and its parameters are reported in the graph. (F) Equilibrium pressure obtained using FC-72 at different temperatures. The dashed line shows the values predicted by the VLE model (Eq. 16). Each point

represents the average over at least 62 and up to 87811 pressure measurements after the system has equilibrated.

Model for VLE pressure generation using perfluorohexane (FC-72)

To find the predicted pressure at VLE, the fugacities of perfluorohexane in both liquid (right hand side in Eq. 13) and gas (left hand side in Eq. 13) phases are set equal. The general expression for VLE is:

$$\hat{\phi}_{FC} y_{FC} P = \gamma_{FC} x_{FC} \phi_{FC}^{\text{sat}} P_{FC}^{\text{sat}} \exp \left[\frac{V_{FC}^L (P - P_{FC}^{\text{sat}})}{RT} \right] \quad (\text{Eq. 13})$$

where: $\hat{\phi}_{FC}$ = fugacity coefficient of FC-72 in gas phase at T, P

y_{FC} = equilibrium mole fraction of FC-72 in the gas phase at T, P

P = equilibrium system pressure

γ_{FC} = FC-72 activity coefficient in liquid phase

x_{FC} = equilibrium mole fraction of FC-72 in the liquid phase at T, P

ϕ_{FC}^{sat} = fugacity coefficient for pure FC-72 at T, P^{sat}

P_{FC}^{sat} = FC-72 saturation pressure at T, obtained from Antoine equation

V_{FC}^L = FC-72 liquid molar volume

R = ideal gas constant

T = system temperature

To simplify the calculation, we made the following assumptions:

- Liquid phase is pure FC-72 (ignoring air dissolving in FC-72), $x_{FC} = 1$
- Liquid phase behaves ideally, $\gamma_{FC} = 1$
- Gas phase also behaves ideally, $\hat{\phi}_{FC} = 1$ and $\phi_{FC}^{sat} = 1$, and that Dalton's law applies:
 - $P = \sum_i p_i = p_{air} + p_{FC}$, where $p_{FC} = y_{FC}P$
- T is constant

After simplification, the equation becomes:

$$y_{FC}P = P_{FC}^{sat} \exp \left[\frac{V_{FC}^L (P - P_{FC}^{sat})}{RT} \right] \quad (\text{Eq. 14a})$$

Or, equivalently:

$$V_{FC}^L (P - P_{FC}^{sat}) = RT \ln \left(\frac{P - p_{air}}{P_{FC}^{sat}} \right) \quad (\text{Eq. 14b})$$

14b)

Because the Poynting factor (exponential term in Eq.14a) is close to unity, the equilibrium system pressure P is almost equal to the initial pressure plus FC-72 saturation pressure. This equation was analysed numerically to calculate the predicted total pressure in the system (equal to P). If vapor pressure pumping is used in combination with the pumping lid approach, the final pressure P_1 should be used in place of p_{air} .

The values of P_{FC}^{sat} were obtained with the Antoine equation:

$$\ln(P_{FC}^{sat} [\text{atm}]) = 9.19734 - \frac{2488.59}{T [^\circ\text{C}] + 213.42} \quad (\text{Eq. 15})^{34}$$

Model for temperature dependence of VLE pressure

Vapor pressure of the volatile liquid, and therefore the performance of this pumping approach, is affected by temperature. To make accurate predictions of the pressure generated by this vapor pressure pump, the ideal gas law was substituted for p_{air} (the initial pressure), which allowed us to take into account both the change in vapor pressure and gas expansion as the temperature is changed:

$$V_{\text{FC}}^L (P - P_{\text{FC}}^{\text{sat}}) = RT \ln \left(\frac{P - \frac{n_{\text{air}} RT}{V}}{P_{\text{FC}}^{\text{sat}}} \right) \quad (\text{Eq. 16})$$

Eq. 16 was used to calculate the predicted value of P at different temperatures. The total volume available for gas in the device (V) was calculated in CAD software. The initial number of moles of air in the gas compartment (n_{air}) remains constant, and is dictated by the temperature at which the compartment was initially sealed from atmosphere (21.5° C). The device was designed specifically to avoid any compression during the turning of the lid, to isolate the effects of VLE on pressure. For VLE pumping, we neglected the vapor pressure of the aqueous sample, because the vapor pressure of water is much lower than that of perfluorohexane (0.025 atm vs. 0.248 atm) at 21.5° C.

Pressure and flow generation using the VLE method

The experimental behavior of pressure agreed with the theoretical predictions (Figure 4-7C). The equilibrium pressure obtained experimentally approached the pressure predicted by the simplified VLE model (Eq. 14), and the system was used to pump 20 μL of water through a microfluidic device in ~ 280 s (4.7 min). The VLE method could be used for pumping volumes in the milliliter range, for example 2 mL of water was pumped in more than 7 h, showing less than 30% reduction in the input pressure using a lid with a 30 mL gas compartment (Figure 4-7D). This reduction was caused by the fact that the volume

previously occupied by sample became available to the gas phase to expand. As expected, larger lids took longer to equilibrate because more liquid needed to evaporate. However, the pressure remained stable when pumping was not in progress (Figure 4-7D), so equilibration can be done prior to the pumping experiment. Alternatively, if the pressure does not need to be controlled precisely, the pumping can be started as soon as evaporation is initiated.

Tuning of VLE pressure by changing composition of the volatile liquid or temperature

To test our second hypothesis, we investigated generating pumping pressures by liquids with different vapor pressures. The equilibrium gauge pressure reached by the VLE system is related (but not necessarily equal) to the vapor pressure of the volatile liquid, according to Eq. 13. For a mixture of liquids, vapor pressure depends on the molar fraction of each component, amongst other factors. We measured the equilibrium pressures for different mixtures of FC-40 (vapor pressure 0.003 atm at 21.5° C) and FC-72 (vapor pressure 0.248 atm at 21.5° C). Equilibrium VLE pressure scaled linearly with the FC-72 molar fraction ($R^2 = 0.9999$) and approached ~ 0.003 atm for pure FC-40 (Figure 4-7E), as expected.

To test our third hypothesis, we investigated pressure generated by this vapor pressure pump at different temperatures using FC-72 as the volatile liquid. Because vapor pressure is a function of temperature (Eq. 15 and Eq. 16), the equilibrium pressure of FC-72/air system increased with temperature, yielding values consistent with those predicted by the VLE model (Figure 4-7F). Note that the change in pressure with temperature far exceeded the one predicted for heating of an ideal gas in a closed volume. This presents

an opportunity to incorporate simple microfabricated heaters^{35,36} to precisely control the pressures provided by this pump, and emphasizes the importance of temperature control for the operation of the vapor pressure pump. As mentioned earlier, VLE pumping can potentially be used in combination with the pumping lid gas compression or expansion. When generating positive pressure, the compression can be used to increase the range of pressures that can be achieved with the VLE approach. In the case of gas expansion, the use of VLE sets a lower limit to the pressure that can be obtained to the vapor pressure of the volatile liquid. The long-term stability of volatile liquids in the acrylic-based resins used for 3D-printing was not characterized, but preliminary experiments with the same liquids pre-packed in blister packs showed that it is possible to obtain similar pressures.

Conclusions

Here we described a way of generating positive and negative pressures with an equipment-free pumping lid and demonstrated its utility to induce flow in microfluidic devices. We used multi-material 3D printing to produce the parts, allowing fast prototyping without reducing their quality. This fabrication process is attractive because it allows rapid design iterations, and can also be scaled up to mass production using overmolding techniques. Here, pumping cups were attached to the device post-fabrication, but they can be included as part of the device during manufacturing. The first method described in this work relies on controlled compression or expansion of gas. While compression of gas has been demonstrated previously for pumping in microfluidic applications,³⁷ this work extends the previous approach. It demonstrates new capabilities, including (i) enabling the generation of both positive and negative pressures, (ii) the capability to adjust pressure in a programmed way while pumping is in progress, (iii) the

use of multiple lids or a composite lid to control pressure at different inlets within the same device, and (iv) in addition to device loading applications, here we show more complex fluid manipulations, such as stable long-term laminar flow of multiple solutions and nanoliter droplet formation in two-phase flows. Furthermore, this work will enable others to use this approach more easily because (i) the method has been modeled and the model was quantitatively validated by experimentally measuring the pressures generated by the pumping lids, and (ii) the model was used to provide guidelines for the design of cups and pumping lids. We also demonstrated a complementary second method for generating pressure via evaporation of a volatile liquid in the pumping lid. The equilibrium pressure generated with this approach (before pumping starts) depends on the nature of the volatile liquid and on its temperature, but is not dependent on the geometry of the lid used for the experiment.

The approaches described in this work address many of the fluid-handling challenges that are faced when working with microfluidic devices¹⁻¹⁵ including those involving laminar flow,^{22,38} droplets,^{21,39-41} and cell culture experiments.⁴²⁻⁴⁴ The simplicity of this pumping method overall and the use of the guiding structures make it robust to differences in pushing/pulling force; the user simply places a sample at the inlet and then pushes/pulls the pumping lid to generate the flow. Even when the user is applying excessive force (see video³⁰), the method still operates as programmed; this makes it suitable for even the most minimally trained users. The pumping lid approach is thus appropriate for a variety of applications in different settings. Experiments taking place in a research lab can benefit from this compact and equipment-free approach, reducing the need for external connectors and simplifying the workflow, especially when experiments are conducted in

the controlled environments of a cell culture incubator⁴²⁻⁴⁴ or an anaerobic chamber.⁴⁵ Additionally, contamination from the external environment and evaporation are minimized because the sample is contained in the pumping cup during the entire experiment. The pumping lid also allows flow rates to be tuned in real time while the experiment is in progress. The isolation and containment of samples is a characteristic that is highly desirable for cell culturing,⁴² particularly when dealing with biohazardous samples and “organs-on-chip” technologies.^{43,44} Such experiments are usually performed in controlled conditions (temperature, gas composition, etc.) and often require long pumping times.¹⁵ With this approach, the entire pumping lid setup can be placed inside an incubator, without the need for external controllers. The use of VLE pumping is particularly suitable for temperature-controlled environments. Due to its portability and programmability, the pumping lid can also benefit applications in resource-limited settings, specifically for portable diagnostic devices.^{6,7,24,26,28,46,47}

Acknowledgements

This work was funded in part by DARPA Cooperative Agreement HR0011-11-2-0006 and National Institutes of Health NRSA training grant 5T32GM07616NSF (to D.A.S.). This material is also based upon work supported by a National Science Foundation Graduate Research Fellowship under Grant No. DGE-1144469 (to D.V.Z.). This paper does not necessarily reflect the position or policy of the U.S. government or these agencies, and no official endorsement should be inferred. We wish to thank Mikhail Karymov for preliminary experiments, Roberta Pocevičute for help with the theoretical analysis, and Natasha Shelby for contributions to writing and editing this manuscript. We

also wish to thank the 6-year-old volunteer for performing the demonstrations shown in Figure 4-6. Disclosure: R.F.I. and L.L. have a financial interest in SlipChip Corp.

References

- 1 Herr, A. E. *et al.* Electroosmotic Capillary Flow with Nonuniform Zeta Potential. *Analytical Chemistry* **72**, 1053-1057, doi:10.1021/ac990489i (2000).
- 2 Choi, K., Ng, A. H. C., Fobel, R. & Wheeler, A. R. Digital Microfluidics. *Annual Review of Analytical Chemistry* **5**, 413-440, doi:doi:10.1146/annurev-anchem-062011-143028 (2012).
- 3 Darhuber, A. A., Valentino, J. P., Davis, J. M., Troian, S. M. & Wagner, S. Microfluidic actuation by modulation of surface stresses. *Applied Physics Letters* **82**, 657-659, doi:doi:<http://dx.doi.org/10.1063/1.1537512> (2003).
- 4 Tang, S.-Y. *et al.* Liquid metal enabled pump. *Proceedings of the National Academy of Sciences*, doi:10.1073/pnas.1319878111 (2014).
- 5 Futterer, C. *et al.* Injection and flow control system for microchannels. *Lab Chip* **4**, 351-356, doi:10.1039/b316729a (2004).
- 6 Martinez, A. W., Phillips, S. T., Whitesides, G. M. & Carrilho, E. Diagnostics for the Developing World: Microfluidic Paper-Based Analytical Devices. *Analytical Chemistry* **82**, 3-10, doi:10.1021/ac9013989 (2009).
- 7 Martinez, A. W., Phillips, S. T., Butte, M. J. & Whitesides, G. M. Patterned Paper as a Platform for Inexpensive, Low-Volume, Portable Bioassays. *Angewandte Chemie International Edition* **46**, 1318-1320, doi:10.1002/anie.200603817 (2007).

- 8 Osborn, J. L. *et al.* Microfluidics without pumps: reinventing the T-sensor and H-filter in paper networks. *Lab Chip* **10**, 2659-2665, doi:10.1039/c004821f (2010).
- 9 Safavieh, R. & Juncker, D. Capillarics: pre-programmed, self-powered microfluidic circuits built from capillary elements. *Lab Chip* **13**, 4180-4189, doi:10.1039/c3lc50691f (2013).
- 10 Zimmermann, M., Schmid, H., Hunziker, P. & Delamarche, E. Capillary pumps for autonomous capillary systems. *Lab Chip* **7**, 119-125, doi:10.1039/b609813d (2007).
- 11 Resto, P. J., Berthier, E., Beebe, D. J. & Williams, J. C. An inertia enhanced passive pumping mechanism for fluid flow in microfluidic devices. *Lab Chip* **12**, 2221-2228, doi:10.1039/c2lc20858j (2012).
- 12 Walker, G. M. & Beebe, D. J. A passive pumping method for microfluidic devices. *Lab Chip* **2**, 131-134, doi:10.1039/b204381e (2002).
- 13 Dimov, I. K. *et al.* Stand-alone self-powered integrated microfluidic blood analysis system (SIMBAS). *Lab Chip* **11**, 845-850, doi:10.1039/c0lc00403k (2011).
- 14 Liang, D. Y., Tentori, A. M., Dimov, I. K. & Lee, L. P. Systematic characterization of degas-driven flow for poly(dimethylsiloxane) microfluidic devices. *Biomicrofluidics* **5**, -, doi:doi:<http://dx.doi.org/10.1063/1.3584003> (2011).
- 15 Hsu, Y.-H., Moya, M. L., Hughes, C. C. W., George, S. C. & Lee, A. P. A microfluidic platform for generating large-scale nearly identical human

- microphysiological vascularized tissue arrays. *Lab Chip* **13**, 2990-2998, doi:10.1039/c3lc50424g (2013).
- 16 Bruus, H. *Theoretical microfluidics*. Vol. 18 (Oxford University Press, 2008).
- 17 Duffy, D. C., McDonald, J. C., Schueller, O. J. A. & Whitesides, G. M. Rapid Prototyping of Microfluidic Systems in Poly(dimethylsiloxane). *Analytical Chemistry* **70**, 4974-4984, doi:10.1021/ac980656z (1998).
- 18 Anna, S. L., Bontoux, N. & Stone, H. A. Formation of dispersions using “flow focusing” in microchannels. *Applied Physics Letters* **82**, 364-366, doi:doi:<http://dx.doi.org/10.1063/1.1537519> (2003).
- 19 Song, H., Tice, J. D. & Ismagilov, R. F. A Microfluidic System for Controlling Reaction Networks in Time. *Angewandte Chemie International Edition* **42**, 768-772, doi:10.1002/anie.200390203 (2003).
- 20 Thorsen, T., Roberts, R. W., Arnold, F. H. & Quake, S. R. Dynamic Pattern Formation in a Vesicle-Generating Microfluidic Device. *Physical Review Letters* **86**, 4163-4166 (2001).
- 21 Baroud, C. N., Gallaire, F. & Dangla, R. Dynamics of microfluidic droplets. *Lab Chip* **10**, 2032-2045, doi:10.1039/c001191f (2010).
- 22 Kenis, P. J. A., Ismagilov, R. F. & Whitesides, G. M. Microfabrication Inside Capillaries Using Multiphase Laminar Flow Patterning. *Science* **285**, 83-85, doi:10.1126/science.285.5424.83 (1999).
- 23 Ismagilov, R. F., Stroock, A. D., Kenis, P. J. A., Whitesides, G. & Stone, H. A. Experimental and theoretical scaling laws for transverse diffusive broadening in two-phase laminar flows in microchannels. *Appl Phys Lett* **76**, 2376-2378 (2000).

- 24 Du, W., Li, L., Nichols, K. P. & Ismagilov, R. F. SlipChip. *Lab Chip* **8**, 2286-2292 (2009).
- 25 Li, L., Karymov, M. A., Nichols, K. P. & Ismagilov, R. F. Dead-End Filling of SlipChip Evaluated Theoretically and Experimentally as a Function of the Surface Chemistry and the Gap Size between the Plates for Lubricated and Dry SlipChips. *Langmuir* **26**, 12465-12471, doi:10.1021/la101460z (2010).
- 26 Shen, F. *et al.* Digital Isothermal Quantification of Nucleic Acids via Simultaneous Chemical Initiation of Recombinase Polymerase Amplification Reactions on SlipChip. *Analytical Chemistry* **83**, 3533-3540, doi:10.1021/ac200247e (2011).
- 27 Shen, F., Du, W., Kreutz, J. E., Fok, A. & Ismagilov, R. F. Digital PCR on a SlipChip. *Lab Chip* **10**, 2666-2672 (2010).
- 28 Sun, B. *et al.* Mechanistic Evaluation of the Pros and Cons of Digital RT-LAMP for HIV-1 Viral Load Quantification on a Microfluidic Device and Improved Efficiency via a Two-Step Digital Protocol. *Analytical Chemistry* **85**, 1540-1546, doi:10.1021/ac3037206 (2013).
- 29 Sun, B. *et al.* Measuring Fate and Rate of Single-Molecule Competition of Amplification and Restriction Digestion, and Its Use for Rapid Genotyping Tested with Hepatitis C Viral RNA. *Angewandte Chemie International Edition* **53**, 8088-8092, doi:10.1002/anie.201403035 (2014).
- 30 <http://ismagilovlab.caltech.edu/multimedia/slip_chip_movies.shtml> (
- 31 Witters, D. *et al.* Digital biology and chemistry. *Lab Chip*, doi:10.1039/c4lc00248b (2014).

- 32 Shen, F. *et al.* Multiplexed Quantification of Nucleic Acids with Large Dynamic Range Using Multivolume Digital RT-PCR on a Rotational SlipChip Tested with HIV and Hepatitis C Viral Load. *Journal of the American Chemical Society* **133**, 17705-17712, doi:10.1021/ja2060116 (2011).
- 33 Kreutz, J. E. *et al.* Theoretical Design and Analysis of Multivolume Digital Assays with Wide Dynamic Range Validated Experimentally with Microfluidic Digital PCR. *Analytical Chemistry* **83**, 8158-8168, doi:10.1021/ac201658s (2011).
- 34 Reid, R. C., Prausnitz, J. M. & Sherwood, T. K. *The properties of gases and liquids*. (McGraw-Hill, 1977).
- 35 Takagi, H., Maeda, R., Ozaki, K., Parameswaran, M. & Mehta, M. in *Micro Machine and Human Science, 1994. Proceedings., 1994 5th International Symposium on.* 199 (IEEE).
- 36 Zhizhong, Y. & Andrea, P. A microfluidic 'blinking bubble' pump. *Journal of Micromechanics and Microengineering* **15**, 643 (2005).
- 37 Begolo, S., Shen, F. & Ismagilov, R. F. A microfluidic device for dry sample preservation in remote settings. *Lab Chip* **13**, 4331-4342, doi:10.1039/c3lc50747e (2013).
- 38 Kane, R. S., Takayama, S., Ostuni, E., Ingber, D. E. & Whitesides, G. M. Patterning proteins and cells using soft lithography. *Biomaterials* **20**, 2363-2376, doi:[http://dx.doi.org/10.1016/S0142-9612\(99\)00165-9](http://dx.doi.org/10.1016/S0142-9612(99)00165-9) (1999).
- 39 Song, H., Chen, D. L. & Ismagilov, R. F. Reactions in droplets in microfluidic channels. *Angew Chem Int Edit* **45**, 7336-7356 (2006).

- 40 Teh, S.-Y., Lin, R., Hung, L.-H. & Lee, A. P. Droplet microfluidics. *Lab Chip* **8**, 198-220, doi:10.1039/b715524g (2008).
- 41 Theberge, A. B. *et al.* Microdroplets in Microfluidics: An Evolving Platform for Discoveries in Chemistry and Biology. *Angewandte Chemie International Edition* **49**, 5846-5868, doi:10.1002/anie.200906653 (2010).
- 42 Sackmann, E. K., Fulton, A. L. & Beebe, D. J. The present and future role of microfluidics in biomedical research. *Nature* **507**, 181-189, doi:10.1038/nature13118 (2014).
- 43 Huh, D., Hamilton, G. A. & Ingber, D. E. From 3D cell culture to organs-on-chips. *Trends in Cell Biology* **21**, 745-754, doi:<http://dx.doi.org/10.1016/j.tcb.2011.09.005> (2011).
- 44 Huh, D., Torisawa, Y.-s., Hamilton, G. A., Kim, H. J. & Ingber, D. E. Microengineered physiological biomimicry: Organs-on-Chips. *Lab Chip* **12**, 2156-2164, doi:10.1039/c2lc40089h (2012).
- 45 Ma, L. *et al.* Gene-targeted microfluidic cultivation validated by isolation of a gut bacterium listed in Human Microbiome Project's Most Wanted taxa. *Proceedings of the National Academy of Sciences* **111**, 9768-9773, doi:10.1073/pnas.1404753111 (2014).
- 46 Yager, P. *et al.* Microfluidic diagnostic technologies for global public health. *Nature* **442**, 412-418 (2006).
- 47 Yager, P., Domingo, G. J. & Gerdes, J. Point-of-Care Diagnostics for Global Health. *Annual Review of Biomedical Engineering* **10**, 107-144, doi:doi:10.1146/annurev.bioeng.10.061807.160524 (2008).

Chapter 5:

Instrument for Real-Time Digital Nucleic Acid Amplification on Custom Microfluidic Devices*

Abstract

Nucleic acid amplification tests that are coupled with a digital readout enable the absolute quantification of single molecules, even at ultralow concentrations. Digital methods are robust, versatile and compatible with many amplification chemistries including isothermal amplification, making them particularly invaluable to assays that require sensitive detection, such as the quantification of viral load in occult infections or detection of sparse amounts of DNA from forensic samples. A number of microfluidic platforms are being developed for carrying out digital amplification. However, the mechanistic investigation and optimization of digital assays has been limited by the lack of real-time kinetic information about which factors affect the digital efficiency and analytical sensitivity of a reaction. Commercially available instruments that are capable of tracking digital reactions in real-time are restricted to only a small number of device types and sample-preparation strategies. Thus, most researchers who wish to develop, study, or optimize digital assays rely on the rate of the amplification reaction when performed in a bulk experiment, which is now recognized as an unreliable predictor of digital efficiency. To expand our ability to study how digital reactions proceed in real-time and enable us to optimize both the digital efficiency and analytical sensitivity of digital assays, we built a custom large-format digital real-time amplification instrument that can accommodate a wide variety of devices, amplification chemistries, and sample-

* This chapter is in submission for publication at *PLOS One* with authorship belonging to David A. Selck and Rustem F. Imsagilov.

handling conditions. Herein, we validate this instrument, we provide detailed schematics that will enable others to build their own custom instruments, and we include a complete custom software suite to collect and analyze the data retrieved from the instrument. We believe assay optimizations enabled by this instrument will improve the current limits of nucleic acid detection and quantification, improving our fundamental understanding of single molecule reactions and providing advancements in practical applications such as medical diagnostics, forensics and environmental sampling.

Introduction

This paper describes a custom-built instrument and accompanying software for real-time digital nucleic acid amplification studies that can be used to develop, study, or optimize a wide variety of digital assays for numerous applications in a device-agnostic manner.

Digital nucleic acid amplification works by partitioning a sample into many parallel individual samples. Of these partitioned samples, some may contain a target nucleic acid molecule (positive) while others do not (negative). By comparing the number of positive amplifications to the total number of partitioned samples, the absolute concentration of a sample can be calculated based on a Poisson distribution. Some of the advantages provided by a digital readout are that it can provide absolute quantification without standard calibration curves,¹⁻³ it is robust to environmental conditions, including temperature, reagent quality and sample purity,⁴ and it can provide high resolution (< 1.5 fold change),⁵ sensitivity,⁵ and accuracy¹ at low concentrations. Digital readouts enable precise counting of single molecules, including rare mutations and analyses of gene expression, which make them invaluable to assays that require detection at low concentrations, such as viral load in occult infections.³ The digital method is also

versatile; it can be coupled to many amplification technologies, including isothermal amplification chemistries, which in bulk reactions are limited in their ability to quantify very low concentrations of target molecules as a result of kinetic variations among samples.⁶

Although reactions performed in a digital format provide these and many other advantages, few assay optimizations have been fully characterized. Thus, information on the quality of a reaction is confined to the end-point readout and little is known about how these reactions proceed in real time.² Currently, most optimizations for digital assays are performed in bulk by using the rate of the reaction as a proxy for efficiency.^{7,8} However, rate doesn't necessarily correlate with efficiency in all digital reactions and both "fate" and "rate" of individual digital amplification reactions should be measured in digital format.⁹ Thus, to measure the digital efficiency of a reaction, optimization should be done in a digital format using real-time kinetic information for each compartmentalized reaction to determine the performance of and variation between all independent single molecule reactions.

One commercial option for performing real-time digital analyses on microfluidic devices is the Fluidigm Biomark HD. This instrument can be used to optimize digital assays because for each digital reaction, it can collect real-time traces (to determine the kinetic rate of the amplification) and melt curves (to determine false from true positive samples). While these real-time digital instruments have been used in a number of applications,^{1,2,10} they are limited to proprietary microfluidic devices with pre-established sample handling protocols. In addition to the commercial implementations, some laboratories have constructed real-time digital instrumentation for specific needs.¹¹⁻¹⁷ Many

implementations of the digital format do not meet the requirements of commercially available real-time instruments; these include isothermal assays where the sample and amplification enzymes cannot be mixed until the sample has been partitioned^{18,19} and single devices that include compartments of different volumes to increase the assay dynamic range.²⁰

An ideal real-time digital instrument would be fully customizable to work under a broad range of conditions, yet be simple enough for the average user to fully leverage its capabilities. Specifically:

- It should have accurate, precise and fully programmable temperature control to within 1 °C across the full range of relevant temperatures.
- The imaging system should have sufficient resolution to accurately measure the kinetics of nanoliter amplification reaction volumes over a large field of view.
- It should incorporate multiple fluorescent channels to enable the analysis of multiplex reactions and non-standard chemistries.
- It should be compatible with collection and analysis software that is easy to use and capable of measuring the kinetics of reactions in any custom device.
- It should be easily adaptable to work with a wide variety of devices and architectures of varied sizes and materials.
- Its performance should be comparable with commercially available instruments that capture real-time performance in bulk reactions.
- It should be suitable for use a wide variety of amplification chemistries.

To expand our ability to study how digital reactions proceed in real-time, including our capability to elucidate which factors affect the digital efficiency or analytical sensitivity of a reaction, we built a custom large-format digital real-time amplification instrument that can accommodate a wide variety of devices, assays and conditions. This instrument has been used previously to optimize a loop-mediated isothermal amplification (LAMP) assay for hepatitis C virus (HCV) quantification⁹ and to develop a method to both quantify and genotype HCV infections in a single step.²¹ In this paper, we provide the schematics of the instrument used in these previous studies and we validate its performance using well characterized chemistries (real-time digital reverse transcription PCR) and a previously validated microfluidic device (SlipChip). We compare instrument performance to an Illumina Eco real-time PCR system using HCV RNA as the template. We also provide the relevant calibration and performance characteristics of the instrument, and the complete custom software suite used to collect and analyze data retrieved from the instrument.

Results and Discussion

Temperature control design and calibration

To obtain reliable real-time data from nucleic acid amplifications in either a bulk or digital format, temperature control must be precise and accurate. We have shown previously that while digital reactions can be robust to wide temperature changes⁴ the kinetics of a reaction will vary as a function of temperature. Others have constructed thermal control units using Peltier elements;¹²⁻¹⁴ however, to increase reliability and accuracy we chose instead to modify an existing thermocycler. We used a PTC-200 thermocycler with a stated temperature range of -5 °C to 105 °C and accuracy of ± 0.3

°C. This specific model was chosen because it can be fully controlled by third-party software through an ASCII control interface. Although it is no longer manufactured, it is widely available on the used-equipment market, and customization is simplified because the heated block is physically separated from the base instrument.

The thermocycler in its standard state is incompatible with custom devices because they are standardized to the well-plate format; thus, we customized the thermocycler block. We designed and machined from aluminum an *in situ* thermal block with the same thermal mass as a standard 96-well block to retain the rated ramp rate of the PTC-200 thermocycler (which is up to 3 °C/s). The thermal block assembly contains a set of four different Peltier elements: a heatsink, a circuit board, thermal transfer sheets, and thermistors. The thermal block is kept in electrical isolation and thermal contact through the use of a Tgard K52 polyimide sheet in conjunction with a Tgon 805 graphite sheet, and the temperature of the custom block is reported to the thermocycler with three different 20K ohm thermistors. We assembled the block this way to closely match the standard thermal assembly to maintain optimal performance and require only minimal calibration.

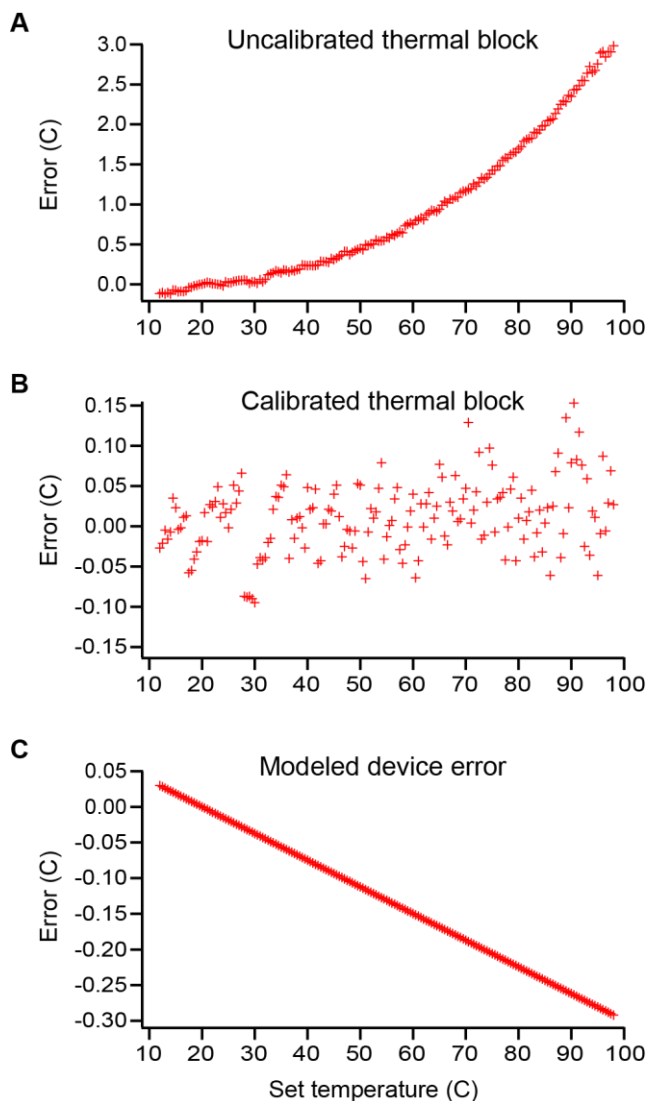


Figure 5-1. Temperature characterizations of the modified thermal block used in the PTC-200 thermocycler (A–B) and a Comsol-model to determine the on-device error (C). The deviation in the actual and reported temperatures are provided for the uncalibrated thermal block (A) and for the block after calibration (B). The Comsol-modeled deviation (C) provides the difference between the actual block temperatures and the theoretical reaction temperatures of the well volumes in a SlipChip microfluidic device. Error values are the difference between the thermocycler-reported thermal block temperature and either the actual thermal block temperatures (measured by a type K thermocouple) or the modeled device temperature; a positive number indicates that the thermal block temperature is higher than the device temperature.

The temperature calibration experiments were performed over the range of 12–98 °C with a temperature interval of 0.5 °C. As expected, at room temperature the reported and

actual readings were in close agreement because this class of thermistors has a defined resistance of 20K ohms at 25 °C. As the temperature deviates from 25 °C, the difference between the actual and reported temperatures of the block can vary by as many as 3 °C (at a set temperature of 98 °C) (Fig. 5-1A). This is caused by a slight mismatch in the performance curves of the chosen thermistor as compared with the thermistor for which the thermocycler was originally calibrated. To compensate for this mismatch, a sixth-order polynomial correction is performed in the custom GUI based software, which brings the actual and reported differences of the custom thermal block to within 0.15 °C (Fig. 5-1B). This correction makes the difference in actual and reported temperatures lower than the rated 0.3 °C variation of the thermocycler and thus falls well within desired performance characteristics; thus validating both the accuracy and precision of our custom *in situ* thermal block.

Calibration of the block does not control for the temperature of a reaction done on a device in the instrument. The temperature of a device may differ from the block as a result of convective cooling because a device is heated only from one side. In our lab, we primarily use custom SlipChip devices, and no commercially available temperature-sensing elements could be easily adapted; however, the sizes and geometries of SlipChip devices are well known and highly accurate, so can model the temperature error for SlipChip devices can be modeled using Comsol multiphysics (Fig. 5-1C). The model was a stationary experiment with the same resolution and range as the calibration experiments we performed with the block. The Comsol model was based on a 1" x 3" x 0.02" glass with a thermal conductivity of 1.38 W/(m*k) SlipChip device that was separated from the thermal block with a 50 µm gap filled with mineral oil having a thermal conductivity of

0.162 W/(m²*k) and a convective cooling rate of 10 W/m²K. Using these parameters, the temperature difference between the block and the SlipChip device deviates -0.29 °C from the set temperature at maximum block temperature (98 °C). This offset is well within the required performance characteristics of our instrument.

Optical design and validation

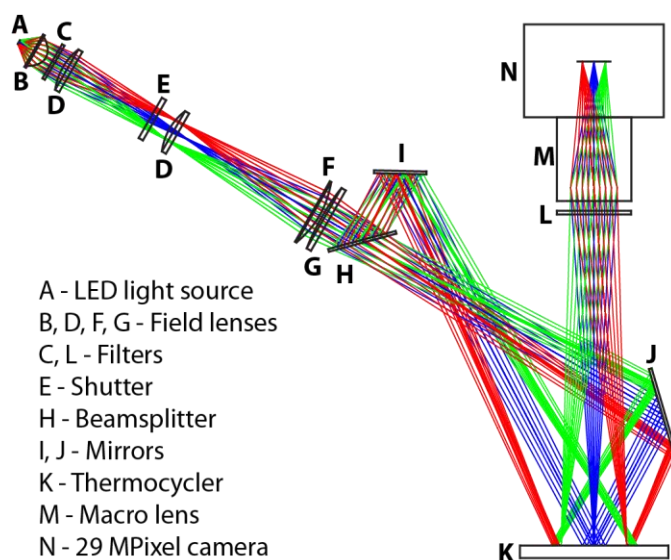


Figure 5-2. A schematic showing a scale representation of the physical layout of the custom real-time digital nucleic acid amplification instrument. Colored lines indicate ray paths.

The optical system of the instrument was designed to provide high illumination intensity over the full field of view (~5500 mm²) (Fig. 5-2). We chose to prioritize lighting intensity over lighting uniformity because uniformity deviations can be corrected after imaging with simple flat-field corrections. We chose a white LED spotlight module because it has a dense power delivery (rated 1175 lumens from a total area of 64 mm²), which allows us to use common and reasonably sized optics. Although there are light sources that can provide greater illumination intensities, these lights would have a larger surface area and thus would require the field optics that direct the light to be much larger

to compensate, which reduces the number of compatible standard lenses necessitating custom optics and much larger excitation fluorescence filters. In this custom real-time instrument, the largest cost in the optics is the fluorescence filters. Because filter cost is proportional to filter area, it is advantageous to keep the filters as small as possible.

The standard illumination geometry has 0-degree angle of incidence (perpendicular to the surface of device) because this minimizes gradients in the illumination field. Because the bottom of the device in this system is inaccessible due to the presence of a thermocycler, to use an angle of incidence of 0 degrees, we would need to image and illuminate from the same lens. Although this is commonly done, it creates a strong specular reflection of the excitation beam, which requires better emission filter blocking, and there are no commercial lenses of this type that can image the full field of view at high numerical aperture. Thus, to allow us to use standard optics, we set the angle of incidence at 27.5 degrees. To eliminate illumination gradients caused by the non-zero angle of incidence we added a beam splitter and mirror system (Fig. 5-2). This geometry provides added flexibility; if a single light source provides insufficient illumination intensity, a second optical source and optics can be set up in lieu of a beam splitter and mirrors for a maximum of four separate light sources possible. In our system, we found that a single source provided sufficient illumination intensities with power values of up to 1 mW/cm² of power with the 475 nm channel, 4.3 mW/cm² with the 560 nm channel, and 4.6 mW/cm² with the 630 nm channel. At the time this instrument was constructed, there was only one color (white 3000K) available for the LED module; however, there are currently many additional colors available. Different colors may better suit certain applications by shifting the higher power to the 475 nm channel.

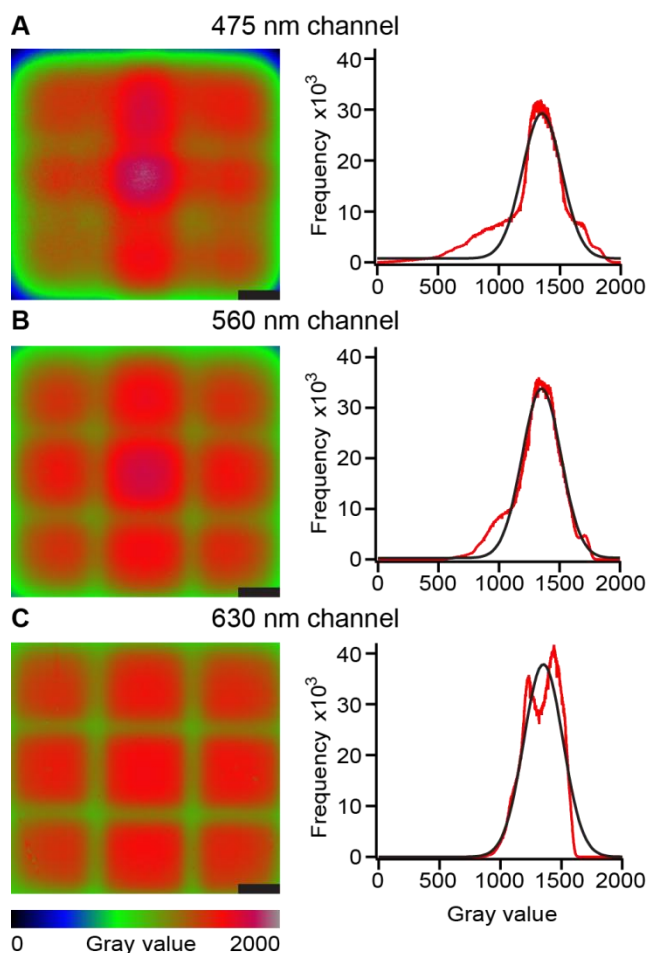


Figure 5-3. Results of the optical characterization of the real-time digital nucleic acid amplification instrument. Heat maps (left) and histograms (right) of custom fluorescence standards show the uniformity of illumination over the field of view as quantified in each of three fluorescent channels. Results from each channel were scaled to equalize each channel's average gray value. The gray values from the heat maps and histograms are truncated to between 0 and 2000 as reported by the instrument's built-in camera at each channel: (A) 475 nm, (B) 560 nm, and (C) 630 nm. Scale bars are 10 mm.

To validate the illumination uniformity at different excitation wavelengths, full-field fluorescence standards were created and imaged. Results from each channel were scaled by a constant to equalize each channel's average gray value. In this system, we used non-apochromatic optics, so the focal ranges for each of the excitation wavelengths vary and illumination is not uniform over each of the channels. The 475 nm channel is both the

most used and the lowest power, so it was aligned to have the highest power density while still maintaining sufficient uniformity; this was achieved by focusing the channel down to slightly less than full field, which reduces the illuminated area. This is not a problem for imaging as long as the reactions being imaged do not extend past the illuminated area. With this alignment, all channels achieve sufficient uniformity (Fig. 5-3). The best-fit Gaussian curves for each channel have full width at half max values of ~228 units, or 17% of the average Gaussian value. A flat-field correction easily compensates for this variation while only minimally impacting noise.

Software design and implementation

The software we created for the instrument was written to be amenable to a wide variety of different amplifications, analyses, and device geometries. Temperature programs are established by mixing ramp, temperature, and cycle steps in any order or combination, and imaging parameters are fully adjustable to any combination of exposure times and fluorescent channels in one of three imaging modes: (i) cycle-based imaging as done in standard quantitative PCR, (ii) time-based imaging where images are taken at set intervals throughout an experiment, or (iii) combination imaging where images are taken at set intervals only during a certain temperature step. The timing of the images can be set in one of two ways. If either time-based or combination imaging is used, the timing is controlled by software and is based on the time since the start of the previous acquisition. Thus, if an imaging step is longer than an imaging interval, image acquisition is continuous throughout the experiment. If imaging is cycle-based, the timing of image acquisition is controlled by the thermocycler. The thermocycler is set on a program; when it reaches an imaging step, it is allowed to proceed until there are 2 seconds remaining, at

which time the running program is paused, the temperature is held, all defined images are acquired, and then the program resumes. If the imaging step occurs during a step which is cycled, an image is acquired during each cycle. Melt temperature data can be automatically collected after any experiment by defining a low temperature, high temperature, resolution, and relevant imaging parameters. As a quality assurance mechanism, we implemented an error-checking system into the software; if a required variable is either left undefined or improperly configured, the software will inform the user of the required changes before a run can be started.

The software enables full control over all of the instrument components to tune the instrument settings to a specific application. The camera control and configuration are set up to be agnostic to equipment models. Any GigE-compliant camera can be used with the software and all functions that are defined by the GenICam specification are controllable. A simplified configuration is provided in the software for defining exposure time, camera gain, framerate, and region of interest. The thermocycler can be configured to maintain a set temperature for a period prior to the start of any program. This can accommodate devices that need to be maintained in a specific temperature range prior to the start of an experiment, such as isothermal reactions that are active at room temperature.¹⁸ Control over the positions and interactions of the filter wheels allows the user to define and name any combination of emission and excitation filters for imaging.

The software also contains a full suite of tools for data analysis. Results from an analysis of digital multivolume real-time PCR experiments²⁰ using lambda DNA as a template are shown in Fig. 5-4 with each graph (Fig. 5-4B-D) directly exported from the analysis software as line art and scaled. These results were obtained by first creating a mask of the

sections of the device containing reactions of interest (Fig. 5-4A). A mask-creation tool is used to define the locations of compartments in images collected during an experimental run by using several built-in functions, including: thresholding, edge detection, region selection, removal of features based on area, automated removal of features on the edge of the image, and the ability to both “paint in” and “paint out” features. To account for potential device shifting during the experiment, the software has built-in tracking that recreates the mask with each individual step of the amplification and correlates relocated spots among the images based on nearest-neighbor calculations. During an analysis, each compartmentalized reaction is tracked across all of the stages of amplification and a full suite of statistical data is collected at each step for each region defined by the mask. The average value of each compartmentalized reaction is then plotted as a function of assay progress producing real-time curves for each individual reaction with full correlation back to the mask region as shown in Fig. 5-4B. Additional software functions enable baseline correction, thresholding for determination of the quantification cycle (C_q), plotting the number of positive wells as a function of assay progress (Fig. 5-4C), plotting C_q frequency as a function of assay progress, the determination of the derivative of any dataset and the generation and export of reports and datasets.

Melt curve data is initially processed in the same manner as amplification data, via creation of a mask and individually analyzing its corresponding regions (Fig. 5-4D). The data can then be processed using functions such as: data smoothing via algorithms, determination of the negative derivative of the dataset, configurable peak melt temperature detection, correlation of melt curves to amplification curves including only

showing melt curves from positive reactions, report generation, and ability to export any generated plot or dataset.

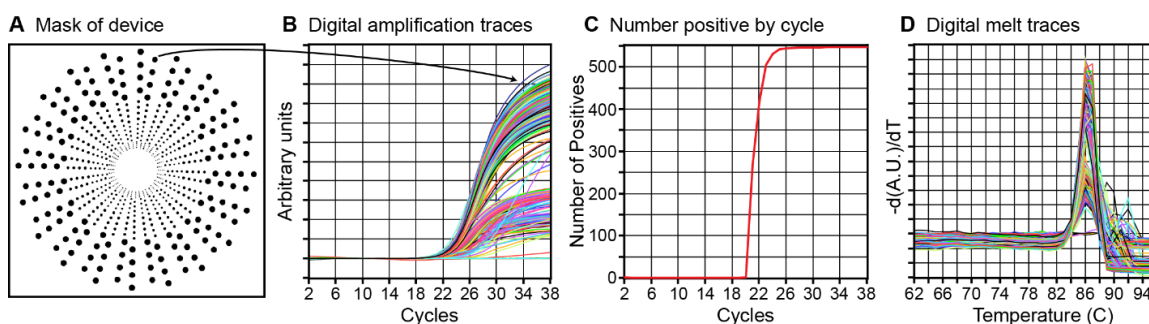


Figure 5-4. Types of data output provided by the custom analysis software of the real-time digital nucleic acid amplification instrument after a multivolume PCR reaction using lambda DNA on a multivolume SlipChip device. Each graph (B–D) was exported as line art and scaled. (A) An image depicting the mask created to define the locations of each compartmentalized reaction on a multivolume microfluidic device. (B) Baseline-corrected amplification traces from each of the reaction wells on the microfluidic device. Two intensity groups result because in this multivolume microfluidic device there are two well depths (the two larger volumes are 100 μm deep and the two smaller volumes are 50 μm deep).²⁰ The arrow shows the correlation of a single compartmentalized reaction (A) to its real-time trace (B). (C) A graph depicting the number of positive reactions as a function of amplification cycle from the data generated in (B). (D) A graph depicting the negative derivative of the collected melt curve traces from each of the positive reactions.

Digital real-time PCR validation

We validated the overall performance of the instrument in a real-time digital reverse transcription PCR experiment using HCV RNA as the template. We used a previously validated microfluidic SlipChip device⁹ and well-characterized chemistry^{9,20,22} to isolate the performance of the instrument and compare it to an Illumina Eco real-time PCR system. The assay was run at three concentrations (each separated by a 100x difference) in parallel on microfluidic SlipChip devices. In the lowest concentration tested, the wells of the device were stochastically loaded with HCV RNA molecules; in the higher concentrations, all wells were fully loaded. The lowest concentration was calculated at 6

$\times 10^4 \pm 8 \times 10^3$ molecules of HCV RNA per milliliter of reaction solution with a total of 202 positive reactions out of a possible 1218 after 40 cycles of amplification. This concentration corresponds to 0.18, copies of HCV RNA loaded per 3 nL digital compartment. The two concentrations which were 100x and 10,000x higher therefore correspond to 18, and 1800 copies of HCV RNA loaded per 3 nL digital compartment. Melt curve analysis was performed on each of the 202 positive reactions; all but five had a melt temperature indicative of the correctly amplified product. The error in the assay associated with false positive reactions accounted for 1×10^3 copies/mL, which is much smaller than the 8×10^3 error estimated by Poisson statistics, thus signifying suitable assay performance.

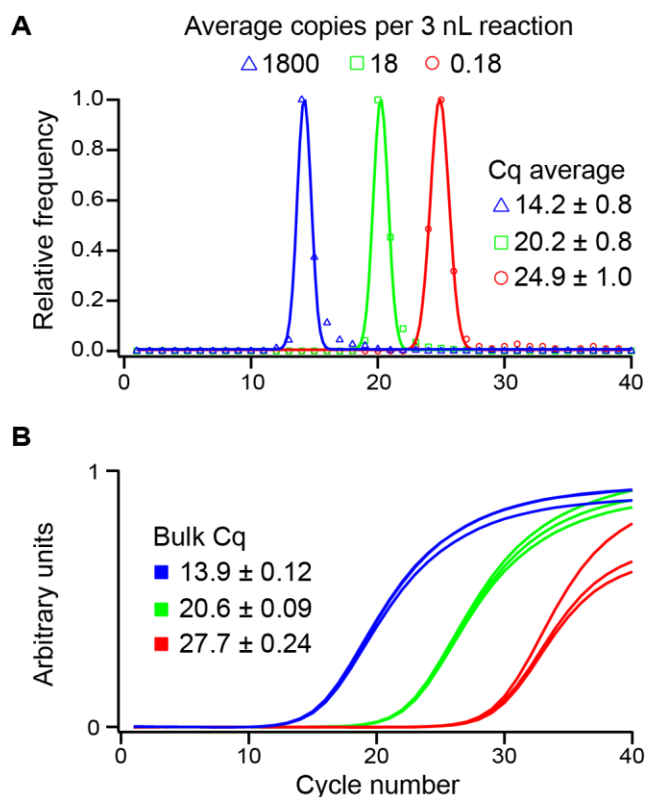


Figure 5-5. Comparison of digital (A) and bulk (B) results of real-time reverse transcription PCR experiments of HCV RNA at three different concentrations. Digital and bulk experiments were run at the same three concentrations (each separated by a

100x difference). In (A), symbols show a histogram of the relative frequency of Cq values obtained in the experiment for the denoted concentration; solid lines depict the Gaussian fit for each concentration. Points denote the calculated histogram of Cq values at each concentration. Average Cq values are the maximum of the Gaussian fit and the errors are the full width at half maximum value of the Gaussian fit. (B) Bulk traces of reverse transcription PCR of HCV RNA. Average Cq values are shown; error denotes S.D. among the replicates (N = 3).

Because we have a known change in concentration between the three tested concentrations, we can run a variety of checks to ensure that the assay performs as expected kinetically. The first analysis that can be run is to look for the variation among replicates at the same concentration. Each of the three different bulk concentrations were run in triplicate, and the standard deviation of the replicates was less than 1% of the Cq value (Fig. 5-5B) in each of those reactions indicating that the kinetic rate within each concentration was highly reproducible and the assay is suitable for deeper quantitative analysis. In addition to analyzing the kinetic reproducibility of replicates, we can also analyze the reproducibility between different concentrations by analyzing the Cq difference observed at each concentration change. Under ideal amplification conditions a doubling in concentration would be observed at each cycle. Using a perfect amplification assumption, an expected Cq difference between concentrations can be calculated based on the equation $\log_2 x$, where x is the fold change in concentration between the two samples. Running this analysis on the bulk results at a 100-fold change results in an expected Cq difference of 6.6. When comparing the high and middle concentrations a Cq difference of 6.7 is observed, and when comparing the middle and low concentrations a Cq difference of 7.1 is observed (Fig. 5-5B).

When the same comparative analyses are run on the real-time digital results, similar effects are observed as those in bulk. At each concentration due to that the experiments

were run on device many hundreds of reactions were run at each concentration, however, the standard deviation in the Gaussian fit of each concentration varies between 4% and 6%. This variation is higher than that observed in bulk, however, each population can be uniquely identified and is well separated. The results also compare favorably to those in bulk on a commercial instrument. As at the high and middle concentrations the assay was run with the digital device full the Cq values in digital should match those in bulk. This is observed with a Cq difference of 0.3 at the high concentrations, and a Cq difference of 0.4 at the middle concentrations when comparing the digital averages to the bulk averages. Where we would expect to see a deviation in Cq values compared to bulk is at the low concentration. As the low concentration is run in the digital regime on device, each compartment which contained a piece of HCV RNA did so at a concentration of 1 copy/3 nL. In bulk, although the same concentration of RNA was used, the concentration in solution was 0.18 copies/3 nL. Therefore, we would expect the on-device concentration to be 5.6 times higher which would result in a Cq difference of 2.5 between the bulk and digital results at the low concentration. When the bulk and digital Cq values at the low concentration are compared a difference of 2.8 is observed which has a deviation of 0.3 from the expected value which is within the same range as the high and middle concentrations. When this same analysis is run comparing the results from different concentrations in digital, Cq difference of 6.6 and 4.2 are expected for comparisons of the high and middle concentrations and the middle and low concentrations, respectively, which compare well with the observed differences of 6 and 4.7. From these results it is clear that the digital real-time instrument is able to provide

informative and reproducible results about the kinetics of amplification on digital microfluidic devices.

Digital real-time isothermal validation

Many amplification chemistries are compatible with digital assays and could benefit from knowledge of kinetic information and digital optimization. Loop-mediated isothermal amplification (LAMP) has been used extensively in a digital format; however, the amplification efficiency of many LAMP reactions is consistently less than expected.^{4,9,19,23} Because reaction efficiency is consistent, quantification can still be performed in the absence of optimization, however optimizing LAMP reactions performed in a digital format would both increase confidence in the final calculated concentrations and lower the current limits in detection and quantification. Such optimization is not possible using bulk reactions because changes in reaction rate do not necessarily correlate with changes in reaction efficiency.⁹ We have shown previously⁹ using the real-time digital instrument described herein that the efficiency of a reverse transcription LAMP reaction targeting HCV RNA can be optimized quickly and effectively by using real-time information combined with digital information. The amplification efficiency of HCV RNA through the usage of real-time digital data was improved from ~20% to ~70%, significantly increasing the confidence of the calculated concentration and lowering the detection limit of the assay.⁹

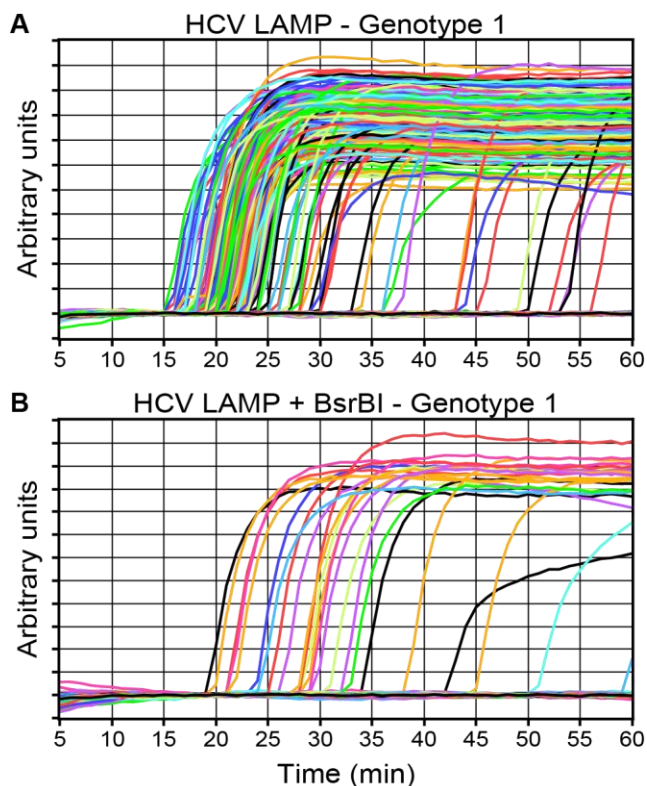


Figure 5-6. Results of reverse transcription LAMP of HCV RNA reactions in the presence (A) and absence (B) of a competing restriction digestion enzyme, BsrBI. In (A) the reaction is allowed to proceed normally with high reaction efficiency and fast reaction rates. In (B) the reaction efficiency and rate are significantly lower because BsrBI degrades the template.

We have also previously used this instrument to optimize and verify an assay to simultaneously quantify and genotype HCV RNA.²¹ This was done by performing a competition reaction between LAMP amplification and genotype-selective degradation of the template using restriction enzymes. In bulk assays, the restriction enzymes were shown to delay the reaction; however, in the digital format the competition reaction significantly decreased the number of positive digital reactions. Using the real-time digital instrument, we were able to show that the digital competition reactions on HCV genotype 1 (Fig. 5-6B) that amplified did so with a decreased reaction rate compared to a positive control (Fig. 5-6A). We further showed that the decrease in reaction rate in

digital format was similar to the decrease in reaction rate that was observed in bulk reactions. Having this detailed information about the kinetics of individual reaction volumes enabled us to establish that the so-called “fate” of a reaction (i.e. whether or not the reaction will proceed) is determined in the first steps of a reaction; and once that fate is determined, the competition reaction affects only the rate. This paper and our paper showing the lack of correlation between reaction speed and analytical sensitivity⁹ wouldn't have been possible without this instrument. We are continuing to use this instrument in our lab to develop and enable new analytical capabilities for a wide range of sample and device types.

Conclusions

We developed an instrument for real-time digital nucleic acid amplification studies and accompanying software that can be used to develop, study, or optimize a wide variety of digital assays for numerous applications, including medical diagnostics, forensics and environmental sampling. The instrument is device-agnostic and it is compatible with a variety of nucleic acid amplification chemistries, including PCR, reverse transcription PCR, LAMP, and reverse transcription LAMP in a competition reaction with restriction enzymes. We validated this real-time instrument using two types of microfluidic devices, one that contained a large number of reactions in compartments of the same size, and a second device that processes larger volumes with a range of different reaction sizes. We also presented a simple, intuitive, GUI-based software package that allows the user to easily set up, collect, and analyze digital experiments using real-time fluorescence information from a wide variety of possible devices with a total precision-heated and viewable area of $\sim 5500 \text{ mm}^2$.

The capabilities provided by this instrument will be invaluable for researchers who wish to track the progress of reactions at high resolution with a large field of view and its use will enable the study and optimization of a wider variety of digital reactions in real time. Although the error in the temperature control is well within our required performance, this and other device error can be corrected via in-software calibrations that can be customized for any specific device. The instrument was designed to be modular so that it is amenable to further customization, such as to increase illumination intensity, enable heating of non-flat devices, increase the field of view, or increase the resolution of the captured area as new technologies are introduced they can be easily incorporated without a significant engineering effort. We hope that by sharing the details of this instrument and software, others will be able to construct their own purpose-built custom instruments or modify existing commercial solutions to characterize and optimize digital reactions, making digital methods even more powerful.

Materials and Methods

Chemicals and materials

All chemicals were purchased from commercial sources. The LoopAmp® RNA amplification kit (Eiken Chemical Co., Ltd., Japan) was purchased from SA Scientific (San Antonio, TX, USA). The LoopAmp® RNA amplification kit contains 2X Reaction Mix (RM) (40 mM Tris-HCl pH 8.8, 20 mM KCl, 16 mM MgSO₄, 20 mM (NH₄)₂SO₄, 0.2% Tween20, 1.6 M Betaine and dNTPs 2.8 mM each), Enzyme Mix (EM) (mixture of Bst DNA polymerase and AMV reverse transcriptase), and distilled water (DW). Bovine serum albumin (BSA) was purchased from Roche Diagnostics (Indianapolis, IN, USA).

Bio-Rad (Hercules, CA, USA) SsoFast Evagreen Supermix, Phage lambda DNA (500 μg), SUPERase In RNase Inhibitor (20 U/ μL), mineral oil (DNase, RNase, and Protease free), and tetradecane were purchased from Thermo Fisher Scientific (Hanover Park, IL, USA). All primers were produced by Integrated DNA Technologies (Coralville, IA, USA). Dichlorodimethylsilane was purchased from Sigma-Aldrich (St. Louis, MO, USA). Photomasks were designed in AutoCAD 2013 and ordered from CAD/Art Services, Inc. (Bandon, OR, USA). Soda-lime glass plates coated with layers of chromium and photoresist were ordered from the Nanofilm (Westlake Village, CA, USA). The PTC-200 thermocycler was purchased second-hand off of Ebay (San Jose, CA, USA) and was manufactured by MJ Research (Waltham, MA, USA). The Tgon 805, Tgard K52, and PR103J2 thermistors were purchased from Digikey (Thief River Falls, MN, USA). The illumination optics were purchased from Edmund Optics (Barrington, NJ, USA) (part numbers 46-685, 48-247, 48-372, 63-496, 48-904, 48-451, 48-453). The LED light source, power supply, and heat sink were purchased from Future Electronics (Montreal, Canada). The filter wheels were purchased from Finger Lakes Instrumentation (Lima, NY, USA). The camera for the instrument was purchased from Vision Systems Technology (Vista, CA, USA). The camera lens was purchased from Digitalrev.com (Kowloon, Hong Kong). The green fluorescent filter set was purchased from Semrock (Rochester, NY, USA). The other filter sets for Texas red and Cy5 dyes were purchased from Omega Optical (Brattleboro, VT, USA). The thermocouples and digital acquisition device were purchased from Omega Engineering (Stamford, CT, USA). The various aluminum extrusions, filter holders, lens holders, optical posts, and other ancillary equipment to construct the shell of the instrument were purchased from either Thorlabs

(Newton, NJ, USA), Edmund Optics (Barrington NJ, USA), Newport Corp. (Irvine, CA, USA), Grainger (Lake Forest, IL, USA), or 80/20 (Columbia City, IN, USA). Custom CNC milled parts were ordered from Protolabs (Maple Plain, MN, USA).

Microfluidic device design

A multivolume rotational SlipChip device was used as a model to illustrate some of the capabilities of the instrument for performing amplification reactions on custom microfluidic devices. Use of this particular multivolume device was first published in Shen *et al.*²⁰. Briefly, the device has four different sized wells of 1, 5, 25, and 125 nL. There are 160 different wells of each volume on the device; the two smaller wells have a depth of 50 μm and the two deeper wells have a volume of 100 μm .

A single-volume microfluidic device was used to perform reverse-transcription PCR (RT-PCR) and compare the performance of the instrument in different concentration regimes with traditional quantitative PCR. This particular single-volume device is a lightly modified version of the device used by Sun *et al.*¹⁹ It contains 1280 reaction wells each with a 3 nL volume. All wells and channels in the device are etched to a depth of 50 μm .

Microfluidic device fabrication

Microfluidic devices were fabricated using standard photolithography followed by wet chemical etching with hydrofluoric acid.²⁴ After etching the devices to the proper depths and drilling access holes with a diamond-coated bit, devices were subjected to a previously described silanization process.²⁵

Assembling and loading microfluidic devices

The microfluidic devices were assembled under degassed oil consisting of a combination of 75% mineral oil and 25% tetradecane (v/v). Both the top and bottom sections of the microfluidic device were immersed in oil before being aligned under a stereoscope (Leica, Wetzlar, Germany). The devices were then clamped together using standard 1" binder clips. Solutions were introduced into the microfluidic devices by drawing the solution to be loaded on the device into a pipettor (Eppendorf, Hamburg, Germany), placing the end of the pipette tip into the pre-drilled access holes on the device to create a seal, and applying a pressure of 0.1 atm.

Illumination setup

The illumination setup of the instrument was designed to be composed of standard and easily obtainable illumination and optical components. A white LED module (LSX8-PW30, Fig. 5-2A) was used as the optical source of the instrument and provides 1175 lumens of flux from an 8mm x 8mm area. Five lenses were set up to direct the light to the imaging platform; these consisted of: a 40 mm aspheric lens (46-685, Fig. 5-2A), two 50 x 125 mm plano-convex lenses (48-247, Fig. 5-2D), a 75x 200 mm plano-convex lens (48-372, Fig. 5-2F), and a 75x 500 mm plano-convex lens (63-496, Fig. 5-2G). The excitation wavelengths are chosen by a five-position filter wheel (CFW-1-5, Fig. 5-2C) that holds a selection of three 50.8 mm excitation filters: a 475 nm centered filter (FF02-475/50-50.8-D), a 560 nm centered filter (560QM55), and a 630 nm centered filter (630QM50). After passing through the field lenses, the light is split by a 50-50 beamsplitter (48-904, Fig. 5-2H) before either reflecting off of a 75 X 75 mm mirror (48451, Fig. 5-2I) or a 75 x 100 mm mirror (48-453, Fig. 5-2J). The optics are designed to provide demagnified and slightly defocused light to an imaging area of ~72 x 72 mm.

The light must be slightly defocused to attain a relatively constant illumination intensity over the full area as the source is a 3 x 3 grid of smaller light emitting diodes.

Imaging setup

The instrument uses a six-position filter wheel (CFW-6-6, Fig. 5-2L) that is equipped with a set of three 79 mm emission filters: a 540 nm centered filter (FF01-540/50-79-D), a 645 nm centered filter (645QM75), and a 695 nm centered filter (695QM55). With these filter sets, we are capable of imaging dyes such as fluorescein, Texas red, and Cy5. We used a VX-29MG-M2-A0-F-2 29-megapixel camera (Vieworks, Anyang, South Korea) that utilizes a KAI-29050 6576 x 4384 sensor (ON Semiconductor, Phoenix, AZ, USA). This camera has a 23 mm sensor with a pixel pitch of 5.5 x 5.5 μm , a 12-bit low noise amplifier, a GigE vision interface, and a standard Nikon F lens mount. The lens used is a Makro-Planar T* 100mm f/2 ZF.2 lens (Ziess, Oberkochen, Germany) which has a wide f/2 aperture and the ability to focus on an area as small as 48 x 72 mm. The camera is triggered via an OMB-DAQ2408-2AO data acquisition board (Measurement Computing, Norton, MA, USA) through an analog output with millisecond accuracy. The data acquisition board is also used to control the shutter of the system and collect temperature data. This imaging setup enables us to image the full 72 x 72 mm field of view wherein each pixel is equivalent to 16 x 16 μm real-world resolution.

Fluorescence standards

Because the total viewable area on the custom-built instrument is rather large, no commercially available fluorescence standards were found that were large enough to encompass the full field of view in a single image. Fluorescence standards for the 475 nm

and 560 nm emission channels were created by coating one side of a 72 mm x 76.2 mm piece of soda-lime glass with Rust-Oleum 1932830 or 1959830 paint. A fluorescent standard for the 630 nm channel was created by gluing a Rosco Roscolux #2001 storaro red filter between two pieces of soda-lime glass cut to a size of 72 mm x 76.2 mm with Loctite® #349 optical adhesive.

Temperature control

Temperature control is provided by a PTC-200 thermocycler (Bio-Rad, Hercules, CA, USA). The thermocycler was chosen for its simple ASCII programming interface, which is via an RS-232 port, and because blocks are easy to interchange. The heating block used in the instrument is a heavily modified 96-well alpha block. This custom thermal block was designed and fabricated from aluminum and contains a raised flat section measuring 72 x 76.2 mm that has the same thermal mass as the block included in the system. The block is in thermal contact with the Peltier elements of the alpha block using first a ceramic filled polyimide sheet (Tgard K52) and second a thermally conductive graphite sheet (Tgon 805). The block incorporates three 10K ohm at 25 °C thermistors (PR103J2) in the standard alpha block locations, which were soldered directly to the circuit board. All temperature measurements are recorded with type-K thermocouples (5TC-TT-K-40-36).

Temperature readout of thermal block

Temperature readings of the thermal block are collected with a 5TC-TT-K-40-36 thermocouple attached to an OMB-DAQ2408-2AO digital acquisition instrument. The thermocouple is in thermal contact with the heated block using Arctic MX-4 thermal

paste. Temperature readings for calibration and validation of the thermal block can be collected between a range of 4 °C and 98 °C with a resolution of 0.1 °C and a frequency of 1 kHz. In the validation experiments performed here, data was between 12 °C and 98 °C at a resolution of 0.5 °C collected by setting the thermocycler to hold the desired temperature, and waiting until the temperature stabilized within a 0.1 °C for a total of 30 s. The temperature readings collected over the 30 s period were then averaged and used for all calculations.

Nucleic acid amplification reagents

PCR experiments were carried out using 2x SsoFast EvaGreen supermix with a 1 µM concentration of primers and varied concentrations of template. The template used in the multivolume PCR experiments was lambda DNA with primer sequences (GAA TGC CCG TTC TGC GAG, TTC AGT TCC TGT GCG TCG). The temperature profile used in those experiments was a 5-minute melt at 95°C followed by 40 cycles of 1 min at 95 °C, 30 s at 58 °C, and 30 s at 72 °C. The PCR experiments done to compare reactions in digital to reactions in bulk used hepatitis C virus (HCV) RNA with primer sequences (GAG TAG TGT TGG GTC GCG AA, GTG CAC GGT CTA CGA GAC CTC). The temperature profile used in those experiments was a 30-min 50 °C reverse transcription step followed by a 3-min melt at 94 °C followed by 40 cycles of 1 min at 94 °C, 30 s at 62 °C, and 30 s at 72 °C.

Collection software

Simple and easy-to-use GUI based custom software was designed for the real-time digital instrument using the LabVIEW 2013 development suite with the vision acquisition,

OpenG, and System Controls 2.0 add-on packages. Control over the camera is achieved using the National Instruments IMAQdx driver to control any GIGE compliant camera. Control over the filter wheels is achieved using the FLI Software installation kit (4/14/2010 update) and version 1.104 of the FLI SDK. Control over the thermocycler is achieved using the ASCII commands outlined in the PTC-200 user manual and the RS-232 driver in LabView. The data acquisition board is controlled through Omega DAQ software (v. 6.22) utilizing the ULx LabView drivers. The software includes a variety of different modules for the collection of amplification data, melt temperature data, and temperature calibration data, as well as acting as a generalized large-format fluorescence imager. The software also allows the user to save experimental programs and settings, including full experimental profiles, camera settings, and temperature calibration settings for individual assays.

Analysis software

Simple and easy-to-use GUI based custom software was designed for the analysis of collected data using the LabVIEW 2013 development suite with the vision acquisition, OpenG, System Controls 2.0, and the report generation toolkit for Microsoft Office add-on packages. The software is able to open and analyze all generated data from the collection software including the ability to recall all temperature data, experimental conditions, and presets. The software includes a variety of different modules for analysis of the data including all amplification and melt temperature data, mask generation for defining digital reaction locations in custom microfluidic devices, and report generations and export to Microsoft Word and Excel. The analysis software is also able to export raw or analyzed data as well as any plot in a variety of formats.

The software is able to create independent amplification curves from each discrete digital reaction through the usage of a user created mask which defines the reaction location in space. Once a location is defined, full statistical information about that independent reaction is available for that point during the reaction. A full suite of tools is available for creating the mask including thresholding, edge detection, size discrimination, location selection and rejection, and manual editing. If during the course of the amplification some reaction volumes move outside of their masked area, tracking software can be activated in the software which rebuilds the mask at each point in the amplification based on the process defined by the user and correlates the reaction volumes between images based on nearest neighbor calculations. After amplification curves have been established, baseline correction, C_q calling, report generation, and correlation of each reaction trace to its discrete reaction volume can be performed. Melt curve analysis can be performed in much the same way, although added features such as peak calling, correlation to amplification reactions, and curve smoothing can be performed.

Acknowledgements

We thank David H. Tracy for designing the optical system for the instrument and Natasha Shelby for contributions to writing and editing this manuscript.

References

1. Sanders, R. *et al.* Evaluation of digital PCR for absolute DNA quantification. *Anal. Chem.* **83**, 6474–6484 (2011).
2. Huggett, J. F. *et al.* The digital MIQE guidelines: Minimum information for publication of quantitative digital PCR experiments. *Clin. Chem.* **59**, 892–902

- (2013).
3. White, R. A., Quake, S. R. & Curr, K. Digital PCR provides absolute quantitation of viral load for an occult RNA virus. *J. Virol. Methods* **179**, 45–50 (2012).
 4. Selck, D. A., Karymov, M. A., Sun, B. & Ismagilov, R. F. Increased robustness of single-molecule counting with microfluidics, digital isothermal amplification, and a mobile phone versus real-time kinetic measurements. *Anal. Chem.* **85**, 11129–11136 (2013).
 5. Whale, A. S. *et al.* Comparison of microfluidic digital PCR and conventional quantitative PCR for measuring copy number variation. *Nucleic Acids Res.* **40**, 1–9 (2012).
 6. Mekata, T. *et al.* Real-time quantitative loop-mediated isothermal amplification as a simple method for detecting white spot syndrome virus. *Lett. Appl. Microbiol.* **48**, 25–32 (2009).
 7. Murakami, T., Sumaoka, J. & Komiyama, M. Sensitive isothermal detection of nucleic-acid sequence by primer generation-rolling circle amplification. *Nucleic Acids Res.* **37**, (2009).
 8. Kimura, Y. *et al.* Optimization of turn-back primers in isothermal amplification. *2011 IEEE Int. Conf. Bioinforma. Biomed. Work. BIBMW 2011* **39**, 909–911 (2011).
 9. Khorosheva, E. M., Karymov, M. A., Selck, D. A. & Ismagilov, R. F. Lack of correlation between reaction speed and analytical sensitivity in isothermal

amplification reveals the value of digital methods for optimization: validation using digital real-time RT-LAMP. *Nucleic Acids Res.* **44**, e10 (2016).

10. Bhat, S., Herrmann, J., Armishaw, P., Corbisier, P. & Emslie, K. R. Single molecule detection in nanofluidic digital array enables accurate measurement of DNA copy number. *Anal. Bioanal. Chem.* **394**, 457–467 (2009).
11. Angione, S. L., Chauhan, A. & Tripathi, A. Real-time droplet DNA amplification with a new tablet platform. *Anal. Chem.* **84**, 2654–2661 (2012).
12. Beer, N. R. *et al.* On-chip, real-time, single-copy polymerase chain reaction in picoliter droplets. *Anal. Chem.* **79**, 8471–8475 (2007).
13. Beer, N. R. *et al.* On-chip single-copy real-time reverse-transcription PCR in isolated picoliter droplets. *Anal. Chem.* **80**, 1854–1858 (2008).
14. Hatch, A. C. *et al.* 1-Million droplet array with wide-field fluorescence imaging for digital PCR. *Lab Chip* **11**, 3838 (2011).
15. Sundberg, S. O., Wittwer, C. T., Gao, C. & Gale, B. K. Spinning disk platform for microfluidic digital polymerase chain reaction. *Anal. Chem.* **82**, 1546–1550 (2010).
16. Zhang, Y., Zhu, Y., Yao, B. & Fang, Q. Nanolitre droplet array for real time reverse transcription polymerase chain reaction. *Lab Chip* **11**, 1545–1549 (2011).
17. Tanner, N. A. *et al.* Real-time single-molecule observation of rolling-circle DNA replication. *Nucleic Acids Res.* **37**, 2–7 (2009).
18. Shen, F. *et al.* Digital isothermal quantification of nucleic acids via simultaneous

- chemical initiation of recombinase polymerase amplification reactions on SlipChip. *Anal. Chem.* **83**, 3533–3540 (2011).
19. Sun, B. *et al.* Mechanistic evaluation of the pros and cons of digital RT-LAMP for HIV-1 viral load quantification on a microfluidic device and improved efficiency via a two-step digital protocol. *Anal. Chem.* **85**, 1540–1546 (2013).
 20. Shen, F. *et al.* Multiplexed quantification of nucleic acids with large dynamic range using multivolume digital RT-PCR on a rotational SlipChip tested with HIV and hepatitis C viral load. *J. Am. Chem. Soc.* **133**, 17705–17712 (2011).
 21. Sun, B. *et al.* Measuring fate and rate of single-molecule competition of amplification and restriction digestion, and its use for rapid genotyping tested with hepatitis C viral RNA. *Angew. Chemie - Int. Ed.* **53**, 8088–8092 (2014).
 22. Meng, S. & Li, J. A novel duplex real-time reverse transcriptase-polymerase chain reaction assay for the detection of hepatitis C viral RNA with armored RNA as internal control. *Virology* **7**, 117 (2010).
 23. Zhu, Q. *et al.* Self-priming compartmentalization digital LAMP for point-of-care. *Lab Chip* **12**, 4755–63 (2012).
 24. Du, W., Li, L., Nichols, K. P. & Ismagilov, R. F. SlipChip. *Lab Chip* **9**, 2286 (2009).
 25. Shen, F. *et al.* Nanoliter multiplex pcr arrays on a slipchip. *Anal. Chem.* **82**, 4606–4612 (2010).

Chapter 6:

Measuring the Fate and Rate of Single-Molecule Competition of Amplification and Restriction Digestion, and Its Use for Rapid Genotyping Tested with Hepatitis C Viral RNA*

Abstract

We experimentally monitored, at the single-molecule level, the competition among reverse transcription, exponential amplification (RT-LAMP), and linear degradation (restriction enzymes) starting with Hepatitis C viral RNA molecules. We found significant heterogeneity in the rate of single-molecule amplification; introduction of the restriction enzymes affected both the rate and the “fate” (the binary outcome) of single-molecule amplification. While end-point digital measurements were primarily sensitive to changes in fate, the bulk real-time kinetic measurements were dominated by the rate of amplification of the earliest molecules, and not sensitive to fate of the rest of the molecules. We showed how this competition of reactions can be used for rapid HCV genotyping with either digital or bulk readout. This work advances our understanding of single-molecule dynamics in reaction networks and may help bring genotyping capabilities out of clinical labs and into limited-resource settings.

Results Discussion and Conclusions

This paper presents single-molecule kinetic measurements of how the competition between exponential amplification of RNA molecules and their linear degradation affects

* This chapter was first published in *Angewandte Chemie* with authorship belonging to Bing Sun, Jesus Rodriquez-Manzano, David A. Selck, Eugenia Khorosheva, Mikhail A. Karymov, and Rustem F. Ismagilov. The original manuscript can be found at: <http://dx.doi.org/10.1002/anie.201403035>

both the “rate” and “fate” of amplification, and shows how such competition can be used to design assays for rapid genotyping of the hepatitis C virus.

A wide range of diagnostic solutions for global health are urgently needed,^{1,2} including for HCV, which infects 130-170 million people worldwide.³ These patients can now be treated with recently approved small-molecule drugs,⁴ which replace or reduce interferon therapy, but genotyping is still required to determine the treatment each patient should receive. However, most of these patients or their primary care doctors are located in limited-resource settings. High-complexity molecular tests such as commercially available HCV genotyping assays are not well suited for such settings (see SI).

Therefore, a rapid (<1 hr), robust, and simple system for genotyping remains an unmet need. HCV genotypes differ by sets of mutations, with overlap between sequences of some but not all genotypes. Instead of attempting to design a separate detection reaction for each genotype, we wished to test whether we could design a competition reaction network (Figure 6-1): the detection for multiple HCV genotypes takes place in a single core amplification reaction, and the specificity for genotypes is achieved by the competing sequence-specific inhibition reactions.

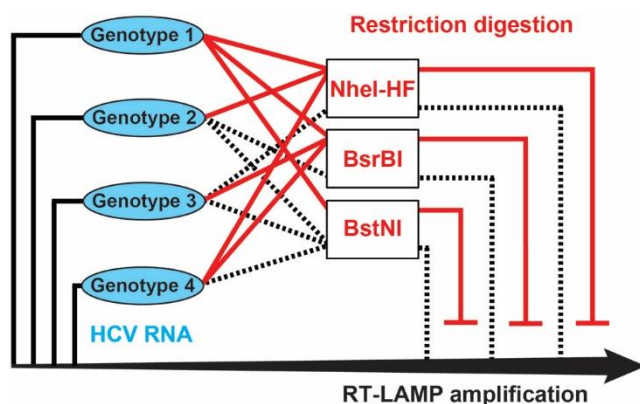


Figure 6-1 Schematic of a network based on competition between amplification (solid black lines and arrow) and inhibition (solid red). Any one of four HCV genotypes could be independently amplified by one RT-LAMP reaction and inhibited specifically by different restriction digestion reactions. When the restriction enzyme (RE) is specific to that genotype, it produces an inhibition feedback to the amplification (solid red). When the RE is not specific to the genotype, there is no inhibition even in the presence of RE (dashed black).

The use of competition among reactions to achieve regulation is common in biological systems; in our personal favorite example of the blood coagulation cascade,^{5,6} the core autocatalytic amplification cascade is held in check by multiple inhibitors. Here, we wished to use a competition system consisting of reverse transcription loop-mediated isothermal amplification (RT-LAMP) as the amplification reaction, and restriction enzyme (RE) digestion as the inhibition reaction. Single-molecule, or “digital”^{7,8} LAMP^{9,10} is attractive for quantification under limited-resource settings due to its high intensity fluorescent output with calcein chemistry.^{11,12} Digital RT-LAMP for the quantification of human immunodeficiency virus RNA was shown to be robust to perturbations in reaction conditions, imaging, temperature, and automatic cloud-based analysis, enabling robust cell phone-based quantification.¹² In this work, we used RT-LAMP primers (see Table S1 in Supporting Information (SI)) modified from previous

work targeting the conserved 5'- untranslated region (5'UTR) of HCV.¹³ RE-based digestion is a reliable method to recognize specific nucleic acid sequences of multiple letters in length and cleave at specific sites.¹⁴ We hypothesized that RE digestion could be used to compete with RT-LAMP amplification in situ in both bulk and digital formats.

Although the kinetics of single-molecule amplification has been studied for some reactions such as enzymatic turnover of a substrate⁸ or digital PCR,⁷ it has not been studied for sequence-specific isothermal amplification reactions, especially when competing reactions are involved. Therefore, before we could test this idea, we first had to answer three fundamental questions: i) How significant is the heterogeneity in the rate of digital RT-LAMP amplification? We expected some heterogeneity because LAMP itself has a complex mechanism, and RT-LAMP introduces an additional reverse transcription step from RNA molecules with heavy secondary structures. ii) Would introduction of RE affect the rate, or the fate, of digital RT-LAMP amplification (Figure 6-2A)? For simplicity, here we defined "rate" as the inverse of the "time-to-positive," or time it takes the amplification to produce a particular level of a signal; competition from RE could decrease the rate of amplification by consuming some of the amplification products. We defined "fate" as whether or not amplification ultimately succeeds to provide that level of signal from a single molecule. For example, in the RT-LAMP/RE mechanism (Figure 6-2B), one fate-determining step could occur once the first double-stranded DNA (dsDNA) is formed (structure (1) in Figure 6-2B): either RE can bind to the strand and cleave it, or primer annealing followed by polymerase binding could lead to the formation of the double-looped template that can be further amplified. Such stochastic fate determination could also occur elsewhere during the early stages of the

reaction as long as the number of molecules remains small. iii) Would this competition affect the bulk reaction differently from the single-molecule reactions? Given that this reaction system has significant nonlinearity, it is predicted¹⁵ to be affected by the spatial distribution and compartmentalization.

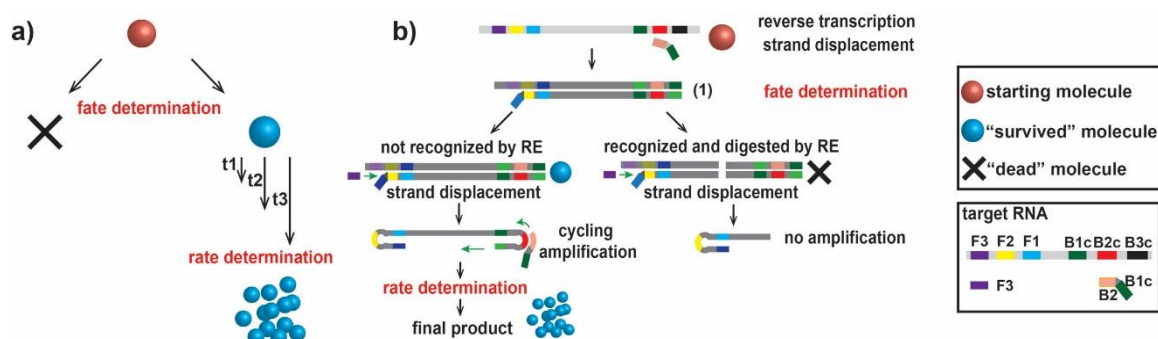


Figure 6-2 Schematic overview of the definition of “fate” and “rate” in general (a) and specifically for the competition between RT-LAMP and restriction digestion (b). See text for details.

To answer the first two questions, we performed real-time digital RT-LAMP/RE experiments with HCV genotype 1 (GT1) RNA and BsrBI as the RE. HCV GT1 isolate was obtained commercially and sequenced after RNA purification to confirm the genotype assignment (Table S2 in SI). BsrBI cuts dsDNA at sequences CCGCTC, and this sequence exists in the RT-LAMP amplicon of GT1 RNA. With negative control experiments, we identified the highest possible BsrBI concentration that did not trigger ab initio DNA synthesis within the time of interest under reaction conditions.¹⁶ The concentration was determined by performing a RE dilution experiment in the presence of all RT-LAMP components except HCV RNA and choosing the concentration for which ab initio synthesis was not observed within 50 min. We used a SlipChip microfluidic device modified based on previous publication¹⁰ to compartmentalize the reaction mixture and monitored the progress of amplification for each single molecule using a

CCD-based imaging system (Figure 6-3). Even in the amplification reaction in the absence of the RE, we found significant heterogeneity among rates of amplification of different molecules (Figure 6-3A). Addition of BsrBI did not abolish this heterogeneity (Figure 6-3B). On average, even though the rates of the reactions decreased upon addition of BsrBI, the shift in reaction times (approximately 5 min, for the first well that turned positive) was small relative to the width of the distribution of the reaction times (over 30 min). On the other hand, the fate of single-molecule amplification did change significantly upon addition of BsrBI: ~10-fold fewer molecules gave rise to successful amplification (with a p-value of 0.00033), indicating that in digital RT-LAMP, BsrBI affects fate more than it affects rate.

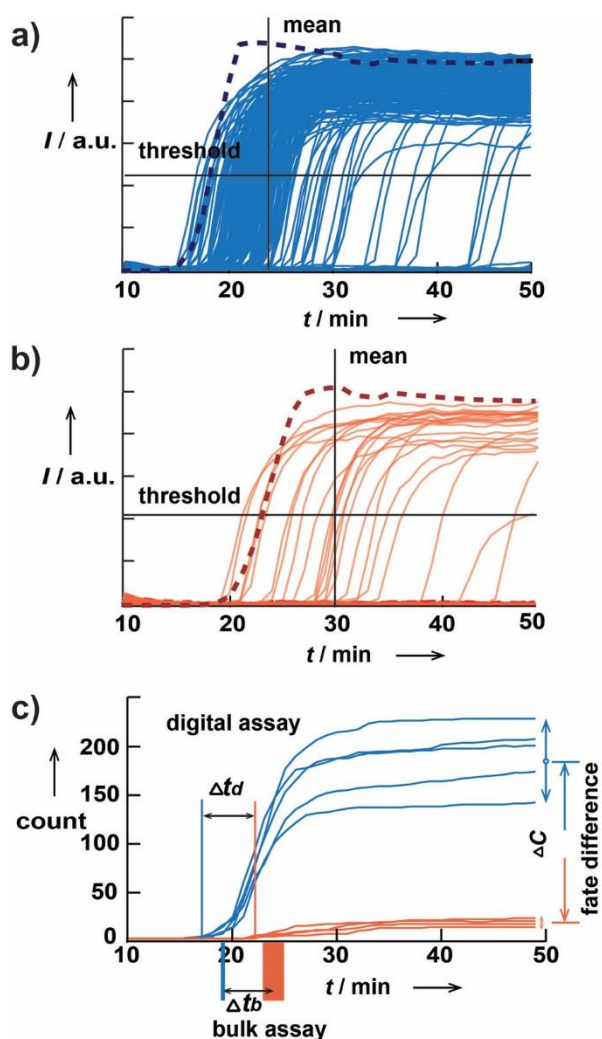


Figure 6-3 Results of real-time, single-molecule digital RT-LAMP/RE experiments for HCV RNA. a, b) Graphs showing 1280 fluorescence traces for the RT-LAMP amplification process of all the wells on a SlipChip device (solid light blue) and normalized averaged fluorescence curve in bulk (dashed dark blue) in the absence of RE (a) and the traces for digital (solid light red) and for bulk (dashed dark red) in the presence of RE BsrBI (b). Horizontal solid lines indicate the threshold levels to consider a well positive. Vertical solid lines show the mean of the time-to-positive distribution. The intensity (I) scales in (a) and (b) are the same. c) Graph showing the change of cumulative counts over time for wells exceeding the threshold in (a), blue, and (b), red. The two bars below the x-axis show time-to-positive for real-time bulk experiments, the widths of which stand for standard deviation for the bulk assay (n=5).

To answer the third question, we performed the same competition experiments in the bulk real-time format using an RNA concentration of $\sim 3.3 \times 10^5$ copies/mL (estimated based on

digital RT-LAMP results), equivalent to the concentration of a single molecule in a 3 nL well. Without BsrBI, the reaction in this bulk experiment was approximately 5 min faster than the mean amplification time in the corresponding digital experiment (Figure 6-3A); it was closer to the time of the amplification of the first molecule (approximately 2 min slower) (Figure 6-3C). Upon addition of BsrBI, the bulk reaction showed increased variance and slowed down by $\Delta t_b = 4.9 \pm 1.9$ min (Figure 6-3C); this delay was similar to the delay of the time-to-positive of the first molecule in the digital format, $\Delta t_d = 4.2 \pm 1.1$ min (Figure 6-3C). These data suggest that once exponential amplification of some molecules takes off, this process dominates the reaction mixture and is not affected by the amplification of the molecules that amplify later in the digital format—the bulk reaction has ended by then. In other words, the bulk experiment is dominated by the rate of amplification of the earliest molecules, and not sensitive to the fate of the rest of the molecules. We then tested if this concept could be applied to perform HCV genotyping. Our goal was not to validate a genotyping assay with a broad panel of clinical samples from across the globe. Instead, we wished to understand whether a proof-of-concept experiment was possible, and therefore we focused on HCV samples of the four most common genotypes in the USA¹⁷ which were readily available to us from commercial sources (see Experimental section in SI). Sequencing results of the 5'UTR of these samples confirmed their genotype assignment (Table S2 in SI).

Based on consensus obtained by aligning sequences of each genotype obtained from LANL¹⁸, three REs thermostable under RT-LAMP conditions were chosen to target the sequence differences between these four genotypes within the RT-LAMP amplicon. NheI-HF (targeting GCTAGC) should recognize genotypes 1, 2, and 4; BsrBI (targeting

CCGCTC) should recognize genotypes 1, 3, and 4; and BstNI (targeting CCWGG) should recognize only GT1 (Figure 6-4A). We have confirmed that under LAMP conditions these three enzymes remained active and sequence specific; such tests should be performed if additional REs are included. Because one RE can probe multiple genotypes, in principle unambiguous genotyping panels can be designed with fewer reactions than genotypes (e.g., three REs to differentiate four genotypes here). We note that this approach is well-suited for probing multiple mutations within the same amplification region; alternatively, several amplification reactions can compete with several cleavage reactions for higher multiplicity.

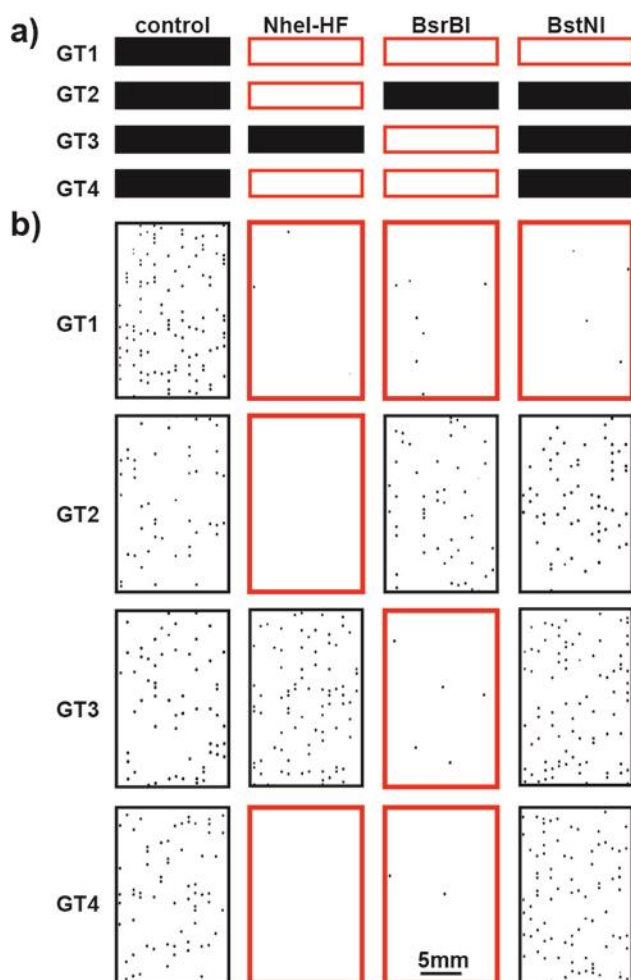


Figure 6-4 a) Predicted HCV genotyping pattern based on REs used and b) photographs (inverted intensity) of end-point digital experimental genotyping results (only a part of each chip is shown). The first column in both sections represents the positive control in the absence of RE and the following three columns indicate experiments with different REs. Each row represents a genotype (GT) of HCV RNA. Red frame indicates predicted inhibition.

For each genotype, we performed four digital experiments: one positive control without RE, and three experiments with one RE each. The positive control also provided a measurement of the viral load and validation for performing digital experiments (see Table S3 in SI). The experimental results (Figure 6-4B) agreed with the inhibition pattern predicted (Figure 6-4A). Amplification of GT1 was inhibited by all three REs; amplification of GT2 was inhibited by NheI-HF only; amplification of GT3 was inhibited

by BsrBI; and amplification of GT4 was inhibited by NheI-HF and BsrBI. The fate of molecules for each combination was dependent somewhat on the RE being used, but in all cases the inhibition was strong and statistically significant (Figure 6-5B).

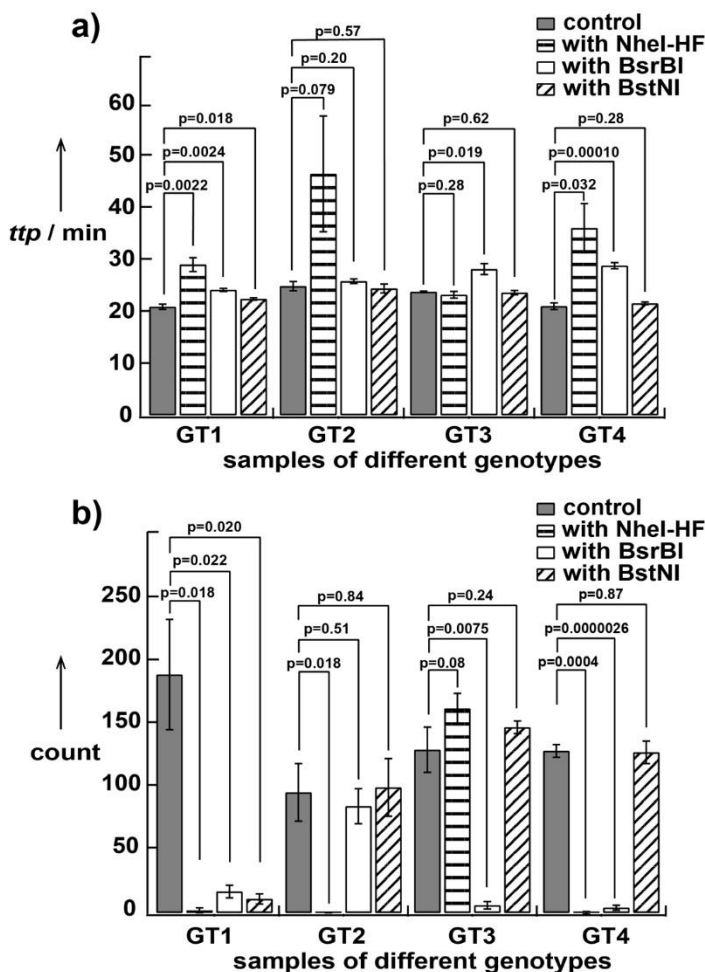


Figure 6-5 Graphs showing a comparison of HCV genotyping results using a) real-time bulk assay (ttp: time-to-positive) and b) end-point digital assay (n=3).

We then compared the performance of this HCV genotyping approach in a digital format to that in a real-time bulk format (Figure 6-5). Experimental repeats were performed on different days to ensure these experiments were not merely technical replicates. Both formats agreed with the prediction shown in Figure 6-4A. In the digital format (Figure 6-5B), reactions with RE specific to the genotype showed reduced counts by at least 10

fold, giving statistically significant results ($p < 0.022$). In the bulk format (Figure 6-5A), reactions with RE that are specific to the genotype were all delayed by a certain amount of time ranging from 2 min (~10% relative to time-to-positive of positive control) to 20 min (~100% relative to time-to-positive of positive control). Acceptable p-values were obtained for three of the four genotypes ($p = 0.079$ for GT2 and $p < 0.032$ for others). As the strength of inhibition by the RE increased, (e.g., NheI-HF in Figure 6-5B), in digital, lower counts and smaller p-values were observed. Paradoxically, stronger inhibition by RE in real-time bulk experiments led to a larger variation of reaction times and therefore did not improve p-values. Presumably, strong inhibition brings bulk amplification into the stochastic regime; this connection between digital “fate” and bulk “rate” deserves to be investigated further.

Here, we performed real-time kinetic measurements of competition between two reactions at the single-molecule level, and found that this competition affects both the rate and fate of single-molecule amplification. We observed significant heterogeneity in the rate of amplification of individual molecules, both in RT-LAMP amplification of HCV RNA, and in its competition with REs. We found that the introduction of the RE impacts both the rate and the fate of single-molecule amplification. We found a difference in how this competition is reflected in the readouts we used. Both fate and rate can be measured with real-time digital experiments. End-point digital experiments ignore the rate and measure fate, while bulk real-time experiments ignore the fate and rate of the majority of molecules and instead measure the rate and fate of the early amplification events. We demonstrated that both of these simplified measurements could in principle be used to derive genotype information from the competition of amplification and RE

digestion. The advantage of the real-time methodology is that it is well-established and does not require development of microfluidic devices. We, however, prefer the end-point digital format for limited-resource settings: it does not require complex instrumentation for performing kinetic measurements, it is expected to be robust to fluctuation in conditions (although this robustness remains to be studied for competition reactions),^{12,19} and it can be read-out with a cell phone,^{12,20} which we confirmed here as well. Although not described here, research is underway to integrate this method with user-friendly sample preparation techniques to enable full deployment in limited-resource settings.

Further, the end-point digital format gives viral load information directly in the control—although, while digital amplification is often claimed to provide absolute concentration, determining the true concentration of molecules requires carefully measuring and adjusting for the efficiency of the processing and amplification, which we have not investigated in this manuscript. For genotyping, absolute measurements are not required, as only the magnitude of the decrease of digital counts upon introduction of the RE needs to be measured, which essentially sets the requirement for resolution of the platform used. For a specific digital device, resolution and dynamic range (i.e., the range of viral concentrations over which the genotyping measurement can be reliably performed on a given device) are in balance with one another—the lower the requirement for resolution, the larger dynamic range it has. For example, in a published multivolume SlipChip^[15] device, the dynamic range for 5-fold resolution is 67 to 2×10^7 copies/ mL. In this RT-LAMP/RE system, the requirement for resolution is only 10 fold and a better inhibition chemistry would further lower the required resolution and increase the dynamic range of the digital measurement. The results presented in this paper raise a number of additional

questions: What is the right theoretical framework within which to analyze both rate and fate in single-molecule competition reactions? What are the molecular details of the mechanisms responsible for fate and rate determination in such systems? Can robustness of output of these systems be predicted a priori? What are the best amplification and inhibition chemistries with which to implement such competition reactions for genotyping and other genetic analyses?

References

- 1 Martinez, A. W., Phillips, S. T., Whitesides, G. M. & Carrilho, E. Diagnostics for the Developing World: Microfluidic Paper-Based Analytical Devices. *Analytical Chemistry* **82**, 3-10, doi:10.1021/ac9013989 (2009).
- 2 Whitesides, G. M. A glimpse into the future of diagnostics. *Clinical chemistry* **59**, 589-591, doi:10.1373/clinchem.2013.204347 (2013).
- 3 Lavanchy, D. Evolving epidemiology of hepatitis C virus. *Clinical Microbiology and Infection* **17**, 107-115, doi:10.1111/j.1469-0691.2010.03432.x (2011).
- 4 Sheridan, C. FDA approvals usher in the post-interferon era in HCV. *Nat Biotech* **32**, 3-5, doi:10.1038/nbt0114-3 (2014).
- 5 Runyon, M. K., Johnson-Kerner, B. L. & Ismagilov, R. F. Minimal Functional Model of Hemostasis in a Biomimetic Microfluidic System. *Angewandte Chemie International Edition* **43**, 1531-1536, doi:10.1002/anie.200353428 (2004).
- 6 Kastrup, C. J., Runyon, M. K., Shen, F. & Ismagilov, R. F. Modular chemical mechanism predicts spatiotemporal dynamics of initiation in the complex network

- of hemostasis. *Proceedings of the National Academy of Sciences* **103**, 15747-15752, doi:10.1073/pnas.0605560103 (2006).
- 7 White, R. A., 3rd, Blainey, P. C., Fan, H. C. & Quake, S. R. Digital PCR provides sensitive and absolute calibration for high throughput sequencing. *BMC genomics* **10**, 116, doi:10.1186/1471-2164-10-116 (2009).
- 8 Rissin, D. M. *et al.* Single-molecule enzyme-linked immunosorbent assay detects serum proteins at subfemtomolar concentrations. *Nat Biotech* **28**, 595-599, doi:<http://www.nature.com/nbt/journal/v28/n6/abs/nbt.1641.html#supplementary-information> (2010).
- 9 Gansen, A., Herrick, A. M., Dimov, I. K., Lee, L. P. & Chiu, D. T. Digital LAMP in a sample self-digitization (SD) chip. *Lab on a chip* **12**, 2247-2254, doi:10.1039/c2lc21247a (2012).
- 10 Sun, B. *et al.* Mechanistic Evaluation of the Pros and Cons of Digital RT-LAMP for HIV-1 Viral Load Quantification on a Microfluidic Device and Improved Efficiency via a Two-Step Digital Protocol. *Analytical Chemistry* **85**, 1540-1546, doi:10.1021/ac3037206 (2013).
- 11 Tomita, N., Mori, Y., Kanda, H. & Notomi, T. Loop-mediated isothermal amplification (LAMP) of gene sequences and simple visual detection of products. *Nat. Protocols* **3**, 877-882 (2008).
- 12 Selck, D. A., Karymov, M. A., Sun, B. & Ismagilov, R. F. Increased Robustness of Single-Molecule Counting with Microfluidics, Digital Isothermal

- Amplification, and a Mobile Phone versus Real-Time Kinetic Measurements. *Analytical Chemistry* **85**, 11129-11136, doi:10.1021/ac4030413 (2013).
- 13 Kargar, M., Askari, A., Doosti, A. & Ghorbani-Dalini, S. Loop-Mediated Isothermal Amplification Assay for Rapid Detection of Hepatitis C virus. *Indian Journal of Virology* **23**, 18-23, doi:10.1007/s13337-012-0067-2 (2012).
- 14 Nathans, D. & Smith, H. O. Restriction endonucleases in the analysis and restructuring of dna molecules. *Annual review of biochemistry* **44**, 273-293, doi:10.1146/annurev.bi.44.070175.001421 (1975).
- 15 Pompano, R. R., Li, H.-W. & Ismagilov, R. F. Rate of Mixing Controls Rate and Outcome of Autocatalytic Processes: Theory and Microfluidic Experiments with Chemical Reactions and Blood Coagulation. *Biophysical journal* **95**, 1531-1543 (2008).
- 16 Liang, X., Jensen, K. & Frank-Kamenetskii, M. D. Very Efficient Template/Primer-Independent DNA Synthesis by Thermophilic DNA Polymerase in the Presence of a Thermophilic Restriction Endonuclease. *Biochemistry* **43**, 13459-13466, doi:10.1021/bi0489614 (2004).
- 17 Blatt, L. M. *et al.* Assessment of hepatitis C virus RNA and genotype from 6807 patients with chronic hepatitis C in the United States. *Journal of viral hepatitis* **7**, 196-202 (2000).
- 18 <http://hcv.lanl.gov/content/sequence/NEWALIGN/align.html>.

- 19 Shen, F. *et al.* Digital Isothermal Quantification of Nucleic Acids via Simultaneous Chemical Initiation of Recombinase Polymerase Amplification Reactions on SlipChip. *Analytical Chemistry* **83**, 3533-3540, doi:10.1021/ac200247e (2011).
- 20 Martinez, A. W. *et al.* Simple telemedicine for developing regions: camera phones and paper-based microfluidic devices for real-time, off-site diagnosis. *Anal Chem* **80**, 3699-3707, doi:10.1021/ac800112r (2008).

Chapter 7:

Lack of Correlation between Reaction Speed and Analytical Sensitivity in Isothermal Amplification Reveals the Value of Digital Methods for Optimization: Validation Using Digital Real-Time RT-LAMP*

Abstract

In this paper, we asked if it is possible to identify the best primers and reaction conditions based on improvements in reaction speed when optimizing isothermal reactions. We used digital single-molecule, real-time analyses of both speed and efficiency of isothermal amplification reactions, which revealed that improvements in the speed of isothermal amplification reactions did not always correlate with improvements in digital efficiency (the fraction of molecules that amplify) or with analytical sensitivity. However, we observed that the speeds of amplification for single-molecule (in a digital device) and multi-molecule (e.g. in a PCR well plate) formats always correlated for the same conditions. Also, digital efficiency correlated with the analytical sensitivity of the same reaction performed in a multi-molecule format. Our finding was supported experimentally with examples of primer design, the use or exclusion of loop primers in different combinations, and the use of different enzyme mixtures in one-step reverse-transcription loop-mediated amplification (RT-LAMP). Our results show that measuring the digital efficiency of amplification of single-template molecules allows quick, reliable comparisons of the analytical sensitivity of reactions under any two tested conditions, independent of the speeds of the isothermal amplification reactions.

* This chapter was first published in *Nucleic Acids Research* with authorship belonging to Eugenia M. Khorosheva, Mikhail A. Karymov, David A. Selck, and Rustem F. Ismagilov. The original manuscript can be found at: <http://dx.doi/10.1093/nar/gkv877>

Introduction

The detection and quantification of nucleic acids using quantitative PCR (qPCR) amplification^{1,2} has been well established, with published guidelines for protocol optimization,^{3,4} interpretation of reaction kinetics, and accurate results reporting.⁵⁻⁹ Isothermal amplification is an alternative approach for nucleic acid amplification that does not require temperature cycling.¹⁰⁻¹² Many isothermal amplification techniques allow rapid amplification reactions,^{13,14} do not require expensive equipment for thermocycling, allow both simple visual and fluorescence-based multiplex read outs,¹⁵⁻¹⁸ and have the potential to improve diagnostics in point-of-care and limited-resource settings.¹⁹ Nucleic acid quantification using real-time isothermal amplification has been described in many methods, including RPA,²⁰ LAMP,¹⁸ NASBA,²¹ and RCA,²² by interpreting the standard dilution curves of exponential amplification profiles, an approach similar to the well-established one used in qPCR.

Microfluidic methods have contributed to shorter amplification reaction times²³ and reduced reaction volume, and enable digital quantification as an alternative to real time (kinetic) quantification.²⁴⁻²⁶ When the digital method is applied to PCR, absolute and reliable quantification can be achieved.²⁷⁻³⁰ Reliable quantification via digital methods has also been shown for some isothermal amplification reactions, such as RPA,³¹ RT-LAMP and LAMP,^{32,33} and RCA.³⁴ In the digital amplification-on-a-chip format, a solution containing templates is loaded into a device with multiple wells at a low enough volume that each well is likely to contain either 0 or 1 template molecule. Every individual template that amplifies gives rise to a fluorescent signal in its separate well. The number of positive wells can then be counted optically to deduce starting

concentration of the target nucleic acid. If all loaded template molecules amplify, absolute quantification is possible, but this only occurs in well-optimized amplification reactions.²⁸ However, even if not all loaded template molecules amplify, digital quantification still provides precise comparisons of the relative template concentrations.³⁵ The key parameter for evaluating the performance of an amplification reaction is its “digital efficiency,” the percentage of templates that successfully amplify from the total template pool. Digital efficiency impacts assay accuracy (the ability to accurately quantify a loaded number of template molecules), and impacts analytical sensitivity (the ability to detect even a small number of template molecules in a reaction)—the standard parameters in the “Minimum Information for Publication of Quantitative Real-Time PCR Experiments”.⁵ In this paper, we utilize the SlipChip digital platform,^{31,35,36} which allows both single-molecules amplification and real-time monitoring of amplification reactions for each template molecule^{36,37} (Figure 7-1).

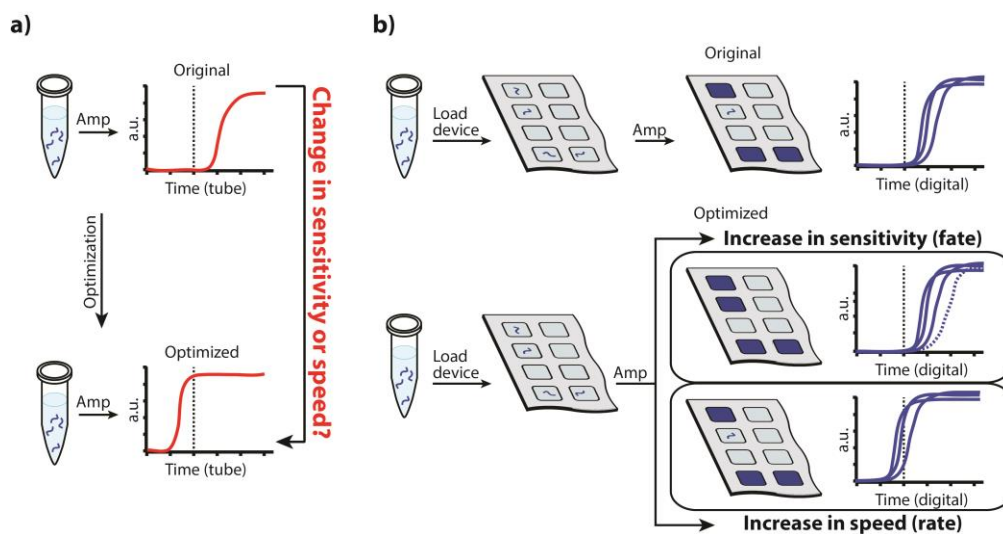


Figure 7-1. A schematic comparison of isothermal amplification in a tube (A), and in a digital single-molecule microfluidic device (B), responding to a change in conditions during optimization. (A) Increased non-digital reaction speed may either indicate a faster amplification of a few successful molecules and their products, or suggest that more template molecules initially participated in exponential amplification—indicating therefore an improved analytical sensitivity. Each template molecule is shown as a blue wavy line, and the accumulation of the amplification product is indicated as the solid red curves on the graphs. (B) The digital single-molecule method allows for independent measurements of reaction rate and analytical sensitivity during amplification of each template molecule (or lack thereof) within each well (squares in the grey device) to give rise to amplification product (blue-filled squares in the device and solid blue curves on the graphs).

During optimization, primer variants and reaction conditions must be compared empirically to ensure the nucleic acid sequences of interest are being detected reliably through amplification. While PCR approaches for selecting the best conditions are well-standardized,¹³ guidelines for optimizing isothermal amplification reactions are not as well developed. As a rule, in qPCR the best primer pair will yield the product with the lowest average cycle threshold (Ct) at equal template concentrations and under identical experimental conditions.³⁸ In qPCR systems, the Ct value is dependent only on amplification efficiency, the number of starting template copies, and background fluorescence. The best primer pair also provides the highest possible analytical sensitivity in a multi-molecule format (e.g. in a PCR tube or well plate) and the highest possible digital efficiency in a digital format.

Reaction speed would seem to be an attractive criterion of efficiency when estimating isothermal amplification reaction performance³⁹ as well as when testing primers and conditions during optimization, as it is more convenient than performing dilutions and determining the limit of detection (LOD, the template concentration that can be detected with reasonable certainty, e.g. 95% confidence⁵) for each condition. However, this

approach, widely used in qPCR, had not been rigorously tested for isothermal reactions, and we predicted that it may not hold for isothermal reactions due to differences in the way isothermal reactions proceed. While isothermal amplification is “chained,” similar to PCR, and exhibits exponential kinetics, there are no cycles defined by temperature. In qPCR, all the steps of amplification are time-synchronized and the number of cycles is counted rather than the absolute time of the reaction being measured. Time is allotted for each process (denaturation, annealing, elongation) in each cycle; if this time is sufficient for each process to complete, one will often not detect any minor differences in the efficiency of each process for amplification of different copies of the template molecule. In contrast, in isothermal reactions all biochemical events take place in parallel and the total time of the reaction is measured rather than the number of cycles. Thus, we hypothesized that changes in kinetics of any of the processes will more noticeably affect the time to threshold in isothermal reactions, compared to qPCR.

There are many factors that could theoretically affect speed and analytical sensitivity in isothermal amplification reactions. Consider these three examples. First, sometimes more than one enzyme is used simultaneously (e.g. in NASBA,²¹ strand displacement amplification (SDA),⁴⁰ helicase dependent amplification (HDA),⁴¹ and isothermal and chimeric primer-initiated amplification of nucleic acids (ICAN)⁴²) and all reverse transcription isothermal amplifications are performed in one step, such as in one step RT-LAMP^{43,44}). Some of these co-occurring biochemical reactions could influence each other in isothermal reactions (similarly to how reverse transcriptase inhibits amplification in the non-isothermal reaction RT-PCR⁴⁵). Second, sometimes numerous annealing events have to be coordinated to prevent them from competing with each other (e.g. in LAMP).

Some annealing events influence the speed of isothermal reactions dramatically, e.g. the annealing of turn back primers,^{46,47} which is required for amplification, and the optional annealing of loop primers¹³ and stem primers⁴⁸ in LAMP. Although the products of amplification from the extensions of two additional loop primers in LAMP do not contribute to the pool of exponentially amplifying DNA sequences nor are they required for the basic amplification mechanism,⁴³ their presence is known to improve reaction sensitivity.¹³ But stem primers' effect on amplification reaction sensitivity has not been addressed in publications. Third, the absence of multiple denaturation steps in isothermal amplification reactions suggests that reaction speed would be dependent on the template's innate secondary structures. Thus, an isothermal reaction's speed and analytical sensitivity are related in a more complex way than in PCR and cannot be predicted *a priori*.

We hypothesize that each component of an ongoing isothermal amplification reaction may potentially affect the reaction in one of the following ways: (i) it may limit the reaction's speed (the time it takes for an amplification reaction to produce a threshold level of signal) (ii) it may influence each single template molecule's "fate" (whether it is amplified giving rise to a detectable signal, or lost from the amplification chain) thus affecting the analytical sensitivity, or (iii) it may affect both the fate and the rate of amplification events.

When isothermal amplification reactions take place in a multi-molecule format (e.g. in a PCR tube or well plate) it is difficult to identify whether a change in time to threshold observed upon a change in primers or reaction conditions is the result of a larger fraction of templates amplifying (improved "fates") or a change in reaction rate only (Figure 7-

1A). In contrast to a multi-molecule format, digital experiments would separately measure the “fate” (expressed as digital efficiency) of template molecules, allowing a more sensitive reaction design (Figure 7-1B). Real time imaging of single-molecule amplification in each well measure both the change in “fates” and also changes in amplification “rates” (expressed as time to positive) as a result of a new primer or reaction condition. Here, we asked whether accelerating isothermal amplification reactions in a multi-molecule format in response to an introduced change in conditions always reflects improved analytical sensitivity and digital efficiency. This is an important question to answer in order to determine whether the standard qPCR approach using kinetics comparisons (speed of amplification) to find the best primers and conditions is also applicable to isothermal reactions. In this paper, we tracked amplification of single template molecules of HCV 5’UTR RNA in real time under several different RT-LAMP conditions, and compared these observations to data on real-time multi-molecule amplification reaction speeds performed in a well plate.

Materials and Methods

Chemicals and materials

All common reagents were purchased from commercial sources with the exception of RTx Bst 2.0 enzyme mixture (provided by New England Biolabs, NEB). Commercial reagents used were the same as described in Sun *et al.* (31), with the exception of SUPERase-In™ RNAase Inhibitor (Ambion by Life Technologies, Carlsbad, CA, USA) and Ultra-Pure distilled DNAses and RNAses free water (Invitrogen by Life Technologies, Carlsbad, CA, USA).

RNA template

AcroMetrix® HCV-S panel RNA was extracted either with the QIAamp Viral RNA Mini Kit (QIAGEN Inc., Valencia, CA, USA) or with Maxwell® 16 Viral Total Nucleic Acid Purification Kit (Promega, Madison, WI, USA) according to the manufacturer's instructions. Nucleic acid extractions were immediately diluted using Ultra-Pure distilled DNAses and RNAses free water (Invitrogen), partitioned into about 100 separate 10 µL aliquots and stored at -80° C. Each 10 µL aliquot was further diluted and re-aliquoted to use as a template in RT-amplification. RNA fragment sequence was determined using RT-PCR reaction and Laragen Inc sequencing services. RNA concentrations were estimated through RT-PCR as described below.

Estimation of HCV RNA concentration using RT-PCR amplification on the SlipChip device

HCV viral RNA was added to the RT-PCR mix contained the following: 20 µL of 2X SsoFast EvaGreen SuperMix, 1.0 µL of each primer (10 µM/L), 2.0 µL of BSA solution (20 mg/mL), 1.0 µL of SuperScript® III Reverse Transcriptase, 1.0 µL of SUPERase-In™ RNAase Inhibitor, 13 µL of nuclease-free water, and 1 µL of template solution. RT-PCR primers used for HCV RNA template quantification were described previously^{36,49}. The amplifications were performed using SlipChip devices and a custom built real-time instrument, using the following protocol: an initial 15 min at 50° C was applied for reverse transcription, then 2 min at 95° C for enzyme activation, followed by 40 cycles of 1 min at 95° C, 30 sec at 55° C and 45 sec at 72° C. Images of all 1,280 wells on each device were acquired for each cycle at 72° C. After the final cycle, a final elongation step was applied for 5 min at 72° C. This thermal cycling program was applied to all real-time

digital experiments except for those done with end-point read-out on the PCR master cycler machine (Eppendorf) where 33 cycles were selected as a single end-point imaging cycle. End-point readout was done as described previously³⁶. At least six RT-PCR amplification reaction replicas on SlipChip devices were done to determine RNA concentration, and this concentration was used as a reference for all the future experiments.

Real time and real time digital measurements

To confirm that time to threshold values (Ct) in a digital format correlates with the Ct in a multi-molecule format, we used custom-built real-time instrument imaging and software that allowed us to observe the process of amplification in each well initially containing a single template molecule. SlipChip devices have been used most often to see only the end-point amplification in each well. Here, we used real-time imaging of the chip³⁷ to track the amplification progress of each well in real time and record amplification curves, as described below. We used digital measurements of digital efficiency, real-time digital measurements of both digital efficiency and reaction rates, and then compared these results to real-time kinetic measurements performed in a well plate, done in parallel for each condition tested. Due to heterogeneity among the rates of amplification of different molecules the reported “time to positive” in the digital experiments was selected as the time to a fluorescent signal in a first positive SlipChip device well (or the first few wells when they show a positive signal simultaneously), which is immediately followed by the appearance of a subsequent series of signals from other positive wells.

Fabrication and design of the SlipChip device

The SlipChip used was fabricated, cleaned, assembled, and loaded as described previously^{32,50}. The device contained a total of 1,280 wells etched to a depth of 55 μm for a loading well volume of 3 nL on each side (6 nL when device is loaded from both sides); however, devices were always loaded from one side and the second half was filled with oil and used for a thermo-expansion volume⁵¹.

Real-time digital imaging

Real-time digital experiments were performed on a custom-built instrument that uses a Bio-Rad PTC-200 thermocycler with a custom machined block for thermal control/incubations at chosen temperatures. The block has a flat 3 in x 3 in area that accommodates microfluidic devices. The excitation light source was a Philips Luxeon S (LXS8-PW30) 1315 lumen LED module with a Semrock filter (FF02-475). Image Acquisition was performed with a VX-29MG camera, a Zeiss Macro Planar T F2-100mm lens, and a Semrock filter (FF01-540) for emission.

Real-time digital analysis

Acquired images were analyzed using custom LabVIEW software. The data were analyzed by first creating a mask that defined the location of each reaction volume in the device. The masked spots were then used to extract the average intensity information of each digital well over the course of the experiment. Threshold was then manually set as half the height of the averaged and background-corrected maximum intensity, and the time to positive of each reaction was determined as the interpolated point at which the real-time curve crossed the defined threshold. Poisson statistics were used in automated

software calculations of the loaded template concentrations, based on the percentage of wells that showed template presence.

RT-LAMP primer design, and primer sets used

For primer design we used Oligo 7.0 software (Cascade, CO, USA); alignment of available HCV 5'UTR sequences was done using Geneious 6.1.6 software (Biomatters Ltd, Auckland, NZ) to select the most conserved fragments to position the 5' and 3' ends of FIP and BIP. HCV 5'UTR fragment of interest secondary structure has been evaluated at different temperatures using NuPack, as RNA and as both single strands DNA form⁵².

We followed recommendations on LAMP primer design from the Guide to LAMP Primer Designing on the EIKEN web site⁵³ and used the primers in recommended relative concentrations ranges⁴³. A few primer variants were experimentally tested via digital efficiency evaluation, and compared with HCV “best published primers” (BPP) from the literature⁵⁴. We designed back primers (BIP, loopB and B3) ourselves and we modified the BPP set forward primers (FIP, loopF and F3) to design our versions to place the important primer parts into the most conservative HCV sequence alignment fragments. We tested all planned primer alterations for forward and back primers independently, introduced them one by one, and measured the relative change in digital efficiency for at least three replicates, and used the BPP set performance in dRT-LAMP as a reference. We selected the primers with the highest digital efficiencies in dRT-LAMP amplification reactions and we named this set “digitally optimized primers” (DOP):

BIP 5'-TTGGGCGTGCCCCCGCAAGTT

TTCAGTACCACAAGGCCTTTCGCGACC-3'

FIP 5'-TCCAAGAAAGGACCCGGTCTTTTT
CTGCGGAACCGGTGAGTAC-3'

LoopB 5'-CTGCTAGCCGAGTAGTGTTG-3'

LoopF 5'-GTCCTGGCAATTCCGGT-3'

F3 5'-CCTCCCGGGAGAGCCATAG-3'

B3 5'-GCACTCGCAAGCACCTATC-3'

The same DOP set, modified to determine four circulating HCV genotypes by incorporation inosine bases, was used previously ³⁷.

Four variants of DOP set were designed for testing the correlation of the speed and sensitivity of isothermal amplification. Through elongation of the F1c part of FIP, we designed “long FIP” (LFIP) primer 5'-

GGTTGATCCAAGAAAGGACCCGGTTTTTCTGCGGAACCGGTGAGTAC-3' to use in a model DOP-LFIP primer set. Through elongation of the B1c part of BIP primer we designed “long BIP” (LBIP) primer 5'-

GAGATTTGGGCGTGCCCCGCAAGTTTTTCAGTACCACAAGGCCTTTCGCGAC C-3' to use in a model DOP-LBIP set. The variants of the DOP sets “no loop F” (DOP-NLF) and “no loops” (DOP-NL) were used to test the effect of loop primer presence on the speed and sensitivity of amplification. The DOP-NLF set was the same as the DOP but the loopF primer was excluded (only loopB primer was present). The DOP-NL set was the same as the DOP set but lacked both loopB and loopF primers.

RT LAMP primers and conditions

Digital RT-LAMP using SlipChip device, and RT-LAMP in a well plate were performed with all the primer set variants in one step as described previously³⁷, with the following modifications: We used 1.7 μL of enzyme in 40 μL of total reaction mixture instead of 2 μL , and standard 3 μL of Acrometrix HCV-s RNA template solution (or nuclease-free water for negative controls). In all the primer sets, both the B3 and B2 parts of BIP served as gene-specific primers for reverse transcription. Enzymes tested were: 1) EM (EIKEN), used for all the experiments, and 2) A mix of Bst 2.0 (NEB) with an experimental lot of NEB RNaseH active thermostable reverse transcriptase Rtx used only for one experiment on comparison different enzymes (Fig. 7-5). Amplification products detection was performed with calcein (FD)(EIKEN). Real-time bulk RT-LAMP data analysis was done as described previously³⁷.

Results

To test whether reaction rate and digital efficiency always correlate in the case of isothermal reactions, we used digital amplification on SlipChip to reanalyze two common approaches believed to improve performance of LAMP: (i) selecting primers in the recommended melting temperature (T_m) ranges to ensure correct annealing order⁴³, and (ii) using loop primers to increase speed and sensitivity¹³. First, we used the digital optimization process described in this paper to optimize a set of primers, which we call “digitally optimized primers” (DOP). In the comparisons of speed and efficiency, we compared this DOP set to four other primer set variants: DOP with an elongated BIP primer (DOP-LBIP), DOP with an elongated FIP primer (DOP-LFIP), DOP with no loopF primer (DOP-NLF), and DOP with no loops (DOP-NL). We also tested for a

correlation between digital efficiencies and rates of reactions performed with each of two variants of reverse-transcriptase/Bst polymerases enzymes mixtures.

The effect of turn back primers (FIP and BIP) on amplification speed and sensitivity.

We compared the reaction rates and digital efficiencies of reactions using DOP and those using either the DOP-LBIP primer set or the DOP-LFIP primer set. The rationale for this experiment is that we assumed that the order of the primer annealing in a LAMP reaction strongly affects digital efficiency (Figure 7-2). Ideally, F1c and B1c anneal first, F2 and B2 anneal second, and F3 and B3 anneal last. These considerations are in line with the recommendations listed in a Guide to LAMP Primer Designing⁵³.

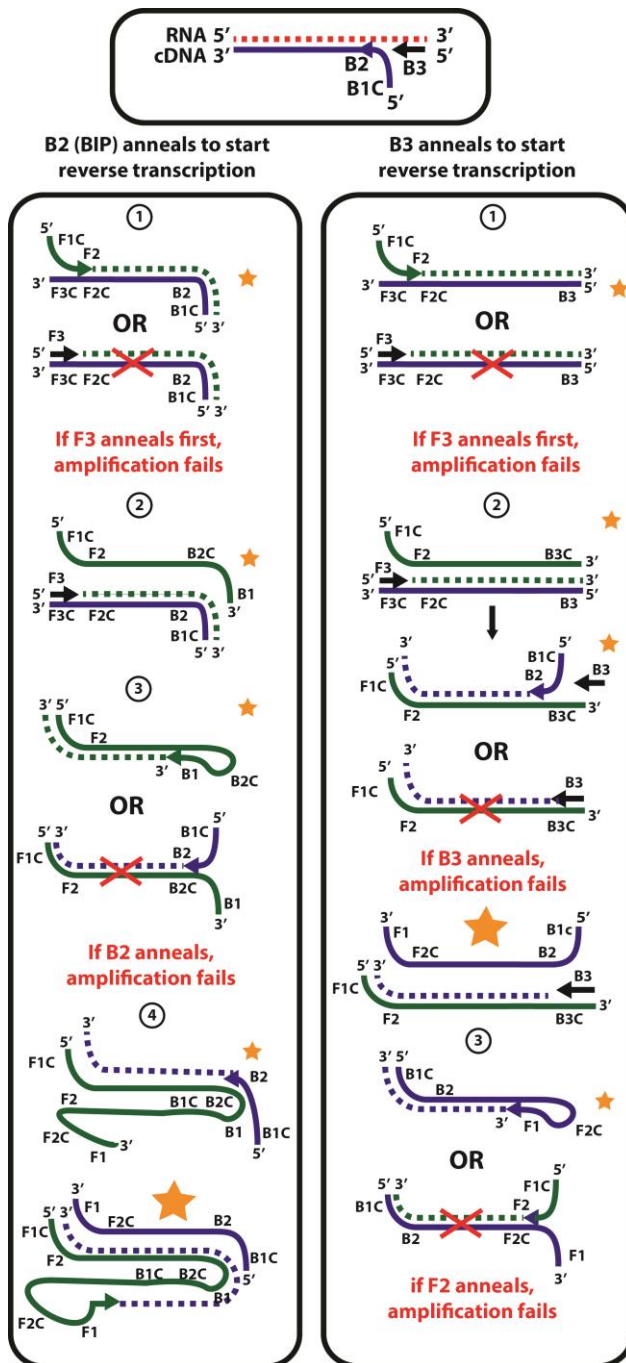


Figure 7-2. Diagram of annealing events during RT-LAMP amplification. Synthesis of cDNA starts either from the B3 primer or from the BIP primer (which consists of B2 and B1c fragments). The RNA template is degraded through RNaseH activity of reverse transcriptase. Afterward, competition between different primers' annealing occurs, affecting the "fate" of each cDNA molecule and its products (i.e. whether they will remain in or be excluded from the pool of amplifying molecules). F1 and B1 annealing

should occur before the F2 and B2 annealing, and B2 and F2 annealing should occur before B3 and F3 annealing for optimal amplification.

Primer annealing to template depends on each primer's T_m and the template's secondary structure. The interplay of these two factors is addressed through the concept of net T_m , which is the temperature at which half of the template is bound by the oligonucleotide^{55,56}. While we do not know the exact secondary structure of a LAMP amplicon under reaction conditions, we modeled the predicted secondary structure for our amplifying DNA fragment using NuPack software.⁵² This modeled secondary structure appears to be very similar to the published secondary structure for HCV 5'UTR RNA.^{57,58} It's possible that making B1c and F1c longer in LBIP and LFIP not only increased the primers' T_m (Table 7-1), but also affected their net T_m as a result of positioning the B1c and F1c ends into template regions that were richer in secondary structures. Additionally, making B1c and F1c longer may have affected the probability of non-paired state at the 5'-end regions of the turn back primers, which is known to influence amplification.⁴⁶ If secondary structures are significantly more abundant in the template fragments, only empirical testing can verify that primers work better after optimization via increased calculated T_m .

Table 7-1. Annealing sequences of the standard primer set and the elongated primer variants, the nucleotide sequence, and the melting temperatures (T_m) at a standardized concentration of primers.

Annealing sequence	Nucleotide sequence (5' to 3')	T_m
F1c of FIP (as in DOP)	TCC AAG AAA GGA CCC GGT C	68.4° C

F1c elongated (of FIP) to use in DOP-LFIP	GGT TGA TCC AAG AAA GGA CCC GG	70.7° C
F2 (of FIP)	T CTG CGG AAC CGG TGA GTA C	70.2° C
F3	CCT CCC GGG AGA GCC ATA G	65.9° C
B1c of BIP (as in DOP)	TTGGGCGTGCCCCCGCAAG	73.7° C
B1c elongated (of BIP) to use in DOP-LBIP	GAGATTTGGGCGTGCCCCCGCAAG	76.3° C
B2 (of BIP)	CAGTACCACAAGGCCTTTTCGCGACC	73.7° C
B3	GCACTCGCAAGCACCTATC	66.0° C

In our experiments, for both DOP-LFIP and DOP-LBIP primer sets, elongation of FIP or BIP primers led to a drop in digital efficiency compared to the DOP set. For DOP-LFIP, the digital efficiency dropped by $40\% \pm 6\%$ (S.E.) of DOP ($P = 2.4 \times 10^{-4}$) and for DOP-LBIP the digital efficiency dropped by $34\% \pm 5\%$ ($P = 3.7 \times 10^{-3}$) (Figure 7-3B).

However, the change in reaction speed was different for the two primer sets. In the case of elongated BIP, the drop in efficiency was accompanied by a decrease in speed (longer time to positive), as would be expected in analogy to qPCR. Here, time to positive increased from $18.6 \text{ min} \pm 0.1$, to $21.4 \text{ min} \pm 0.2$ ($P = 1.7 \times 10^{-11}$). Surprisingly, in the

amplification reaction using elongated FIP, the drop in efficiency was not accompanied by a change in time to positive; the DOP-LFIP time to positive was similar to DOP, 18.7 min \pm 0.2 ($P = 0.585$) (Figure 7-3A). Thus, reaction speed and digital efficiency do not always correlate in isothermal amplification reactions.

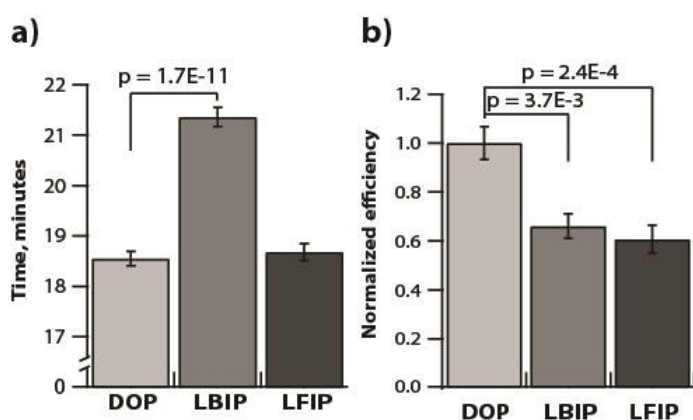


Figure 7-3. Comparison of time to positive and RT-LAMP reaction efficiencies for the “digitally optimized primers” (DOP) set and the elongated BIP and FIP sets (DOP-LBIP and DOP-LFIP) through real-time measurements of reaction speeds (time to threshold values in min) and real-time digital measurements of the template molecules’ “fates” (expressed as normalized digital efficiencies). (A) Plot comparing times to positive in multi-molecule experiments for standard and elongated BIP and FIP primers with 5’ ends placed into the secondary structures. $N = 9-24$; (B) Plot of normalized relative digital efficiencies for single-molecule experiments using standard and elongated BIP and FIP primers. P-values are above brackets and error bars designate S.E.; $N = 3-8$.

These results suggest that selecting primers for LAMP in the recommended T_m ranges isn’t enough to ensure better reaction performance, as in one case we observed a drop in reaction speed and in both cases we observed a decreased ability to determine template concentrations with high sensitivity (detected as a drop in a digital efficiency).

Measurements of reaction speed alone did not allow a reliable comparison of the tested primers, whereas digital measurements of the cumulative fates of the template molecules (Figure 7-3B) provided a tool for a direct comparison of primers efficiencies. These

experiments specifically show that, in some cases, two isothermal reactions performing at the same speed may differ in their digital efficiencies.

The effect of loop primer presence on amplification speed and sensitivity.

We compared the effect of loop primers on digital amplification efficiency, as well as on the speed of the reaction in both digital and multi-molecule formats, using the DOP set and its two variants: the DOP set with no loops (DOP-NL) and the DOP set with no loop F (DOP-NLF). The DOP-NL set was significantly slower and about half as efficient $53\% \pm 2\%$ (S.E.) as the DOP set. The average times to positive in the reaction with DOP were $18.5 \text{ min} \pm 0.1 \text{ min}$, and those with DOP-NL were $37.4 \text{ min} \pm 0.7$ (Figures 7-4A,7-4B). This result supports the published observation¹³ that using loop primers improves primarily the speed of the reaction and also its sensitivity.

When we compared the primer set with no loop F (DOP-NLF) to the DOP set, which contained both loops, we found that the speed of the reaction with DOP-NLF ($23.2 \text{ min} \pm 0.2$) was about 4.7 min slower than the DOP set ($18.5 \text{ min} \pm 0.1 \text{ min}$; $P = 3.1 \times 10^{-4}$) (Figure 7-4A). However, surprisingly, the digital efficiencies did not differ significantly between the DOP and DOP-NLF sets ($P = 0.37$). This comparison of the corresponding reaction efficiencies showed that the presence of only one loopB primer was sufficient to maintain the same ability to determine template concentrations with high sensitivity (detected as digital efficiency), as with both loop primers, despite the drop in reaction speed (Figure 7-4B).

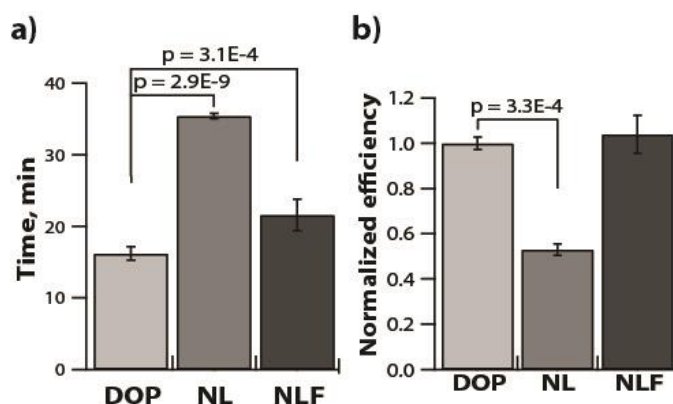


Figure 7-4. Real-time measurements of reaction speeds (time to threshold values in min) and real-time measurements of single molecule amplification fates (expressed as normalized digital efficiencies). (A) Plot comparing times to positive in a well plate for the “digitally optimized primers” set and the DOP set with no loop primers (DOP-NL) and the set with no loop F primer (DOP-NLF), $N = 12-24$. (B) Normalized relative digital efficiencies with DOP and DOP-NL and DOP-NLF. Significant P-values are designated above the brackets; error bars are S.E.; $N = 4-8$.

The lack of correlation between reaction speed and efficiency in the case of only loopB primer presence in the reaction mixture, may be partially explained by the fact that the products of loop primer amplification by design¹³ cannot efficiently participate in subsequent exponential amplification. Despite having a primary “signal amplifying” function, loop primers still improve digital efficiency (Figure 7-4B), which is in agreement with previous work showing their positive effect on sensitivity¹³. For the first time we show that despite a drop in reaction speed, having just one loop primer in a reaction mixture is sufficient to maintain the high digital efficiency seen in experiments containing both loop primers. Measurements of speed alone did not allow reliable detection of the changes in sensitivity that resulted from different loop primers being present, whereas digital measurements of the cumulative fates of the template molecules (Figures 7-4B) provided a tool for a direct detection of the changes. These experiments

specifically show that, in some cases, two isothermal reactions performing at the same digital efficiency may differ in their reaction speeds.

The effect of using different enzyme mixtures on amplification speed and sensitivity.

We also tested whether different enzyme mixtures affected reaction speeds and digital efficiencies in a correlating way. Reverse transcription adds a few uncertainties to subsequent amplification outcomes. First, its efficiency directly affects the fate of RNA molecules—whether they are reverse transcribed and used as cDNA copies in a subsequent amplification chain, or lost from the template pool. Second, the temperature at which different enzymes exhibit optimal activity affects the outcome of reverse transcription of the secondary structure-rich templates⁵⁹, especially when gene-specific primers are used, or when reaction is done as a one-step RT-LAMP performed at 63° C. Third, reverse transcriptase may interfere with polymerase performance⁴⁵, as reverse transcriptase binds to the primers/DNA complexes and may also exhibit some limited DNA/DNA polymerase activity.

We used digital amplification to test an enzyme mixture of RNaseH active thermostable reverse transcriptase RTx and Bst 2.0 polymerase enzymes (from NEB). Our preliminary check of performance of this enzyme mixture showed later times to positive compared to an analogous reaction using a commercial enzyme mixture (EM, from EIKEN).

However, when we tested how many HCV RNA templates were correctly detected from a known number of loaded RNA templates, we discovered that despite being slower than EM, the RTx Bst 2.0 enzyme provided higher digital efficiency (Figure 7-5). These data show once again that isothermal reaction speed and efficiency do not always correlate,

and could be untangled using digital measurements of the cumulative fates and rates of the template molecules (Figures 7-5A), but not using multi-molecule format alone.

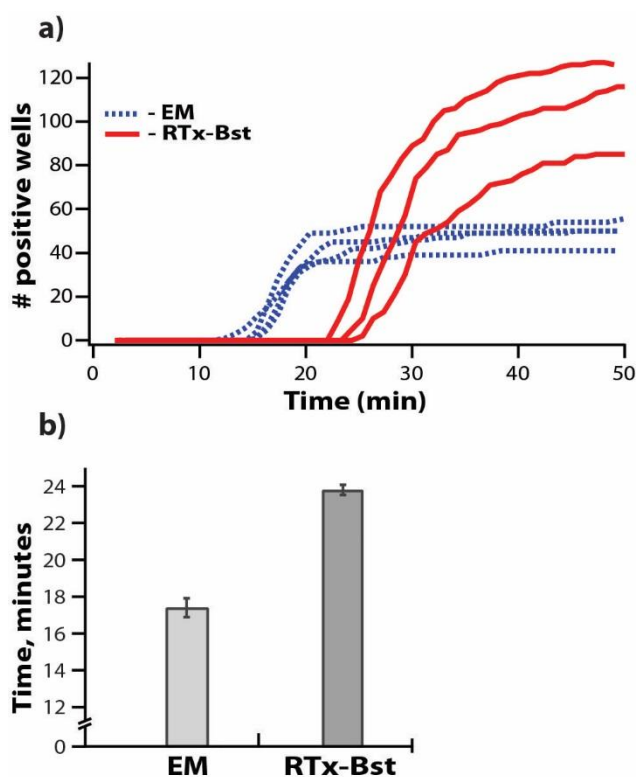


Figure 7-5. Comparison of the effect of two different RT-LAMP enzyme mixtures on amplification using (A) real time, digital single-molecule and (B) real time bulk approaches. (A) Real-time digital measurements of single-molecule amplification fates and rates in a microfluidic device shown as the number of wells that reached a signal threshold over time in each experiment (N=3). We compared a commercially available enzyme mixture (EM, blue dashed lines) and an experimental lot of RTx Bst 2.0 enzyme mixture (red solid lines). (B) Real-time measurements of reaction speeds (time to threshold in min) in a multi-molecule format. In all enzyme experiments we used DOP primers with an FIP primer identical to the one from the BPP set. Error bars are S.E. and N=3.

Characterizing “digitally optimized primers” (DOP) and “best published primers” (BPP) using digital experiments and experiments in a multi-molecule format.

To address whether digital efficiency correlates with analytical sensitivity (measured using multi-molecule format), we compared the DOP set to a set of primers taken from

the literature for HCV 5'UTR RNA, which we refer to as "best published primers" (BPP)⁵⁴. We used digital measurements of efficiency, and real-time digital measurements of both efficiency and reaction speed. We also did real-time kinetic measurements of reaction speed and determined analytical sensitivity (determined as the limit of detection, LOD) in a multi-molecule format using standard PCR well plates for each condition. We found good agreement between digital efficiency and LOD measured in well plates for both the DOP and BPP sets. The normalized BPP digital efficiency measured in a microfluidic device was 34% of the DOP digital efficiency (Figure 7-6A) ($P = 1.05 \times 10^{-6}$). In the multi-molecule format, the LOD for the BPP set was determined to be 75 template copies/10 μ L, while the LOD for DOP set was found to be 18 copies/10 μ L (Figure 7-6C). The LOD values in PCR tubes and digital efficiencies measured in microfluidic devices correlated well in this example. At a very low template concentration of ~ 1.2 copy/10 μ L, the DOP set enabled detection of 44% of the wells in the well plates, whereas there were no positive signals detected at the same template concentration with the BPP set (Figure 7-6C), which is a result of the higher analytical sensitivity of the DOP set.

To ensure that in all cases the results of the reactions in digital format were in accordance with those of reactions performed in a multi-molecule format, we measured the absolute time of the reaction in both formats (Figure 7-6D). The single-molecule enzymatic reaction start time was stochastic. Due to heterogeneity among the rates of amplification of different template molecules, the reported "time to positive" in the digital experiments was defined as the time to the first positive well (fluorescent signal) in a microfluidic device that was immediately followed by a subsequent series of signals from other

positive wells. We found that for all primers used in our experiments under similar conditions, the times to positive in a digital format in a microfluidic device correlated well with the times to positive in multi-molecule reactions performed in a PCR well plate (Figure 7-6D). Our data indicate that the digital format resulted in a faster readout (Figure 7-6D), which is consistent with the higher concentration of template molecules in the digital reactions. While we started with identical solutions for multi-molecule and digital experiments, the effective concentration of single template molecules confined in microfluidic wells on a digital microfluidic device was ~5 times higher than the concentration of the templates in corresponding reactions performed in a PCR well plate, because ~80% of wells on the digital device lacked template molecules and therefore all of the template molecules were concentrated into the ~20% of the wells. This correlation (Figure 7-6D) between the times to positive of multi-molecule reactions and earliest amplification reactions in corresponding digital experiments³⁷ is consistent with the “winner takes all” dynamics in multi-molecule amplification: the products of the first few successful amplification events become the primary source of amplicons for subsequent exponential reactions. We also plotted the average times to threshold values for BPP, DOP, and DOP-NLF sets to illustrate that the relative efficiency of a primer set cannot be deduced through reaction speed alone (Figure 7-6B). Time to positive signal was shorter for DOP (18.5 min \pm 0.1) compared to BPP (21.9 min \pm 0.2) sets, but the DOP NLF set had a longer times to positive (23.2 min \pm 0.2), although the DOP NLF set had the same efficiency as the DOP set (Figure 7-4B).

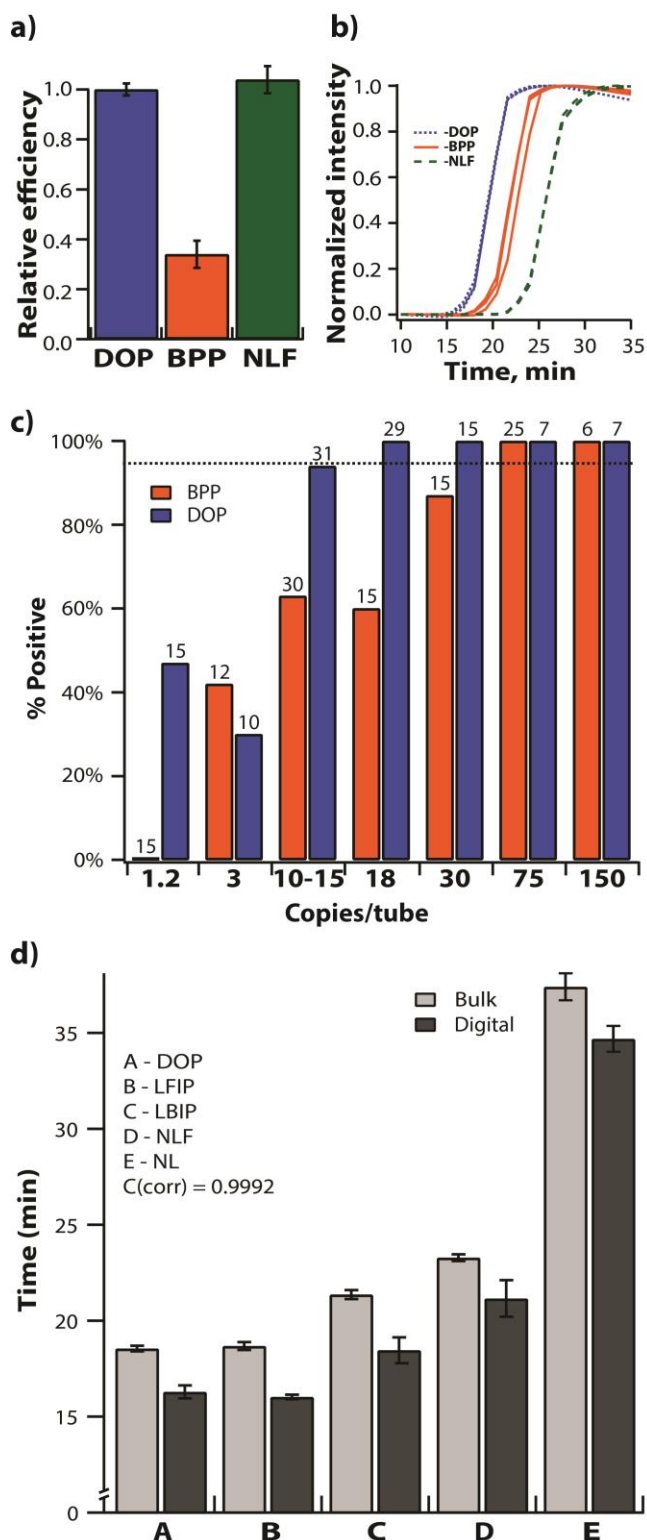


Figure 7-6. (A) The digital efficiency of the “best published primers” (BPP) set normalized to the “digitally optimized primers” (DOP) set, $N = 6$. (B) Normalized fluorescence intensity over time for amplification using the BPP (orange lines), DOP

(blue lines) and DOP-NLF (green dashed lines) sets, $N = 3$ (C) Percent of positive wells in a PCR well plate at different template concentrations with the DOP and BPP sets (N indicated above each bar). (D) Measured times to positive of LAMP reactions in a multi-molecule format in PCR well plates (light grey) and in the digital format on a microfluidic device (dark grey) for all primer sets. Error bars indicate S.E., $N = 4-8$ in digital; $N = 16-40$ for well plates.

Digitally optimized primers had better analytical sensitivity compared to the best published primers set. The LOD for the DOP set was 18 molecules in 10 μL , while the LOD for the BPP set was 75 template molecules in 10 μL . However, in our multi-molecule format experiments, before we could determine these LOD values with statistical significance we had to test 104 PCR wells for the DOP set and 103 PCR well plate wells for the BPP set. In contrast, in the digital experiments comparing DOP and BPP sets, just one device per condition was enough to observe clear differences in the sensitivity of detection of loaded templates, and additional replicates confirmed statistical significance.

Discussion

Isothermal reactions provide a useful tool for nucleic acid amplification tests, particularly in point-of-care settings. Designing reliable tests requires finding the best isothermal amplification primer variants and reaction conditions. The digital format provides an invaluable tool for assessing the efficiency of an isothermal amplification reaction by directly detecting the percentage of successfully amplified template molecules from the known number of loaded template molecules. Our results show that digital efficiency correlates with analytical sensitivity, and that amplification reaction speed in a digital format correlates with reaction speed in a multi-molecule format (e.g. in a PCR well plate or tube). Thus, observations made about digital efficiency and reaction speed in nanoliter-

scale volumes are directly applicable to the same reactions performed in a large-volume, multi-molecule format.

Applying the digital method to isothermal amplification experiments revealed a number of surprising results that contradict the intuition derived from qPCR experiments. First, and perhaps most interestingly, reaction speed does not correlate with digital efficiency (and analytical sensitivity) in isothermal amplification reactions. Specifically, testing FIP and BIP primer variants showed that the digital efficiency in one-step RT-LAMP reactions may be significantly higher for one of the tested primer variants, even without an observed change in the speed of the reaction (Figure 7-3). We also found a lack of correlation between speed and sensitivity (digital efficiency) in the experiments using different enzymes mixtures, where we observed reactions with higher digital efficiency having substantially longer times to positive (Figure 7-5).

Digital experiments confirmed that the presence of two loop primers in the LAMP reaction mixture slightly improved sensitivity to determine template concentration, in addition to their primary function of accelerating the accumulation of amplification products¹³. However, an unexpected result was that having just one loop primer in a reaction mixture was sufficient to maintain the same improved digital efficiency, despite the expected partial drop in reaction speed compared to reactions containing both loops (Figure 7-4).

We conclude that the well-known qPCR approach for selecting optimal primers and conditions based on earlier times to positive is not applicable to all isothermal amplification reactions. In all of the reaction conditions we tested, deriving conclusions about optimization based only on observed changes in reaction speed could have been

misleading. As a consequence, a kinetic-based evaluation of an isothermal reaction's performance (e.g. an evaluation based on the proposed isothermal doubling time (IDT) parameter³⁹, would not discriminate between a slow, sensitive reaction, and a less sensitive (e.g. inhibited) reaction. Therefore, faster reaction speed is not an appropriate way to determine better reaction conditions or primers in the case of isothermal amplification reactions. Detailed analyses of optimization process are typically not reported for new assays. The final analytical sensitivities of newly developed isothermal assays are either reported through LOD⁶⁰ or more typically evaluated by using 10-fold serial template dilutions that are then compared to the sensitivities of a standard PCR method as a way to demonstrate the value of each developed isothermal test⁶¹⁻⁶³.

An alternative approach to accurately evaluate different primer variants or conditions used in isothermal reaction is to perform experiments to estimate a limit of detection (LOD)⁵ in a multi-molecule format for each introduced change in reaction conditions. However, this approach has a number of disadvantages: (i) sometimes a single introduced change in conditions may only slightly affect analytical sensitivity (ii) some introduced changes may have cumulative or interactive effects on analytical sensitivity, (iii) LOD experiments are not easy to perform at low dilutions especially for RNA due to its potential degradation, (iv) experiments must be done side-by-side for both tested conditions to exclude variation related to reagent freshness and reaction setups, and, as emphasized below (v) a large number of replicates is required to establish statistical power.

Using digital methods during optimization can be a reliable tool for finding primers and conditions that allow the best analytical sensitivity in a standard multi-molecule format—

providing faster results and requiring lower replication. To further illustrate the advantage of digital measurements in optimization, we performed a back-of-envelope analysis of a question: How many experimental replicates are needed (i.e. what is the “sample size” necessary) to distinguish a change in digital efficiency (Target Difference, TD) between two reaction conditions in a digital format? We sought to answer this question in a way that would be applicable to both single-molecule amplification (e.g. digital formats) and multi-molecule amplification (e.g. in a PCR tube or well plate). In both cases, we calculated the minimum number of replicates (N) required to differentiate with statistical power which reaction had higher digital efficiency.

First, in the context of digital experiments, we calculated the standard deviation for the number of positive wells in a single device^{36,64,65}. For a device with 1,280 wells of 3 nL and a concentration of 5×10^4 molecules/mL, the standard deviation σ of $\ln(\lambda)$ is 0.075 (Eq. 1):

$$\sigma = \frac{1}{\lambda v \sqrt{\frac{n}{e^{v\lambda} - 1}}} \quad (\text{Eq. 1})$$

Here, λ is the concentration in molecules/mL, v is the well volume in mL, and n is the total number of wells in the digital device. We calculated TD as an absolute difference between the natural logarithms of two measured efficiencies (for this example a 20% difference in efficiency was selected), to match standard deviation. Next, we calculated the standardized difference, $SD = 2.98$, from:

$$SD = \frac{TD}{\sigma} \quad (\text{Eq. 2})$$

Finally, we calculated the minimum number of experimental replicates (N) required to achieve the TD ⁶⁶:

$$N = \frac{2}{SD^2} \times C_{p,power} \quad (\text{Eq. 3})$$

Here, $C_{p,power}$, a constant defined by the combination of P-value (typically set to 0.05) and statistical power (set to 95%), is equal to 13.0⁶⁶. Under these assumptions, $N \sim 3$ (2.93), or only three SlipChip devices for each of the two conditions being compared are necessary to establish a 20% difference in detection efficiency between these reactions with 95% confidence and a P-value of 0.05. To establish a 25% difference in efficiency with the same parameters, we would need only $N \sim 2$ (1.76) SlipChip devices.

Next, using the same approach, we calculated the theoretical number of replicates needed to achieve this level of statistical power in a standard, multi-molecule reaction when using ~ 1 template copy per reaction (Eqs. 1-3). If one uses 10 wells (of 10 μL each in a well plate) per experiment, each loaded with 1 template molecule/well, 90 independent trials would be necessary, for a total of 900 reactions per condition (or 9 trials using 100 tubes each) which is impractical. Pragmatically, experiments are not done on this scale and therefore it has not been possible to optimize reactions by directly measuring small differences in detection efficiency, whereas digital experiments open this possibility.

The digital format provides accurate measurements of reaction efficiency, independent of reaction speed and we suggest that it provides an efficient tool for optimizing new assays based on isothermal amplification reactions. Isothermal amplification chemistries beyond RT-LAMP should also be tested for the lack of correlation between reaction speeds and analytical sensitivities. We anticipate that the use of digital methods will be

useful both to understand mechanistic details of various isothermal amplification reactions and to improve these reactions for practical applications.

Acknowledgements

We thank Dr. Nathan Tanner for providing the New England Biolabs enzyme system RTx Bst 2.0 specially designed for performing RT-LAMP reactions in one step; Matthew S. Curtis for HCV LAMP amplicon secondary structure predictions; Jesus Rodriguez-Manzano for his advice and help with bioinformatics and for independent validation experiments; and Natasha Shelby for contributions to writing and editing this manuscript. Disclosure: R.F.I. has a financial interest in SlipChip Corp.

Funding

This work was supported in part by DARPA Cooperative Agreement No. HR0011-11-2-0006, National Institutes of Health grant R01EB012946; the NIH Director's Pioneer Award DP1OD003584; NIH NRSA training grant 5T32GM07616NSF (to D.A.S.); and the Caltech Innovation Initiative CI2. The content of this article does not necessarily reflect the position or the policy of the Government, and no official endorsement should be inferred.

References

- 1 Heid, C. A., Stevens, J., Livak, K. J. & Williams, P. M. Real time quantitative PCR. *Genome Research* **6**, 986-994, doi:10.1101/gr.6.10.986 (1996).
- 2 Higuchi, R., Dollinger, G., Walsh, P. S. & Griffith, R. Simultaneous amplification and detection of specific DNA-sequences. *Bio-Technology* **10**, 413-417, doi:10.1038/nbt0492-413 (1992).

- 3 Pfaffl, M. in *A-Z of quantitative PCR* (ed Stephen A. Bustin) Ch. Chapter 3 , pages 87 - 112 (International University Line (IUL) 2004).
- 4 Nolan T., B. S. *PCR Technology: Current Innovations, Third Edition*. 457 (CRC Press, 2013).
- 5 Bustin, S. A. *et al.* The MIQE Guidelines: Minimum Information for Publication of Quantitative Real-Time PCR Experiments. *Clinical Chemistry* **55**, 611-622, doi:10.1373/clinchem.2008.112797 (2009).
- 6 Schmittgen, T. D. Real-Time Quantitative PCR. *Methods* **25**, 383-385, doi:<http://dx.doi.org/10.1006/meth.2001.1260> (2001).
- 7 Klein, D. Quantification using real-time PCR technology: applications and limitations. *Trends in Molecular Medicine* **8**, 257-260, doi:10.1016/s1471-4914(02)02355-9.
- 8 Wittwer, C., Hahn, M., and Nakagawara, K. *Rapid Cycle Real-time PCR: Methods and Applications*. (Springer, 2004).
- 9 Tichopad, A., Dilger, M., Schwarz, G. & Pfaffl, M. W. Standardized determination of real-time PCR efficiency from a single reaction set-up. *Nucleic Acids Research* **31**, e122, doi:10.1093/nar/gng122 (2003).
- 10 Gill, P. & Ghaemi, A. Nucleic acid isothermal amplification technologies - A review. *Nucleosides Nucleotides & Nucleic Acids* **27**, 224-243, doi:10.1080/15257770701845204 (2008).
- 11 Kim, J. & Easley, C. J. Isothermal DNA amplification in bioanalysis: strategies and applications. *Bioanalysis* **3**, 227-239, doi:10.4155/bio.10.172 (2011).

- 12 Yan, L. *et al.* Isothermal amplified detection of DNA and RNA. *Molecular BioSystems* **10**, 970-1003, doi:10.1039/c3mb70304e (2014).
- 13 Nagamine, K., Hase, T. & Notomi, T. Accelerated reaction by loop-mediated isothermal amplification using loop primers. *Molecular and Cellular Probes* **16**, 223-229, doi:<http://dx.doi.org/10.1006/mcpr.2002.0415> (2002).
- 14 Piepenburg, O., Williams, C. H., Stemple, D. L. & Armes, N. A. DNA detection using recombination proteins. *Plos Biology* **4**, 1115-1121, doi:10.1371/journal.pbio.0040204 (2006).
- 15 Tomita, N., Mori, Y., Kanda, H. & Notomi, T. Loop-mediated isothermal amplification (LAMP) of gene sequences and simple visual detection of products. *Nat. Protocols* **3**, 877-882 (2008).
- 16 Tanner, N. A. & Evans, T. C., Jr. Loop-mediated isothermal amplification for detection of nucleic acids. *Curr Protoc Mol Biol.* **105**, Unit 15.14, doi:10.1002/0471142727.mb1514s105 (2014).
- 17 Goto, M., Honda, E., Ogura, A., Nomoto, A. & Hanaki, K.-I. Colorimetric detection of loop-mediated isothermal amplification reaction by using hydroxy naphthol blue. *Biotechniques* **46**, 167-172, doi:10.2144/000113072 (2009).
- 18 Mori, Y., Kitao, M., Tomita, N. & Notomi, T. Real-time turbidimetry of LAMP reaction for quantifying template DNA. *Journal of Biochemical and Biophysical Methods* **59**, 145-157, doi:<http://dx.doi.org/10.1016/j.jbbm.2003.12.005> (2004).
- 19 Craw, P. & Balachandran, W. Isothermal nucleic acid amplification technologies for point-of-care diagnostics: a critical review. *Lab on a Chip* **12**, 2469-2486, doi:10.1039/c2lc40100b (2012).

- 20 Crannell, Z. A., Rohrman, B. & Richards-Kortum, R. Quantification of HIV-1 DNA using real-time recombinase polymerase amplification. *Analytical chemistry* **86**, 5615-5619, doi:10.1021/ac5011298 (2014).
- 21 Weusten, J. J. A. M., Carpay, W. M., Oosterlaken, T. A. M., van Zuijlen, M. C. A. & van de Wiel, P. A. Principles of quantitation of viral loads using nucleic acid sequence-based amplification in combination with homogeneous detection using molecular beacons. *Nucleic Acids Research* **30**, e26, doi:10.1093/nar/30.6.e26 (2002).
- 22 Nilsson, M., Gullberg, M., Dahl, F., Szuhai, K. & Raap, A. K. Real-time monitoring of rolling-circle amplification using a modified molecular beacon design. *Nucleic Acids Research* **30**, e66, doi:10.1093/nar/gnf065 (2002).
- 23 Kopp, M. U., de Mello, A. J. & Manz, A. Continuous flow PCR on a chip. *Science* **280**, 1046-1048 (2000).
- 24 Witters, D. *et al.* Digital biology and chemistry. *Lab on a Chip* **14**, 3225-3232, doi:10.1039/c4lc00248b (2014).
- 25 Baker, M. Digital PCR hits its stride. *Nat Meth* **9**, 541-544 (2012).
- 26 Tjhung, K. F., Burnham, S., Anany, H., Griffiths, M. W. & Derda, R. Rapid Enumeration of Phage in Monodisperse Emulsions. *Analytical chemistry* **86**, 5642-5648, doi:10.1021/ac500244g (2014).
- 27 Huggett, J. F. *et al.* The Digital MIQE Guidelines: Minimum Information for Publication of Quantitative Digital PCR Experiments. *Clinical Chemistry* **59**, 892-902, doi:10.1373/clinchem.2013.206375 (2013).

- 28 White, R., Blainey, P., Fan, H. C. & Quake, S. Digital PCR provides sensitive and absolute calibration for high throughput sequencing. *BMC Genomics* **10**, 116 (2009).
- 29 Whale, A. S. *et al.* Comparison of microfluidic digital PCR and conventional quantitative PCR for measuring copy number variation. *Nucleic Acids Research* **40**, e82, doi:10.1093/nar/gks203 (2012).
- 30 Hatch, A. C. *et al.* 1-Million droplet array with wide-field fluorescence imaging for digital PCR. *Lab on a Chip* **11**, 3838-3845, doi:10.1039/c1lc20561g (2011).
- 31 Shen, F. *et al.* Digital Isothermal Quantification of Nucleic Acids via Simultaneous Chemical Initiation of Recombinase Polymerase Amplification Reactions on SlipChip. *Analytical chemistry* **83**, 3533-3540, doi:10.1021/ac200247e (2011).
- 32 Selck, D. A., Karymov, M. A., Sun, B. & Ismagilov, R. F. Increased Robustness of Single-Molecule Counting with Microfluidics, Digital Isothermal Amplification, and a Mobile Phone versus Real-Time Kinetic Measurements. *Analytical chemistry* **85**, 11129-11136, doi:10.1021/ac4030413 (2013).
- 33 Gansen, A., Herrick, A. M., Dimov, I. K., Lee, L. P. & Chiu, D. T. Digital LAMP in a sample self-digitization (SD) chip. *Lab on a Chip* **12**, 2247-2254, doi:10.1039/c2lc21247a (2012).
- 34 Jarvius, J. *et al.* Digital quantification using amplified single-molecule detection. *Nat Meth* **3**, 725-727, doi:http://www.nature.com/nmeth/journal/v3/n9/supinfo/nmeth916_S1.html (2006).

- 35 Sun, B. *et al.* Mechanistic Evaluation of the Pros and Cons of Digital RT-LAMP for HIV-1 Viral Load Quantification on a Microfluidic Device and Improved Efficiency via a Two-Step Digital Protocol. *Analytical chemistry* **85**, 1540-1546, doi:10.1021/ac3037206 (2013).
- 36 Shen, F. *et al.* Multiplexed Quantification of Nucleic Acids with Large Dynamic Range Using Multivolume Digital RT-PCR on a Rotational SlipChip Tested with HIV and Hepatitis C Viral Load. *Journal of the American Chemical Society* **133**, 17705-17712, doi:10.1021/ja2060116 (2011).
- 37 Sun, B. *et al.* Measuring Fate and Rate of Single-Molecule Competition of Amplification and Restriction Digestion, and Its Use for Rapid Genotyping Tested with Hepatitis C Viral RNA. *Angewandte Chemie International Edition* **53**, 8088-8092, doi:10.1002/anie.201403035 (2014).
- 38 Bustin, S. A. & Nolan, T. in *Real-time PCR: Advanced Technologies and Applications* (eds N. Saunders & M. Lee) 284 (Horizon Press, 2013).
- 39 Nixon, G. J. *et al.* A novel approach for evaluating the performance of real time quantitative loop-mediated isothermal amplification-based methods. *Biomolecular Detection and Quantification* **2**, 4-10, doi:<http://dx.doi.org/10.1016/j.bdq.2014.11.001> (2014).
- 40 Walker, G. T. *et al.* Strand displacement amplification: An isothermal, in vitro DNA amplification technique. *Nucleic Acids Research* **20**, 1691-1696, doi:10.1093/nar/20.7.1691 (1992).
- 41 Vincent, M., Xu, Y. & Kong, H. M. Helicase-dependent isothermal DNA amplification. *Embo Reports* **5**, 795-800, doi:10.1038/sj.embor.7400200 (2004).

- 42 Uemori, T. *et al.* Investigation of the molecular mechanism of ICAN, a novel gene amplification method. *Journal of Biochemistry* **142**, 283-292, doi:10.1093/jb/mvm137 (2007).
- 43 Notomi, T. *et al.* Loop-mediated isothermal amplification of DNA. *Nucleic Acids Research* **28**, e63, doi:10.1093/nar/28.12.e63 (2000).
- 44 Parida, M., Posadas, G., Inoue, S., Hasebe, F. & Morita, K. Real-time reverse transcription loop-mediated isothermal amplification for rapid detection of West Nile virus. *Journal of Clinical Microbiology* **42**, 257-263, doi:10.1128/jcm.42.1.257-263.2004 (2004).
- 45 Suslov, O. & Steindler, D. A. PCR inhibition by reverse transcriptase leads to an overestimation of amplification efficiency. *Nucleic Acids Research* **33**, e181, doi:10.1093/nar/gni176 (2005).
- 46 Kimura, Y. *et al.* Optimization of turn-back primers in isothermal amplification. *Nucleic Acids Research* **39**, e59-e59, doi:10.1093/nar/gkr041 (2011).
- 47 Tanaka, Y. *et al.* Effects of the turn-back primer on intermediate product generation in isothermal DNA amplification. *Biotechniques* **49**, 888-892, doi:10.2144/000113566 (2010).
- 48 Gandelman, O., Jackson, R., Kiddle, G. & Tisi, L. Loop-Mediated Amplification Accelerated by Stem Primers. *International Journal of Molecular Sciences* **12**, 9108-9124, doi:10.3390/ijms12129108 (2011).
- 49 Meng, S. & Li, J. A novel duplex real-time reverse transcriptase-polymerase chain reaction assay for the detection of hepatitis C viral RNA with armored RNA as internal control. *Virology Journal* **7**, 1-9, doi:10.1186/1743-422x-7-117 (2010).

- 50 Du, W., Li, L., Nichols, K. P. & Ismagilov, R. F. SlipChip. *Lab on a Chip* **9**, 2286-2292, doi:10.1039/b908978k (2009).
- 51 Shen, F., Du, W., Kreutz, J. E., Fok, A. & Ismagilov, R. F. Digital PCR on a SlipChip. *Lab on a Chip* **10**, 2666-2672, doi:10.1039/c004521g (2010).
- 52 Zadeh, J. N. *et al.* NUPACK: Analysis and design of nucleic acid systems. *Journal of Computational Chemistry* **32**, 170-173, doi:10.1002/jcc.21596 (2011).
- 53 Eiken Chemical Co., L. A Guide to LAMP primer designing (PrimerExplorer V4) 18 (2014).
- 54 Kargar, M., Askari, A., Doosti, A. & Ghorbani-Dalini, S. Loop-Mediated Isothermal Amplification Assay for Rapid Detection of Hepatitis C virus. *Indian Journal of Virology* **23**, 18-23, doi:10.1007/s13337-012-0067-2 (2012).
- 55 SantaLucia J, H., D. . The thermodynamics of DNA structural motifs. *Annual Review of Biophysics and Biomolecular Structure* **33**, 415–440 (2004).
- 56 Peyret, N. *Prediction of nucleic acid hybridization: parameters and algorithms* Ph.D. thesis, Wayne State University, (2000).
- 57 Beales, L. P., Rowlands, D. J. & Holzenburg, A. The internal ribosome entry site (IRES) of hepatitis C virus visualized by electron microscopy. *Rna-a Publication of the Rna Society* **7**, 661-670, doi:10.1017/s1355838201001406 (2001).
- 58 Honda, M. *et al.* Structural requirements for initiation of translation by internal ribosome entry within genome-length hepatitis C virus RNA. *Virology* **222**, 31-42, doi:10.1006/viro.1996.0395 (1996).
- 59 Fuchs, B., Zhang, K. B., Rock, M. G., Bolander, M. E. & Sarkar, G. High temperature cDNA synthesis by AMV reverse transcriptase improves the

- specificity of PCR. *Molecular Biotechnology* **12**, 237-240, doi:10.1385/mb:12:3:237 (1999).
- 60 Dittrich, S. *et al.* Loop-mediated isothermal amplification for *Rickettsia typhi* (the causal agent of murine typhus): problems with diagnosis at the limit of detection. *J Clin Microbiol* **52**, 832-838, doi:10.1128/jcm.02786-13 (2014).
- 61 Aryan, E. *et al.* A novel and more sensitive loop-mediated isothermal amplification assay targeting IS6110 for detection of *Mycobacterium tuberculosis* complex. *Microbiological Research* **165**, 211-220, doi:<http://dx.doi.org/10.1016/j.micres.2009.05.001> (2010).
- 62 Kaewphinit, T. *et al.* Detection of *Mycobacterium tuberculosis* by Using Loop-Mediated Isothermal Amplification Combined with a Lateral Flow Dipstick in Clinical Samples. *Biomed Res Int* **2013**, 926230, doi:10.1155/2013/926230 (2013).
- 63 Yang, B.-Y. *et al.* Rapid and sensitive detection of human astrovirus in water samples by loop-mediated isothermal amplification with hydroxynaphthol blue dye. *Bmc Microbiology* **14**, 38, doi:10.1186/1471-2180-14-38 (2014).
- 64 Hurley, M. A. & Roscoe, M. E. Automated statistical analysis of microbial enumeration by dilution series. *Journal of Applied Bacteriology* **55**, 159-164, doi:10.1111/j.1365-2672.1983.tb02660.x (1983).
- 65 Kreutz, J. E. *et al.* Theoretical Design and Analysis of Multivolume Digital Assays with Wide Dynamic Range Validated Experimentally with Microfluidic Digital PCR. *Analytical chemistry* **83**, 8158-8168, doi:10.1021/ac201658s (2011).

- 66 Whitley, E. & Ball, J. Statistics review 4: Sample size calculations. *Critical Care* **6**, 335-341 (2002).

Chapter 8:

Progress toward 3-Dimensional Mapping of Nuclear Compartments in Single-Cells Using a Novel Sequencing Based Method

Introduction

All cells within a multicellular organism contain the same genetic code, so cells need mechanisms to determine which of the encoded genes will be expressed in each cell type. One of the mechanisms that controls gene regulation is the 3-dimensional structure of the nucleus,¹⁻³ which changes dynamically with cellular state and is often organized around cell function. However, it is yet unknown, how this 3-dimensional organization is established and how it is reorganized during cell reprogramming.^{4,5} There are a variety of modalities by which specific chromosomal arrangements can be interrogated including methods to determine: euchromatin distributions,⁶⁻⁸ protein-DNA interactions,^{9,10} DNA-DNA interactions,^{11,12} and RNA-DNA interactions.¹³⁻¹⁵ Classically, these methods have been performed as averages over a large number of cells but this fails to capture the heterogeneity of a cell population,¹⁶ and may report chromatin arrangements that are either mutually inclusive or mutually exclusive.^{17,18} Recently, there has been a strong push to perform these types of studies at the single-cell level to mitigate these problems.^{8,9,18}

One of the least studied areas of chromosomal organization is RNA-DNA interactions. These interactions are clearly involved in organization of chromatin; for example, large concentrations of messenger RNA are retained by the nucleus and localized to nuclear speckles¹⁹ and other chromatin-associated regions,^{20,21} disruption of RNA transcription has shown nuclear rearrangement without disrupting protein translation,²² and the long

non-coding RNAs have been shown to exploit 3-dimensional organization to silence targets.²³⁻²⁹ One of the main reasons for the lack of detailed information about RNA-DNA interactions is that current methods are highly specific and developed protocols are designed for single RNA targets, so they are unable to capture the entire set of RNA-DNA interactions. In addition, the data provided by these methods do not include information about higher order interactions to determine whether a single RNA molecule interacts with multiple DNA sequences, or whether a population of RNA molecules interacts with a distinct set of DNA sequences.³⁰

Therefore, new technologies and methodologies must be developed to truly understand 3-dimensional nuclear structure and the role of all nucleic acids involved. First, suitable technologies must be capable of determining structure at the single-cell level. Second, these technologies must address global RNA interactions in the context of DNA interactions. Third, new methods should capture information on distinct nuclear compartments of multiple interacting species, not be restricted to only contact pairs.^{18,31} Here, progress towards developing a method to map the 3-dimensional nuclear structure of nucleic acid interactions (DNA/RNA) in single cells is presented. First, I present a brief discussion of the proposed sequencing method for mapping nuclear nucleic acid interactions. Second, I present a microfluidics-based method for segregating and processing single cells based on the bulk mapping protocol. Third, I discuss a simplified method for preparing single cells for mapping in a format that is amenable to a wide variety of different segregation technologies.

Split-and-Pool Barcoding

The method for mapping higher order 3-dimensional nucleic acid interactions in nuclei, as developed by Sofia Quinodoz in Prof Mitchell Guttman's Caltech lab, starts by cross-linking cells using a combination of formaldehyde and DSG. This crosslinking method has previously^{28,32} been shown to be effective at preserving RNA-DNA interactions through sequencing preparation. After the cells have been fixed, nuclei are isolated, and the DNA and RNA are fragmented using controlled enzymatic digestions with DNase 1 and RNase 1 to bring the resultant nucleic acid fragments into a range of ~200–700 nucleotides in length. After the nucleic acids are fragmented, they are isolated from the solution using a large excess of NHS-activated magnetic beads through a coupling reaction that targets proteins associated with nucleic acids. The coupling of the complexes to an excess of magnetic beads allows for the capture of unique complexes of interacting sequences to single beads, and the use of denaturing wash steps prevents the aggregation of non-crosslinked complexes. The beads also provide a convenient handle for manipulation throughout the procedure. After coupling, the fragmented ends are repaired (DNA ends are also dA-tailed) before ligation of a universal adapter that contains a “sticky end” (single-stranded overhang). This single-stranded overhang then provides a handle onto which a succession of barcodes can be added through a split-and-pool barcoding method.

The split-and-pool barcoding method is designed to identify compartments of nuclear DNA and RNA by assigning a unique barcode to each compartment. Since unique complexes are isolated on magnetic beads, if each bead can be uniquely barcoded for sequencing, then complexes can be determined by grouping together all sequences with

the same barcode. Complexes are barcoded by taking beads to which complexes have been bound and adapted with a universal adapter, and splitting these beads on a 96 well plate where unique sequences ligate to the universal adapter, effectively pooling together samples with the same complexes. There are two sets of adapters: “A” adapters ligate only to “B” adapters and “B” adapters only ligate with “A” adapters. This prevents the creation of chimeras and polymers in any one step of the process. By subjecting a sample to n rounds of split-and-pool barcoding a possible 96^n barcodes are generated. After five rounds of this procedure, a total of 8.15×10^9 unique barcodes are possible and therefore each bead should have a unique barcode, and nuclear compartments in a sample can be uniquely identified.

After paired-end sequencing, interactions can be identified by aligning the genetic sequences from one end of the pair to barcodes on the other end. Once this relationship is established, all aligned sequences resulting from identical barcodes can be grouped together as a higher-order interacting complex. This approach to determining 3-dimensional structure has a number of advantages over existing methods. Specifically, (i) the method provides information about all DNA associated RNA molecules within a genome in a single reaction as opposed to a single species. (ii) The method provides information about chromosome-associated RNA within the context of overall nuclear structure, effectively combining the output of two experiments into one.^{18,28,31} (iii) The method has a higher information content than that of existing experiments, which rely on contact pairs to identify interactions.^{18,31} In a Hi-C experiment, 10 reads have the potential to result in 10 contact pairs. In a split-and-pool experiment, however, the number of contact pairs resulting in a single experiment depends on the number of

sequences in a single complex and scales as $\sum_1^n n - 1$. Therefore, if in a split-and-pool experiment all 10 reads belong to the same complex, that results in 45 contact pairs. In addition to the contact pairs, the split-and-pool method provides higher-order information about the relationships between contact pairs by preserving complexes, which existing methods can only achieve in the ensemble.

Microfluidic Method for Single-Cell Mapping

This split-and-pool barcoding approach is uniquely suited to single-cell analyses. The cell can be thought of as one dimension of a higher-order structure in a sequencing dataset. The deconvolution can be performed by ensuring that all of the complexes from a single cell receive an initial unique barcode. One simple way of manipulating single cells and providing unique barcodes to each is by using microfluidics.^{9,33–37} There are a number of different steps that all need to be performed on the microfluidic device (Fig 8-1) to prepare cells for the split-and-pool procedure including fragmentation, washing, bead coupling, and ligation.

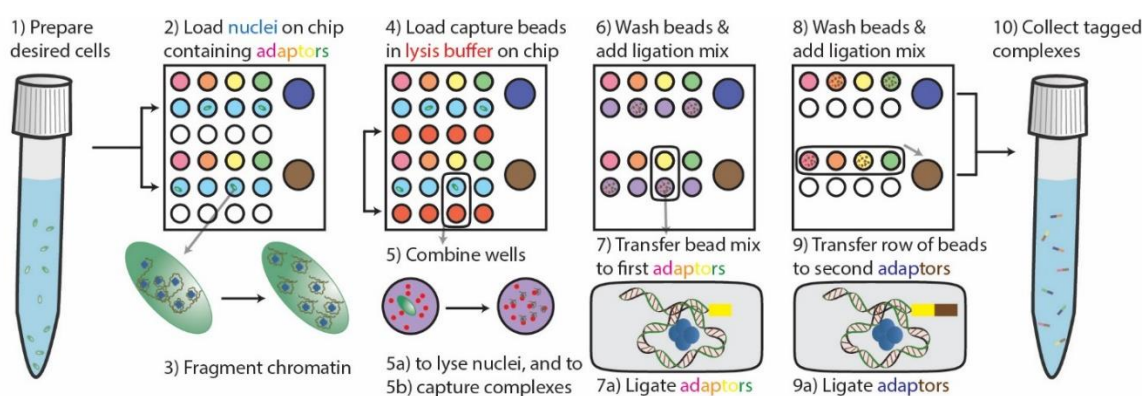


Figure 8-1 Schematic of required steps the microfluidic device must perform to prepare individual cells for split and pool mapping.

One microfluidic technology that is well suited for complex manipulations and multiple steps is the SlipChip technology.³⁸⁻⁴⁹ SlipChip microfluidic devices are ideal for complex procedures because they can be “programmed” to include numerous fluid handling steps, and have previously been validated for isolating single cells.^{38,50} A SlipChip device suitable for performing the steps outlined above is shown in Fig 8-2. This device incorporates four different positions: two are used for loading; two are used for mixing loaded solution. This type of device has a few unique advantages compared with alternative single-cell microfluidic techniques.^{9,33,34,36,37,51} On a SlipChip, the user is able to visually confirm and image the loading of single nuclei, and relate sequenced results back to a specific device and compartment. The ability to relate sequenced results back to a specific well on a specific device is due to the ability to robustly and deterministically spot a precise amount of adapters onto a SlipChip device prior to assembly. This can be beneficial when validating a sequencing dataset as cell loading is Poisson based, and results can be confirmed to come from a single cell as opposed to multiple.

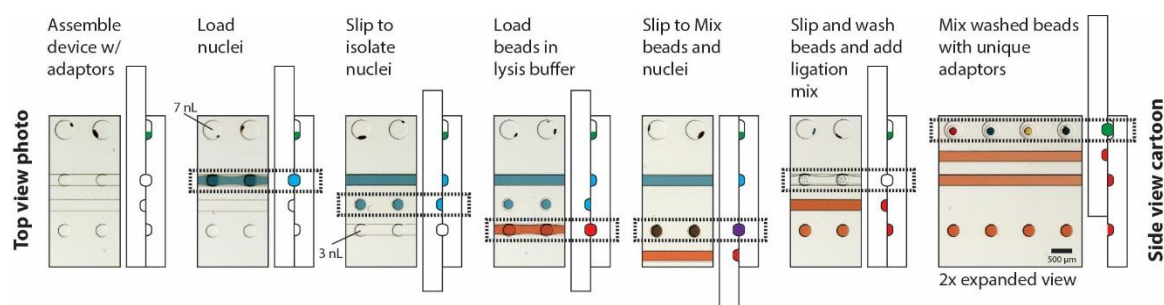


Figure 8-2 A SlipChip device suitable for preparing single nuclei for split and pool barcoding is shown. This device has four different programmed positions in which all required procedures can be completed. Unique adapters are spotted deterministically on the device prior to assembly.

The first challenge that needed to be overcome in the development of a microfluidic technology for preparing cells for split-and-pool barcoding was a method to reliably

handle magnetic beads. It is critical that during all of the on-device steps, the magnetic beads do not shift to other compartments prior to tagging. Therefore, a magnetic setup can be used to exert a force strong enough to prevent the beads from transferring to accompanying wells under fluid flow during washing. The best geometry for magnets would be to have a point source field directly beneath each microfluidic well.⁵² With this geometry, magnetic beads would have a force applied drawing them toward the center of the well against fluid flow. Another easier to manufacture magnetic setup would be to have a line source magnetic field transverse to the flow in the system directly under the wells containing magnetic beads. Neither of these types of geometries, however, are practical because it would be difficult to align to the device due to precision requirements in the tens of micrometers. Misalignment would draw beads out of their respective separate wells and the protocol would fail. A simpler, and easier to implement, solution with a wide tolerance to misalignment would be to have line sources along the channels of the device. In this geometry, there would be no direct force keeping the beads from flowing through the channel, however, as long as the magnetic force can overcome the force induced by flow the beads would remain in the wells (depressions) on the device. The flow in the microfluidic device must be tightly controlled to not overpower the magnetic force on the beads. Flow control in SlipChip microfluidic devices is achieved using a constant pressure source. Constant pressure sources are easy and inexpensive to implement with a simple pipettor, and are ideal for SlipChip devices because the pressure used to drive the flow can be precisely controlled to avoid leakage.⁵³ One problem with constant pressure sources, however, is that the flow rate is uncontrolled. For the split-and-pool barcoding method, a constant flow rate source is needed and this can be

implemented with a syringe pump. Syringe pumps are slightly challenging to use on a SlipChip, however, due to the need to interface the syringe pump with the microfluidic device. To solve the interface problem, a piece of Teflon tubing was used to connect the pump's syringe to a 3D-printed gasket. The gasket was designed to have an interference fit for the tubing and is successfully able to withstand flow rates of up to 10 mL/hr with no leakage. The gasket is printed from TangoPlus material on a Connex 3D printer and attached to the SlipChip using UV curable optical adhesive. When combining this pumping strategy with 2" x 0.25" x 0.1" neodymium magnets aligned to the SlipChip channels using a custom 3d printed holder we were able to maintain the position of the magnetic beads in the wells of the device at flow rates of up to 1 mL/hr which is sufficient for all processing steps.

A second challenge that needed to be overcome for preparation of nuclei on device for split-and-pool barcoding was determining a way to keep the magnetic beads suspended in solution during enzymatic steps. Maintaining dispersion of the beads during enzymatic steps is critical to ensure that all of the complexes attached to the beads are exposed to the reaction solution and available for modification. In bulk reactions this is easily performed using a shaker, however, these methods are incompatible with microfluidic devices because there is no dead space in device wells. One option for dispersing the beads on the device would be through magnetic mixing.⁵⁴ This option, while providing effective mixing for the solution the beads are in, keeps beads clumped together as opposed to dispersing them. An alternative option would be to rotate the microfluidic device at a frequency that would keep the majority of beads in solution based on settling times. The settling time of magnetic beads on device can be estimated based on terminal

velocity calculations using Eq. 8-1 where V is the terminal velocity of the beads, ρ_p is the bead density, ρ_f is the fluid density, μ is the dynamic viscosity, g is acceleration due to gravity, and R is the hydrodynamic radius of the beads.

$$V = \frac{2}{9} \frac{(\rho_p - \rho_f)}{\mu} g R^2 \quad (\text{Eq. 8-1})$$

Based on this formula, and using parameters of 2 g/mL bead density, 1 g/mL fluid density, 0.001 kg/(m*s) dynamic viscosity, and a bead radius of 50 μm , a terminal velocity of $\sim 0.5 \mu\text{m}/\text{sec}$ was calculated. Because acceleration to terminal velocity is nearly instantaneous and the total depth of the chamber containing the beads is 100 μm , we expect complete settling of the beads in ~ 3 min. This mixing method was tested by taking controlled amounts of beads that were complexed to nuclear components that were digested, repaired, and dA-tailed and performing ligation of adapters on and off device. When ligation was performed on device without keeping the beads dispersed in solution, the difference in C_q was 2.9 which corresponds to a relative yield of $\sim 14\%$. When maintaining dispersion of beads on device using a custom rotisserie, the difference in C_q was only 0.6 which corresponds to a yield of $\sim 66\%$ (Fig. 8-3). This shows that we can keep beads non-motile under changing conditions when required, and that we can disperse those beads when new conditions have been established to significantly increase yield.

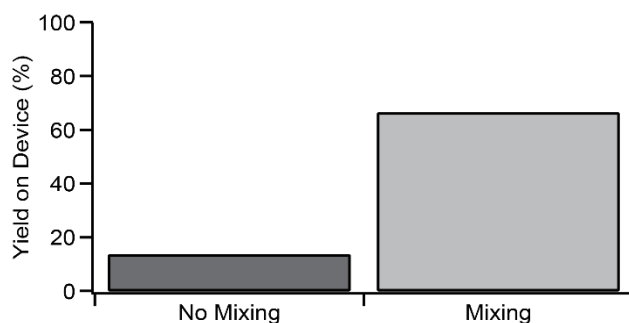


Figure 8-3 The percentage difference in yield when ligation is performed on-device versus off-device, separated by whether or not mixing was performed on-device. In all experiments, the number of beads was controlled. The yield for on-device ligation without mixing was 14% as compared to off-device ligation. The yield for on-device ligation with mixing was 66% as compared to off-device ligation. Ligation was measured by qPCR.

Simplified Single-Cell Preparation Technique

Although it is feasible to perform all preparation steps on-device, to make the method easier to optimize, more accessible, and more transferrable, we perform as many steps as possible off-device. Optimization is simplified as moving steps off of device allows us to use existing chemistries where possible which have already been validated for bulk reactions. The method becomes more accessible when more steps are able to be performed off-device as more of the techniques will be familiar to standard molecular biology labs, and the resulting device is more simple to operate with less training. The method also becomes more transferrable as it is easier to make changes and optimizations where necessary as there is no need to redesign and validate a microfluidic device with each modification.

A significant challenge to performing more processing steps off-device is the need to keep the nuclear contents separate during all processing steps. A method has been developed,^{18,55} to solve this problem, and involves porating nuclei and using the porated nucleus as a contained environment in which to perform all enzymatic processing steps.

This nuclear poration protocol has also already been validated as a way to maintain nuclear structure in single-cells via Hi-C analysis to determine DNA-DNA contact pairs^{18,55} and also as a way to increase the yield in the Hi-C protocol.^{31,56} The method takes cells that have been formaldehyde crosslinked, and performs a nuclear isolation, followed by a nuclear poration using sodium dodecyl sulfate. After the nuclear poration, the chromatin in the nuclei is digested using a restriction enzyme. In our modified protocol, the restriction enzyme used is HpyCH4V which cuts on the sequence TGCA leaving a blunt end. After digestion of the chromatin, the DNA ends are dA-tailed in-nuclei prior to ligation of the universal adapters. After this point, the nuclei are lysed, and the split-and-pool protocol proceeds. In this nuclear poration protocol, all steps prior to ligation of the universal adapter can be performed in bulk with many cells. Ligation of the universal adapter would require separation of the nuclei to ensure that each nucleus received a uniquely barcoded adapter through isolation on a simplified microfluidic device or 96-well plate. Operation of a SlipChip device for this step would also be simpler than the previously described protocol. Because there is no need to handle magnetic beads on device, we can use simple constant pressure loading and we can significantly reduce the number of “programs” on-device.

The first step in developing an in-nuclei processing approach is to determine the proper restriction enzyme or mixture of enzymes to fragment the chromatin into 300–700 bp fragments. A 4-base cutter would be preferable because given a random genome the enzyme would cut the DNA on average every 4^4 or 256 bases. One suitable enzyme is the HpyCH4V enzyme, which cuts on the recognition sequence TGCA and under experimental procedures is capable of digesting 1% formaldehyde PSM-33 mouse

embryonic stem cells (Fig 8-4A). The range of fragment sizes after cutting with the HpyCH4V restriction enzyme was lower than expected based on average cutting frequency, however, it is likely that some of the digestion sites are inaccessible due to either the formaldehyde crosslinking or because they are protected by bound proteins such as histones. After digestion, the nuclei were prepared for ligation using the NEBNext dA-tailing module, and as a bulk control had a universal adapter ligated. These nuclei were then lysed and the contents of the nuclei were coupled to beads. To confirm that the nuclei were processed correctly throughout the dA tailing, ligation, and coupling steps; a small portion of the beads were used to check for PCR amplification from the universal barcodes Fig 8-4b. The remainder of the beads were then processed using the split-and-pool barcoding method through five rounds of barcoding before PCR amplification Fig 8-4c.

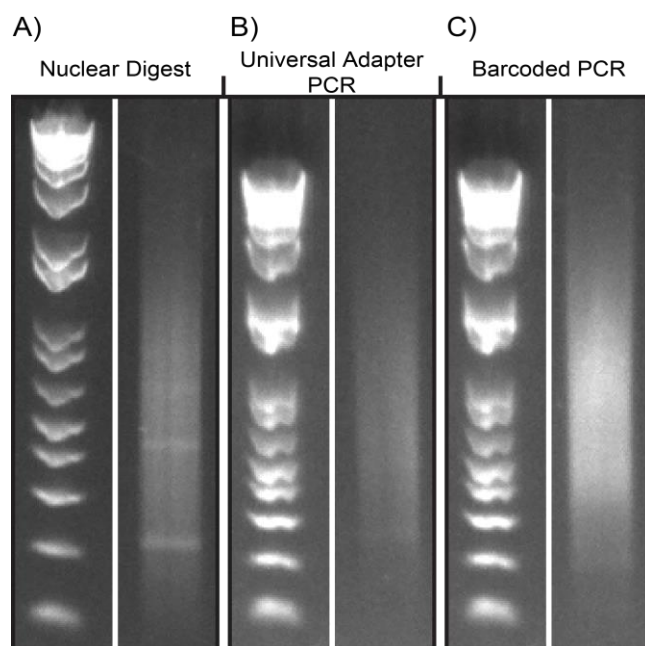


Figure 8-4 Gel images show the state of a sample of nuclei used for split-and-pool barcoding after in-nuclei ligation: (A) the distribution of fragments obtained after restriction digest; (B) the distribution of amplified product acquired from (A) after addition of a universal adapter by in-nuclei ligation followed by lysis and bead-coupling;

and (C) the distribution of amplified product acquired from (B) after in five rounds of split-and-pool barcoding. Products (B–C) were amplified using PCR. In the left side of each panel, an E-Gel 1kb plus ladder is shown.

Upon successful split-and-pool barcoding, the amount of template attached to beads was quantified by amplifying the contents of 1% of the beads for 13 cycles, and checking the concentration of the resultant DNA using an Agilent Bioanalyzer. A 2.5% portion of the sample representing 20M unique fragments was then submitted for 200-cycle Hi-seq, aiming for 2x coverage. The resultant sequencing reads were analyzed by grouping together aligned sequences based on barcode, and preparing heat maps based on the frequency of interactions among the Mb regions of each chromosome (Fig 8-5a). As expected, the sequencing run showed most interactions occurred along the diagonal; however, there are a number of areas that have a higher density of interactions, and we also observed a number of off-diagonal structures. Overall, the sequencing results share many of the same features of the DNase nuclear preparation method described earlier (Fig 8-5b) but there is more noise with the in-nuclei results. One plausible explanation for the noise is that the lower depth at which the sample was sequenced may have resulted in a sparser dataset.

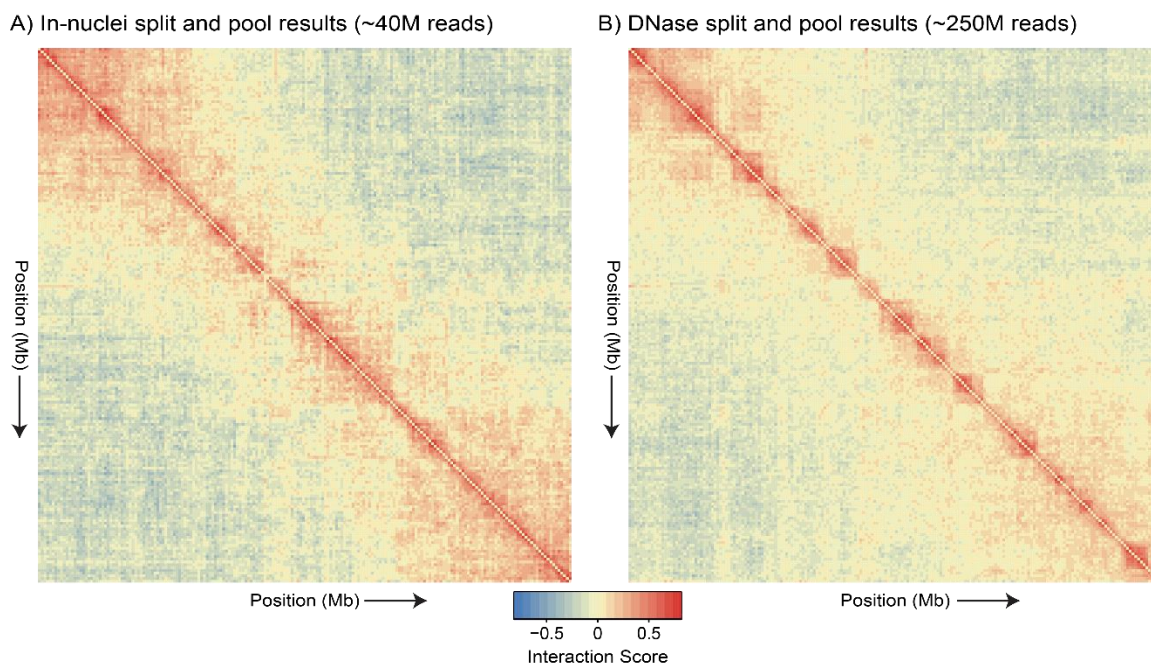


Figure 8-5 Heat maps comparing the observed interactions in chromosome 1 at the megabase scale between samples prepared using in-nuclei ligation (A) or using DNase treatment (B). The unpublished results shown in (B) were obtained from Sofia Quinodoz, Guttman Lab, Caltech.

A different explanation for the noise in the sequencing dataset could lie in the number of fragments of DNA per sequenced complex. It is critical during the initial stages of the protocol to ensure that all complexes are separated onto separate beads. If many complexes end up on the same bead, this would add noise to the system by incorrectly calling interactions where none exist. As seen in Fig 8-6a, the largest complex size in the dataset analyzed contained 65,523 sequences, which equates to 2,146,599,003 contact pairs. In contrast, there are only 21,197 complexes that contain two sequences equating to 21,197 contact pairs. Therefore, there are five orders of magnitude more pair-wise interactions identified in a complex of many fragments, compared with a large number of smaller complexes. While it is likely that the multi-component complexes contain real interactions, these interactions may be over much longer length scales leading to a greater number of interactions further off-diagonal which may appear as noise. One explanation

for these large complex sizes is that complexes are composed chiefly of sections of closed chromatin that may not be highly accessible to restriction enzymes, and therefore not sufficiently digested. This hypothesis can be tested by comparing the complex size to the percentage of open chromatin in a complex as defined by DNase hypersensitivity datasets. If the hypothesis is correct, we would expect that small complexes would be enriched in open chromatin and large complexes would be enriched in closed chromatin. This is not what we observed, however, when we compare the percentage of open chromatin in a complex against the number of components that the complex contained (Fig 8-6B). Other options for determining the identity of the large complexes could be that they are sections of chromatin which is not necessarily higher in percentage of closed chromatin, however, is much denser. These sections could be enriched in known compartments such as nucleoli, or, other fragments which could be chiefly composed of insoluble chromatin.

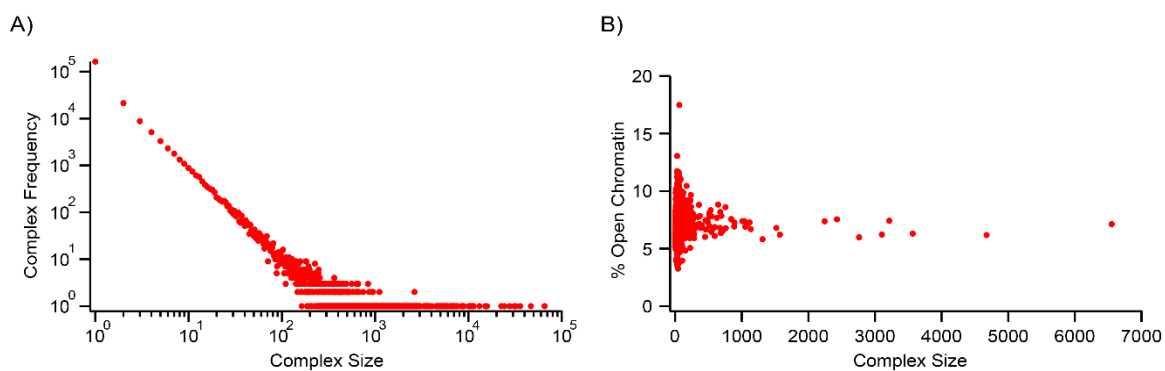


Figure 8-6 The sizes of sequenced complexes as a factor of complex frequency and as a factor of the percentage of open chromatin. (A) Complex frequency (the number of times a complex of a specific size was observed by sequencing) compared to its size. (B) The percentage of open chromatin as a function of complex size.

In order to test whether or not the large complexes observed above were known compartments such as the nucleolus, the coverage across each of the clusters can be determined of which chromosomes are represented. If these structures are nucleoli, it

would be expected that they would be enriched in chromosomes 12, 15, 16, 17, 18, and 19.⁵⁷ The analysis was first performed by taking all clusters which contained greater than 10,000 fragments, determining the representative numbers of fragments from each chromosome, normalizing to the number of expected fragments based on that chromosome size, and calculating a percent representation (Fig 8-7A). This was then repeated on just the largest cluster (Fig 8-8A). As can be seen, there is no significant variation between the chromosomes which decreases the likelihood that these large clusters are representative of nucleoli, and are instead more likely to be noise associated with insoluble chromatin.

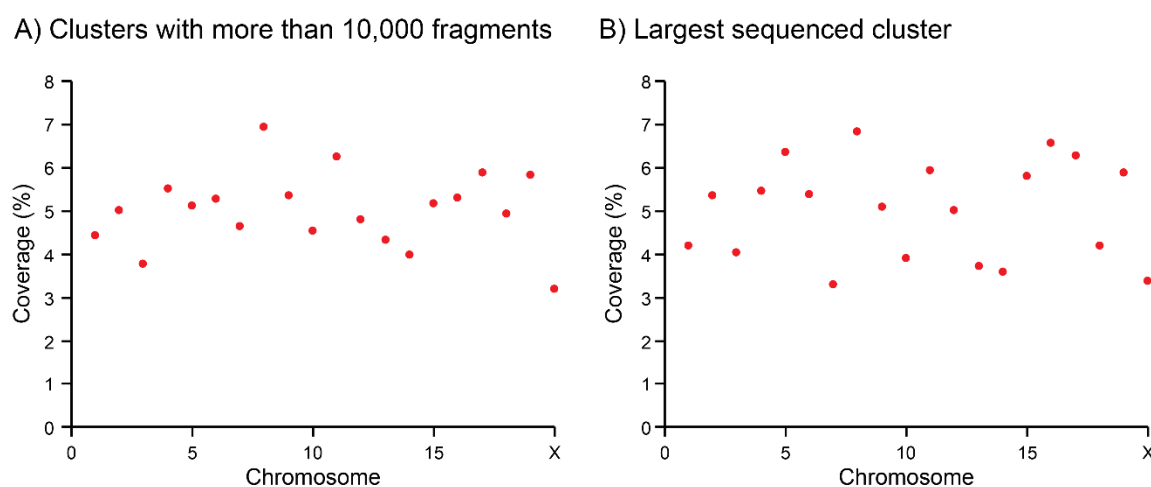


Figure 8-7 The normalized percent coverage as a function of chromosome on different clusters. (A) An analysis of percent coverage as a function of chromosome on all clusters having greater than 10,000 fragments. (B) An analysis of percent coverage as a function of chromosome on the largest barcoded cluster (65,523 fragments).

Based on the theory that the largest clusters (greater than 10,000 fragments) are more associated with noise than signal, and given that the amount of information contained in a given heatmap exponentially increases with cluster size, one may be able to significantly reduce noise by excluding the largest clusters from analysis. In order to test this hypothesis, all clusters which had greater than 10,000 fragments were excluded from

heatmap generation as based on Fig 8-6A which shows that these points are outside the log-log linear distribution of sizes. When this analysis is performed on chromosome 1, (Fig 8-8) it appears that no features were lost, and qualitatively the data could be less noisy with the largest clusters excluded (Fig 8-8A) than when an analysis of all clusters is performed (Fig 8-8B). This further reinforces the idea that the largest clusters are simply noise associated with things such as insoluble chromatin rather than real nuclear structures. Further analysis, however, of cross-chromosome correlations could reveal underlying macro structures associated with these clusters which cannot be captured in the correlation of a single chromosome.

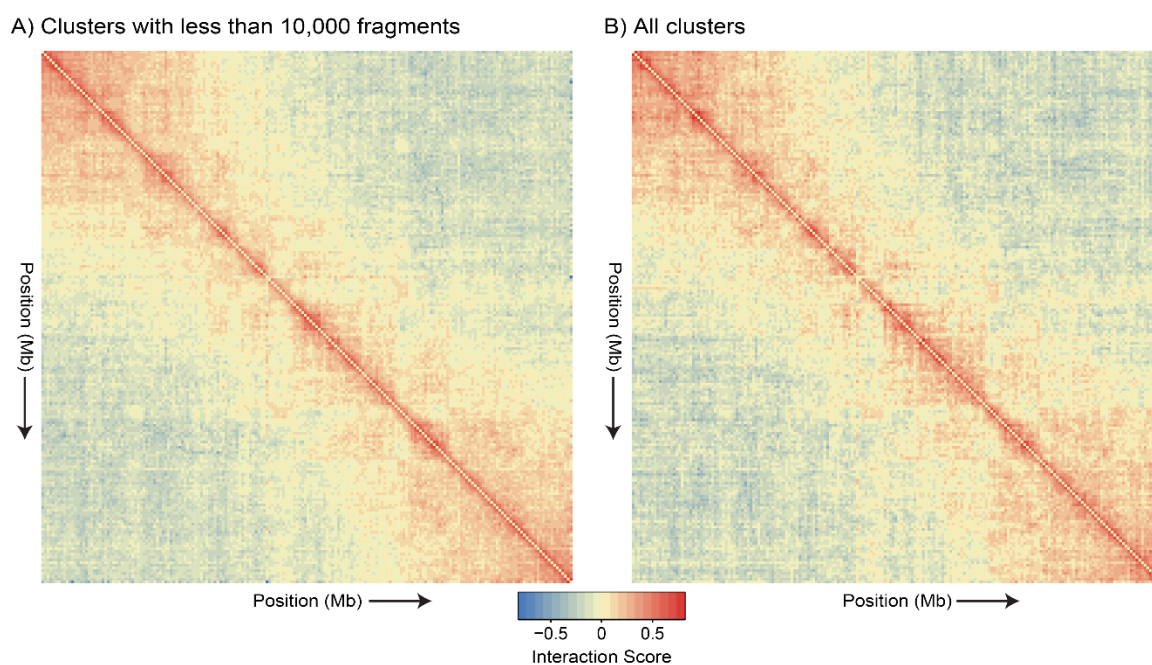


Figure 8-8 Heat maps comparing the observed interactions in chromosome 1 at the megabase scale between samples prepared using in-nuclei ligation and analyzed excluding clusters with greater than 10,000 fragments (A) or analyzing all fragments (B).

One issue that may arise in the in-nuclei digestion protocol is the loss of chromosomal contents. As the nuclei are porated for a significant amount of time, it is possible that nucleic acid fragments can be lost through diffusion. To determine whether we are losing

sample during processing, we analyze read coverage. This allows us to detect regions of chromatin that are not represented and thus determine whether sample was lost. The coverage from in-nuclei ligation of chromosome 1 was determined to be suitable (Fig 8-9). Hi-C is an alternative sequencing preparation method that has the potential to compare well with our results because both methods use restriction digest to fragment chromatin. The read coverage of these two methods showed some similar peaks and troughs across chromosome 1 (Fig 8-9A), however, there is a much stronger correlation to DNase hypersensitivity data (Fig 8-9B). This suggests that the cutting frequency of our restriction digest is limited mainly in regions of closed chromatin due to blockage of recognition sites, which is less likely to occur in sections of open chromatin. It should be noted, however, that even in the case of sections of chromatin with chiefly closed regions, a suitable read coverage is still observed.

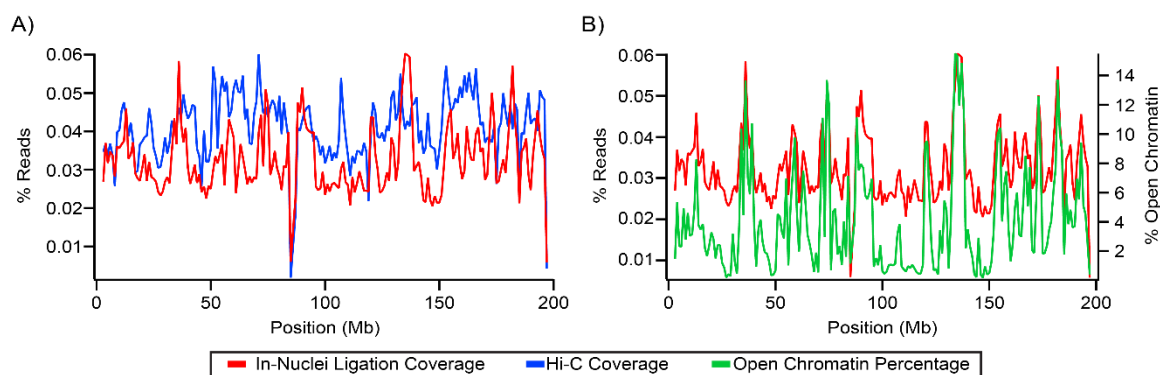


Figure 8-9 The sequencing coverage as denoted by the percentage of reads of total reads contained within Mb bins of chromosome 1 from in-nuclei ligation are compared to the sequencing coverage of Hi-C (A) and the percentage of open chromatin by DNase hypersensitivity (B) testing.

Conclusions

An unmet need in current molecular biology methods is the ability to determine the 3-dimensional structure of nuclear organization, specifically in the context of nuclear-

retained RNAs. Existing methods can determine the DNA binding sites of specific RNA molecules;^{13,28,58} however, many experiments are required to cover all nuclear retained RNAs and do not provide information about chromatin conformation. By performing these types analyses in single-cells as opposed to looking at ensemble measurements, more confidence can be given to the obtained results as population heterogeneity²⁹ is captured and mutually exclusive structures^{18,59} are properly distinguished. To perform this analysis in single cells, Sofia Quinodoz in the lab of Prof Mitchell Guttman developed a split-and-pool barcoding method that determines 3-dimensional structure by attaching unique barcodes to interacting complexes that can then be determined by sequencing. We developed a microfluidic workflow that is compatible with preparing single cells for split-and-pool barcoding using the preparation techniques developed in the Guttman lab. We also developed a modified preparation technique based on single-cell Hi-C work⁵⁵ that simplifies the microfluidic workflow to a single step. This technique was verified in bulk by preparing a plurality of nuclei, barcoding the nuclear contents through split-and-pool barcoding, and then sequencing. The results of the preparation were compared to the results from the Guttman lab and found to match with both nuclear preparation methods providing meaningful interactions.

Future work for this project involves determining proper ways to reduce the amount of the largest clusters (greater than 10,000 fragments) so as to reduce the total number of sequencing reads required to obtain high resolution data as the largest clusters are associated with a sizable proportion of the total number of collected reads. We also need to prepare new microfluidic devices that are compatible with the in-nuclei ligation protocol, and validating that we can perform ligation of universal adapters in-nuclei and

on-device. We also need to ensure that the nuclei prepared on device are compatible with bead coupling followed by split-and-pool barcoding and sequencing. We also need to include RNA within the preparation steps without impacting the overall method outlined above; we don't perceive that this will be an issue because we don't need to include a cell-specific adapter for RNA. We will be able to determine the cell from which a strand of RNA originated using the cell-specific adapter contained on the DNA within the same complex, as denoted by split-and-pool barcoding. Therefore, inclusion of RNA in the protocol could be as simple as adding an RNA-specific universal adapter after in-nuclei ligation and before split-and-pool barcoding.

References

1. Cavalli, G. *et al.* Functional implications of genome topology. *Nat. Struct. Mol. Biol.* **20**, 290–9 (2013).
2. Misteli, T. Beyond the sequence: cellular organization of genome function. *Cell* **128**, 787–800 (2007).
3. Gibcus, J. H. & Dekker, J. The hierarchy of the 3D genome. *Mol. Cell* **49**, 773–82 (2013).
4. Lanctôt, C., Cheutin, T., Cremer, M., Cavalli, G. & Cremer, T. Dynamic genome architecture in the nuclear space: regulation of gene expression in three dimensions. *Nat. Rev. Genet.* **8**, 104–15 (2007).
5. Misteli, T. Beyond the sequence: cellular organization of genome function. *Cell* **128**, 787–800 (2007).

6. Buenrostro, J. D., Giresi, P. G., Zaba, L. C., Chang, H. Y. & Greenleaf, W. J. Transposition of native chromatin for fast and sensitive epigenomic profiling of open chromatin, DNA-binding proteins and nucleosome position. *Nat. Methods* **10**, 1213–8 (2013).
7. John, S. *et al.* Genome-scale mapping of DNase I hypersensitivity. *Curr. Protoc. Mol. Biol.* **Chapter 27**, Unit 21.27 (2013).
8. Buenrostro, J. D. *et al.* Single-cell chromatin accessibility reveals principles of regulatory variation. *Nature* **523**, 486–490 (2015).
9. Rotem, A. *et al.* Single-cell ChIP-seq reveals cell subpopulations defined by chromatin state. *Nat. Biotechnol.* **33**, 1165–72 (2015).
10. Johnson, D. S., Mortazavi, A., Myers, R. M. & Wold, B. Genome-wide mapping of in vivo protein-DNA interactions. *Science* **316**, 1497–502 (2007).
11. Rao, S. S. P. *et al.* A 3D map of the human genome at kilobase resolution reveals principles of chromatin looping. *Cell* **159**, 1665–1680 (2014).
12. Nagano, T. *et al.* Single-cell Hi-C reveals cell-to-cell variability in chromosome structure. *Nature* **502**, 59–64 (2013).
13. Chu, C., Qu, K., Zhong, F. L., Artandi, S. E. & Chang, H. Y. Genomic Maps of Long Noncoding RNA Occupancy Reveal Principles of RNA-Chromatin Interactions. *Mol. Cell* **44**, 667–678 (2011).
14. Simon, M. D. *et al.* The genomic binding sites of a noncoding RNA. *Proc. Natl. Acad. Sci. U. S. A.* **108**, 20497–502 (2011).

15. Engreitz, J. M. *et al.* The Xist lncRNA exploits three-dimensional genome architecture to spread across the X chromosome. *Science* **341**, 1237973 (2013).
16. Hacısuleyman, E. *et al.* Topological organization of multichromosomal regions by the long intergenic noncoding RNA Firre. *Nat. Struct. Mol. Biol.* **21**, 198–206 (2014).
17. Rao, S. S. P. *et al.* A 3D map of the human genome at kilobase resolution reveals principles of chromatin looping. *Cell* **159**, 1665–80 (2014).
18. Nagano, T. *et al.* Single-cell Hi-C reveals cell-to-cell variability in chromosome structure. *Nature* **502**, 59–64 (2013).
19. Huang, S., Deerinck, T. J., Ellisman, M. H. & Spector, D. L. In vivo analysis of the stability and transport of nuclear poly(A)⁺ RNA. *J. Cell Biol.* **126**, 877–99 (1994).
20. Rinn, J. L. & Chang, H. Y. Genome regulation by long noncoding RNAs. *Annu. Rev. Biochem.* **81**, 145–66 (2012).
21. Huang, S., Deerinck, T. J., Ellisman, M. H. & Spector, D. L. In vivo analysis of the stability and transport of nuclear poly(A)⁺ RNA. *J. Cell Biol.* **126**, 877–99 (1994).
22. Nickerson, J. A., Krochmalnic, G., Wan, K. M. & Penman, S. Chromatin architecture and nuclear RNA. *Proc. Natl. Acad. Sci. U. S. A.* **86**, 177–81 (1989).
23. Mao, Y. S., Sunwoo, H., Zhang, B. & Spector, D. L. Direct visualization of the co-transcriptional assembly of a nuclear body by noncoding RNAs. *Nat Cell Biol* **13**,

- 95–101 (2011).
24. Quinodoz, S. & Guttman, M. Long noncoding RNAs: an emerging link between gene regulation and nuclear organization. *Trends Cell Biol.* **24**, 651–63 (2014).
 25. Rinn, J. & Guttman, M. RNA Function. RNA and dynamic nuclear organization. *Science* **345**, 1240–1 (2014).
 26. Maass, P. G. *et al.* A misplaced lncRNA causes brachydactyly in humans. *J. Clin. Invest.* **122**, 3990–4002 (2012).
 27. Quinn, J. J. *et al.* Revealing long noncoding RNA architecture and functions using domain-specific chromatin isolation by RNA purification. *Nat. Biotechnol.* **32**, 933–40 (2014).
 28. Engreitz, J. M. *et al.* The Xist lncRNA exploits three-dimensional genome architecture to spread across the X chromosome. *Science* **341**, 1237973 (2013).
 29. Hacisuleyman, E. *et al.* Topological organization of multichromosomal regions by the long intergenic noncoding RNA Firre. *Nat. Struct. Mol. Biol.* **21**, 198–206 (2014).
 30. Engreitz, J. M. *et al.* RNA-RNA interactions enable specific targeting of noncoding RNAs to nascent Pre-mRNAs and chromatin sites. *Cell* **159**, 188–99 (2014).
 31. Rao, S. S. P. *et al.* A 3D map of the human genome at kilobase resolution reveals principles of chromatin looping. *Cell* **159**, 1665–1680 (2014).
 32. Engreitz, J. M. *et al.* RNA-RNA interactions enable specific targeting of

- noncoding RNAs to nascent Pre-mRNAs and chromatin sites. *Cell* **159**, 188–99 (2014).
33. Nilsson, J., Evander, M., Hammarström, B. & Laurell, T. Review of cell and particle trapping in microfluidic systems. *Anal. Chim. Acta* **649**, 141–157 (2009).
 34. Hosic, S., Murthy, S. K. & Koppes, A. N. Microfluidic Sample Preparation for Single Cell Analysis. *Anal. Chem.* **88**, 354–380 (2016).
 35. Collins, D. J., Neild, A., deMello, A., Liu, A.-Q. & Ai, Y. The Poisson distribution and beyond: methods for microfluidic droplet production and single cell encapsulation. *Lab Chip* 3439–3459 (2015). doi:10.1039/C5LC00614G
 36. Xin, Y. *et al.* Use of the Fluidigm C1 platform for RNA sequencing of single mouse pancreatic islet cells. *Proc. Natl. Acad. Sci. U. S. A.* **113**, 3293–3298 (2016).
 37. Yin, H. & Marshall, D. Microfluidics for single cell analysis. *Curr. Opin. Biotechnol.* **23**, 110–119 (2012).
 38. Liu, W., Chen, D., Du, W., Nichols, K. P. & Ismagilov, R. F. SlipChip for immunoassays in nanoliter volumes. *Anal. Chem.* **82**, 3276–3282 (2010).
 39. Shen, F. *et al.* Nanoliter multiplex pcr arrays on a slipchip. *Anal. Chem.* **82**, 4606–4612 (2010).
 40. Shen, F. *et al.* Multiplexed quantification of nucleic acids with large dynamic range using multivolume digital RT-PCR on a rotational SlipChip tested with HIV and hepatitis C viral load. *J. Am. Chem. Soc.* **133**, 17705–17712 (2011).

41. Sun, B. *et al.* Mechanistic evaluation of the pros and cons of digital RT-LAMP for HIV-1 viral load quantification on a microfluidic device and improved efficiency via a two-step digital protocol. *Anal. Chem.* **85**, 1540–1546 (2013).
42. Sun, B. *et al.* Measuring fate and rate of single-molecule competition of amplification and restriction digestion, and its use for rapid genotyping tested with hepatitis C viral RNA. *Angew. Chemie - Int. Ed.* **53**, 8088–8092 (2014).
43. Selck, D. A., Karymov, M. A., Sun, B. & Ismagilov, R. F. Increased robustness of single-molecule counting with microfluidics, digital isothermal amplification, and a mobile phone versus real-time kinetic measurements. *Anal. Chem.* **85**, 11129–11136 (2013).
44. Ma, L. *et al.* Gene-targeted microfluidic cultivation validated by isolation of a gut bacterium listed in Human Microbiome Project's Most Wanted taxa. *Proc. Natl. Acad. Sci. U. S. A.* **111**, 9768–73 (2014).
45. Ge, S., Liu, W., Schlappi, T. & Ismagilov, R. F. Digital, ultrasensitive, end-point protein measurements with large dynamic range via brownian trapping with drift. *J. Am. Chem. Soc.* **136**, 14662–14665 (2014).
46. Shen, F., Du, W., Kreutz, J. E., Fok, A. & Ismagilov, R. F. Digital PCR on a SlipChip. *Lab Chip* **10**, 2666–72 (2010).
47. Shen, F. *et al.* Digital isothermal quantification of nucleic acids via simultaneous chemical initiation of recombinase polymerase amplification reactions on SlipChip. *Anal. Chem.* **83**, 3533–3540 (2011).

48. Du, W., Li, L., Nichols, K. P. & Ismagilov, R. F. SlipChip. *Lab Chip* **9**, 2286 (2009).
49. Ma, L. *et al.* Individually addressable arrays of replica microbial cultures enabled by splitting SlipChips. *Integr. Biol. (Camb)*. **6**, 796–805 (2014).
50. Ma, L. *et al.* Individually addressable arrays of replica microbial cultures enabled by splitting SlipChips. *Integr. Biol. (Camb)*. **6**, 796–805 (2014).
51. Collins, D. J., Neild, A., deMello, A., Liu, A.-Q. & Ai, Y. The Poisson distribution and beyond: methods for microfluidic droplet production and single cell encapsulation. *Lab Chip* 3439–3459 (2015). doi:10.1039/C5LC00614G
52. Pamme, N. Magnetism and microfluidics. *Lab Chip* **6**, 24–38 (2006).
53. Li, L., Karymov, M. A., Nichols, K. P. & Ismagilov, R. F. Dead-end filling of slipchip evaluated theoretically and experimentally as a function of the surface chemistry and the gap size between the plates for lubricated and dry slipchips. *Langmuir* **26**, 12465–12471 (2010).
54. Lee, S. H., van Noort, D., Lee, J. Y., Zhang, B.-T. & Park, T. H. Effective mixing in a microfluidic chip using magnetic particles. *Lab Chip* **9**, 479–82 (2009).
55. Nagano, T. *et al.* Single-cell Hi-C for genome-wide detection of chromatin interactions that occur simultaneously in a single cell. *Nat. Protoc.* **10**, 1986–2003 (2015).
56. Nagano, T. *et al.* Comparison of Hi-C results using in-solution versus in-nucleus ligation. *Genome Biol.* **16**, 175 (2015).

57. Dev, V. G., Tantravahi, R., Miller, D. A. & Miller, O. J. Nucleolus organizers in *Mus musculus* subspecies and in the rag mouse cell line. *Genetics* **86**, 389–398 (1977).
58. Simon, M. D. *et al.* The genomic binding sites of a noncoding RNA. *Proc. Natl. Acad. Sci. U. S. A.* **108**, 20497–502 (2011).
59. Rao, S. S. P. *et al.* A 3D map of the human genome at kilobase resolution reveals principles of chromatin looping. *Cell* **159**, 1665–80 (2014).

Chapter 8 - Supplement:

Intra-Chromosomal Interaction Matrices

Shown below are the intra-chromosomal correlation heat maps for each of the mouse chromosomes excluding Y. Each of the heat-maps shows the same type of data which is shown in Fig 8-5. The data was generated using the in-nuclei digestion method, followed by split-and-pool barcoding. The total number of desired reads was 40M in this particular run. The data was binned at the megabase resolution, and the correlation score is normalized to the number of reads for a particular bin as to not bias called interactions towards those regions with higher sequencing coverage. The interaction score denotes the either enrichment (positive) or depletion (negative) of interactions as compared to if all interactions were random. Each page shows four different chromosomes with the interaction score shown beneath each figure.

Fig 8S-1 – Chromosomes 1-4

Fig 8S-2 – Chromosomes 5-8

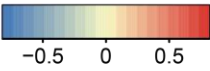
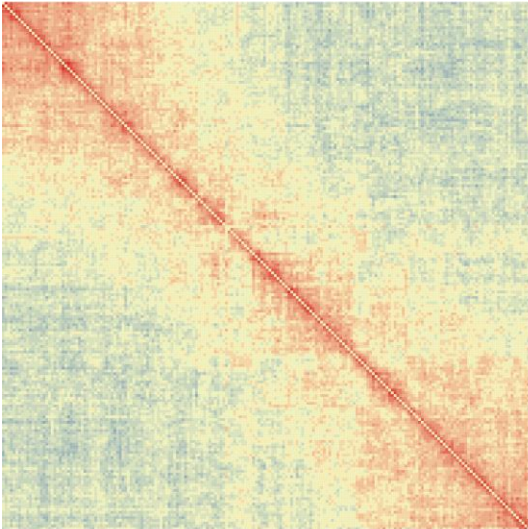
Fig 8S-3 – Chromosomes 9-12

Fig 8S-4 – Chromosomes 13-16

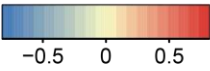
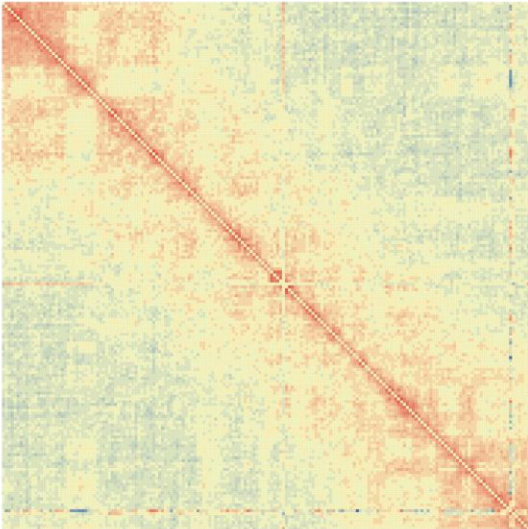
Fig 8S-5 – Chromosomes 17-X

Fig 8S-1

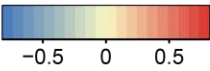
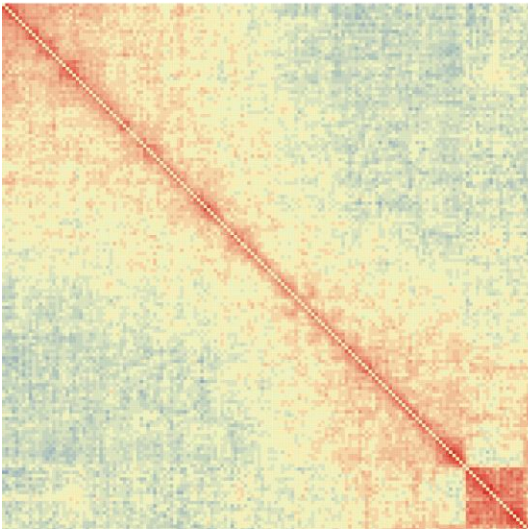
Chromosome 1



Chromosome 2



Chromosome 3



Chromosome 4

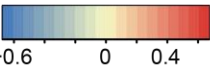
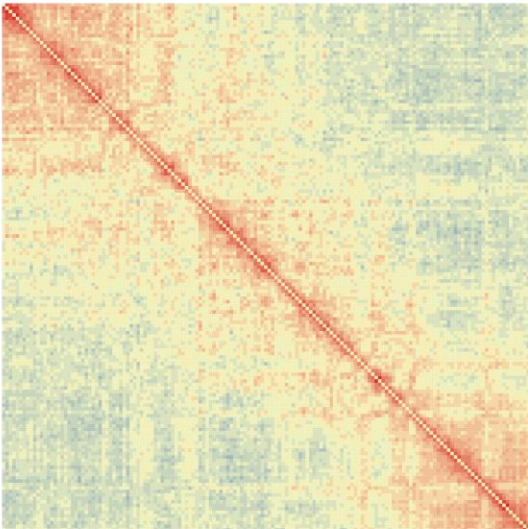
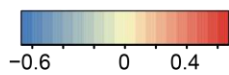
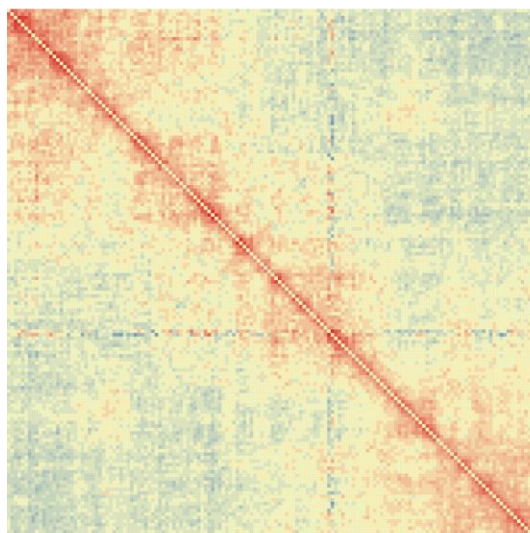
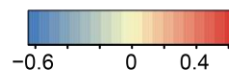
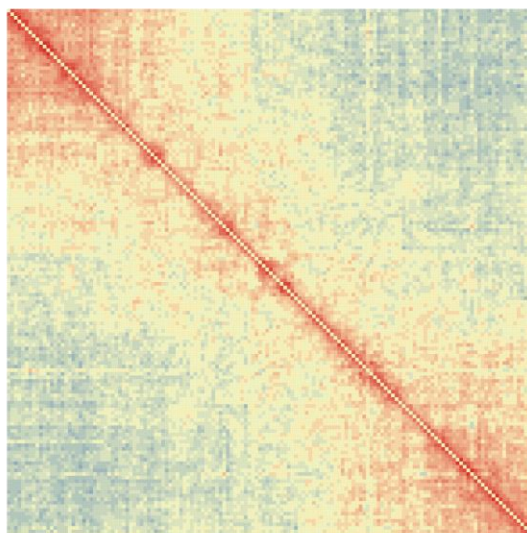


Fig 8S-2

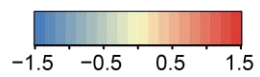
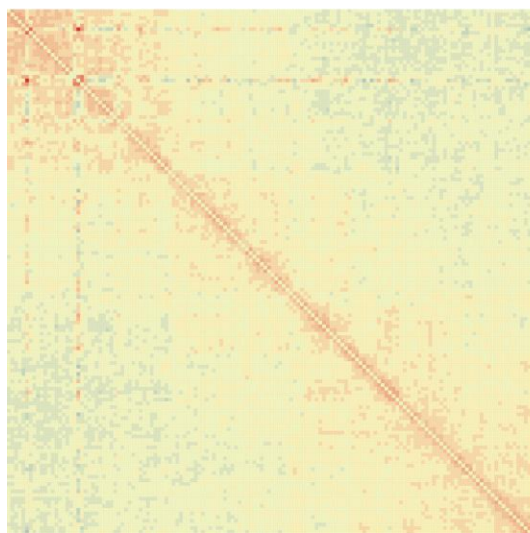
Chromosome 5



Chromosome 6



Chromosome 7



Chromosome 8

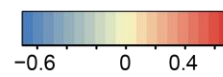
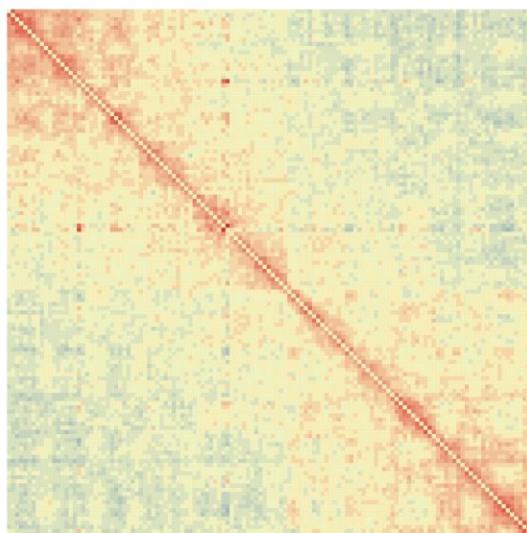
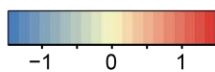
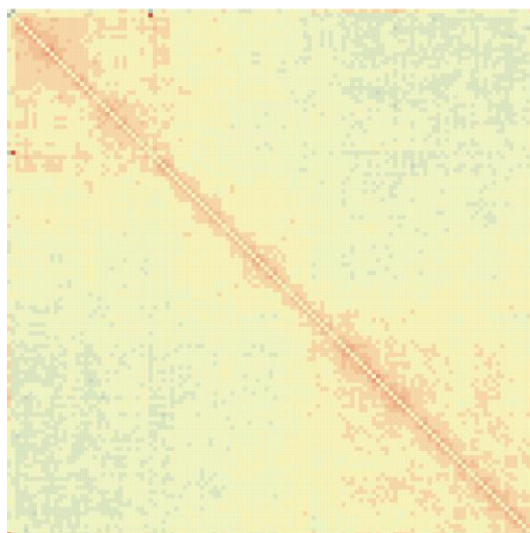
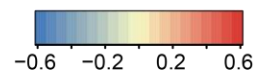
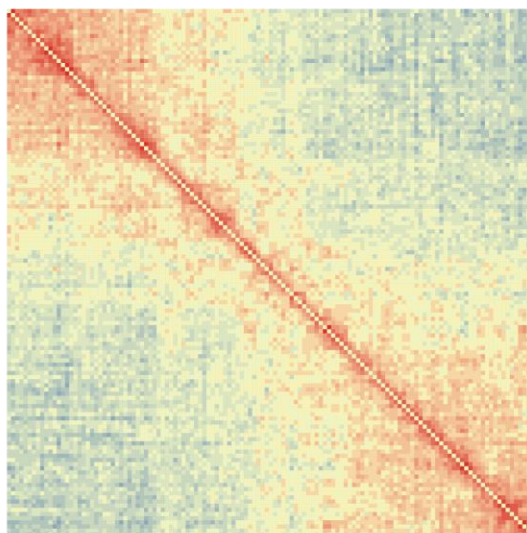


Fig 8S-3

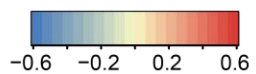
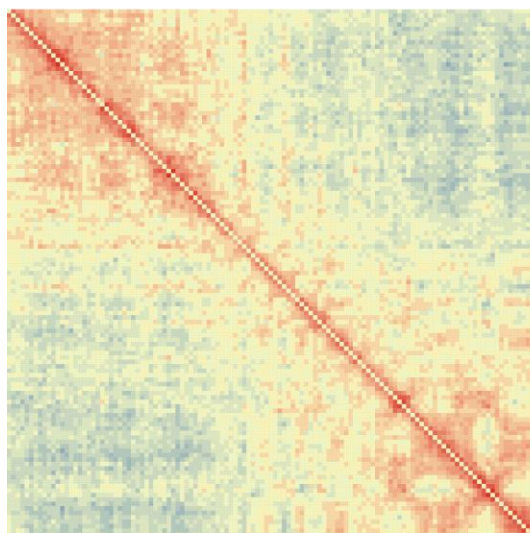
Chromosome 9



Chromosome 10



Chromosome 11



Chromosome 12

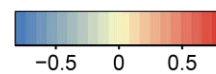
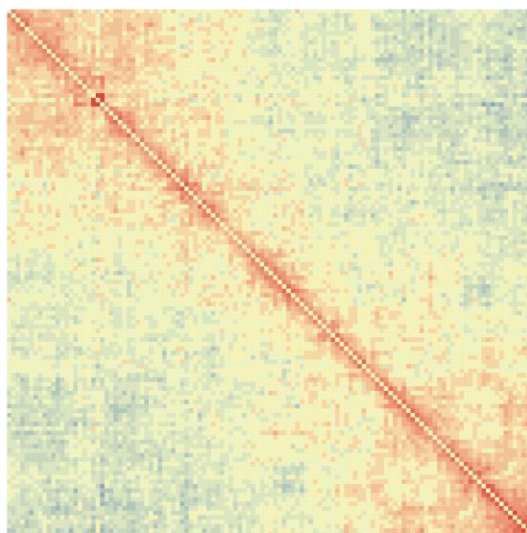
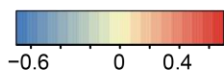
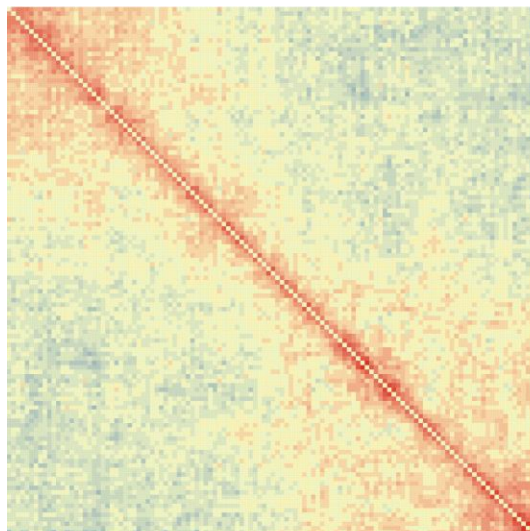
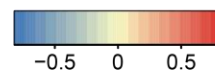
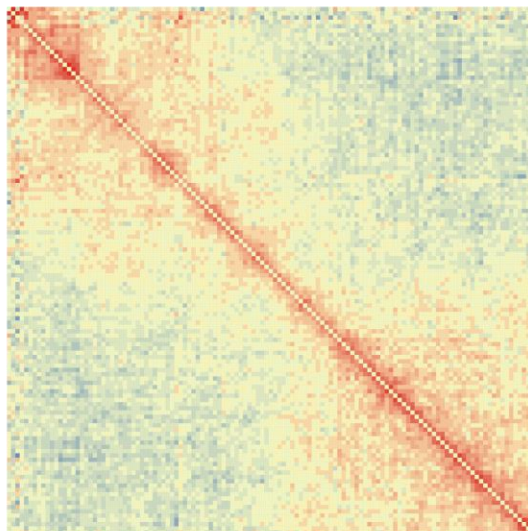


Fig 8S-4

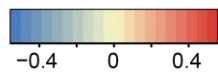
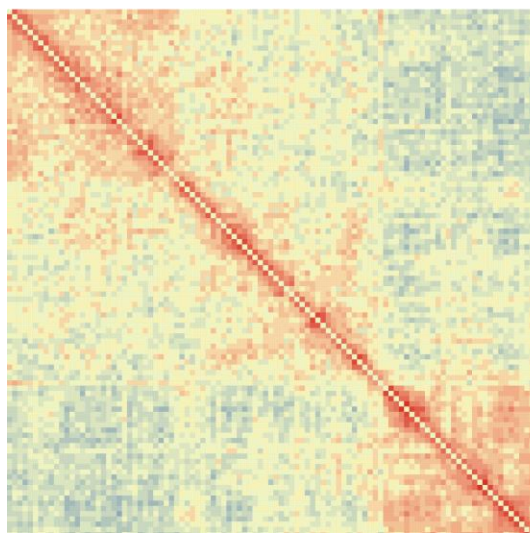
Chromosome 13



Chromosome 14



Chromosome 15



Chromosome 16

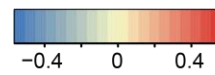
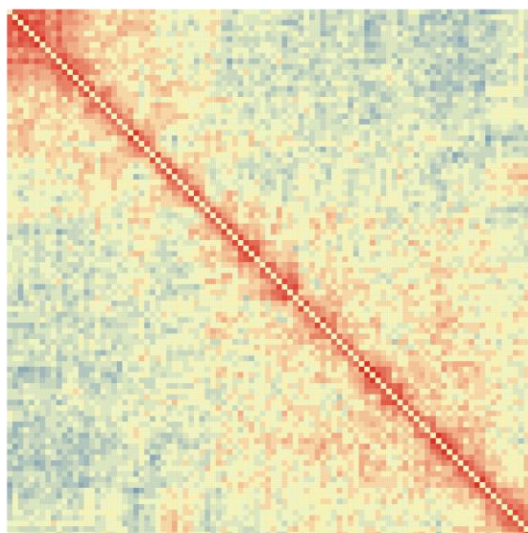
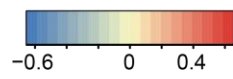
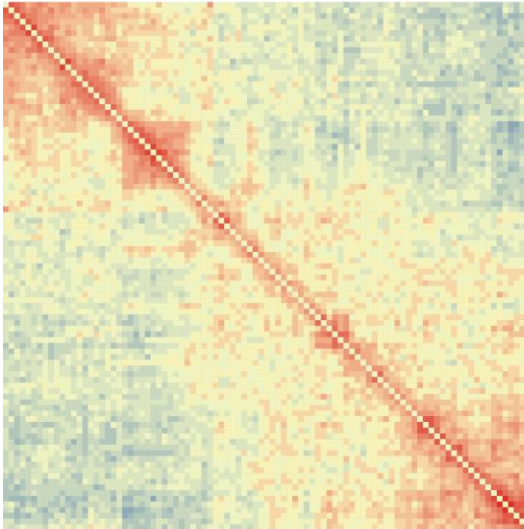
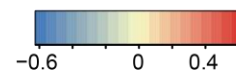
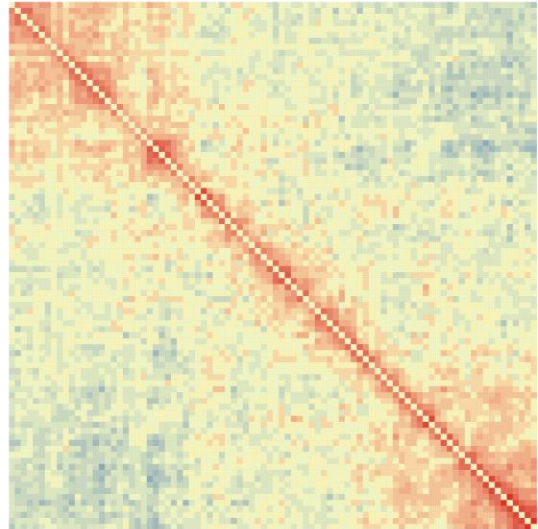


Fig 8S-5

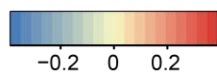
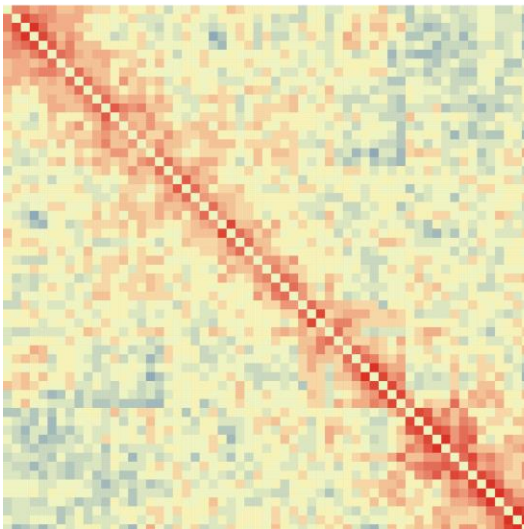
Chromosome 17



Chromosome 18



Chromosome 19



Chromosome X

